Effect of the Environment on the Fatigue Behaviour of Textile Organic Matrix Composite Materials for Aircraft Applications

Federico Foti

THESE

Pour l'obtention du Grade de

DOCTEUR DE L'ECOLE NATIONALE SUPERIEURE DE MECANIQUE ET D'AEROTECHNIQUE

(Diplôme National – Arrêté du 25 mai 2016)

Ecole Doctorale Sciences et Ingénierie en Matériaux, Mécanique, Energétique et Aéronautique

Secteur de Recherche : Mécanique des solides, des Matériaux, des Structures et des Surfaces

Présentée par :

Federico FOTI

****

Effect of the environment on the fatigue behaviour of textile organic matrix composite materials for aircraft applications

-

Effet de l'environnement sur la fatigue de matériaux composites tissés à matrice organique pour applications aéronautiques

****

Directeur de thèse **:** Marco GIGLIOTTI

Co-encadrant : Yannick PANNIER

****

Soutenue le 24 Novembre 2017

devant la Commission d'Examen

****

JURY

Rapporteurs :

Stepan LOMOV, Professeur, Katholieke Universiteit Leuven, Belgium

Valter CARVELLI, Professeur, Politecnico di Milano, Italie

Membres du jury :

Christian HOCHARD, Professeur, Université de Marseille

Nicolas CARRERE, Ingénieur de recherche, SAFRAN Tech- Composites

Pascal DOUMALIN, Maître de Conférences, Université de Poitiers

Marie-Christine LAFARIE-FRENOT, Professeur Emérite, Université de Poitiers-ISAE ENSMA

THESE

Pour l'obtention du Grade de

DOCTEUR DE L'ECOLE NATIONALE SUPERIEURE DE MECANIQUE ET D'AEROTECHNIQUE

(Diplôme National – Arrêté du 25 mai 2016)

Ecole Doctorale Sciences et Ingénierie en Matériaux, Mécanique, Energétique et Aéronautique

Secteur de Recherche : Mécanique des solides, des Matériaux, des Structures et des Surfaces

Présentée par :

Federico FOTI

****

Effect of the environment on the fatigue behaviour of textile organic matrix composite materials for aircraft applications

-

Effet de l'environnement sur la fatigue de matériaux composites tissés à matrice organique pour applications aéronautiques

****

Directeur de thèse **:** Marco GIGLIOTTI

Co-encadrant : Yannick PANNIER

****

Soutenue le 24 Novembre 2017

devant la Commission d'Examen

****

JURY

Rapporteurs :

Stepan LOMOV, Professeur, Katholieke Universiteit Leuven, Belgium

Valter CARVELLI, Professeur, Politecnico di Milano, Italie

Membres du jury :

Christian HOCHARD, Professeur, Université de Marseille

Nicolas CARRERE, Ingénieur de recherche, SAFRAN Tech- Composites

Pascal DOUMALIN, Maître de Conférences, Université de Poitiers

Marie-Christine LAFARIE-FRENOT, Professeur Emérite, Université de Poitiers-ISAE ENSMA

Remerciements

L'accomplissement de ce travail a été possible grâce à la collaboration avec une bonne partie du personnel du Département de Physique et Mécanique de Matériaux de l'ENSMA et grâce au support économique de la région Poitou-Charentes (maintenant Nouvelle Aquitaine).

Le premier remerciement va donc à mes encadrants de thèse Marco Gigliotti et Yannick Pannier, tout d'abord pour m'avoir choisi parmi les plusieurs candidats et ensuite pour leur support (professionnel et moral) durant ces trois années de thèse. Merci pour tous les avis scientifiques, pour vos suggestions et pour toutes les discussions enrichissantes que l'on a eu.

Je tiens à remercier tout le personnel technique du DPMM pour leur support pendant ma campagne d'essais ; un grand MERCI va à David Mellier pour avoir toujours eu deux (…ou plus…) minutes à disposition pour pouvoir chercher ensemble une solution à toutes sortes de soucis techniques. Un remerciement est dû à Brigitte Vigner et Karine Lombard pour le support « administratif », à Gerald Sailly pour le support informatique et à Mikael Gueguen et Yuriy Sinchuk pour l'appui sur la partie numérique de ma thèse.

Je suis reconnaissant à tous les membres du jury, venus de plus ou moins loin pour juger ma thèse et pour avoir animé une discussion très instructive sur mon travail. L'une des plus grandes satisfactions en fin de ce travail est d'avoir eu dans le jury des professionnels de votre niveau qui ont lu et apprécié le résultat de ces trois années de thèse.

De toute façon, dans la thèse il n'y a pas que…la thèse !!

Je dois impérativement remercier toutes les personnes qui ont facilité mon arrivée au labo et avec lesquelles on a partagé des *beaux moments*. Je remercie Jocelyne Bardeau pour m'avoir assisté dans la recherche d'un logement bien avant de me connaître en personne. Merci à l'ATEM 2015 (sans doute le meilleur ATEM de toute l'histoire !!) pour m'avoir aidé à m'intégrer dans le labo malgré les barrières linguistiques et pour m'avoir fait découvrir la pizza Moutarde-Poulet (Maledetti !!!). Pendant ces années j'ai passé beaucoup beaucoup de temps avec mes collègues de bureau : le sage Camille Guigon, le joyeux Andrea Ramazzotti, la « sérieuse » Aude Laurence, le petit Cyril et enfin, la personne avec laquelle j'ai partagé pour le plus long temps la souveraineté du bureau : l'organisatrice de séjours/voyages/repas/… (bon ! tous types d'évènements), Mlle. Gaëlle Chretien. Il ne faut pas oublier tous les doctorants que j'ai croisé durant ces années et qui contribuent à créer une ambiance de travail très agréable. Un merci donc à Nathan, Layla, Alice, Selim, François, Paul, Sami, Ravi, Amélie M. and Amélie P., Louis, Benjamin, Lorena et les autres. Merci également à toutes les personnes du labo : Profs, IE, IR, MdC, Post-doc, etc. pour votre professionnalité et pour les

conversations pédagogiques. A propos de pédagogie, merci à Francine pour toutes les discussions et pour ses enseignements de vie et de langue (Français et Allemand) donnés dans les locaux de la kfet.

Un remerciement très particulier va à la *Famiglia Italiana* !!! Merci à Saverio, Giovambattista, Andrea et Antonio pour l'accueil *Calabrian Style*! Merci à vous et à Vincenzo, Barbara, Flavio, Marina, Nonno Pedoto, Julien et Momo (oui, pour moi vous êtes italiens) pour les moments passés ensemble…grâce à vous la nostalgie de notre pays natal ne se sent pas du tout! Merci à Lord Rotella pour avoir été mon compagnon d'aventure pour les sports, pour les voyages (de l'espoir), pour les sorties et tous types de conneries !! Merci aussi à toute la communauté d'italiens (et *quasi*-italiens) à Poitiers pour m'avoir accueilli et pour avoir partagé votre expérience en « *terre étrangère* » avec moi.

Merci à tous ceux qui sont partis d'Italie et se sont tapé entre 1000 et 2000 km pour être avec moi le jour de ma soutenance, je suis content que malgré les années passées et la distance qui sépare notre amitié, on arrive toujours à former un groupe très solide et…*fêtard* !!

Finalement, il n'y a pas de mots pour pouvoir exprimer ma reconnaissance vers mes parents et ma sœur. Merci pour m'avoir donné la possibilité de faire ce que je voulais vraiment faire sans jamais conditionner mes choix et, au contraire, en me supportant pendant ces années et en étant présents dans les moments difficiles ainsi que dans les moments de joie. Je vous aime !

Le dernier chaleureux remerciement, va à une personne sans laquelle très probablement je n'aurais pas eu la force d'atteindre cet objectif (…et beaucoup d'autres…), ma merveilleuse copine ! GRAZIE ELE…Comme plusieurs fois j'ai dit, « un jour je te sculpterai une statue pour te remercier » et cela ne suffira quand même pas à te faire comprendre ma gratitude. Merci pour avoir égayé mes journées, pour les voyages, pour avoir été là quand j'en avais besoin et pour chaque seconde passée ensemble.

Enfin….Merci à tous !!!

Federico

INDEX

Introduction

The employment of fibre-reinforced composites in the transport industry has significantly increased in the last decades due to their high specific properties (stiffness, strength) and fatigue resistance in the fibre direction. Being strongly interested in the realization of lightweight airframes by using composite materials, the aeronautic industry plays a pioneering role in the employment of these materials. Composite (no structural) parts are used on aircrafts since '50s, and the presence of these materials has increased in the following years. Later, composites have been employed also for structural parts as spoilers, flaps, centre wingbox, fuselage, etc… reaching more than the 50% in weight of the whole structure on the last generation aircrafts. The employment of composites in the realization of many "cold" aircraft components replacing metallic ones is coming to saturation (*see Fig.1*).

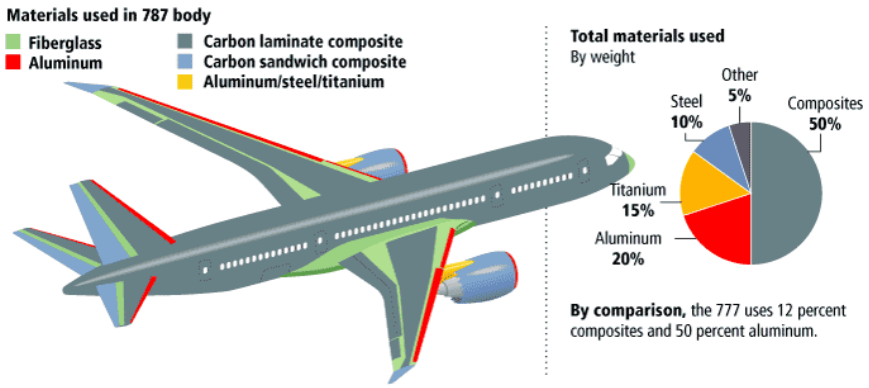

Fig.1 : Composite materials employed in the realization of the new generation aircraft Boeing 787 Dreamliner (www.boeing.com).

To improve the cost-effectiveness of the air transport sector, two of the major world aircraft engine manufacturers (*Safran Aircraft Engine* and *General Electric*) started the development of a new engine named LEAP (Leading Edge Aviation Propulsion), realized using different kind of composite materials to reduce the engine weight and to increase engine efficiency. The introduction of composites in aircraft engines is the actual manufactures trend, moreover, in the future engine generations, Organic Matrix Composite (OMC) will be employed in "warm" engine regions, where the maximal temperatures are in the range 150°-250°C.

To ensure the airworthiness of these composite structures, it is necessary to understand how the composite ageing and the in-service damage could affect the integrity of the composite components. Some components as fan/compressor blades will be exposed, in service, to creep and fatigue loads, furthermore, for these components, high temperatures accelerate the ageing process (oxygen diffusion and all the oxidation reactions of the organic matrix) (Minervino, 2013).

In the literature the fatigue degradation and the oxidation of composite materials is well detailed. A continuous decrease of the mechanical properties is observed as a fatigue load is applied. At a microscopic level, several damage forms are observable as matrix cracks, delamination or debonding. Oxidation leads to an embrittlement of the matrix and to a chemical shrinkage (Olivier, 2008) leading to matrix cracks onset and multiplication. In a unidirectional composite material, fibre/matrix debonding can be observed during thermal cycling without any mechanical load applied to the specimen. The new exposed surfaces resulting from these debonding regions, make the oxygen penetrates deep in the specimen. When this process is associated to a mechanical load, the damage forms related to the applied load could interact with the oxidation creating a synergistic effect between the mechanical damage and the oxidative environment.

The engine environmental conditions are not easy to duplicate during a laboratory test and a procedure to perform accelerated high temperature fatigue test is not already existent. Some authors show as thermo-oxidation test on organic matrix could be accelerated using a (moderate) high oxygen partial pressure. This technique is often used to characterize the long-term ageing effect of an organic resin in a few weeks. However, if a mechanical load is applied during the composite specimen ageing, the synergistic effects between mechanical damage and oxidation could lead to a faster degradation of the specimen; furthermore, the damage mechanisms observed during fatigue and during matrix ageing separately, may interact leading to a new damage scenario, far from which observed during fatigue or ageing individually. Other phenomena as creep/fatigue/environment interaction could appear during high temperature fatigue. The creep deformations, generally not negligible, are a function of the maintain time and an environmental effect on these cumulated deformations during fatigue has not been proven yet.

The present work aims at characterizing the damage forms and the thermo-oxidation effects on damage onset/propagation kinetics during high temperature fatigue of OMC. Specifically developed test machine and highly accurate damage observation techniques have been employed to characterize quantitatively the damaged volume and to identify its orientation, its localization in the volume… Novel approaches are proposed to describe the damage scenario and to evaluate the specimen "health" during fatigue tests. The long-term objective of this study is to provide experimental and numerical tools to enhance the understanding and modelling of mechanical/damage/environment

coupling for durability prediction and for the proposal of realistic accelerated test protocols of "warm" OMC parts.

The results of mechanical fatigue tests are presented and discussed in this thesis; these tests performed in different environmental conditions, will be named *multi-physical fatigue tests* to underline the chemical, physical and mechanical phenomena taking place during this kind of laboratory tests. A specifically developed testing setup is employed to test specimen in *multi-physical fatigue* and for damage assessment. Two organic composite architectures are studied: a $[0_2/90_2]_s$ Carbon fibre/Epoxy matrix unidirectional cross-ply laminate and a $[45_6]$ Carbon fibre/Polyimide matrix 8-harness satin woven laminate. The first architecture is deliberately chosen to minimize the viscous effects, moreover damage in this laminate can be easily quantified and the environmental effects can be analysed using existing analytical models. The second architecture is not a *model* architecture as the first one, but a *real* material having a behaviour and a damage scenario requiring the development of adapted experimental approaches to be characterized. *Multi-physical fatigue* of these woven laminates is the main subject of this work. *In-situ* and *ex-situ* damage observations are performed during fatigue tests: Digital Image Correlation (DIC) is employed for a full-field strain mapping on the specimen surface, while *ex-situ* μ-Computed Tomography (μCT) is used for 3D damage observation. μCT scans allow micro scale damage characterisation and localization, this last is a fundamental damage feature in characterising environmental effects. Information concerning damage orientation and damage localization in the volume are employed in an analytical model developed to identify the micro scale damage effect on the macro scale properties. The developed analytical model is used to understand how an oxidizing environment affects the degradation of macro scale specimen properties and to conceive smart strategies for part design (as damage tolerant approaches…) .

In the **first chapter** a literature review concerning fatigue degradation and matrix ageing is presented. The provided tools, the findings and the highlighted lacks of this chapter represent the initial point for the test methodologies and the results discussion presented in this work.

The **second chapter** is devoted to the presentation of the testing machine, the measurement techniques and the post processing procedures. In particular, some details about full field Digital Image Correlation and μ-Computed Tomography are given. The applicability and the limits of each employed technique and/or post processing procedure is described and discussed.

The *multi-physical fatigue* test results obtained for the cross-ply laminated specimens are reported and discussed in the **third chapter**. The transversal crack multiplication on the lateral edges of the specimens during fatigue in different environmental conditions is studied.

The **fourth chapter** presents the *multi-physical fatigue* test results obtained for the woven laminated specimens. Macroscopic properties evolution and the observed damage scenario are described. The

uncertain relation between damage development, environmental acceleration factor and macroscopic properties evolution leads to a deeper investigation on creep/fatigue interaction on the woven laminates behaviour and about damage distribution inside the specimens.

In the **fifth chapter**, DIC is employed to characterize both damage evolution at the micro-scale and at the macro-scale. μCT allows having a *ply-by-ply* damage description that is integrated in an analytical *ply-by-ply* specimen mechanical model, developed to study the macro-scale effects of the damage at the micro-scale.

Chapter 1

Literature survey

This chapter presents a literature survey concerning fatigue, damage characterization and thermo-oxidation behaviour of organic matrix composite materials. It is shown that numerous work are addressed to composite fatigue and thermo-oxidation characterization, while only few studies on interaction between mechanical loads and oxidation are available in literature, highlighting that this subject is, actually, poorly explored.

Summary

The bibliographic review reported in this chapter is intended to give a short introduction on composite materials and on the most recurrent methods used in the literature for damage characterization. In these first paragraphs, some items concerning the behaviour and the damage mechanisms related to particular composite architectures is depicted to support the analysis on damage scenario of the following chapters. The focus of this chapter is, however, on the thermo-oxidation of organic matrix and organic matrix composites: the synergic effect *oxidation-damage* is highlighted in order to clarify the interaction of several physical, chemical and mechanical aspects involved in the experimental activity presented in the Chapter 3 and Chapter 4.

1.1 Composite materials

A material composed of two or more distinct phases is one of the possible definitions of a composite material. Thus a composite materials is an heterogeneous material and, in such a way, all the materials could be considered as composite materials if the analysis level is sufficiently small (C.T. Herakovich, 1998). Some particular industrial applications require the employment of materials having properties that in conventional materials (metals and metal alloys, ceramics, polymers) are not achievable (Callister, 2007). An example is the increasingly searching of the aeronautical industry for structural elements light, strong and stiff at the same time. In this field, fibrous composites are widely employed: for these materials a phase acts as a reinforcement for a second phase called matrix.

The fibrous reinforcement is chosen weighting several criteria as the price, the mechanical and the physical properties. Different kinds of fibre are available on the world market (natural fibres, metal fibres, ecc…), but generally *advanced fibres* are foreseen for structural applications. These fibres allow having a high *specific stiffness* (stiffness divided by density) and high *specific strength* (strength divided by density). *Fig.1.1* shows the Young *modulus* (E) of some fibres as a function of their density: the higher specific properties characterize the fibre types lying to the upper-left side of the graph. In detail, carbon fibres offer the better specific properties and for this reason are commonly employed for structural components on aircrafts, moreover carbon fibres show an excellent thermal stability until 1200°C (Lamouroux et al., 1999), consequently are forecast also for the realization of cold/warm parts.

The matrix choice is generally dictated by the application temperatures, by the fibre/matrix interface properties and by its mechanical properties. Polymers are the most employed matrix (Gornet, 2008), while ceramic, carbon or metallic matrix are forecast for particular high temperature applications. Polymeric or *organic* matrix can be subdivided in thermoplastics and thermosets: the former have low

mechanical properties, they are low-cost processing and can withstand temperature until 200°C (Gabrion et al., 2016).

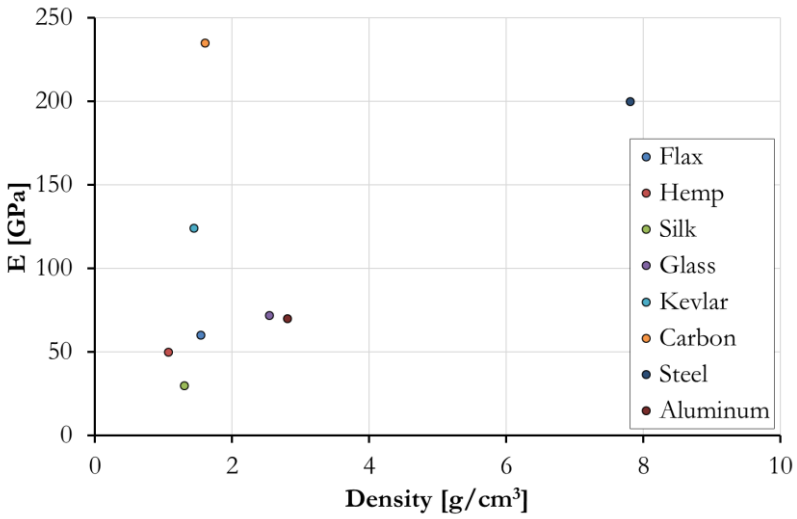

Fig.1.1 : Young *modulus* (E) of different fibre types as a function of their density.

This category includes PPS (polyphenylene), PEEK (poly-eter-eter-ketone), PEKK (poly-eter-ketone-ketone) and others. To the second category belong the polyesters, epoxies and polyimides. These resins are lightweight, inexpensive and the useful temperature range upward is 100°C. Recent developments of polyimide resins led to the fabrication of some matrix having a better thermal stability as the PMR-15 (Meador et al., 1996), a PMR (Polymerisation of Monomer Reactants – 15 is the molecular weight of the oligomer 1.5 g/mol) thermoset resin developed in the mid-1970s at the NASA Lewis Research Centre and widely used for composite applications in the temperature range 260-288°C (Mangalgiri, 2005). The industrial interest in using this last matrix brought a large number of scientists to characterize this resin and the derived composites in terms of mechanical response and thermal stability. In the 1980s some chemical reagents used during the fabrication process have been declared dangerous for the human health. Many aircraft manufacturers keep using the PMR-15 due to the additional costs related to the development and to the employment of a new production process and the potential liability in use this matrix. Several replacements for this resin have been proposed as the POSS (Polyhedral Oligomeric Silsesquioxane Dianiline) (Lamb, 2016) or the MVK-14, jointly developed by Maverick and GE aviation and having service temperature, provided by the manufactured, up to 316°C.

The PMR-15 and MVK-14 resin systems are appropriated for warm components fabrication because the mechanical properties do not significantly degrade up to 200/300°C. Other phenomena, related to the aging of these resins at high temperature, are presented in paragraph 1.7.

1.2 Composite architectures

The simplest composite architecture is the unidirectional (UD) lamina *Fig.1.2*. In a unidirectional lamina, all the fibres oriented along the same direction. It can be fabricated by filament winding, pultrusion, resin transfer molding (RTM) or using pre-impregnated. For a UD lamina the stiffness and the strength along the fibre direction is much greater than in the transverse directions and the mechanical properties are generally orthotropic in the principal material coordinates, reported in *Fig.1.2* using the coordinate system 1, 2, 3. Other architectures can be obtained grouping fibres to have yarn or tow, then interlaced to create a fabrics 2D or 3D.

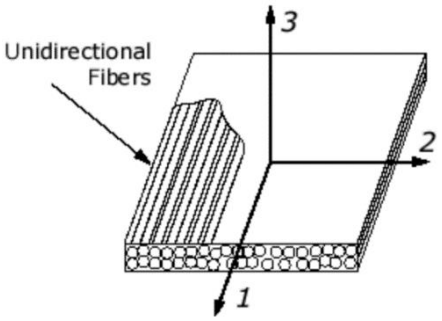

Fig.1.2 : Unidirectional lamina and principal coordinate system. (efunda, 2017)

A detailed classification of the different fabric types is illustrated in *Fig.1.3*. From a mechanical point of view, a textile allows having similar properties in the longitudinal and transversal direction, contrarily to an UD *lamina*.

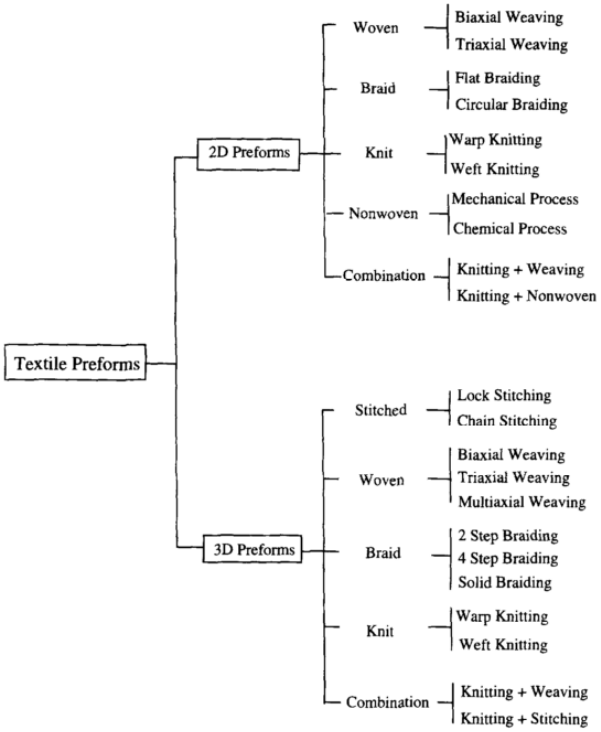

Fig.1.3 : Various techniques of manufacturing textile fibre preforms. (Ramakrishna, 1997)

Between fabrics, one of the more used preforms is the 2D woven. Some weave patterns are represented in *Fig.1.4*. The choice of the weave pattern is commonly based on two items: first of all the easy handling of the woven ply and, on the other hand, the loss of mechanical properties due to the fibre crimp angle. Concerning this last point, in (Daniel, Luo and Schubel, 2008) the longitudinal properties of a 5 harness satin (5HS) and of an UD fabricated using the same matrix and the same fibres are compared: the 5HS woven shows a stiffness and a strength that are roughly half those measured for the UD. The authors assume that this behaviour is due to the similarity of the 5HS woven to a two UD *laminae* superposed and perpendicular. One of the most used weave pattern is the 8HS woven, where each weft fibre tow passes over seven warp tows and one under, this pattern brings to a fabric that can be used to fit easily very complex curve shape.

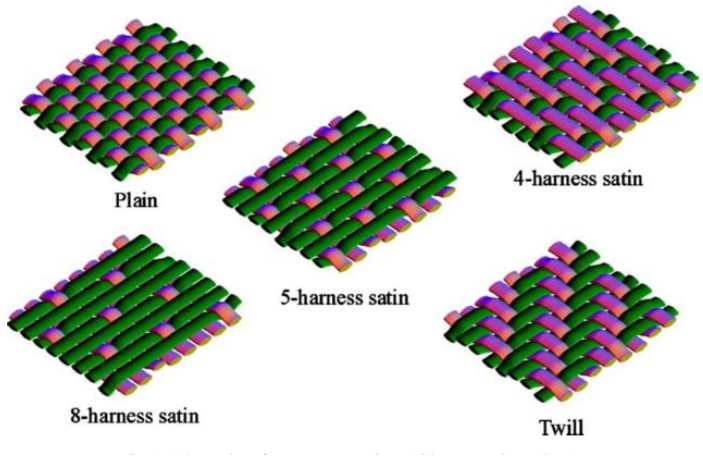

Fig.1.4 : Schematic of 2D woven composites. (Tang et al., 2005)

UD *laminae* or 2D fabric plies can be used to form a laminate. A laminate is realised by stacking layers of fabric or UD having the same or different fibre orientation. The laminate mechanical properties vary with the orientation, thickness and stacking sequence of the individual plies (C.T. Herakovich, 1998). Two laminates realised using UD layers are shown in *Fig.1.5*. In the first case the laminate is fabricated using layers oriented in same manner, the resulting laminate has an orthotropic behaviour.

The second laminate is fabricated using *laminae* differently oriented, the particular stacking sequence of this laminate, results in a composite having a quasi-isotropic behaviour. The notation used to refer to the first laminate is $[0_8]$, where the zero is the layer orientation and the subscript 8 is the number of layers. In the same manner, the notation for the second laminate is $[0/90/45/-45]_s$, where the subscript *s* out of the brackets means that the stacking sequence is symmetrical about the mid-plane of the laminate. A particular interest is devoted in the literature to angle-ply and cross-ply laminates, characterized by $[\theta_n/-\theta_m]_s$ and $[0_n/90_m]_s$ staking sequence, where *n* and *m* are the number of layers and θ is the tilt angle with respect to a common reference direction.

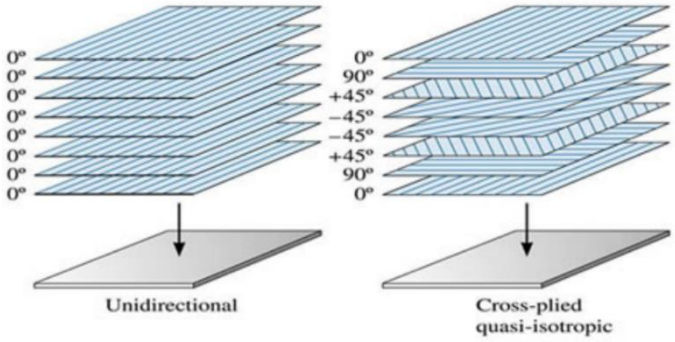

Fig.1.5 : Laminates composed by UD layers. UD laminate is obtained using only 0° layers, while a quasi-isotropic laminate is obtained varying the layers orientation. (Quartus, 2017)

The notation for 2D woven ply laminates is similar to that of UD laminates, some authors use a subscript F to specify that a layer is a fabric layer (*e.g.* $[0_{6F}]$), while other authors use the fibre orientations in the pattern (*e.g.* $[\pm 45_6]$).

The practical interest in using fibrous composite materials led many researchers to develop various experimental techniques for testing and characterizing the behaviour and the response of composite sample submitted to several mechanical, physical and chemical conditions. The next paragraph is devoted to a review on the damage characterization techniques developed for composite sample loaded in traction and fatigue.

1.3 Damage characterization of fibrous composite laminates

Two approaches are proposed in the literature for damage characterization: one based on the study of the specimen response during fatigue/traction and a second based on the study of the damage mechanisms.

In the first approach damage characterization follows often a phenomenological approach. An example is reported in (Talreja, 1985; Gao et al., 1999; Pandita et al., 2001) where the authors measure a stiffness reduction during fatigue of woven laminates and the same stiffness reduction is observed by (Berthelot, El Mahi and Leblond, 1996; Singh and Talreja, 2008; Ma et al., 2016) for fatigued UD laminates (*see Fig.1.6*). Alternatively, in (Petermann, 2004; Montesano et al., 2012; Vieille and Albouy, 2015) the authors quantify the damage as a growth of the free length of the specimen during fatigue (*see Fig.1.7*).

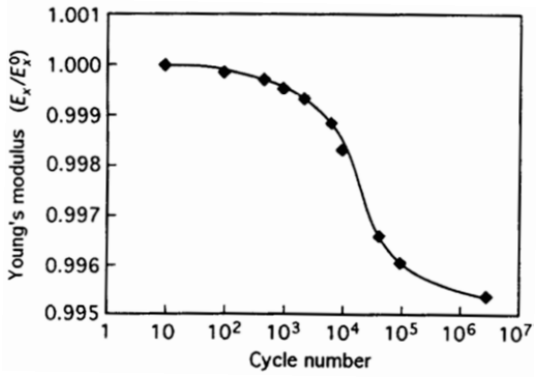

Fig.1.6 : Stiffness reduction for a UD laminate composite during fatigue. (Berthelot, El Mahi and Leblond, 1996)

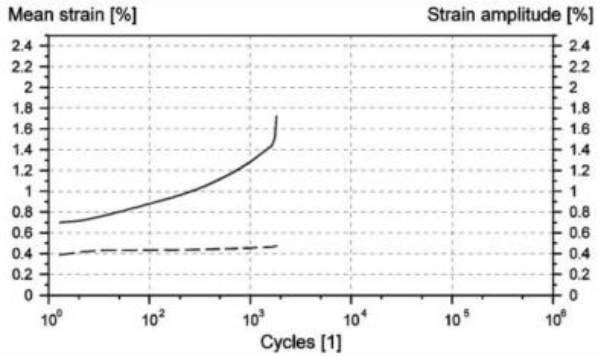

Fig.1.7 : Mean strain evolution during fatigue of UD laminates. (Petermann and Schulte, 2002)

The second approach focuses on the comprehension of the damage mechanisms and is based on the direct damage observation, consequently the damage characterization techniques of fibrous composite laminates are strictly linked to the observation scale. As argued in (Singh and Talreja, 2008) in a composite material, the damage has a multi-scale nature. Some authors (Ivanov, 2009; Rakotoarisoa, 2013) describe the damage scales making an analogy with the three characterization scales used to describe the mechanical response of a composite laminate (Lomov et al., 2007):

micro-scale, is the fibre/matrix scale and fibre/matrix debonding or inter-fibre crack formation are typical damage forms at this scale;

meso-scale, is the scale considering a fibrous ply or a whole tow, the damage at this scale includes intra-tow cracks, inter-tow delaminations and crack propagation in a UD ply;

macro-scale, at this scale the damage forms are the separation of delaminated yarns and the fibre breakage.

In *Fig.1.8* the structural hierarchy of the damage in a textile composite is represented as a function of the observation scales.

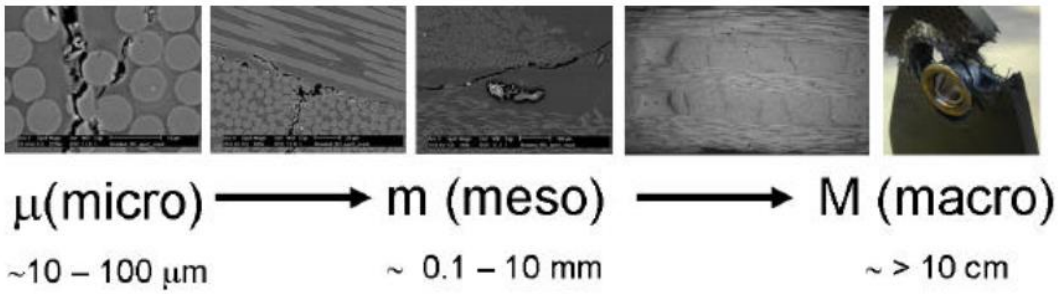

Fig.1.8 : Structural hierarchy of the damaged textile composite. (Ivanov, 2009)

For a detailed investigation on the damage mechanisms at the micro-scale several techniques have been developed. In (Osada, Nakai and Hamada, 2003) the authors use a replica film applied on the polished edge of a woven ply laminate to observe damage forms during interrupted tensile tests. Photographs of these replica are reported in *Fig.1.9*.

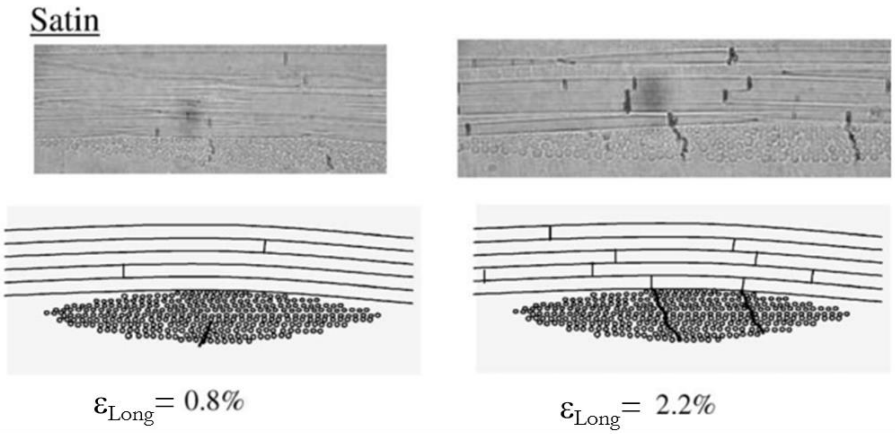

Fig.1.9 : Photograph obtained by replica observation. (Osada, Nakai and Hamada, 2003)

Optical techniques are widely employed for micro cracks observation. In (Gao et al., 1999) micro cracks images are issued by optical microscope, while in (De Greef et al., 2011; Backe, Balle and Eifler, 2015; Lisle et al., 2015) micro cracks are observed using a scanning electron microscope (SEM). The optical method has been improved in (Duplessis Kergomard et al., 2010) where in-situ microscope observations were enhanced by the introduction of a penetrant inspection dye to increase cracks detectability.

Recently, high resolution μ-Computed tomography (μCT) has been used in (Scott et al., 2011, 2012) for micro cracks observation (*see Fig.1.10*) and in (Raz-Ben Aroush et al., 2005) for fibre fracture detection. In particular, this last technique allows having a 3D image of the micro crack and quantifying the crack volume.

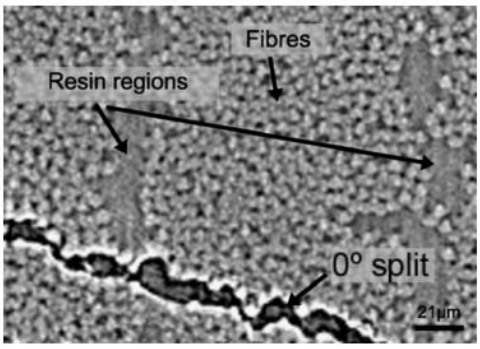

Fig.1.10 : Micro crack observed by μCT. (Scott et al., 2012)

The damage characterization at the macro/meso-scale is often based on the concept of *crack density*. The crack density evaluation is employed on both UD based laminates and woven based laminates. To estimate the *crack density* in a specimen during fatigue or traction, the meso cracks are, first of all observed and then, by a manually or an automatically procedure, counted. The crack density is finally obtained as the number of crack divided by a reference length. Several meso crack detection methods are reported in the literature. One of the more diffused is the X-Ray photograph, commonly used on textiles (Lomov, Ivanov, et al., 2008; De Greef et al., 2011) and UD laminates (Sun, Daniel and Luo, 2003; Lafarie-Frenot and Ho, 2006). Similar results are achievable on translucent material systems, using a light source and a camera for image acquisition as made in (Carvelli et al., 2009, 2010; Topal et al., 2015; Shen et al., 2017). An X-Ray photograph and a crack observation by retro-illumination method are reported in *Fig.1.11*: looking these pictures the cracks appear as black lines, consequently no information about crack thickness is available.

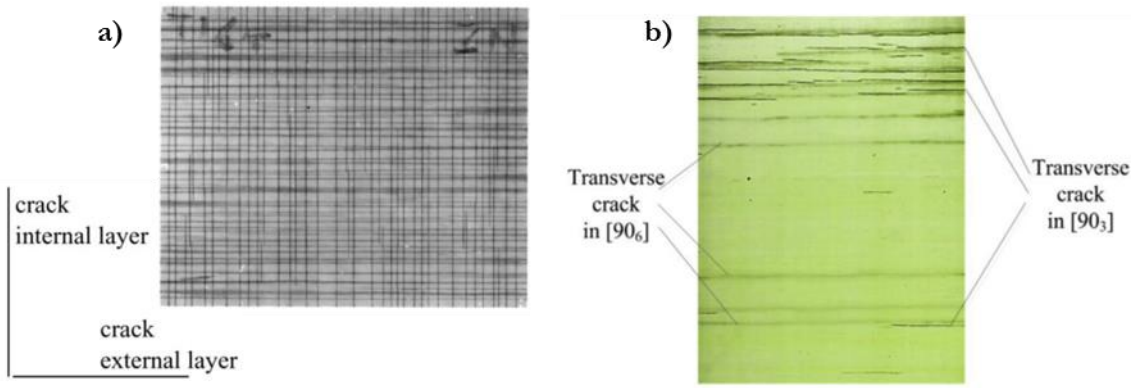

Fig.1.11 : Crack detection by **a)** X-ray photograph and **b)** by specimen retro-illumination. (Lafarie-Frenot, Hénaff-Gardin and Gamby, 2001; Shen et al., 2017)

As for the micro scale damage, a 3D characterization of the meso damage can be obtained using μCT scans. Moreover, by segmentation procedure, the crack counting is performed automatically and the thickness of the crack is useful for total damaged volume calculation. The μCT scan segmentation technique is widely employed on UD based laminates (Schilling et al., 2005; Sket, Aldareguia, et al., 2014; ElAgamy, Laliberte and Gaidies, 2015; Sket et al., 2015) and textile based laminates (De Vasconcellos, Touchard and Chocinski-Arnault, 2014; Yu et al., 2016).

A further useful aspect in using μCT for damage characterization is the possibility to characterize the damage in each ply of a laminate as in (Sket, Enfedaque, et al., 2014): the graph issued from this publication in *Fig.1.12* shows the evolution of the matrix crack density as a function of the shear strain in each ply of the tested specimen. This kind of information may not be issued from a simple X-ray image providing only 2D crack projections (Rotem and Hashin, 1975; Johnson and Chang, 2001).

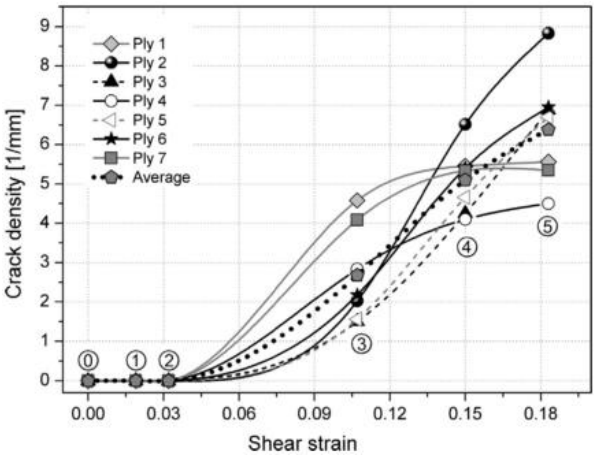

Fig.1.12 : Evolution of matrix crack density in each ply as a function of the applied shear strain. (Sket, Enfedaque, et al., 2014)

Optical microscope images are used in (Gamstedt and Sjögren, 1999) for crack detection on cross-ply laminate surfaces. The observation of the specimen surface can be used to detect damage location using Digital Image Correlation (DIC) as in (Ivanov et al., 2006; Montagnier et al., 2015; Whitlow, Jones and Przybyla, 2016). Despite this, a quantitatively evaluation of the crack extension has not yet been proposed in the literature for composite materials at best author knowledge.

There exist damage characterization methods not simple to include in the above described sections. This kind of damage characterization techniques are based on indirect measured quantities and not on direct crack observations. For this reason, to better describe the damage mechanisms, these techniques are generally coupled to one of the observation methods already described. Between these, one of the most used is the *Acoustic Emission technique* (AE); in (Carvelli et al., 2013) AE are used to describe damage evolution during fatigue of textile composites and μCT scans are employed for investigation on damage mechanisms; in (Truong et al., 2005) AE are coupled to X-Ray images and optical microscope observations, while in (Malpot, Touchard and Bergamo, 2015) AE are employed for a comparative study on fatigued organic composite specimens having different moisture contents and in (Pandita et al., 2001) acoustic events are related to the damage evolution in a woven composite during fatigue. Due to the extensive application of this method, an extended literature exits concerning AE, see for example (Maillet et al., 2012, 2014; Carvelli, D'Ettorre and Lomov, 2017). Another experimental technique not included in the previous classification is the Ultrasonic C-scan, very useful for damage detection on large components, often employed for Non-Destructive Testing (Blitz and Simpson, 1995) and used, for example in (Lomov, Ivanov, et al., 2008), for a "rough" damage detection then refined by X-ray images.

During fatigue of composite materials, some authors characterize damage by temperature measurements on the specimen surfaces. Recent applications of infrared thermography are reported

in (Toubal, Karama and Lorrain, 2006; Nixon-Pearson et al., 2013; Lisle et al., 2015) where a rise in temperature of the specimen during fatigue is correlated to damage development.

All the cited damage characterization techniques could be differently classified for instance by differentiating *in-situ* and *ex-situ* methods or again *contact* and *non-contact* detection systems, *etc*… . In a large number of the mentioned work, the authors look for a direct link between the damage evolution at the different scales, for this reason in this paragraph the damage observation means have been groped according to the observation scale. A particular attention has been granted to the μCT damage characterization technique, in fact this technique allows a 3D characterization of damage forms and extracting some *volumetric* information (such as crack volume, crack shape and crack localization), impossible to have otherwise. In the next chapters, interaction models between damage characterization at the micro/meso-scale and damage characterization at the macro-scale are proposed and validated for the tested specimens to investigate the environmental effects on fatigue of UD and woven laminates. The next paragraph presents the traction and the fatigue damage scenario for some recurrent fibrous composite architectures, while the environmental effects on organic matrix composites are presented in the sections 1.9.

1.4 Tensile and fatigue damage of fibrous composite laminates

The damage observation scales cited in the previous section are employed in the present paragraph to introduce the mechanical response and the damage mechanisms of fibrous composites. The damage mechanisms for these materials are strictly linked to the fibre architecture, in this paragraph the discussion is limited to a presentation of the response and the damage scenario for cross-ply UD based laminates and woven based laminates that are the composite architectures employed in the experimental activity presented in the next chapters.

An UD laminate submitted to a tensile load in the fibre direction and in the transversal fibre direction shows a linear behaviour, generally the specimen stiffness along the fibre direction is ten times that along the transversal direction (Okuta Baba, 2006). Also a cross-ply laminate has a linear behaviour and, during traction, the specimen stiffness slightly decreases as the load increases due to damage onset and propagation (Kashtalyan and Soutis, 2000). A schematic representation of the different damage forms in a cross-ply laminate is illustrated in *Fig.1.13*. During traction, transverse cracks onset on the sample edges, as result of the coalescence of initial micro-debonding on the fibre/matrix interface (Carvelli, Jain and Lomov, 2017), and propagate in the transversal plies; as the load increases transverse cracks induce local stress concentration at the crack tips involving interlaminar

delamination between 0° and 90° layers (Takeda and Ogihara, 1994; Berthelot and Le Corre, 2000). At the same time, splitting in the 0° layers appears as a consequence of the Poisson's ratio difference between 0° layers and 90° layers (Wang, Kishore and Li, 1985). Further load increase causes longitudinal fibre breakage and sample failure.

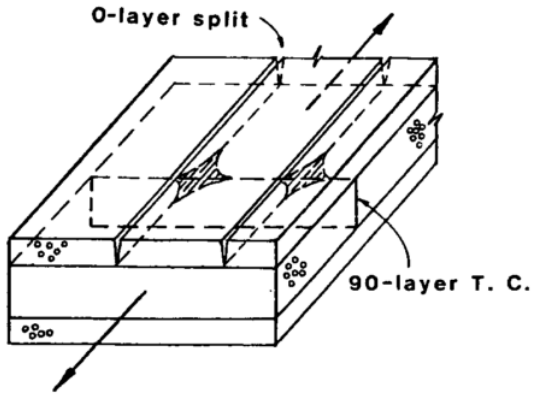

Fig.1.13 : Schematic representation of transverse crack, intralaminar delamination at the transversal crack tip and longitudinal splitting in a cross-ply laminate. (Wang, Kishore and Li, 1985)

The fatigue behaviour of cross-ply laminates is quite similar to the tensile ones, the cycle number take the place of the load level: as the number of fatigue cycles increases the stiffness decreases and a damage scenario similar to that observed during traction takes place.

The behaviour and the damage development in traction and fatigue for a woven based laminate is analogous to that described for cross-ply laminates. In addition to the described damage mechanisms for cross-ply laminates, a tensile load along the warp fibre direction in a woven ply leads bending in weft (transverse) tows (Osada, Nakai and Hamada, 2003) as illustrated in *Fig.1.14*. These additional stresses promote additional damage mechanisms. Consequently the woven weave pattern is a fundamental parameter in characterizing the mechanical behaviour of a woven laminate (Osada, Nakai and Hamada, 2003).

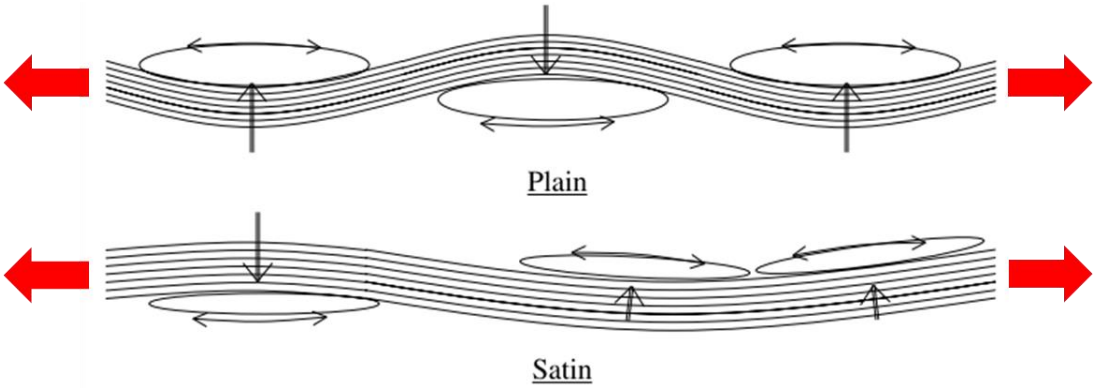

Fig.1.14 : Additional bending due to traction load in a plain and satin woven plies. (Osada, Nakai and Hamada, 2003)

The typical tensile response of a woven laminate loaded along the fibre direction is represented in Fig.1.15. The response is quite linear until failure and two slopes of the stress-strain curve can be observed: a knee point marks the slope change on the stress-strain curve. This knee point on stress-strain curve is directly linked to the damage process of the woven specimens. Another important issue of Fig.1.15 is the different response of the satin weave and the plain weave pattern. A satin pattern has a stress threshold for damage onset higher than the plain weave and the same goes for the failure load, this because an important crimp ratio brings to a higher local stress in the transverse tows. Compared to a satin woven, a plane woven has a higher crimp ratio and consequently it has an anticipated damage onset.

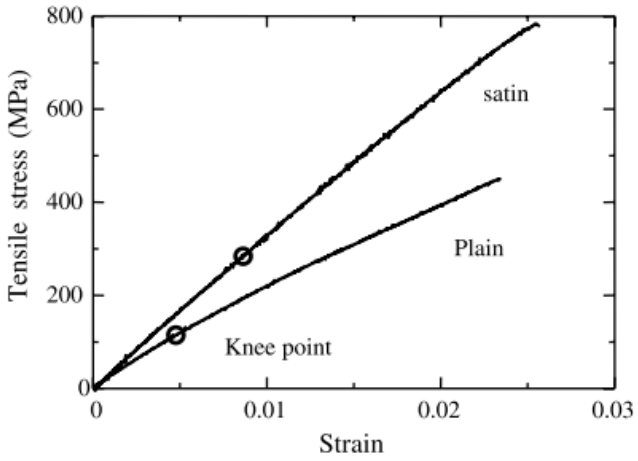

Fig.1.15 : Stress-strain curve of both a plain and a satin woven fabric laminates. (Osada, Nakai and Hamada, 2003)

The damage scenario for satin woven laminate is the same for monotonic traction and traction-traction fatigue load (Rakotoarisoa, 2013). Four damage stages can be identified: the first stage is the onset of matrix cracks in the transverse tows where the local bending-induced tensile stress reaches its maximum (Carvelli and Lomov, 2015) (*see Fig.1.9*). Secondly, these cracks propagate along resin rich regions or grow towards the longitudinal tow of the same woven ply bringing to a *meta-delamination*. The third and fourth damage stages are the transverse cracks propagation and the longitudinal tow failure respectively. In (Daggumati et al., 2011) the authors remark a delayed onset of transverse cracks in the surface tows of a 5HS woven carbon fibre/PPS matrix, *see* red circle in *Fig.1.16*. The authors conclude that cracks onset firstly where the bending is constrained, consequently a surface tow, more free to deform in the out-of-plane direction, will crack ever after an inner tow. In (Yu et al., 2016) the surface tows of a 3D woven glass fibre/epoxy matrix are the first cracked tows and the authors assume that the major out-of-plane tow deformation brings to the anticipated damage development in these tows. The difference between these two cases could be linked to the different constituents (Song and Otani, 1998) or to the different woven architectures.

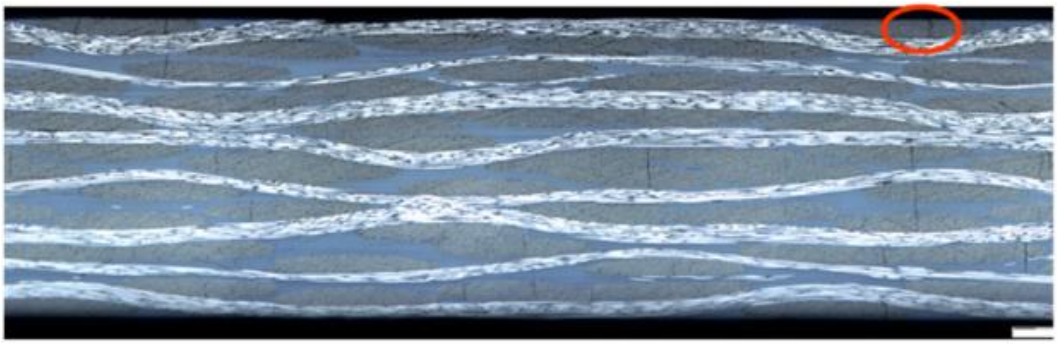

Fig.1.16 : Damage location on the edge of a 5HS woven based laminate. (Daggumati et al., 2011)

For the off-axis woven laminates, the behaviour is dominated by the matrix. In (Pandita et al., 2001) the authors observe that the main damage form is matrix/fibre debonding, followed by fibre reorientation and then sample failure, while in (Carvelli and Lomov, 2015) the authors observe transverse cracks in the resin rich regions at the bundle's top and bottom in the early fatigue stages. After a multiplication and a coalescence of these matrix cracks, intralaminar and interlaminar delaminations grow. The result of the extensive delaminated area is the longitudinal and transversal sliding between warp and weft tows leading to an important evolution of the longitudinal strain. The failure of the sample is related to the delamination increasing and the damage localization in a specific region and generally it consists in a relative slide of the warp and weft tows in absence of broken fibres.

In (Long, 2007) the author describes the shear behaviour of UD and woven based composites (*see Fig.1.17*). For both UD and woven composites the stress-strain curve shows a non-linear behaviour since the test beginning. As the load is applied, some fibre straightening and slippages between tows is observed as well as the fabric shears.

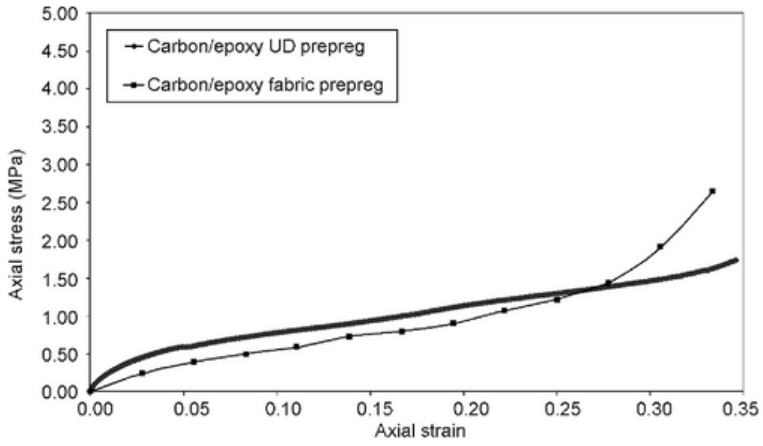

Fig.1.17 : Stress-strain curve for bias extension tests on one ply of [±45] prepreg fabric and two plies [+45,-45] of prepreg. (Long, 2007)

In this stage, a "yielding" effect could appear in the resin. The second stage is characterized by a shear deformation increasing as the shear load increases. Further load increase can gives rise to fibre locking in the woven resulting in a stiffener response of the woven specimen to shear. Fabric locking or jam is dependent on the weave type, on the tow spacing and on the resin characteristics. Shear fibre reorientation is observed also in (Lomov, Boisse, et al., 2008) for woven cloth without resin impregnation.

The macroscopic behaviour of composite is the result of the interaction between the different damage forms observed during monotonic or fatigue load. The dependence of the damage development on the composite architecture, load direction and constituent properties has been highlighted. The description of the fatigue macroscopic response of fibrous composite laminates is the main objective of the next paragraph.

1.5 Fatigue behaviour of fibrous composite laminates

The damage forms illustrated in *Fig.1.13* for a cross-ply UD laminated affect the macro-scale specimen response during fatigue. The longitudinal *modulus* evolution during fatigue of cross-ply specimens is documented in (Berthelot, El Mahi and Leblond, 1996; Shen et al., 2017): for the stacking sequence $[0/90_2]_s$ a stiffness degradation is observed from the apparition of the first transverse crack and until the specimen failure. Transverse cracks onset is anticipated using higher maximum fatigue loads, consequently also the stiffness degradation will be anticipated by using high maximum fatigue loads. In (Kashtalyan and Soutis, 2000) the longitudinal *modulus* is calculated using analytical models and plotted as a function of the transverse crack density.

For a woven composite the macro-scale fatigue response is similar to a cross-ply UD laminate: a longitudinal *modulus* degradation is observed from the beginning of fatigue up to the specimen failure (Naik, 2001; Pandita et al., 2001; Toubal, Karama and Lorrain, 2006). The evolution of longitudinal elastic properties is widely investigated in literature (*see Fig.1.6*). In (Vallons et al., 2007) the degradation of the stiffness of a C/Epoxy specimen tested in the bias direction is linked to matrix cracking for the entire test duration and it is highlighted that the elastic *modulus* degradation rate of fabric stitched composites loaded along the fibre direction is slower than the degradation observed for specimens loaded in the off-axis direction. Matrix cracking in the early stage of fatigue has been also observed in (Quaresimin, Carraro and Maragoni, 2016) for an UD laminated glass fibre/epoxy matrix composite loaded along the off-axis direction.

During fatigue the area enclosed in load/unload fatigue cycles shows an evolution as reported in *Fig.1.18*. As shown in this figure, the hysteresis loop area decreases in the early fatigue stages, after that a slower decreasing is observed until a rapid rise in the latter 10% of specimen life (Montesano et al., 2012; Topal et al., 2015).

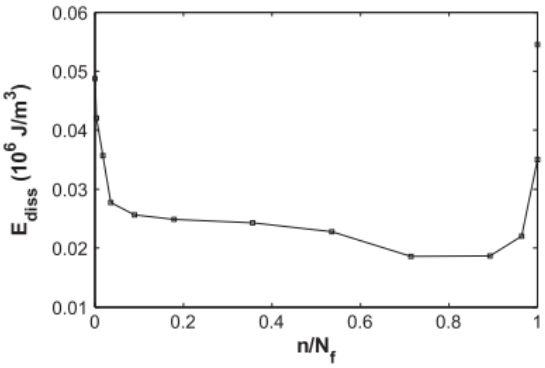

Fig.1.18 : Plot of the hysteresis loop area during fatigue. (Montesano et al., 2012)

In (Topal et al., 2015) the trend in the early stage of fatigue could be due to a rapid matrix crack accumulation in the specimens, while in (Kristofer Gamstedt, Redon and Brøndsted, 2002) the initial evolution of the hysteresis loop area is supposed to be due to viscoelastic deformation of the matrix.

Fatigue damage accumulation is defined in (Petermann and Schulte, 2002; Albouy, Vieille and Taleb, 2014b) using a damage parameter issued from the longitudinal strain values recorded during fatigue. About the authors, for composites exhibiting some viscous phenomena or fibre rotation during fatigue, the longitudinal strain is more meaningful than the longitudinal *modulus* to describe fatigue degradation. During fatigue the viscous nature of the matrix affecting the strain evolution can be not neglected, especially for test temperatures higher than room temperature. Some example of high temperature fatigue results are in (Montesano et al., 2012; Albouy, Vieille and Taleb, 2014a, 2014b; Vieille, Albouy and Taleb, 2014) where the longitudinal strain evolution is employed as damage parameter to study the specimen degradation. The temperature effect on longitudinal strain is shown in *Fig.1.19*. A higher initial longitudinal strain and a faster strain accumulation can be observed for the highest temperatures, while at room temperature the accumulated specimen strain is quite small.

As explained in (Petermann and Schulte, 2002), during fatigue, the fatigue load has a twofold effect: one could suppose that the fatigue specimen is statically loaded by the mean fatigue stress and under the action of this load, the material creeps. The interaction creep-fatigue is studied in (Sturgeon, 1978; Sun and Chim, 1981; Drozdov, 2011), the authors highlight the presence of creep when the cycling loading has a non-zero mean; furthermore, as higher is the time under a static load, as longer will be

the fatigue life of the specimens. The publications on this subject refers generally on UD laminated composites, see for example (Al-Haik et al., 2001; Petermann, 2004).

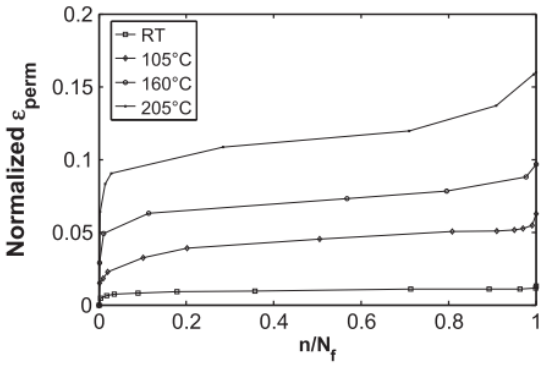

Fig.1.19 : Permanent longitudinal strain evolution during fatigue. (Montesano et al., 2012)

Creep-fatigue interaction on woven composites are poorly explored. In (Vieille, Albouy and Taleb, 2014) the authors investigate the creep retardation effect during a fatigue test of a 5-harness satin composites. The evolution of the strain during creep is described as sum of an instantaneous deformation, achieved during the load step, and of a viscoelastic and viscoplastic contribution. Despite some studies exist about the fatigue/creep/temperature interaction, the effect of the oxidation at high test temperature has not been investigated. Thermo-oxidation phenomena could accelerate the degradation of the tested specimens, but a damage characterization based only on macro-scale properties evolution, does not give the possibility to separate viscous effects from damage. In order to understand the role of micro-scale damage on the global specimen response, in this work, some models are employed to identify material properties and to relate the damage at the micro-scale to the elastic properties degradation. An introduction to these models is in the next paragraph.

1.6 Modelling woven composites

Textile composite materials are structured and hierarchical materials having three structural levels: the macro-level is a characterization of the composite 3D geometry and of the reinforcement properties; the meso-level defines the internal reinforcement structure, "local" at this level means averaging on the scale of several fibres (representative volume element) of properties as the stiffness of the impregnated; finally, the μ-level defines the arrangement of the fibres in the ply or in the tows (Lomov et al., 2007). Generally to reduce the size of the Finite Element (FE) model, only a repetitive unit cell of the composite is modelled and this unit cell is fixed by geometrical symmetry considerations (Tang and Whitcomb, 2003). The geometrical model for the reinforcement could be

build following different ways. Some idealized geometries could be created in CAD or FE software or dedicated software as WiseTex® (Verpoest and Lomov, 2005) or TexGen® (Lin, Brown and Long, 2011). Generally, the real geometry of the reinforcement are not successfully represented by an ideal geometry, for this reason other modelling techniques exist. As explained in (Tabatabaei, Lomov and Verpoest, 2014) the commonly used approach for meso-modelling are the continuous mesh methods or "full modelling" (Hivet and Boisse, 2007) and the non-continuous mesh methods (Fish et al., 1994; Tabatabaei et al., 2014; Tabatabaei and Lomov, 2015) where the matrix and the reinforcement are directly obtained from a "meshed box" using different techniques. A third way is modelling the real geometry of the reinforcement. This technique is more recent than the previous, because requires a 3D image of the composite unit cell that is obtained by μCT scan: from the μCT scan of the composite unit cell, a segmentation is performed to separate the matrix from the reinforcement, after that the segmentation results are used to generate the mesh for FE simulations as reported in *Fig.1.20*. The elements chosen to mesh a segmentation are prisms (Grail et al., 2013; Naouar et al., 2016) or cubes (Kim and Swan, 2003; Green et al., 2014; Straumit, Lomov and Wevers, 2015), more coherent with the voxel of 3D image and a 3D segmentation. In (Doitrand et al., 2015) The mesh employing prisms (or *consistent mesh*) and the voxelized mesh are compared in woven geometry generation; the authors conclude that, in terms of mechanical response, the effects of a different mesh are remarkable only at the yarn surfaces/interfaces, but globally, the unit cell response is not affected.

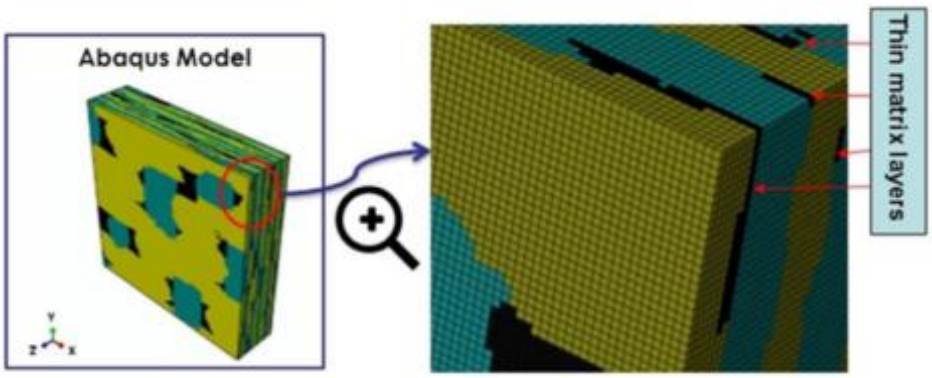

Fig.1.20 : Voxel-mesh model issued from 3D image segmentation. (Sinchuk et al., 2017)

FE unit cell models are widely used for several purposes as the investigation of the damage effect on macroscopic response (Doitrand et al., 2017), to study the moisture diffusion in composite material (Sinchuk et al., 2017), to compare FE model and DIC measured strain field (Nicoletto, Anzelotti and Riva, 2009; Doitrand et al., 2016), to investigate the stress distribution along the thickness of a laminate (Ivanov et al., 2010) and others.

A second kind of model, specifically developed to relate the evolution of some internal damage variables evolution to the macro-scale mechanical response is based on the continuum damage

mechanics (Lemaitre and Desmorat, 2005). From the global formulation, the general theory of continuum damage mechanics has been adapted to the damage forms taking place in composite materials as matrix micro-cracking, fibre/matrix debonding and fibre brittle rupture in (Ladeveze and Ledantec, 1992), to describe the damage development and the related loss of mechanical properties of a cross ply laminated during a traction test. The same model has been used to describe the progressive failure of a woven specimen in (Hochard, Aubourg and Charles, 2001), where the authors adapt the model to describe matrix micro crack damage in warp and weft directions during traction. Successively the same model has been used for fatigue damage development in woven specimens (Payan and Hochard, 2002; Hochard, Payan and Bordreuil, 2006).The employment of this last model was limited to unidirectional plies and balanced woven until (Thollon and Hochard, 2009) where a woven ply architecture has been simplified by two virtual perpendicular unidirectional plies as illustrated in *Fig.1.21*.

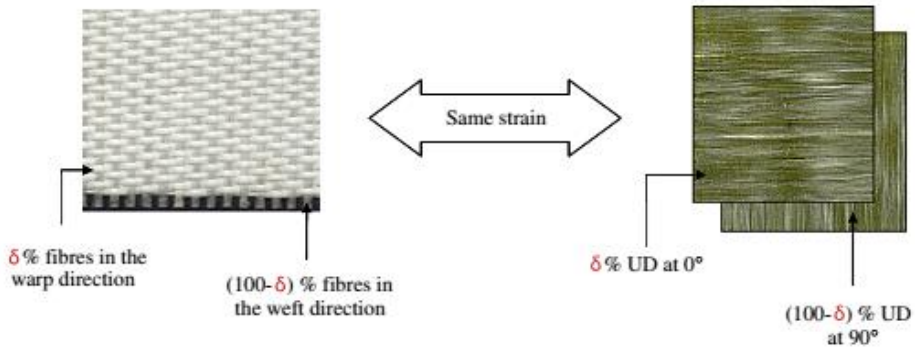

Fig.1.21 : Model generalization by split of an unbalanced woven by two unidirectional plies (Thollon and Hochard, 2009).

By this assumption, the model valid for a unidirectional ply can be applied separately for each virtual ply and the woven behaviour calculated as sum of the single virtual ply contributions. In the same publication the authors validate the hypothesis about the split of an unbalanced woven by traction test simulations and in (Hochard and Thollon, 2010) by fatigue tests.

These analytical models need a damage variables identification step via an experimental procedure. In this work this identification step has not been carried out because the damage in input to the model has been evaluated by direct measures on the tested specimens.

1.7 Thermo-oxidation of organic matrix

Thermosets matrix exposed to temperature higher than 100°C may suffer from thermo-oxidation phenomena (Minervino, 2013; Gigliotti, Minervino and Lafarie-Frenot, 2016). Some authors

documented the thermo-oxidation degradation process for different thermoset resins (Buch and Shanahan, 2000; Lévêque et al., 2005; Pochiraju and Tandon, 2006): generally, due to thermo-oxidation, a thin layer of oxidized matrix (hundreds of micron) is developed starting from the external specimen surface, directly exposed to the environment. In this thin oxidized layer, a gradient of the physical and mechanical properties is observed as the change in colour (Thomas K. Tsotsis et al., 1999), permanent chemical strains (Decelle, Huet and Bellenger, 2003), stiffness, toughness… .

An example of oxidized layer in a bulk resin sample is illustrated in *Fig.1.22*: the oxidized layer is thick around one hundred micron, while the interior region of the sample is completely unoxidized. The darker regions inside and outside the oxidized layer, are two transition regions which are the active "reaction" zones (Tandon, Pochiraju and Schoeppner, 2008).

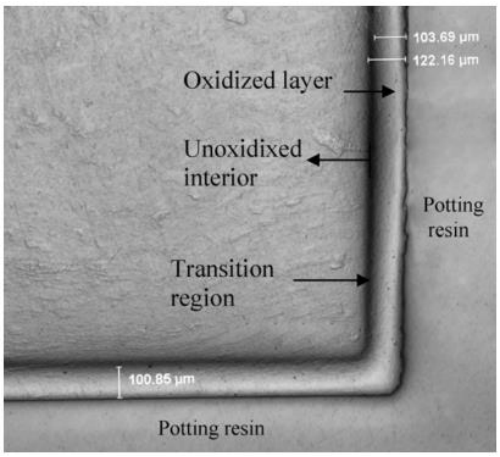

Fig.1.22 : Photomicrograph of PMR-15 resin showing the formation of oxidized region. (Tandon, Pochiraju and Schoeppner, 2008)

The development of this oxidized layer may be explained as a coupled diffusion/reaction phenomena (Bowles et al., 1993): the diffusion supplies the oxygen to the polymer, while the oxygen is consumed by the reaction process between oxygen and free radicals of the polymer. This concept can be summarized using the following equation:

$$\frac{\partial C}{\partial t} = D\nabla^2 C - R(C,T) \qquad \text{Eq.1.1}$$

In *Eq.1.1*, C represents the oxygen concentration that is a function of space, time, temperature and local strain state. The first term on the right side, is the Fick law, describing the oxygen diffusion inside the sample by the matrix of the diffusion coefficients D. When no load is applied to the sample, the boundary condition taking into account the oxygen concentration limit on the specimen

surface C_S can be expressed using the Henry law as $C_S=pS$, where p is the partial oxygen pressure and S is the oxygen solubility in the polymer. The second term on the right side is related to the reaction process. As argued in (Minervino, 2013) the dependence of this term on the oxygen concentration is intuitive: more oxygen is available and more numerous will be the sites where the oxidation process will act. The temperature is an index of the chemical reactions that could or could not take place. This last term is modelled using two different approaches: a mechanistic approach developed by Colin and Verdu (Colin, Marais and Verdu, 2001; Colin, Audouin and Verdu, 2004; Colin, 2005; Colin and Verdu, 2005) and a phenomenological one proposed by Schoeppner, Tandon and Pochiraju (Pochiraju and Tandon, 2006, 2009; Tandon, Pochiraju and Schoeppner, 2008). The first approach is devoted to the study of the oxidation kinetics of an epoxy resin by decomposition of the different reaction acting during the thermo-oxidation process. They identify new chemical species and volatile chemicals as oxidation products. Macroscopically, the volatile chemicals bring to a mass loss and to a permanent chemical strain (Decelle, Huet and Bellenger, 2003). The second approach uses the variable ϕ to describe the oxidation state ($\phi=1$ for unoxidized material and $\phi=\phi_{ox}$ for fully oxidized material) as shows *Fig.1.23*.

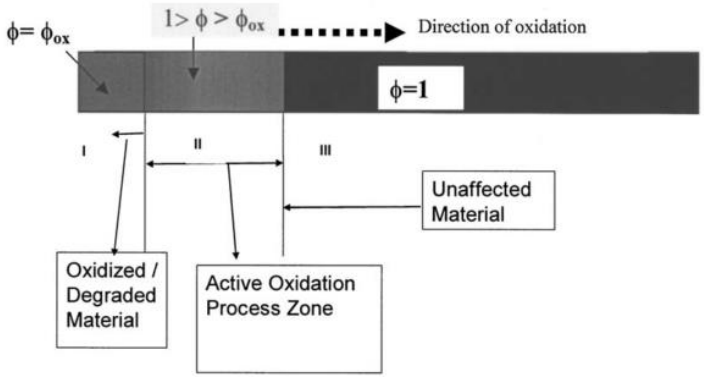

Fig.1.23 : Schematic illustration of the three zones in thermo-oxidation. (Pochiraju and Tandon, 2006)

The oxidation scenario reported in *Fig.1.23* shows that the oxidized region is followed by an active zone separating the oxidized and unoxidized regions. In this approach the variable ϕ is directly linked to the specimen mass loss/gain.

A phenomenological approach is introduced in the next section for the characterization of the oxidation effects on an aged organic resin. The knowledge of the oxidation state of the resin is a preliminary stage in the understanding of the thermo-oxidation behaviour of organic matrix composites.

1.8 Characterization of the thermo-oxidation of organic matrix

In this paragraph the experimental techniques for the evaluation of the thermo-oxidation effects on organic matrix are presented, a focus concerning the development of an oxidized layer, the matrix shrinkage and the indentation modulus of an oxidized specimen is made, while the results obtained on specimen dynamic response evolution and mass gain/loss are not cited.

In (Olivier et al., 2008) is explained that the local change in mechanical properties linked to thermo-oxidation can be quantified by ultra-micro and nano-indentation tests. The procedure for the specimen preparation issued from (Olivier, 2008) is illustrated in *Fig.1.24*. The aged specimens are cut along the transverse direction and polished.

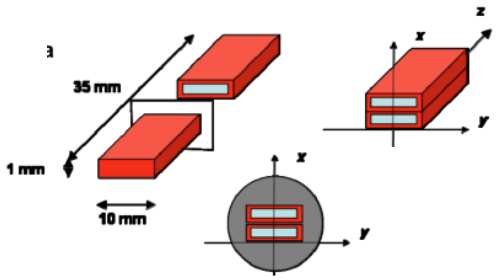

Fig.1.24 : Specimen preparation for oxidation characterization. (Olivier, 2008)

Optical microscope observations on these specimens are shown in *Fig.1.25*. The specimen in *Fig.1.25* are aged in 2 bar O_2 at 150°C, the four images are relative to four different ageing times. The initially homogeneous resin becomes a heterogeneous material, the exposed surfaces tend to develop an oxidized layer having a thickness dependent from the exposure time that appears as a darker zone narrowed the external zones of the coupons.

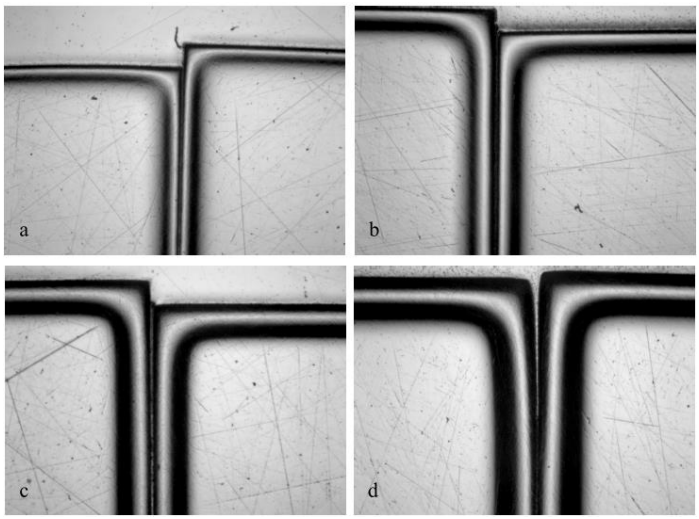

Fig.1.25 : Optical microscope observations. TACTIX 942 specimens aged in 2 bar O_2 at 150°C for **a)** 24hours, **b)** 48 hours, **c)** 72 hours and **d)** 120 hours. (Minervino, 2013)

The coupons of *Fig.1.25* have been observed using an interferometry microscope for the measurement of the magnitude of the matrix shrinkage due to oxidation. The specimen region studied by interferometry microscope are illustrated in *Fig.1.26*, while the results are reported in the images in *Fig.1.27* and in the graph in *Fig.1.28*.

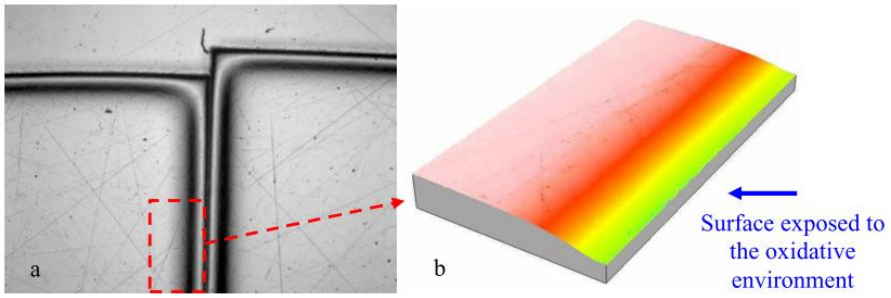

Fig.1.26 : Aged specimen surface observation by **a)** optical microscope and **b)** by interferometry microscope. (Minervino, 2013)

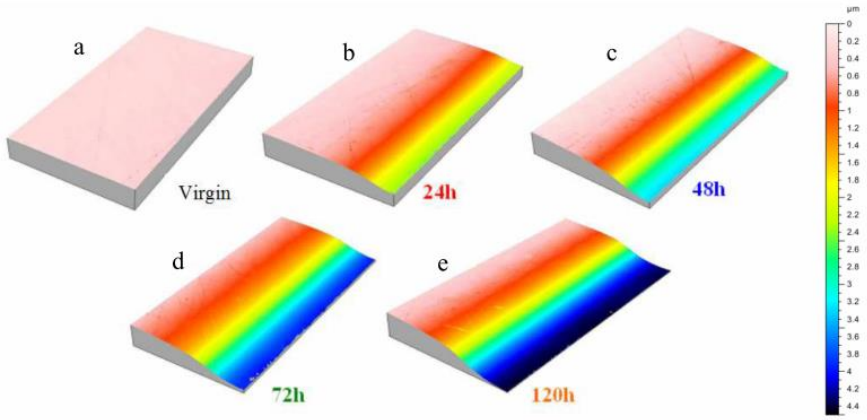

Fig.1.27 : Interferometry microscope observations of the specimen surfaces. Different oxidation conditions: virgin specimen **a)**, 24 **b)**, 48 **c)**, 72 **d)**, 120 **e)** hours in 2 bar O_2 at 150°C. (Minervino, 2013)

The matrix shrinkage as a function of the distance from the exposed surface of the specimen for different ageing times is shown in *Fig.1.28*.

The magnitude of the maximum vertical displacements goes from 2μm for the specimens aged 24 hours to the 4 μm of the specimen aged 120 hours. These vertical displacements are the result of the thermo-oxidation process that gives rise to chemical residual strains in the oxidized region (Minervino, 2013), once the specimens are cut and polished, a relaxation of these residual strains produces the out-of-plane displacements reported in *Fig.1.27* and *Fig.1.28*.

Local properties for the specimens are evaluated by Ultra-Micro-Indentation. Load/unload indentation cycles are performed on points having different distances from the exposed surface.

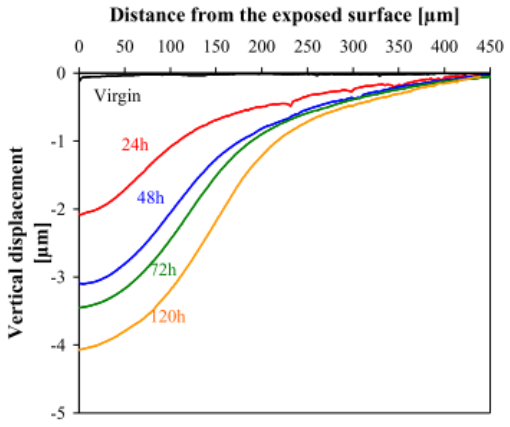

Fig.1.28 : Vertical displacements as a function of the distance from the exposed surface measured by interferometry microscope for the four ageing conditions (24, 48, 72, 120 hours in 2 bar O_2 at 150°C) and for the virgin specimen.

From the curve *load-penetration depth*, an indentation elastic module (EIT) is defined in accord with (Oliver and Pharr, 2004), *see Fig.1.29*.

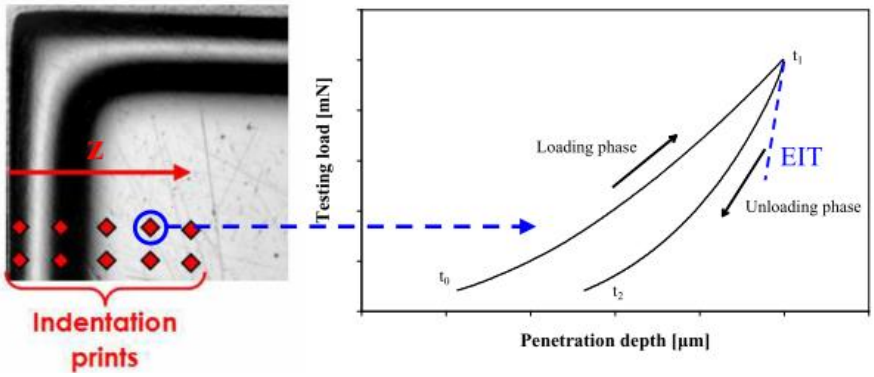

Fig.1.29 : Indentation print locations and procedure for indentation module (EIT) measurement.

The evolution of the EIT for an ageing in air and at 150°C for different ageing durations is reported in *Fig.1.30* ***a)***, where the indentation print more close to the surface exposed of the specimen is at 40µm from the external surface. *Fig.1.30* ***a)*** shows clearly the existence of an oxidized layer in which the EIT goes from a maximum value (close the exposed surface) dependent on the exposure time, to an asymptotic value that is the EIT of the virgin resin. This transition take place in a region having a thickness ever dependent on the exposure time. The evolution of the oxidation concentration products Q as a function of the distance from the specimen edge is shown in *Fig.1.30* ***b)***. The graph has been plotted by resolving the Colin and Verdu model, as for the EIT evolution the value on the sample edge is higher as the ageing time increases, then a decreasing until a stationary value is observed moving toward the sample core.

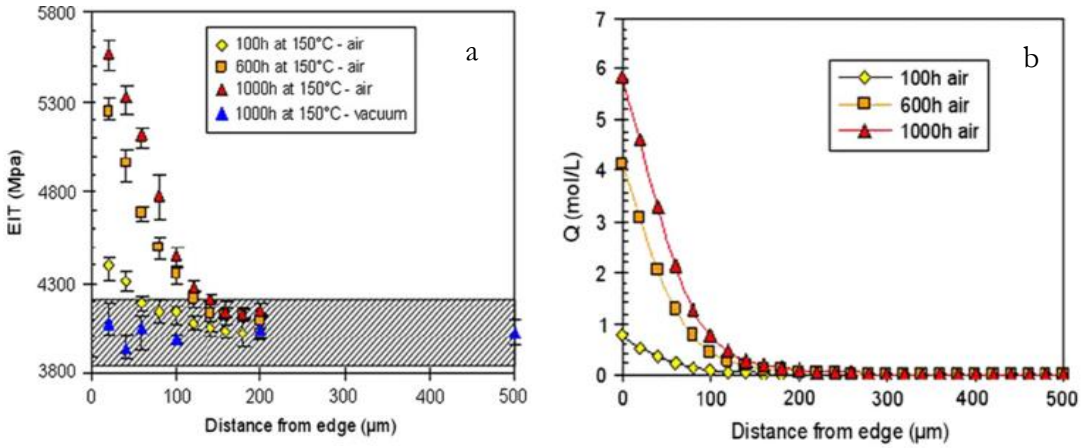

Fig.1.30 : Evolution of the EIT (**a)**) and of the oxidation concentration products Q (**b)**) as a function of the distance from the edge of the sample. (Olivier et al., 2008)

As explained in (Olivier et al., 2008), the EIT is correlated to the concentration of oxidation products Q independently on the ageing conditions. To prove that the change in mechanical properties and the oxidation state of the polymer are strictly related, for different ageing durations the EIT and the oxidation concentration products Q are plotted in the graph in *Fig.1.31* issued from (Olivier et al., 2008).

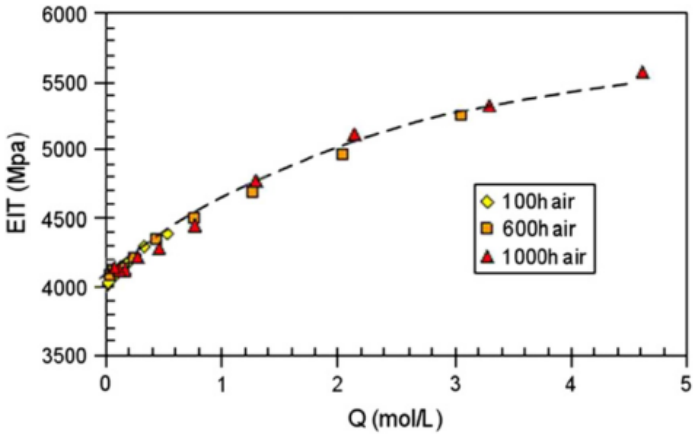

Fig.1.31 : Correlation between the EIT measured by indentation and the oxidation products concentration Q, calculated by Colin and Verdu model. (Olivier et al., 2008)

Different ageing conditions and the corresponding evolutions of EIT are investigated in (Minervino, 2013) for the TACTIX 942 that is an epoxy matrix. Looking at *Fig.1.32*, in the point more close to the external surface after 400 hours of ageing in air at 150°C, the EIT increases from 3.5 GPa of the virgin resin to 5.5 GPa. The rise of EIT for the specimen aged in 2 bar O_2 for 330 hours at 150°C is more important, the maximum measured EIT is 6 GPa. The specimens aged in 2 bar O_2 show a *plateau* for the EIT near the exposed surface for 330 hours of ageing. Being the EIT correlated to the concentration of oxidation products (Olivier et al., 2008), this stabilization could be due to the

saturation of chemical reagents. An important conclusion issued from the observation of *Fig.1.32* is the acceleration of the thermo-oxidation process obtained using 2 bar O_2 compared to the ageing in air: from the virgin matrix EIT value, a rise up to 5.5GPa is reached in air after 400 hours and using 2 bar O_2 after around 60 hours. Briefly, an ageing in 2 bar O_2 at 150°C for the TACTIX 942 gives an acceleration of the ageing phenomena of a factor 7 if compared to the ageing at 150°C in air.

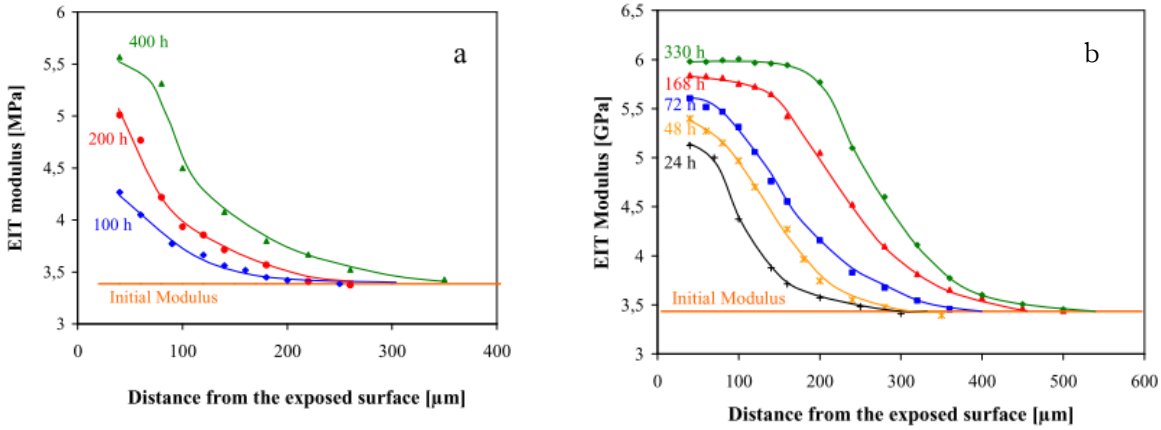

Fig.1.32 : Indentation modulus evolution as a function of the distance from the exposed surface for pure resin specimens (TACTIX 942) aged under different conditions: ageing in air at 150°C **a)** and ageing in 2 bar O_2 at 150°C **b)**. (Minervino, 2013)

The oxidation phenomena presented in this paragraph are related to bulk resin specimens. A large literature is available for different resin types about resin degradation induced by thermo-oxidation; the matrix degradation is, in the present work, a preliminary introduction to the composite degradation process related to oxidation phenomena.

The effect of a thermo-oxidative environment on composite material is the main subject of the next paragraph. The acceleration of the ageing process promoted by the employment of a high oxygen partial pressure has been sufficiently studied for UD based laminates, while oxidation effects on woven based laminates are still poorly explored.

1.9 Thermo-oxidation effects of organic matrix composites

The work of (Vu, Gigliotti and Lafarie-Frenot, 2012; Gigliotti, Minervino and Lafarie-Frenot, 2016) show that during aging, in a UD based laminate, the matrix shrinkage on the exposed sample edge is a function of the fibre spacing and of the aging time, as clearly illustrated in *Fig.1.33*.

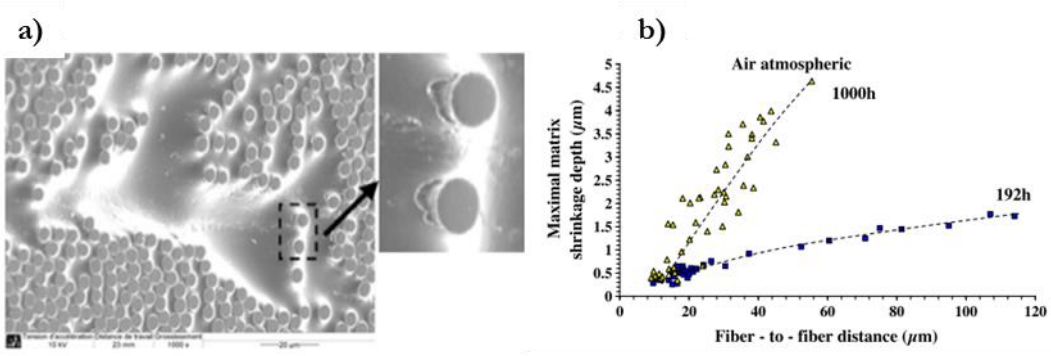

Fig.1.33 : Scanning electron microscope observation of sample edges aged 1000h in air (**a)**) and maximal shrinkage depth as a function of the fibre-to-fibre distance (**b**)). (Vu, Gigliotti and Lafarie-Frenot, 2012)

Moreover, the authors submit the sample to thermo-oxidation using three oxygen concentrations, showing that, as could be expected, increasing the oxygen concentration the shrinkage phenomena are accelerated. A last observation issued from *Fig.1.33* ***a)*** is the existence of debonding regions close the fibre/matrix interfaces. In detail, the authors identify for the aged sample surface a "primary" and a "secondary" shrinkage profile (*see Fig.1.35*): the primary profile is the larger one and the maximal depth is reported on the vertical axis in *Fig.1.33* ***b)***; the "secondary" profile is narrowed close to the fibres, not easy to quantify for all the aging conditions and often represented as a matrix shrinkage discontinuity. The reason of the faster matrix shrinkage development close fibre/matrix interface is not clear also if some scenarios are proposed by some authors as (Vu, 2011). The acceleration of the thermo-oxidation process on composites has been investigated for a C/TACTIX 942 epoxy matrix in (Minervino, 2013) and a summarizing figure is in *Fig.1.34*.

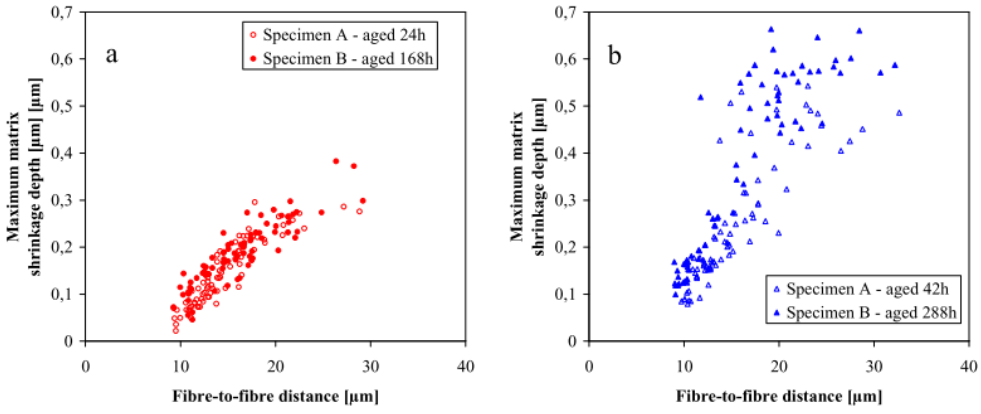

Fig.1.34 : Matrix shrinkage as a function of the fibre-to-fibre distance for **a)** a specimen A aged in 2 bar O_2 at 150°C for 24h (**a)**) and 48h (**a)**) and a specimen B aged in air at 150°C for 168h (**a)**) and 288h (**b)**). (Minervino, 2013)

In *Fig.1.34* ***a)*** data obtained on the specimens A and B are perfectly superposed, showing that for the TACTIX matrix an ageing at 150°C in 2 bar O_2 accelerates by a factor 7 the oxidation process at the

same temperature in air. The same goes looking at *Fig.1.34* ***b)***. This acceleration factor is the same encountered in the previous paragraph and this leads to the conclusion that the thermo-oxidation characterization at the micro-scale on bulk resin specimens is exploitable to identify the acceleration of the thermo-oxidation effects on composites.

The acceleration of the oxidation phenomena and the related debonding, enhances the oxidation effects on organic matrix composites: the matrix shrinkage leads to the formation of overstress regions at the sample surface and furthermore, the debonding zones offer new surfaces for the oxidation process producing an auto-accelerated oxidation phenomena.

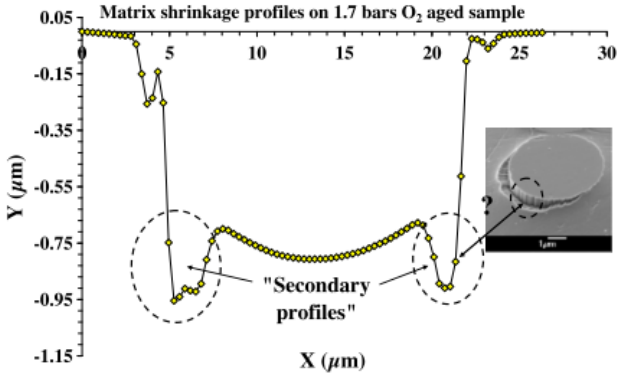

Fig.1.35 : "Secondary" profiles and shrinkage measurements carried out by confocal interferometric microscope. (Vu, Gigliotti and Lafarie-Frenot, 2012)

Observations on the anisotropy of the oxidation kinetics on a laminate composite are reported in (Schoeppner, Tandon and Ripberger, 2007). The axial fibre surface seems to oxidize faster than the lateral sample surfaces and this anisotropy is documented also in (Bowles and Meyers, 1986; Tandon, Pochiraju and Hall, 2009). The oxidation anisotropy is clearly shown in *Fig.1.36* where the oxidation profiles in a cross-ply laminated are drawn on the specimen edge for different ageing times.

On the specimen edge, the 90° layers are perpendicular to the surface, and consequently those are the plies where the oxidation grows faster. In (Lévêque et al., 2005) is investigated the aging effect at the macro scale on the ultimate properties for UD based laminates for different stacking sequences, showing that aged specimens become less ductile. The same observations reported in *Fig.1.36* allow seeing that little cracks propagate from the sample edge towards the specimen core in the more oxidized plies (not clearly visible looking at *Fig.1.36*) that are the 90° plies in *Fig.1.36*. This damage form is a consequence of the oxidation-induced embrittlement of the exposed surfaces acting jointly with the matrix shrinkage, ever related to the oxidation process (Pochiraju, Schoeppner and Tandon, 2012).

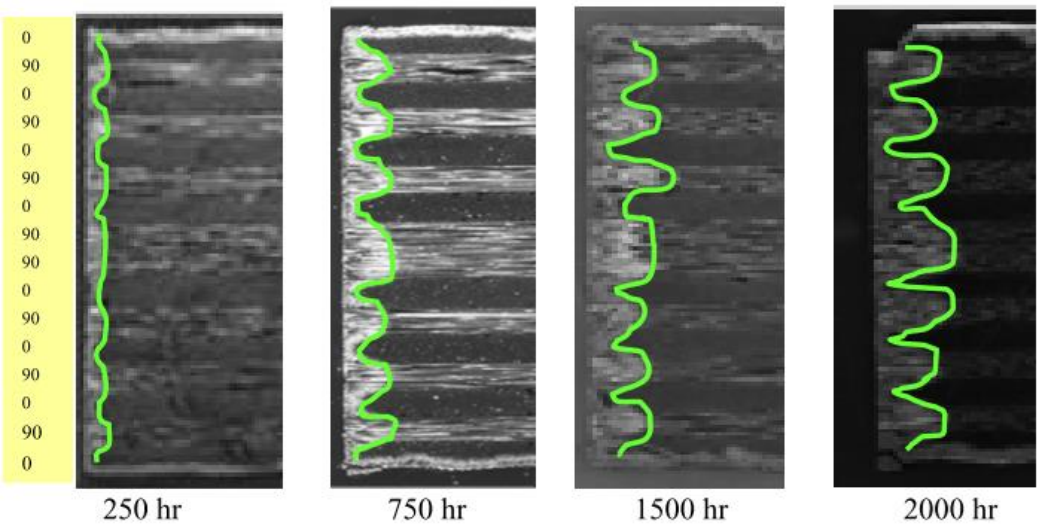

Fig.1.36 : Oxidation profile growth close a UD based cross-ply laminate edge as a function of the aging time (*cross section perpendicular to 0° direction*). (Tandon, Pochiraju and Hall, 2009)

In (Tandon, Pochiraju and Hall, 2009) the anisotropy encountered for the [0/90] laminates is not observed for a $[+45/-45]_{2s}$ laminates, where the oxidation layers growth is relatively uniform on the specimen edges, but an enhanced growth in some regions is observed as the aging time increases due to axial and transverse damage development (Tandon and Ragland, 2011). The dark regions in the zoom of *Fig.1.37* are oxidized zones at the crack edges, proving the existence of a synergistic effect between damage development and sample oxidation. *Fig.1.37* shows the oxidation profiles and the damage development of an aged $[+45/-45]_{2s}$ laminate. Edge cracks along the fibre direction promote the oxidation of the inner ply regions, normally not exposed to the environment.

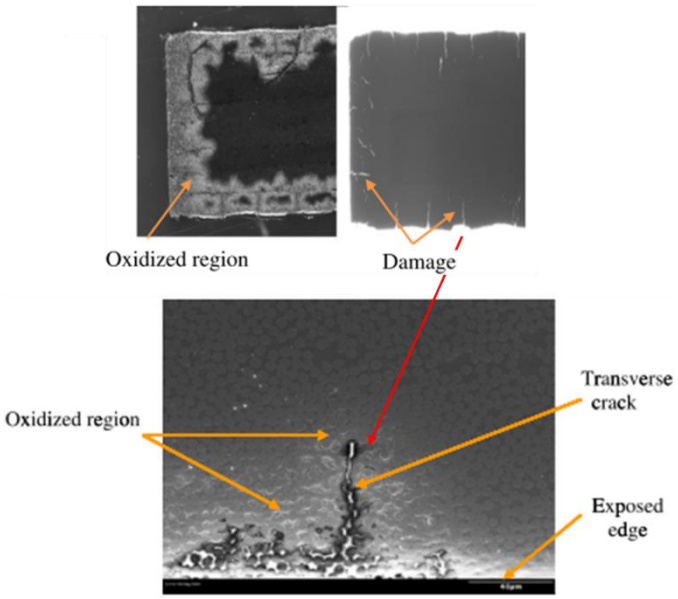

Fig.1.37 : Oxidation layer and damage in a $[45/-45]_{2s}$ aged laminate and zoom on surface damage. (*adapted from* (Tandon and Ragland, 2011))

Work on thermal oxidation of woven laminates are not as numerous as for the UD laminates. Some papers concerning PMR-15 based woven laminates can be found in the NASA *technical memoranda* (Bowles, 1998; Bowles, McCorkle and Ingrahm, 1998; Bowles et al., 2003) where the mass loss, the oxidized layer thickness and the damage induced by oxidation are observed also on 8HS woven carbon fibre/ PMR-15 laminates. For fabric composite the oxidation advances ever preferentially along fibres direction and the oxidation anisotropy for a woven ply is similar to that of a cross-ply laminate (Pochiraju, Schoeppner and Tandon, 2012). The oxidized layers and the damage propagation for a [45_4] laminate is reported in *Fig.1.38*.

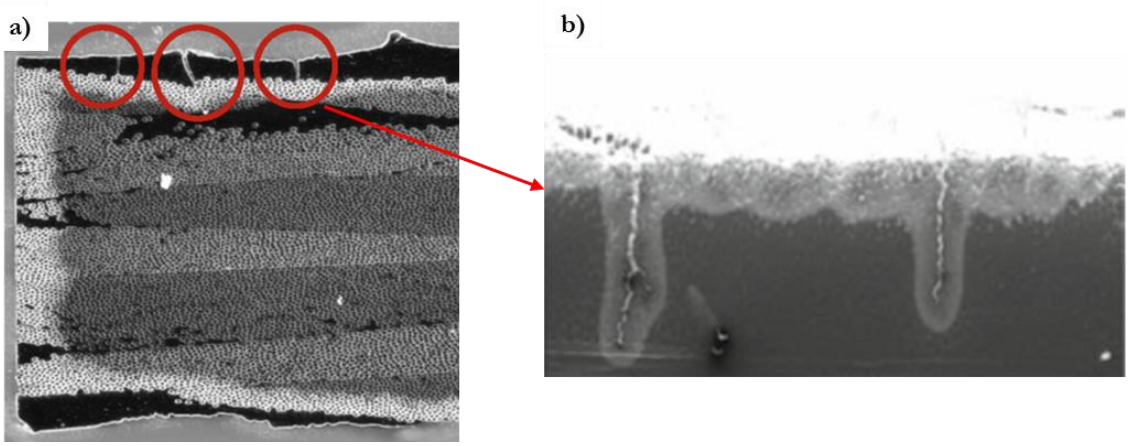

Fig.1.38 : Oxidation growth in a [45_4] woven aged composite (**a)**) and image of damage growth inside the sample (**b)**). (*adapted from* (Pochiraju, Schoeppner and Tandon, 2012))

The oxidized layer thickness is uniform along both fill and warp fibre direction as for a [45/-45] laminate. In *Fig.1.38* ***a)*** cracks onset in the thin resin rich layer on the upper specimen surface and grows along the transverse fibre direction. The zoom proposed in *Fig.1.38* ***b)*** shows an oxidized region surrounding the cracks. This could be seen as a synergistic effect between oxidation and damage development that can lead to an acceleration of the specimen degradation during a fatigue test in an oxidizing environment.

1.10 Mechanical load/thermo-oxidation interaction on organic matrix composites

Many work focus on fatigue, tensile or compression tests on aged and unaged specimens to compare the aging effects on the sample mechanical properties or crack density evolution (T K Tsotsis *et al.*, 1999; Daghia *et al.*, 2015; Khajeh *et al.*, 2015; Zrida *et al.*, 2017).

The synergistic action of a thermo-mechanical load and a thermo-oxidative environment has been investigated in several studies performed by Lafarie *et al.* These studies allow denoting a clear

interaction between oxidation and stress state in laminated composites due to the difference in thermal expansion coefficients of fibre and matrix. In (Lafarie-Frenot and Rouquie, 2004; Lafarie-Frenot et al., 2006) the authors describe the damage evolution for a $[0_3/90_3]_s$ laminated submitted to thermal cycling: cracks onset in correspondence to fibre/matrix interfaces in the 90° plies in form of debonding fibre/matrix; as the duration of the test increases, short micro cracks grow along the 90° plies thickness developing transverse cracks. Further tests are presented for example in (Lafarie-Frenot, 2006) and in (Lafarie-Frenot and Ho, 2006) where the interaction between oxidation and damage is confirmed by thermal cycling in inert environment, in particular the authors observe that the damage onset is delayed in inert gas if compared to the same load conditions but in aggressive environment (oxidizing environment). Further investigations on this theme are in (Lubineau, Violeau and Ladevèze, 2009; Vu, 2011; Vu, Gigliotti and Lafarie-Frenot, 2013) where the main environmental role is the acceleration of the fatigue crack multiplication kinetic of the oxidized specimen as illustrated in *Fig.1.39*.

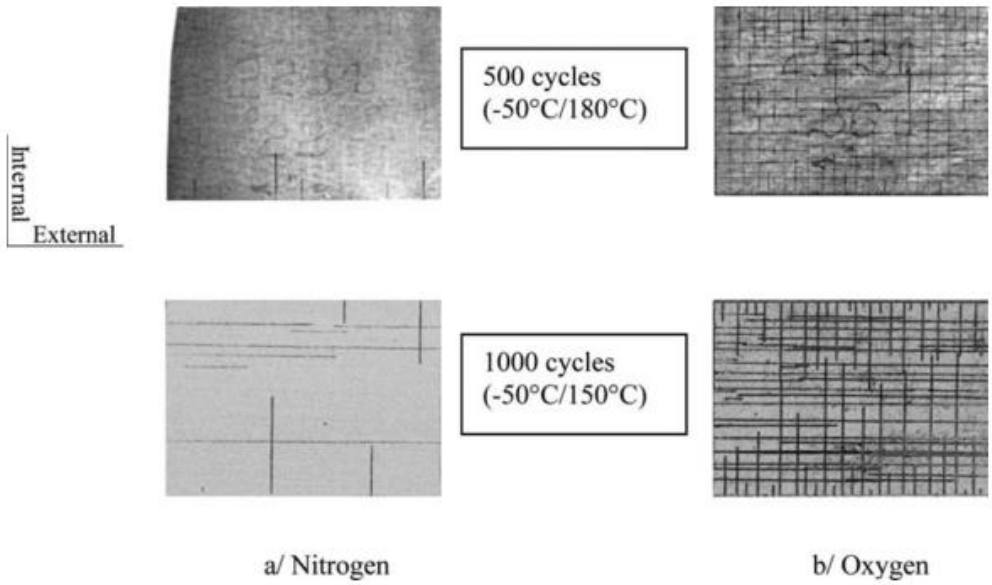

Fig.1.39 : Comparison of cross-ply laminate samples submitted to thermal cycling in inert and oxidative environment. (Lafarie-Frenot, 2006)

In (González, Domínguez and Lasagni, 2014) the authors submit cross–ply specimens to thermal cycling in inert and oxidative environment. The degradation is then evaluated by mechanical fatigue: a faster decrease of the longitudinal *modulus* during fatigue is observed for the specimens submitted to thermal cycles in oxidative environment compared to the specimens cycled in inert environment. In (Marais, Schieffer and Colin, 2003) are presented some investigations on thermo-oxidative creep response of organic matrix composites.

Not too many investigations about the mechanical loads/oxidation interaction on woven laminates are available in literature. Results on thermal cycling on woven laminates are reported in (Owens and Schofield, 1988), where the authors are interested in the quantification of mechanical property loss after thermal cycling without any specific investigations on damage mechanisms.

The acceleration role of the moderate high oxygen partial pressure during thermal cycling has been proven for cross-ply laminates. The interaction of complex load cases (*e.g.* fatigue) and an oxidative environment has not been investigated. Fatigue and oxidation of the surfaces of the specimens could interact accelerating the fatigue expected degradation.

For woven-ply laminates no evidences of interaction load/oxidation has been found in the literature. Moreover, for woven composites damage scenario during fatigue in oxidizing environment could significantly differs from the damage scenario observed during fatigue tests due to the interaction damage/oxidation described in 1.9. The damage in woven laminates could propagate over the external (visible) surfaces, consequently only 3D damage observation technique like μCT should be used for an exhaustive damage characterization/localization.

1.11 Conclusion of the bibliographic review

An introduction about composite material components and architectures has been proposed in the first part of this chapter. The basic components and the architectures are generally chosen to withstand the mechanical, thermal and chemical service conditions and their easy handling.

Organic matrix are sensitive to thermo-oxidation phenomena, especially at high service temperatures. For this reason, in the past years, many researchers have focused their work on thermo-oxidation phenomena on bulk resin samples and then on composite materials. It has also been demonstrated that moderate higher oxygen partial pressure can be used to accelerate thermo-oxidation phenomena. These studies could be considered as "preliminary" for a deeper investigation of the oxidation effect on material degradation due to the application of service loads as thermal loads, creep, traction/compression loads or fatigue. In this chapter, it has been highlighted that:

- For cross-ply UD laminate specimens at the beginning of fatigue transverse crack onset from the lateral specimen edges that are directly exposed to the environment. Transverse cracks propagate along the specimen width leading to a stiffness decrease. An acceleration of the crack onset during

thermal fatigue in oxidative environment has been shown, but no experimental evidences concerning mechanical fatigue test in oxidizing environment are reported in literature;

- For woven-ply laminates the damage scenario includes several damage forms that could onset in external or internal specimen regions. A suitable damage characterization for this kind of composite must to take into account all the damage forms and the damage location in the specimen. The μCT, commonly used for damage characterization on UD laminates, is an appropriate observation mean also for woven composites. However damage quantification by μCT on these latter material is still poorly exploited;
- A synergistic effect between fatigue damage of woven composites and thermo-oxidation has been highlighted by many researchers. Researches about this damage/oxidation coupling during fatigue of woven composites do not still exist;
- It has been shown that woven composites behaviour when loaded along the off-axis direction is dominated by the resin properties. Moreover, an organic resin exposed to high temperatures suffers thermo-oxidation phenomena. Specific studies about the creep/environment interaction for woven composites have not yet been proposed.
- The acceleration of the ageing effect of pure resin and some studies about the oxidation of OMC have been presented. No work about the acceleration of the oxidation process exist for OMC. Moreover, a test protocol allowing the acceleration of fatigue test for OMC during high temperature fatigue has not yet been proposed;
- It has been shown that some modelling strategy exist for woven composites. In particular, some of these are based on *continuum damage mechanics* in which the damage is an internal variable and is not related to direct damage observation/quantification on tested specimens.

For a structural part submitted in its life to cyclic loads, during a laboratory test, cyclic mechanical loads are generally accelerated to reduce the test duration. For structural parts submitted to thermo-mechanical cycling, the acceleration of the load application frequency could no longer rescale the real degradation process. Environmental acceleration should be used jointly to the mechanics acceleration to correctly rescale the real degradation processes. On the other hand, the acceleration effect of an oxidative environment could be used to accelerate environmental degradation during mechanical fatigue tests if not synergistic effects are observed. In fact, chemical diffusion coefficients are strain and temperature dependents: during load the material is strained and damage development leads to a temperature rise; moreover, damage during fatigue promotes the oxidation of some specimen regions normally not affected by oxidation and the sample degradation could be further accelerated by other phenomena not yet observed. In view of the presented lacks, in the following chapters:

- Fatigue tests in different environmental conditions on cross-ply laminates will be performed to improve the knowledge about the effects of a thermo-oxidative environment during mechanical fatigue, in order to show that that an oxidative environment allows accelerating the crack multiplication kinetics;
- A μCT image analysis will be developed in order to compare damage volume/morphology of woven specimens tested in different environmental condition by a quantitative analysis for 4D (3D damage characterization along the time) damage assessment. Furthermore, an *in-situ* damage evaluation technique by DIC at high temperature will be developed for a real-time specimen degradation monitoring;
- Off-axis woven composite will be tested in fatigue using different environmental conditions to understand how thermo-oxidation affects the fatigue damage scenario: the existence of synergistic effect between fatigue damage/thermo-oxidation is evaluated by the observation of the evolution of the damage volume at the micro-scale and of the macro-scale properties;
- Off-axis woven composite will be tested in creep using different environmental conditions to understand how thermo-oxidation affects creep response;
- Analytical models will be employed for fully understand the environmental effect acceleration for the tested specimens and to propose a suitable test protocol for high temperature fatigue test acceleration for OMC;
- Measured cracked volumes, issued from μCT results, will be integrated in an analytical model to describe macro scale property degradation for woven OMC.

Chapter 2

Materials, test facilities and observation tools

This chapter focuses on the experimental techniques employed to study *multi-physical fatigue* of composite materials: the tested materials, the testing facilities and the observation tools are presented as well as the post processing procedure allowing obtaining the test results presented in the next chapters.

Summary

In the first part of this chapter the tested composite materials are introduced. A description of the testing machine, specifically developed to perform fatigue tests on composites under particular environmental test conditions, is given successively. The third part is devoted to the explanation of the damage observation techniques: *in situ* digital image correlation and *ex situ* micro-computed tomography are presented focusing the discussion on their employment for the tested composite materials.

2.1 Materials

Two composite materials have been tested during the experimental activity carried out in this work. These materials are conceived for structural applications in temperatures between 150°C and 300°C. The first material, provided by EADS IW, is a laminated $[0_2/90_2]_s$ cross-ply carbon/epoxy HTS40/TACTIX742 composite. Some information concerning this composite provided by the supplier are reported in *Table 2. 1*. The matrix glass transition temperature is 190°C-250°C (measured by Dynamic Mechanic Analysis [DMA]) and the resin volume in the composite is 34.3%.

Properties	**Value**
Fiber Density [g/cc]	1.78
Cured Matrix Density [g/cc]	1.31
Nominal Prepreg Mass [g/m²]	222.9
Glass Transition Temperature [°C]	190-250
Matrix Volume Ratio	34.3%

Table 2. 1 : HTS40/TACTIX742 composite properties (Minervino, 2013)

The second material, furnished by AIRCELLE (SAFRAN NACELLES), is an 8-harness satin $[0_6]$ woven carbon/polyimide T650-35/MVK-14 composite material (*see Fig.2. 1*) realised by Resin Transfert Molding.

The matrix in this material has a higher glass transition temperature, about 325°C-335°C (DMA results), and the resin volume fraction in the composite is between 34% and 38%. The material properties provided by the supplier are reported in *Table 2. 2*.

In order to obtain the volume fraction in the tow and other characteristic dimensions of the weave pattern, microscope observations have been carried out. To perform these observations, specimens have been polished on one edge using the protocol reported in (Vu, Gigliotti and Lafarie-Frenot, 2012). From the images, the thickness (t_T) and the width (w_T) of the tows as well as the distance between two crimp regions of the same tow (l_{UC}) have been measured.

Properties	Value
Fiber Density [g/cc]	1.74-1.83
Cured Matrix Density [g/cc]	1.25
Nominal Prepreg Mass [g/m²]	586
Glass Transition Temperature [°C]	325-335
Matrix Volume Ratio	34-38%

Table 2. 2 : T650-35/MVK-14 composite properties (Minervino, 2013)

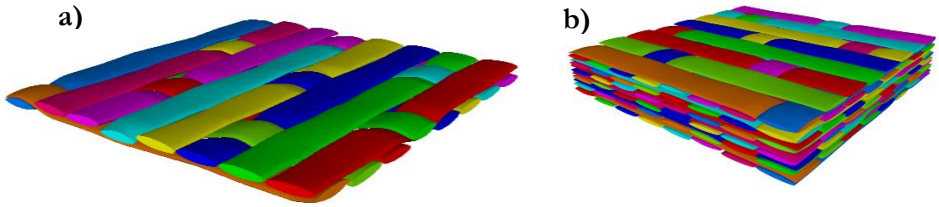

Fig.2. 1 : 8 HS woven architecture **a)** Elementary ply **b)**. Representative Unit Cell. [TexGen®]

All these dimension are schematically reported in *Fig.2. 2* and on a microscope image in *Fig.2. 3*, finally the values in *Table 2. 3* are found as mean of 12 direct measures for each dimension performed in different plies.

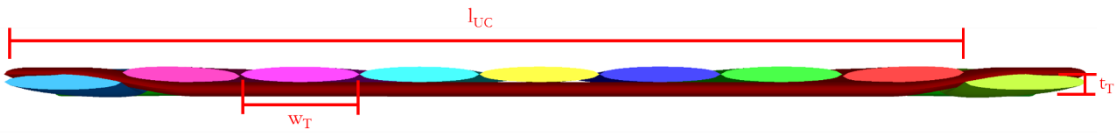

Fig.2. 2 : Schematic representation of an 8HS weave

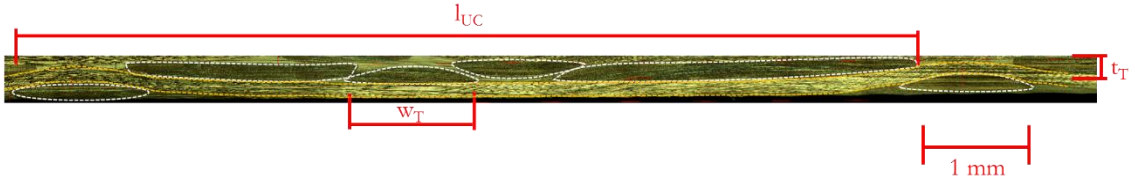

Fig.2. 3 : Crop of specimen edge microscope image

Dimension	Value (µm)
l_{UC}	8477±167
w_T	1250±50
t_T	147±8

Table 2. 3 : Characteristic dimensions of the weave

In *Fig.2. 3*, dashed-lines help to identify the geometry of the tows: white dashed-lines surround frontal (weft) tows while the dashed orange line surrounds the transverse (warp) tow. White dashed lines show that some tows are merged together giving a single tow. This "defect" named *super-yarn* may affects composites when tows are woven separately for the fabric realization, as explained in (Ivens and Verpoest, 1996). Due to the existence of this *super-yarn*, the distance between two crimp regions of the woven is less than eight time the width of a single tow. *Super-yarns* add complexity to the representation of the woven using idealized geometries. In fact, to better understand the material behaviour, a FE model based on the real geometry of the woven has been employed in Appendix-C.

In order to calculate the volume fraction of fibre in the tow V_F, the following procedure has been applied. Starting from microscope images of the specimen cross section as that schematic in *Fig.2. 4*, a mean value for fibre diameter has been found. A square has been drawn on the microscope images (red square in *Fig.2. 4*) and the number of fibres inside this square has been counted. Using the same square area and knowing the number and the mean diameter of the fibres inside it, the volume fraction has been evaluated as the ratio between the square area and the total area of the fibres.

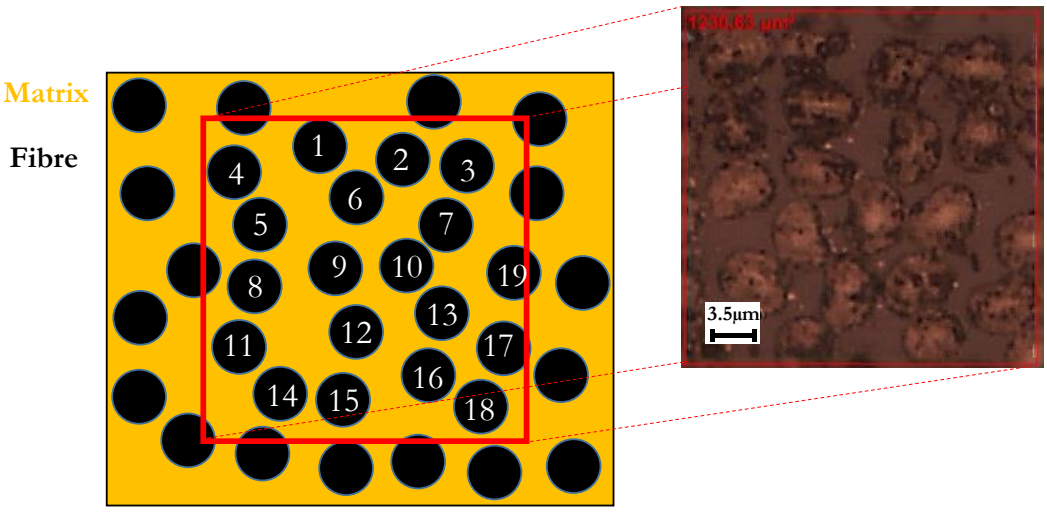

Fig.2. 4 : Schematic and microscope images for fibre volume fraction calculation.

Via statistical analysis on the 24 obtained values a mean of 0.62 ±0.03 has been calculated, no relevant difference between warp and weft direction has been observed in terms of V_F.

2.2 Testing device

All the mechanical tests have been performed using the COMPTINN' test setup illustrated in *Fig.2. 5*. The principal characteristics of this test setup are reported in *Table 2. 4*. This is an INSTRON 1251 equipped by a climatic chamber specifically developed to carry out mechanical tests in controlled

environment (temperature and gas). For the integration of the climatic chamber around the test machine, some important technical arrangements are taken.

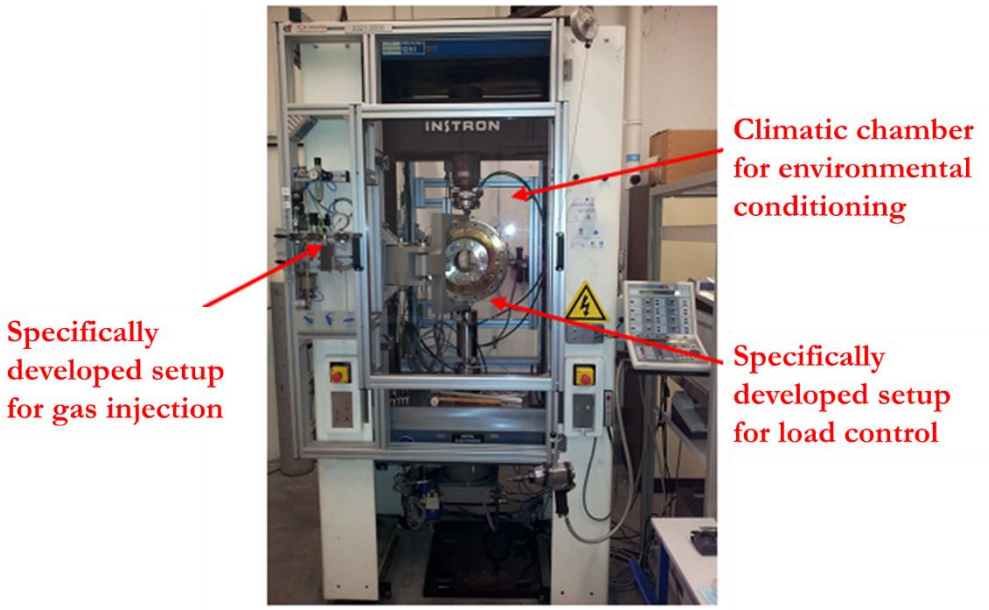

Fig.2. 5 : COMPTINN' multi-physical test machine

Characteristic	Value
T_{MAX} [°C]	350
Gas	Air, O_2, N_2
Max Gas Pressure [bar]	5

Table 2. 4 : COMPTINN' setup performances

The climatic chamber is realised entirely using a 316L stainless steel and is composed by two separated parts in order to mount the specimens in the climatic chamber: the former is attached to the upper mechanical parts of the test machine and the latter is a demountable cover (*see Fig.2. 6* ***a***). The cover serves as a heating element for the climatic chamber and at the centre a transparent porthole allows seeing inside the climatic chamber when this is closed. The closing of the cover is made using twelve stainless steel screws and a graphite seal ensuring the gas tightness of the chamber (*see Fig.2. 6* ***b***). The graphite seal is a circular element cut from a laminated plane sheet realized superposing several graphite layers and putting in the middle of the laminated a ply in metallic material to ensure the easy handling of the final product. Due to a rapid degradation, each time the climatic chamber was open the seal was substituted. Inside the chamber moving part are lubricated using dry lubricant materials (mainly Bronze) because grease lubricants or any flammable substances were forbidden because the oxygen presence.

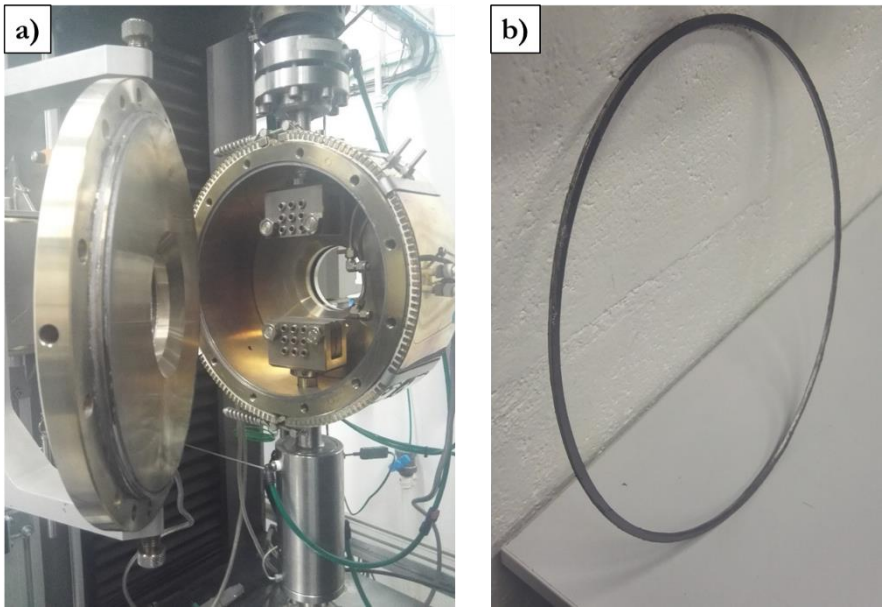

Fig.2. 6 : Details of the test machine: **a)** Climatic chamber **b)** Graphite seal

In the standard test machine the load cell is mounted externally to the climatic chamber and in series to the stationary head that is placed in the upper side of the test machine. The friction introduced by the moving parts, and the weight of the climatic chamber could affect the measured force values giving a noise complicating the realization of load piloted tests. For this reason, a second load cell is mounted in series with the moving piston, directly connected to the movable head in order to reduce the friction noise and to suppress the climatic chamber weight influence on the measured force values. This additional load cell (F_{MAX} = 50 kN) is contained in the same cooling block dedicated to the moving piston. The cooling block is water-cooling, this prevents malfunctions of the force measuring system and allows performing load piloted tests. Furthermore, the moving piston is rotationally self-aligning, in order to minimize bending/torsion due to misalignment during the specimen installation.

The grips used to hold the specimens during tests are composed by three elements of which one is a fixed element and the other two are movables (*see Fig.2. 6*). Nine screws on one side of the grip are tighten to fix the position of the first movable part that will be the same for the two grips. The second movable part remains free in this step. The specimen is mounted between the grips and held tighten the nine screws on the other side of the fixing element. During the tests generally, only this last step is carried out.

A continuous gas supply is installed to avoid pressure variation inside the chamber during the tests due to an imperfect gas tightness that may give a decrease of the internal pressure.

The climatic chamber has an internal volume of 9 litres and is realised using 140 kg of steel. Due to the great thermic inertia, to heat the chamber in reasonable time lapse, the heating element has a power of 7 kW allowing reaching 250°C from the room temperature in 90 minutes.

2.3 *In situ* measurements

The climatic chamber does not allow using gauges for strain measurements due to the tightness of the climatic chamber, so all the measurement techniques are non-contact techniques. In this paragraph the *in situ* observation facilities are described. For each facility is explained how the observation technique has been adapted to the tested material and for the test specifications.

2.3.1 Long distance microscope

Fig.2. 7 shows the microscope employed during tests on laminated composites. The microscope is a QUESTAR QM100 equipped with an AVT Dolphin F-201C camera to convert in digital format the images of the specimens.

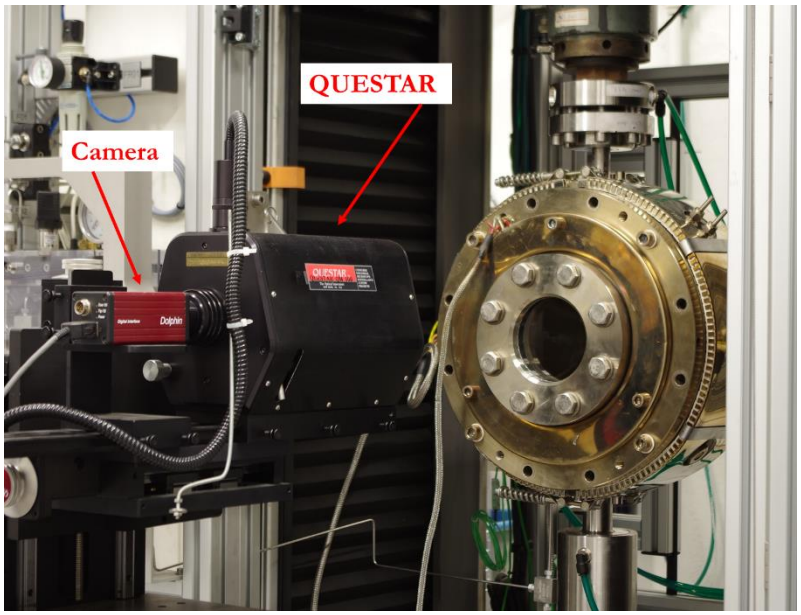

Fig.2. 7 : Long distance microscope during test

The distance between the microscope and the test machine allows having an observation region length on the specimen from 10 to 15 mm with a resolution of 1.2 µm/px. To extend the observed zone up to the maximum admissible by the porthole of the test machine (60 mm), the microscope and its camera were translated along the vertical direction.

In order to count the cracks, the tests were stopped periodically and the number of cracks on the polished edge was manually counted as shown in *Fig.2. 8* for a traction test.

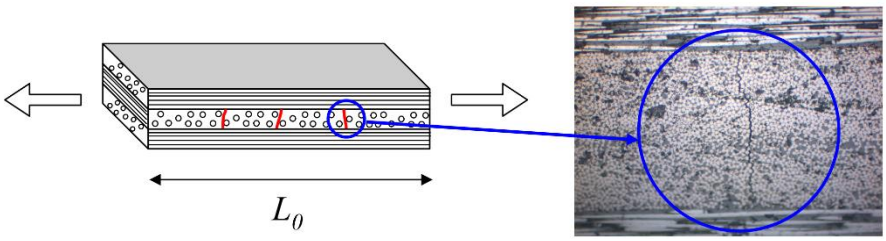

Fig.2. 8 : Cracks counting during a traction test on a $[0_2/90_2]_s$ laminated

2.3.2 Digital Image Correlation

The Digital Image Correlation [DIC] method is a full field non-contact measurement technique used in different domains (Grédiac, 2004). For composite materials the DIC method is widely employed; for example in (Nicoletto, Anzelotti and Riva, 2009; Canal *et al.*, 2012; Laurin *et al.*, 2012; Mehdikhani *et al.*, 2016) the authors compare Finite Element simulation results and DIC measured strains. In (Daghia et al., 2015; Whitlow, Jones and Przybyla, 2016) DIC is used for damage assessment and in (Lomov, Boisse, et al., 2008; Muñoz, González and Llorca, 2015) DIC is employed to compute the shear behaviour of a woven composite loaded along off-axis direction, while in (Lomov, Ivanov, et al., 2008; Daggumati et al., 2011; Doitrand et al., 2016) the strain pattern is matched with the reinforcement architecture. Finally, in (Vieille, Aucher and Taleb, 2013) the shear behaviour of holed laminated specimens is studied during a test at 120°C.

To perform DIC a random speckle pattern is produced on the specimens; this could be given by the natural texture of the material (Jin, Lu and Korellis, 2008) or artificially created. In the latter case, a high contrast, isotropic and non-periodic pattern should be made on the sample surface (Dong, Kakisawa and Kagawa, 2015). One procedure allowing having a speckle pattern with uniform size of speckles is to mix white particles in a darker adhesive coating.

The displacement field is obtained by comparing the digital images of the specimens acquired before and after the deformation (Pan et al., 2010). The theoretical framework is detailed in (Haddadi and Belhabib, 2008; Sutton, Orteu and Schreier, 2009) and here only briefly invoked. The principle of DIC is illustrated in *Fig.2. 9*. In the reference image (A) the point M is at the centre of a pixel having $\underline{X}$=(X,Y) coordinates, while in the deformed image (B) the point M has moved in a new position having $\underline{x}$=(x,y) coordinates.

The determination of the new position of M is made by the minimization of the correlation coefficient c that is:

$$c = 1 - \frac{\sum_{i \in D} f(X_i, Y_i)\, g(x_i, y_i)}{\sqrt{\sum_{i \in D} f^2(X_i, Y_i)} \sqrt{\sum_{i \in D} g^2(x_i, y_i)}} \qquad \text{Eq.4. 1}$$

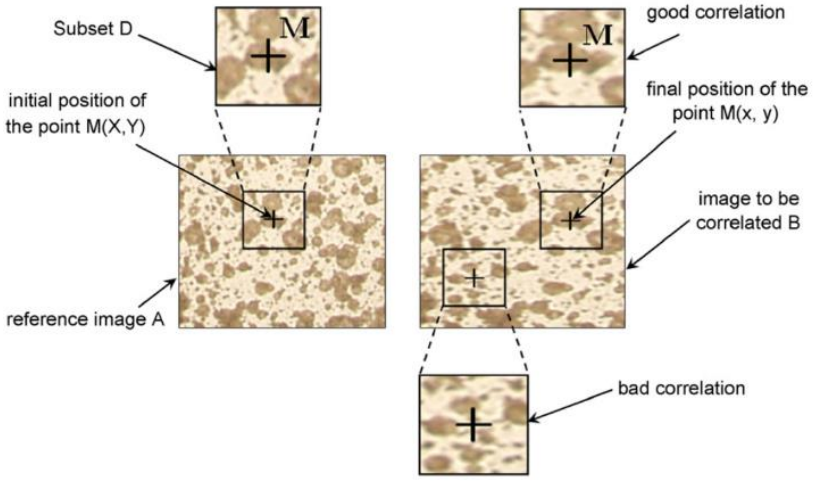

Fig.2. 9 : DIC framework. In the image B the good correlation subset corresponds to the minimal value of the correlation coefficient (Haddadi and Belhabib, 2008).

In *Eq.4. 1* *f* and *g* are the grey levels in the image A and B respectively, while D is the domain where the correlation coefficient is calculated, generally called subset.

The displacements calculation in the range of the pixel fraction is not possible using discrete values of grey levels for the correlation. For this reason, the grey levels in each pixel are interpolated using polynomial functions. For the optical flow conservation, the grey level polynomial function in the deformed subset can be obtained by a material transformation (Bornert, Brémand, Doumalin, J. C. Dupré, *et al.*, 2009). This transformation is named shape function and the approximation of the displacement field depends on the order of these functions: a zero-order shape function could describes a pure translation, while a first-order shape function permits the calculation of translations, rotations, shear and normal strains (Schreier and Sutton, 2002). For the minimization of the correlation coefficient, several optimization algorithms exist as the Newton-Raphson or the Levenberg-Marquard algorithm (Schreier, Braasch and Sutton, 2000). The image correlation is concluded when all subsets are matched, but often in mechanical tests, a supplementary calculus stage is required to compute the strain field from the obtained displacement field.

For this, a possible solution is to define the gradient of the plane transformation **F** as:

$$\mathbf{F} = \frac{\partial \underline{x}}{\partial \underline{X}} \qquad \text{Eq.4. 2}$$

The components of this gradient are calculated by finite differences and, finally, the plane components of the Green-Lagrange strain tensor $\mathbf{E}$ are obtained, using the *infinitesimal strain theory*, from (Barranger et al., 2012):

$$\mathbf{E} = \frac{1}{2}(\mathbf{F}^{T} \bullet \mathbf{F} - \mathbf{I}) \qquad \text{Eq.4. 3}$$

Although DIC is a powerful technique for strain measurement, the measurement errors are not largely discussed in literature and the reduction of the errors is difficult to improve (Nghiem, Al-Heib and Emeriault, 2015). In (Haddadi and Belhabib, 2008) the source of errors are classified in two categories: in the first lie the errors due to the measurement device and the working environment, in the second category are grouped all the errors introduced by the correlation principle itself. The errors due to lighting, optical lens distortion, camera sensor, presence of out-of-plane displacement and the arrangement of all these devices in the workspace belong to the former category. In the second category are assembled the errors linked to the quality of the speckle pattern, the subset distance and their size and the correlation algorithm (grey interpolation, shape function, minimization algorithm). In (Ma, Pang and Ma, 2012) the errors are divided in *systematic* and *random* errors. At the first group belong all the errors related to the DIC algorithm, to the lens distortion and to out-of-plane motion, while the errors linked to the lighting or to other sources having an unpredictable intensity are grouped in the second set. Concerning the error due to the DIC algorithm, in (Schreier and Sutton, 2002) the authors investigate the effect of two different grade for the shape functions, they found that, under some hypothesis on the speckle pattern distribution inside the subsets and on the shape function, a second-order shape function give a more accurately description of the subset deformation without an unacceptable rise in computational time. The grey level interpolation errors are studied in (Schreier, Braasch and Sutton, 2000) where the authors conclude that, for a given speckle pattern, using a cubic interpolation function the errors are dramatic reduced if compared to a linear interpolation function. Furthermore, using an high order for the interpolation function, a later errors reduction is obtained using a low-pass filter, apparently for the common speckle patterns the low frequency information are sufficiently accurate for subset matching. A discussion on the error contribution linked to the speckle pattern is reported for example in (Pan, Lu and Xie; Haddadi and Belhabib, 2008; Barranger *et al.*, 2012). The speckle pattern composed by rigid particles give the same correlation result of a deformable one. Further, a speckle pattern resulting image having a large mean intensity gradient gives the best results if compared with an image where the mean intensity gradient is smaller. The size of the particles composing the speckle pattern and their distribution on the

specimen surface is strictly correlated with the subset size (Pan, Lu and Xie). As reported in (Haddadi and Belhabib, 2008), the increase of the size of the subset enhances the quality of the correlation because larger subsets hold more speckles and can be distinguished more precisely (Pan et al., 2009). However, a larger subset over a given size does not present important improvement in measurement and further, a larger subset leads to major computational time. The subset distance, called *step size* or *grid pitch*, defines the distance of the point that are analysed in DIC. As explained in (Mehdikhani et al., 2016) reducing the step size, more pixels are analysed and a more detailed correlation is possible, identifying more speckle-imperfectly zones; the highest resolution with the lowest strain noise can be achieved by minimizing the step size and using a moderate subset size. The errors due to the correlation algorithm are analysed in (Amiot et al., 2013) where several correlation software are compared, the result is that the noise of the images affects some algorithms more than other, moreover the errors have a periodicity of a pixel. The effect of the systematic errors is generally quantified using the standard deviator of the displacement/strain field: different parameters combinations are used to perform image correlation and at the end the final choice is the parameters combination associated to the lower standard deviation.

The errors due to the measurement device and the working environment are not widely studied in literature. The errors due to the lighting are linked to the variation of grey levels in the images (Haddadi and Belhabib, 2008), hence one can do the same considerations argued for the speckle pattern quality. The error introduced by the camera sensor, with a special regard to temperature variation is studied in (Handel, 2007; Ma, Pang and Ma, 2012); the authors explain that a temperature change of the image camera sensor during image acquisition, results in a translation/expansion of the image and so in an error on the measurement. Other thermal expansions of the camera components could result in an error on the computed displacement/strain fields. The out-of-plane displacement/rotation effect is explained in (Sutton et al., 2008; Sutton, Orteu and Schreier, 2009) where the difference of a strain field calculated by DIC and stereo-correlation is compared in order to give an estimation for the error. By optical considerations, the authors concluded that the strain error is a function of the distance between the specimen and the lens of the optical system and of the out-of-plane displacement/rotation of the specimen.

A detailed description of the error sources during a DIC has been given. For the DIC results presented in this work the errors are taken into account as explained in the following paragraphs. It is important to remark that for the performed experimental activity, computational time and strain field spatial resolution are the priorities for the choice of DIC parameters, no systematic investigations have been conducted for error minimization by optimization of correlation parameters.

For the experimental campaign carried out in this work, a mix of black paint and alumina spherical particles having a mean diameter of 7 μm has been used for room temperature tests. At 250°C this speckle pattern burns and loses its contrast properties. For the tests at 250°C a different speckle pattern is created: white particles are directly deposed on the naturally (dark) surface of the composite specimens. In *Fig.2. 10* is schematically illustrated the procedure applied in order to obtain a reduced size for particles.

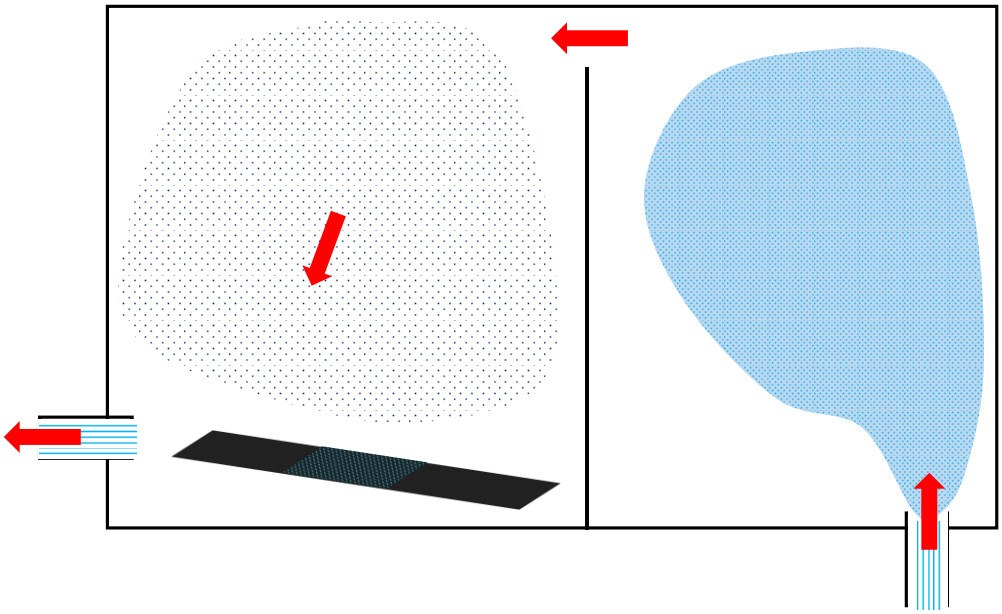

Fig.2. 10 : Speckle pattern application for DIC at 250°C

A commercial white spray for temperature up to 650°C is injected in the right side of the box in *Fig.2.10*. The heaviest drops fall without trespassing the barrier between left and right side of the box. Lighter paint particles move through the barrier toward the left side of the box, where an aspiration system at the exit hole of the box facilitates the particles motion. The diameter of the particles falling on the specimens is difficult to control, but a mean diameter of 10±7 μm has been measured after the speckle pattern application.

The pictures during the test have been taken using a Nikon D3X camera mounting a Sigma 150mm f/2.8 MACRO zoom. The resolution of the pictures is 6048×4032, but the specimen occupies only a fraction of the image. The distance between the camera and the specimen is a crucial parameter: the resolution in terms of μm/pixel of the pictures is directly linked to this parameter, so based only on optical considerations, the smaller is the distance between the camera and the specimen and the more detailed is the images. During the experimental activity, the distance between the specimen surface and the macro-lens, was ever around 180(±5) mm. The DIC setup is shown in *Fig.2. 11*.

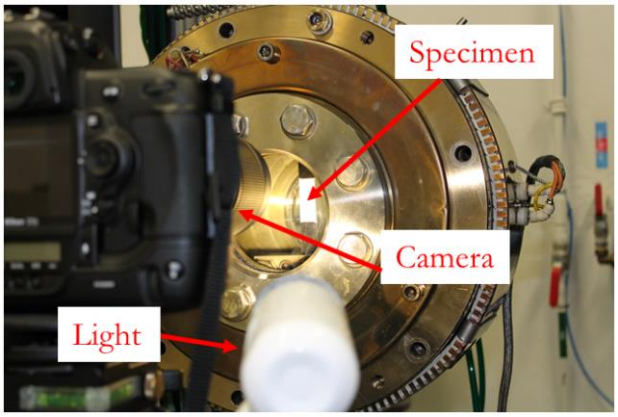

Fig.2. 11 : Picture of the acquisition system

The DIC software employed in this work is CORRELA V.2012. This is a software for DIC-2D developed at the PPRIME Institute, and already employed for example in (Bornert, Brémand, Doumalin, J.-C. Dupré, et al., 2009; Husseini, 2014; Dupré et al., 2015). The maximal specimen area captured by the camera was 2400 × 3700 px² (or around 14.5 × 22.2 mm²) in the central zone of the specimen (*see Fig.2. 12*) taking one picture every 6 seconds. A bi-cubic polynomial is selected for the grey levels interpolation inside each subset and the correlations are performed using an iterative algorithm taking into account also the local displacement gradient.

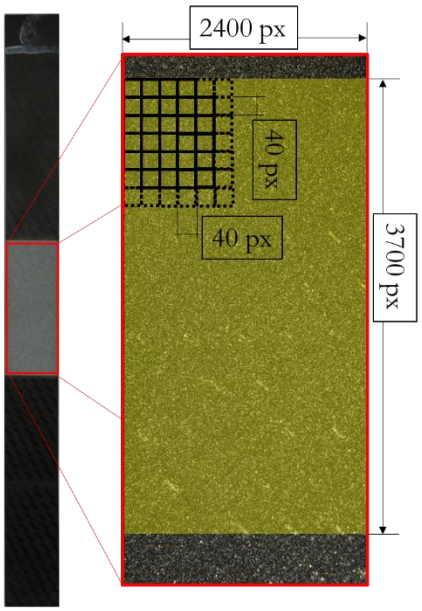

Fig.2. 12 : Parameters for DIC. Dimension of the observed zone, subset size and subset step.

In a first time, DIC has been employed during the test to have real time information on the integrity of the specimens. The subset size has been set at 40px, which is the minimal dimension allowing to correctly matching all the subsets. In order to use all the available surface to perform correlation and,

at the same time, to have the lowest number of subsets on the image (to reduce the computation time), 40px has been chosen as subset step.

The strain field is calculated from the displacement values using finite difference and the Green-Lagrange tensor. The concerned subsets for the strain calculation are dependent on the smoothing value imposed by the operator as reported in *Fig.2. 13* issued from the CORRELA User's Manual. No important differences on the results are remarked using the L configuration or the X configuration, but the choice of the smooth parameter affects the resolution of the strain field: a little value of the smooth parameter could result in a noisy image, while a higher value leads to a degradation of the strain spatial resolution. For the actual experimental campaign a smooth parameter = 1 has been set.

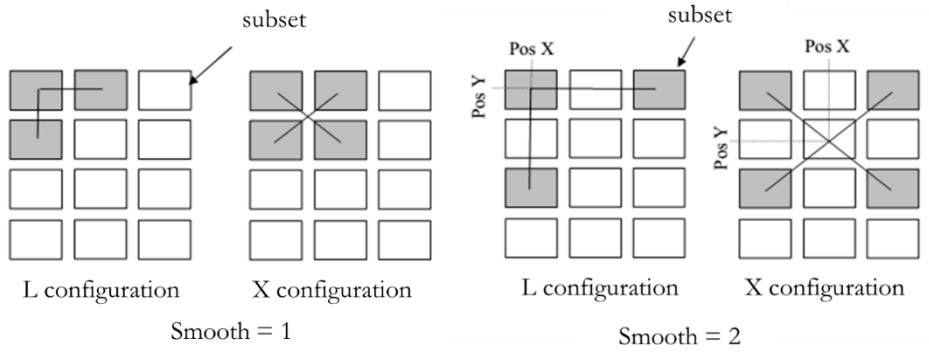

Fig.2. 13 : CORRELA strain calculation [CORRELA Manual]. Smoothing on strain calculus using finite differences.

Finally, a low-pass filter is applied on each image in order to reduce the errors linked to the grey level interpolation (*see* (Schreier, Braasch and Sutton, 2000)). The correlation errors are quantified using an artificially modified speckle pattern images as already done for example in (Schreier, Braasch and Sutton, 2000; Mehdikhani et al., 2016). A tool in ImageJ, a freeware software for image processing, allows resizing the image. Using ImageJ a stack of 11 modified speckle images was created. These images have been gradually stretched up to 19px at the eleventh image, corresponding to a uniform deformation of 0.01002. At the last image, the standard deviation on the strain field was of 2.2×10^{-5}. For an evaluation of the environmental part of the errors, a sequence of 4 images of the specimen mounted on the testing machine at 250°C and without any applied load, have been taken and analysed with CORRELA. From the three strain fields available for the error evaluation, three values for the standard deviation have been calculated. These values are very close and their mean value is 10^{-4}. Errors due to the out-of-plane motions could be related generally to the mounting stage of the specimen on the testing machine or to a tenso-bending coupling in the behaviour of the material. An error of 5×10^{-5} and 1×10^{-4} for an out-of-plane translation and an out-of-plane rotation respectively has been calculated using the formulae reported in (Sutton et al., 2008) for a specimen strain of 1% and starting from the knowledge of the precision in specimens installation on the testing machine.

The tenso-bending coupling is supposed negligible as negligible are supposed all the other sources of errors.

An estimation of the total error is made adding the standard deviation (σ) associated to each considered error. The *Table 2. 5* summarizes the pixel size, the choice in CORRELA parameters and the errors that could affect the calculated strains.

Parameters	**Values**
Pixel size	6-6.2 μm/mm
Subsets step	40 px
Smooth parameter/Local gauge length	1/(2×40px≈0.5mm)
Correlation error (*std*)	$\sigma=2.25\times10^{-5}$
Environmental error (*std*)	$\sigma=10^{-4}$
Max out-of-plane motion error	5×10^{-5} and 10^{-4} at $\varepsilon=1\%$
Max local total error ≈ 2.7×10^{-4}	

Table 2. 5 : Parameters DIC –Fast calculation

A typical strain field observed on the tested woven specimens is reported in *Fig.2. 14*. The output strain field from CORRELA is quite heterogeneous. Several inhomogeneities of the strain field are due to really existing features, for example in the woven architecture of the paragraph 2.1 the tow width is large enough to contain 4 data points.

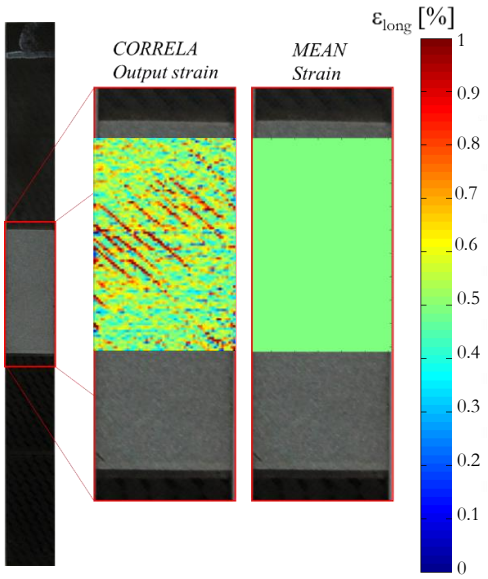

Fig.2. 14 : DIC strain field. Inhomogeneous strain field and the mean value calculated over the studied region.

If some subsets fall on a resin rich region or on a tow or even on a crossover tow, the corresponding strain value could be different from the surrounding data points lying on the surface tows. Cracks are another source of inhomogeneity in the strain field, in fact the employed DIC algorithm allows calculating only continuous strain field, and in this case cracks appear as large strain regions. Some recent approaches are especially conceived to better evaluate crack location. These approaches are detailed in the paragraph 2.3.3.

In order to obtain strain values at the macroscopic scale in a given instant of a traction test an arithmetic mean over the whole stain field is calculated. This gives the same results of a virtual extensometer fixed at the upper and bottom sides of the painted region of the specimen.

2.3.3 DIC crack detection

In the previous paragraph the parameters for DIC calculation have been optimised to have short computational times and a result sufficiently accurate for mean strains determination. In this paragraph is explained how the high strain regions observed in the strain field calculated using CORRELA, have been employed to detect cracks.

Recently some authors developed some methods for a better identification of discontinuity in a strain field as for example the employment of the Heaviside function. In (Valle et al., 2015) the presence of cracks is viewed as a kinematic discontinuity of the strain field. The authors apply a Heavside algorithm (or H^1-DIC) to identify the exact position of the cracks as shown in *Fig.2. 15*.

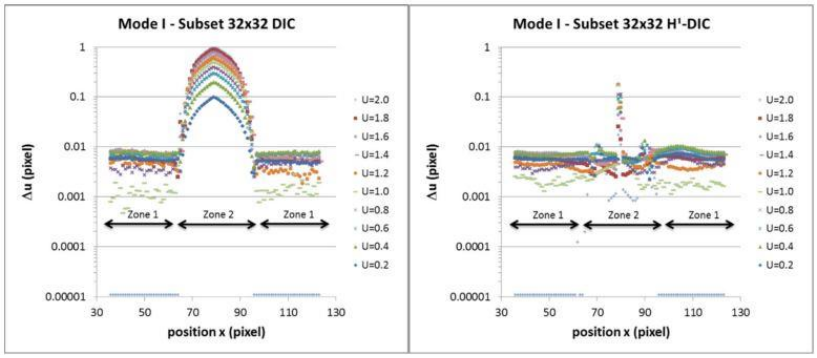

Fig.2. 15 : Classical DIC algorithm and Hevside H^1-DIC algorithm (Valle et al., 2015).

The crack is seen as a local discontinuity, no displacement/strain gradient is recorded in the neighbouring subsets. Another technique is based on the eXtended FEM (X-FEM) algorithm that has been developed to analyse discontinuous displacement fields without re-meshing (Moës, Dolbow and Belytschko, 1999); this algorithm is called eXtended DIC (X-DIC) (Réthoré, Hild and Roux, 2007;

Réthoré, Roux and Hild, 2007; Hild et al., 2015). The application of these two methods requires the modification of the standard DIC algorithm that is not a simple task for commercial users of DIC software (Nghiem, Al-Heib and Emeriault, 2015). Some methods as the DIC-F allowing localizing a cracks from the calculated displacement values (Lam Nguyen et al., 2011), or the methods used in (Nghiem, Al-Heib and Emeriault, 2015), where the displacement field is decomposed for crack identification, are born to answer to the need to develop crack identification algorithms from DIC outputs. In (Lomov, Ivanov, *et al.*, 2008; Feissel *et al.*, 2013) the DIC computed strain field is associated to a hypothetical behaviour of the material, so if the material has a global linear behaviour a crack is represented by a non-linearity. The procedure presented in this work is oriented toward the methods related to the manipulation of the DIC continuous strain field. Hypothesis are made about the crack direction and not on the material behaviour.

The images taken for image correlation as explained in the paragraph 2.3.2 are re-correlated using a different set of parameters, reported in *Table 2. 6*. Comparing *Table 2. 5* and *Table 2. 6* the subset size does not change but the subset step is reduced to 6px and a smooth on the deformation is performed. The decreased subset step results in a very noisy image, so a smooth parameter of 5 subsets was applied to reduce noise level in the final strain field; this results in a local gauge length around 0.42mm. Due to the numerous data points, the corresponding computation time is around 30 hours for eleven images.

Parameters	**Values**
Pixel dimension	6-6.2 µm/mm
Subsets size	40 px
Subset step	6 px
Smooth parameter/Local gauge length	5/(≈0.42mm)

Table 2. 6 : Parameters DIC – Crack detection.

To improve crack detectability, only the strain fields relative to maximum fatigue stress have been analysed. Moreover, the strain fields are calculated from the displacement fields by using the *large strain theory*, which amplifies the strain in the high strain regions, to improve the cracks detectability. A typical DIC strain field is reported in *Fig.2. 16*. High strain zones are related to the architecture of the composite, DIC errors and cracks. To separate cracks from the two former sources of high strain zones, a quantification of the strains related to woven architecture and DIC errors is performed.

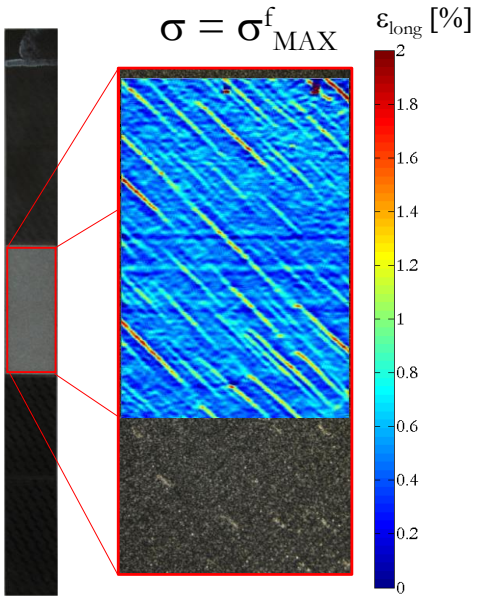

Fig.2. 16 : DIC strain field at $\sigma = \sigma^{f}_{MAX}$. Different sources of strain fluctuations: DIC algorithm errors, weave features and cracks in -45° direction.

For this analysis, an image of a strain field at the maximum fatigue load of a virgin specimen is reported in *Fig.2. 17*. In the represented strain field the strain values fluctuations are only related to DIC errors and woven features. A statistical analysis allows quantifying this kind of fluctuations.

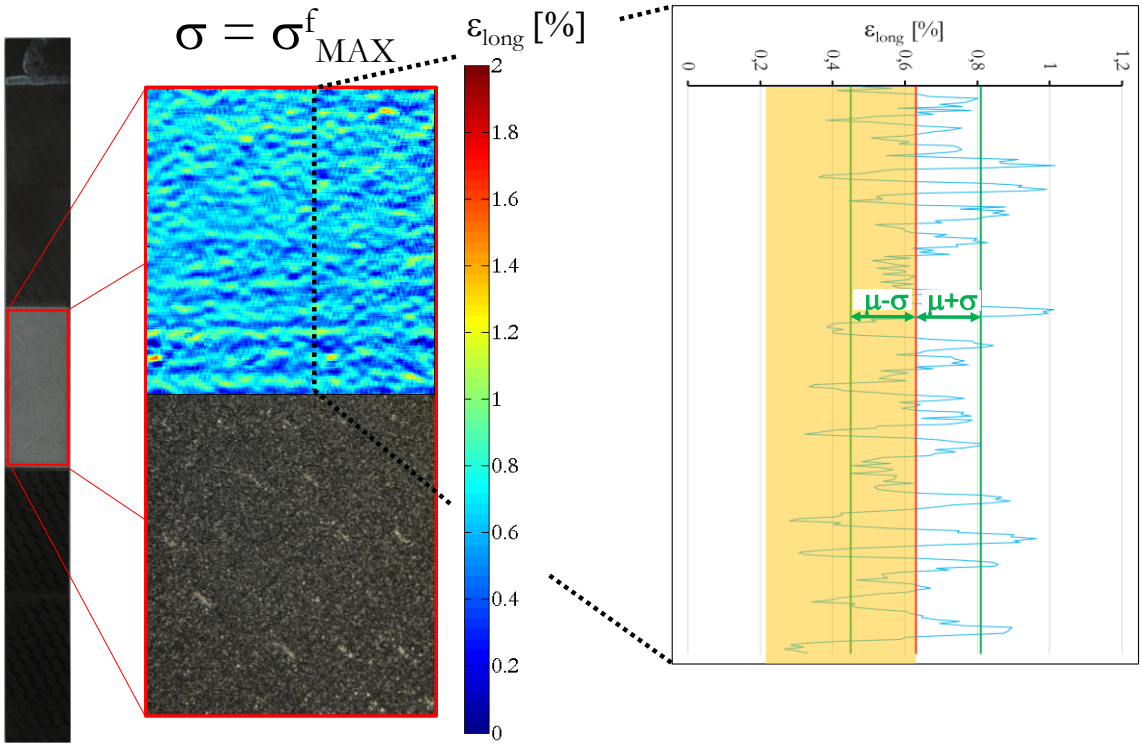

Fig.2. 17 : DIC strain field on virgin specimen. Analysis and quantification of noise.

The strain field of the specimen in *Fig.2. 17* has a mean value (μ) of 0.63% and a standard deviation (σ) of 0.18%. The mean value is represented in *Fig.2. 17* by a red line. For the following analysis, the standard deviator will be added from the mean value of the strain of each strain field relative to a load $\sigma=\sigma^{f}_{max}$. For the analysed images the mean value is re-calculated as in 2.3.2, while the standard deviation, being dependent from correlation errors and weave pattern, is used as a constant value. Strain values exceeding the sum of the mean strain value and the strain field standard deviation are considered as cracks (*see Fig.2. 15*).This is equivalent to fix a threshold value on an image for a thresholding segmentation.

The second part of crack detection is based on image processing. A binary matrix representation of the remaining strain values is created and the image is analysed using Avizo9®. The binary image is segmented using simple thresholding as previously suggested. A *Skeletonization* is then carried out on the segmentation. By this operation, a line is plotted inside each segmented zone, equidistant to shape boundaries of the element. At the end of this step, the DIC strain field is reduced to a map of segments. *Fig.2. 18* shows the original strain field (*Fig.2. 18* ***a)***) and the binarization (*Fig.2. 18* ***b)***). A MatLAB® script is finally employed to suppress segments oriented along directions different from the expected cracks directions (-45° in *Fig.2. 18*), hence high strain zones oriented transversally are not considered. The same script is finally employed to measure the length of the remaining segments, reported in blue in *Fig.2. 18* ***c)***.

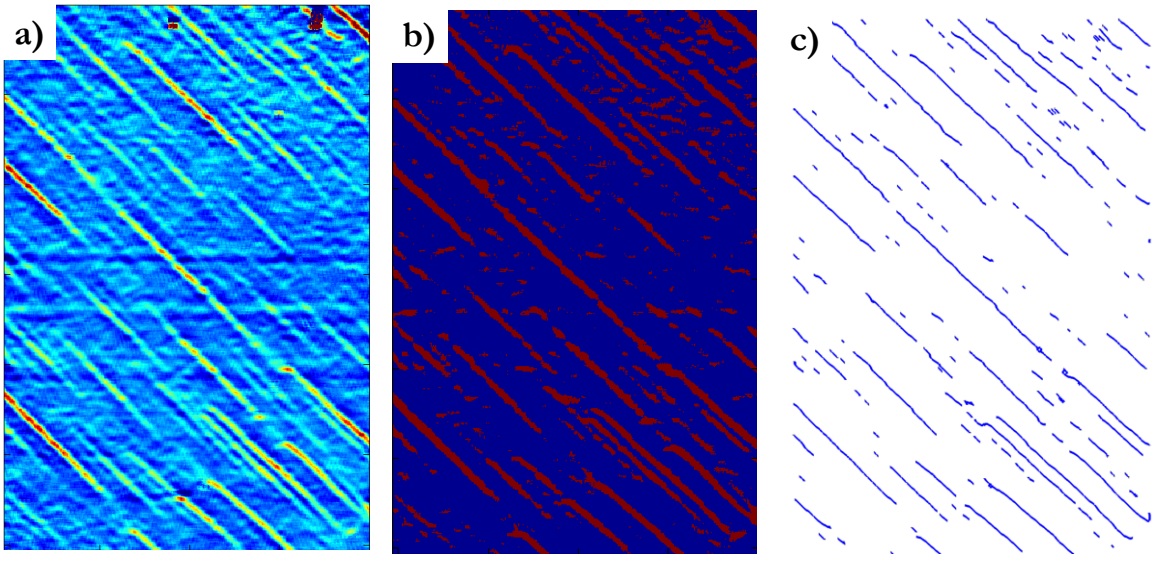

Fig.2. 18 : DIC image processing. **a)** Original strain field representation **b)** binarization result and **c)** skeletonization+MatLab filtering.

2.3.4 Improved stress-strain curves

Due to the limit on DIC acquisition rate (1 image every 6 seconds), DIC do not give a detailed strain evolution during load. A more *continuous* strain measurement has been obtained using corrected displacement data of the movable head recorded by the testing machine. In this paragraph data collection and correction procedure are described.

From the movable head displacement values (s), and knowing the free length of the specimens (l_0) at the beginning of the test, the longitudinal strain of the specimen is calculated, using the *infinitesimal strain theory*, as:

$$\varepsilon_{load-direction} = \frac{(l_0 + s) - l_0}{l_0} \qquad \text{Eq.4. 4}$$

In *Fig.2. 19* is reported a hysteresis loop tracked using the longitudinal values of the deformation obtained by DIC and *Eq.4. 4*, blue line represents the longitudinal strain calculated using the head displacement, while red points are obtained using DIC. For these latter, the error bars are plotted starting from data in *Table 2. 5*: the errors affecting mean values of the measured strain fields are related only to out-of-plane motions. The stress/strain curve in *Fig.2. 19* is relative to the first load/unload cycle, carried out before starting fatigue test. The DIC data and the strains calculated using *Eq.4. 4* are quite close. From the evolution of the longitudinal strain in *Fig.2. 19*, the material behaviour is almost linear in the initial stages of traction, after that it becomes increasingly non-linear. At the maximum load, an increasing strain at constant load is noticeable such as a creep of the specimen. At the end of the unload step, a residual strain is observed when the load decreases to zero.

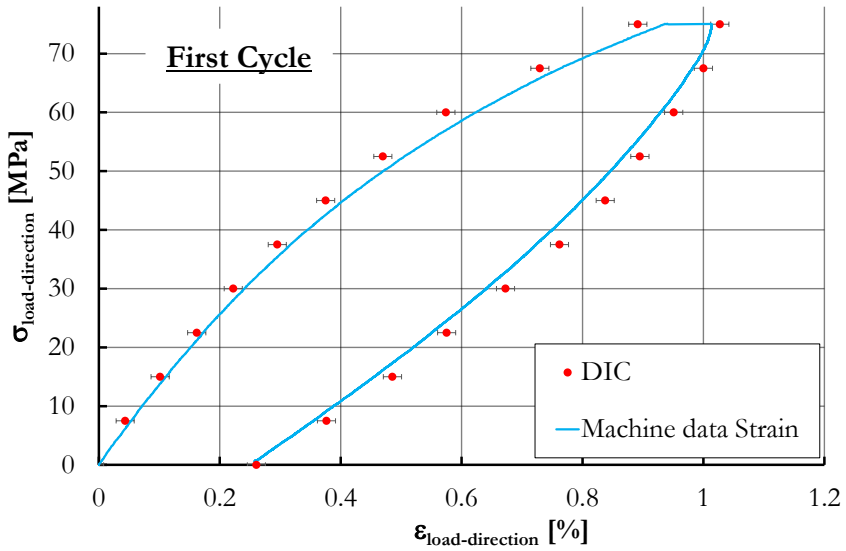

Fig.2. 19 : Longitudinal strain: DIC data and machine data.

Repeating the load/unload cycle after few thousand cycles a difference appears between DIC strains and strain obtained from *Eq.4. 4*. In *Fig.2. 20* is reported the stress/strain curve obtained from a load/unload cycle performed after 100k fatigue cycles.

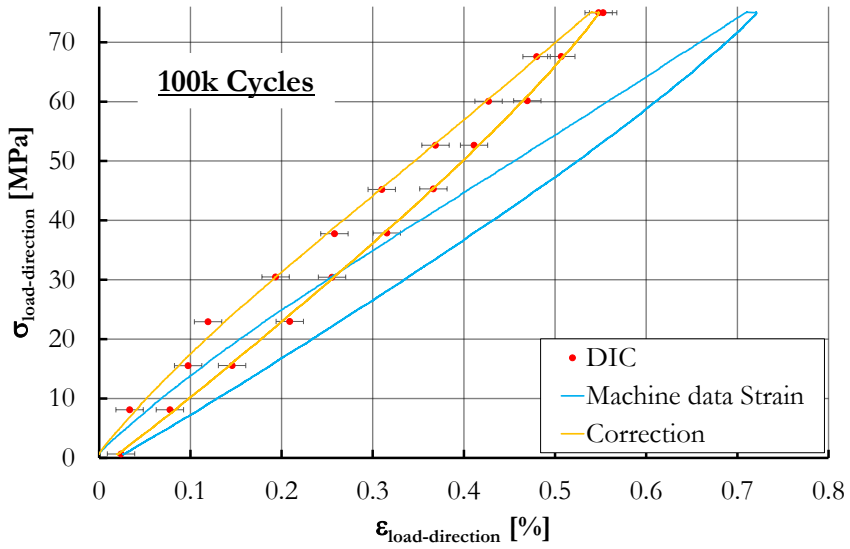

Fig.2. 20 : Load/unload cycle performed after 100k fatigue cycles.

As in *Fig.2. 19*, blue line and red points should be superposed, but in reality, there is a gap that increases as the strain increases. The strain corrected values are reported in *Fig.2. 20* as a yellow line, obtained multiplying the values of the blue line by a correction coefficient. The correction coefficient is calculated as the ratio of the maximum strain calculated by DIC and the maximum strain calculated using *Eq.4. 4*, and its evolution during fatigue is reported in *Fig.2. 21*.

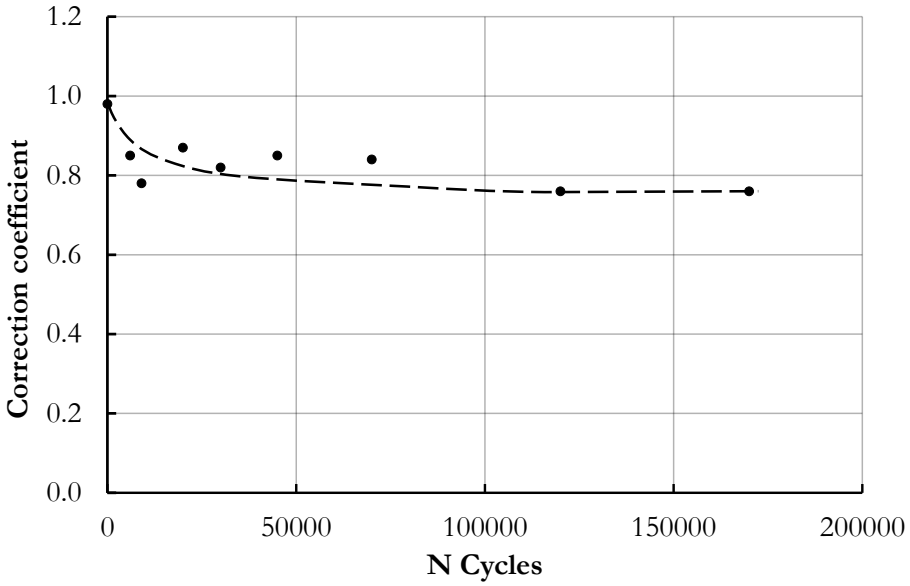

Fig.2. 21 : Evolution of the correction coefficients during fatigue.

As *Fig.2. 21* shows, in the first load/unload cycle the correction coefficient is 1 (see *Fig.2. 19*), then it decreases slightly and after few thousands of fatigue cycles it reaches a stable value (0.76 for the load/unload cycle reported in *Fig.2. 20*). Fatigue tests are periodically interrupted in order to perform *ex situ* observations. Each time the specimens were removed and replaced in the testing machine, the correction coefficient changes in value but keeps the same evolution during cycling (*i.e.* reduction toward a constant value).

The origin of the gap between DIC strains and strains calculated using *Eq.4. 4* is, however, a question still open. In (Xu et al., 2016) the same problem is encountered and the same correction strategy is employed. For the authors the difference between DIC and crosshead data strains was due to the machine compliance. In the situation reported in *Fig.2. 20*, the specimen's stiffness is much lower than the machine components, and moreover, the DIC gives a response of the material stiffer if compared to the response obtained using machine data.

The variation of the actual/real length of the specimens could justify a decrease of the correction coefficient during fatigue of 3-5% that is quite small if compared to the situation illustrated in *Fig.2.21*.

Another error source is the estimation of l_0 (in *Eq.4. 4*): the specimen positioning inside the grips (*see Fig.2. 22*) is made manually, using white marks on the specimen to reproduce the installation after each stop, and manual is also the fastening of the screws.

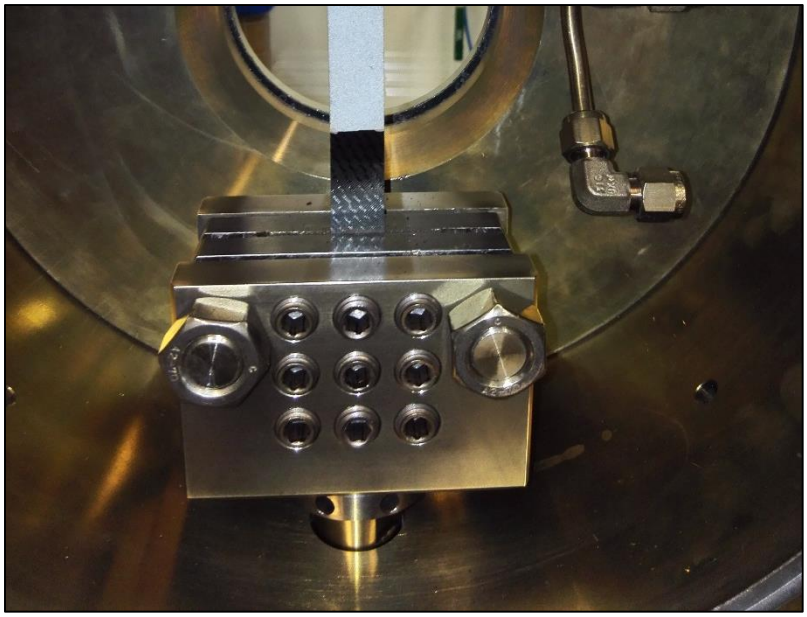

Fig.2. 22 : Grip of the test machine with specimen mounted on.

The positioning of the specimens (and so the free length of the specimens) is measured with a precision of ±2 mm and this could give an uncertainty on the strain about 0.01%, that should not evolve during fatigue. Also the specimen fixing system inside the testing machine could be an error source. During fatigue, vibrations may loosen the screws. A not proper fastening of the screws could results in a major free length of the coupon and consequently an error in using *Eq.4. 4* for strain calculation. It should be highlighted that without DIC this correction would not have been possible.

As will be explained in the next chapter, the correction of the machine data allows plotting an evolution of the elastic properties of the specimens during the test because the yellow line crosses DIC data points giving an evolution of the longitudinal strain also in the early stages of loading step where the data points obtained by DIC are not precise enough for elastic properties calculation.

2.4 *Ex situ* measurements - μ-Computed Tomography

This paragraph is devoted to a brief introduction on the X-Ray techniques in order to give a clear interpretation of the results obtained by μ-Computed Tomography (μCT) in the light of the physical phenomena acting in a μCT scan and the numerical artifacts due to the numerical reconstruction of the 3D images. For this reason the basic principle of an XR tomography scan, the principles of image reconstruction and some details on image processing are briefly resumed.

2.4.1 Computed Tomography – working principle

X-Ray radiography is a technique based on the interaction between a photon beam (X-Ray) generated by a X-Ray source, an X-Ray detector and the object interposed between the source and the detector. In the domain of the materials science this technique is often used for damage assessment, for example in (Lafarie-Frenot and Ho, 2006; De Greef et al., 2011). The limitation of this technique is that the resulting image is 2D hence superimposed damages are not visible and for the visible damages, the extension in the third dimension is unknown. The tomography is based on the principle of the radiography, but the results of a tomography is a sequence of sections of the scanned bodies.

In the composite science, tomography is used for different purposes. In the domain of Finite Element models of a woven composite, a tomographic scan permits to mesh the real architecture of the specimens as is made in (Straumit, Lomov and Wevers, 2015; Naouar et al., 2016). In (Pazmino, Carvelli and Lomov, 2014; Barburski et al., 2015) tomography is used to study the internal architecture of woven, while in (Badel et al., 2009) the object of the analysis is the deformation of tow shape during load application. In (Vignoles and Coindreau, 2007; Gao et al., 2016; Sisodia et al., 2016)

tomography is employed to study the degree of porosity in a material and the influence of the porosity on damage development. Finally an increasing large literature is available on cracks observation like (Scott et al., 2012; ElAgamy, Laliberte and Gaidies, 2015) for laminate composites or (De Vasconcellos, Touchard and Chocinski-Arnault, 2014; Muñoz, González and Llorca, 2015; Jespersen *et al.*, 2016) for fabrics.

An explanation of the principle of this technique helps to find the limits in its employment.

The transmission tomography is widely used in material science and the basic devices are illustrated in *Fig.2. 23*.

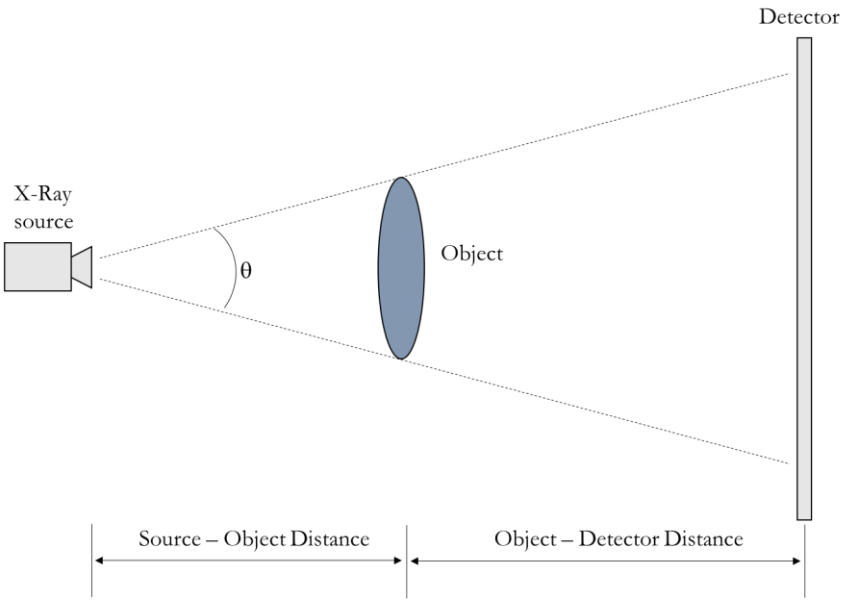

Fig.2. 23 : Cone beam transmission tomography – Geometrical properties.

The transmission tomography is based on the application of the *Beer-Lambert* law, also named *attenuation law* reported in *Eq.4. 5*.

$$I_1 = I_0 e^{-\mu s} \qquad \text{Eq.4. 5}$$

Where I_0 is the number of photons emitted by the source, I_1 is the number of photons transmitted through the scanned body along the line s and μ is the linear attenuation coefficient. This coefficient is a function of the atomic number and of the density of the traversed matter. For each straight line travelled by a photons beam, from the knowledge of the number of photon emitted by the source and the number of photon detected by the detector, it is possible to find the value of μ. The traditional radiography results in one image showing the attenuation coefficient: the quantity of transmitted photons is linked to the thickness of the scanned body and to density variations inside the

body. By repeating the scan from different angles, and using the inverse Radon transform a 3D image of the scanned solid can be reconstructed. For the reconstruction step other methods have been developed starting from the Radon's method, in order to make the reconstruction more accurate, faster and above all to implement this method in a computer. Due to necessity to assist the scan facility by a computer, the technique is named Computed Tomography (CT).

The spatial resolution of the 3D image gives the adjective "*micro*" when this is lesser than 100 μm (Stock, 1999) and the elementary volume is called voxel that is the analogue of the pixel for a traditional 2D image.

Today a large number of reconstruction methods are employed to obtain a 3D image from a series of CT scans. These methods could be grouped in two categories: analytical algorithms and algebraic (or iterative) methods. In the first category, approaches similar to the inverse Radon's transformed are used, these methods are generally fast, but are not able to perform a reconstruction when some radiographies are missing. Direct back projection and filtered back projection lie in this category. The former technique requires the simple application of the Radon's transform, but the results could be affected by star (or streak) artifact. The filter back projection is a method employing a Fourier transform. The scans are analysed in the frequency domain, filtered in order to reduce the noise at each frequency and then reassembled to reconstruct the 3D image using the previous method. The last method, often named Feldkamp algorithm, is more time consuming of the former and the filtering of the image introduces a loss in spatial resolution; on the other hand, it allows having sharply edges (sharpness of the image) in the 3D images, a reduced noise and consequently a high quality image. In literature a large number of articles are available on these techniques, for further details see (Baruchel et al., 2000; Bruyant, 2002).

The algebraic or iterative methods are more time consuming and useful when it is not possible to perform scans all around the specimens but only from a restricted angle range. These methods employ for the reconstruction both the real scans and some regularization function giving information *a priori* known on the scanned object. Some of these methods have been developed in the '70s as the ART (*Algebraic Reconstruction Technique*) (Gordon, Bender and Herman, 1970) or the SIRT (*Simultaneous Iterative Reconstruction Technique*) (Gilbert, 1972), and other more recently as DART (*Discrete Algebraic Reconstruction Technique*) (Batenburg and Sijbers, 2011) or FIRT (*Filtered iterative reconstruction technique with information restoration*) (Chen et al., 2016).

X-Ray generation and detection

In a laboratory setup, X-Rays are produced by an X-Ray tube converting electrical power into X-Rays. A micro-focus tube can generate X-Ray with a small focal spot (5-10μm). In the X-Ray tube (*Fig.2. 24*) are contained a cathode and an anode. A filament crossed by a high voltage electric flow composes the cathode part.

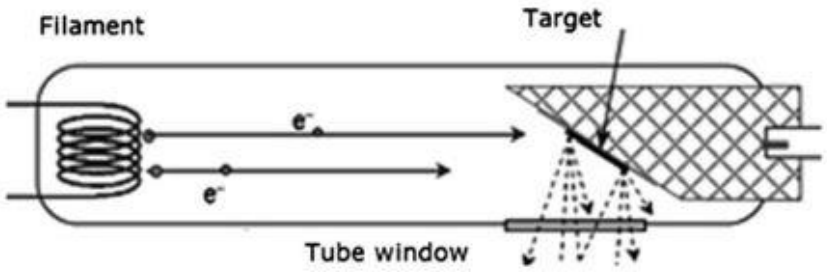

Fig.2. 24 : Scheme of a reflexion X-Ray tube (Haschke 2014).

The filament heats up, while the anode part has a different temperature. For the Seeback-Peltier effect, some electron come loose from the cathode accelerated by the electric potential difference between the cathode and the anode, toward the anode-target. When the electrons hit the anode, they are slowed down and for the Bremsstrahlung effect, a part of the kinetic energy of the electron is converted in photons and the emitted radiation forms a continuous spectrum. A typical X-Ray spectrum obtained using a tungsten and a chromium target is reported in *Fig.2. 25*.

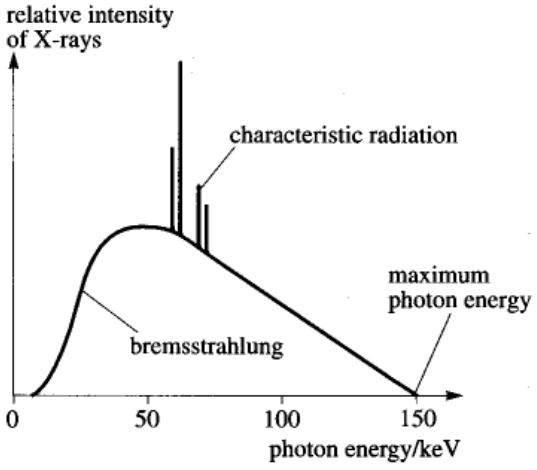

Fig.2. 25 : Typical X-Ray spectrum.

The form of the spectrum in *Fig.2. 25* is dependent on the interaction between electrons and target. In particular, the peaks are linked to an ejection of the electrons of the atoms composing the target, while the continuous parts of the spectrum is correlated to the deviation of the incidents electrons.

From *Fig.2. 25* it is clear that the X-Ray beam is a polychromatic beam and that changing the material of the anode, one can change the X-Ray spectrum of the beam.

Another important feature of this X-Ray generation technique is that the X-Ray beam is conical (*see Fig.2. 23* and *Fig.2. 24*), this allows, during a μCT scan, changing the resolution of the image, by varying the distance between the object and the X-Ray source (*see Fig.2. 26*).

The higher magnification is obtained moving the sample toward the X-Ray tube. In conclusion another important parameter is the size of the X-Ray beam at the exit of the source that is named *focus* of the tube. For a micro-focus tube, the smaller size of the focal spot is generally 5-10 μm.

The transmitted radiation could be detected by two different kind of detectors, but the working principle of this two detectors is almost the same: when a photosensitive material is reached by the radiation this is converted in electrical signal then transferred to the Analogic/Digital converter.

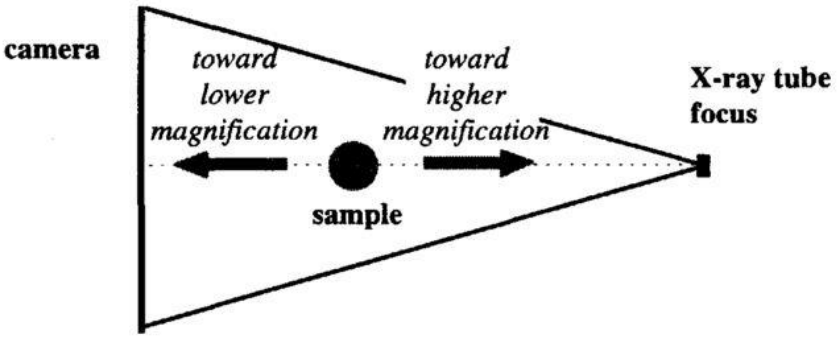

Fig.2. 26 : Example of geometrical magnification (Baruchel et al., 2000).

Artifact

Under the name of artifact are contained all the artificial patterns created during the reconstruction of the image. In the follow some kinds of artifact are described and some artifact reducing/suppressing techniques are discussed.

A first artifact is due to the polychromatic nature of the X-Ray spectrum. When the X-Rays pass through the specimens, the low energy portion of the spectrum is attenuated and the mean value of the spectrum rises. In a reconstruction algorithm this effect is not taken into account and so the density of a homogenous object could appear variable (*Fig.2. 27*). This artifact is named *beam hardening*.

To remove this effect some numerical solutions are proposed (*see* for example (Herman, 1979; Van Gompel et al., 2011)), or a low-pass filter could be applied at the source to truncate the low frequencies (Book *et al.*, 2007).

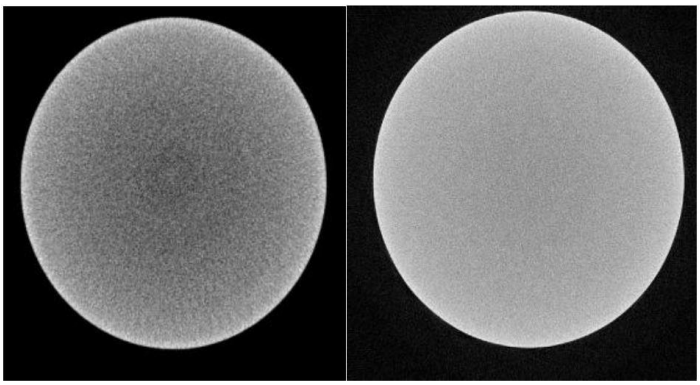

Fig.2. 27 : μCT scan reconstruction with beam hardening effect and after filter application (Sun, Brown and Leach, 2011).

The signal detected by the X-Ray detector has to be digitalized. Very high or very low values, close to the upper and lower bound of the conversion range should be avoided to prevent the *saturation of the detector*. Before each μCT scan, the low level of the digitalization range should be associated to the absence of photons (*black calibration*), while the upper side of the digitalization range should be associated to the situation in which the attenuation of the electrons flux is not due to the sample, but to air for example (*gain calibration*). If this calibration is not correctly performed or if the detector has some inoperative pixels a ring artefact appears on the reconstruction *Fig.2. 28*. Numerical methods are reported in literature for image correction as in (Axelsson, Svensson and Borgefors, 2006).

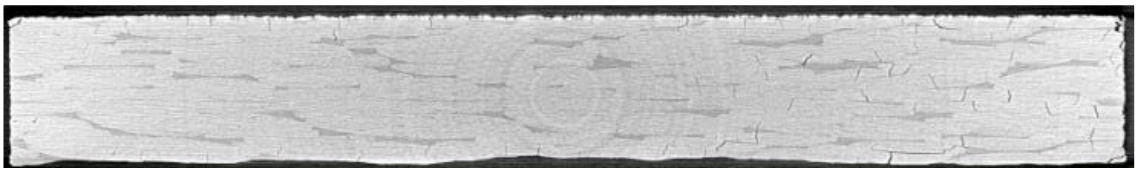

Fig.2. 28 : Ring artifact.

Other artifacts could be due to thermal expansion of the X-ray tube. As explained, for the emission of X-Ray some elements of the tube should be heat and if during the μCT scan the adaptation of the different components composing the tube at the new temperature is not done, the focal position of the beam could change because thermal dilatation of the tube (*beam drift*). To avoid this, the source is generally connected to a cooling system and the temperature in the room where the scan system is placed, has a controlled environment.

These, and other, artifact could coexist in a reconstructed image. Sometimes the correction of the single artifact is carried out by filtering the image, instead for other situations, the correction made by filters could degrade the image more than the artifact, and consequently, in the present work, no filters on the reconstructed images have been applied for artifact suppression.

Laboratory μ-Computed Tomography

A picture of the μCT tomographic setup used for the observation campaign resumed in this work is in *Fig.2. 29*. This is an UltraTom XL computed tomography system provided by RX Solution company. The reconstruction software, X-Act, is provided from the same company and permits the reconstruction of the 3D images and the suppression of some artifact. The three X-Ray sources mounted on the μCT system are: a transmission 160 kV nano-focus tube, a reflexion 230 kV micro-focus tube and a reflexion 150 kV micro-focus tube. For the experimental activity performed in this work, only the last one source has been used. For this source, the working principle is reported in the previous paragraphs.

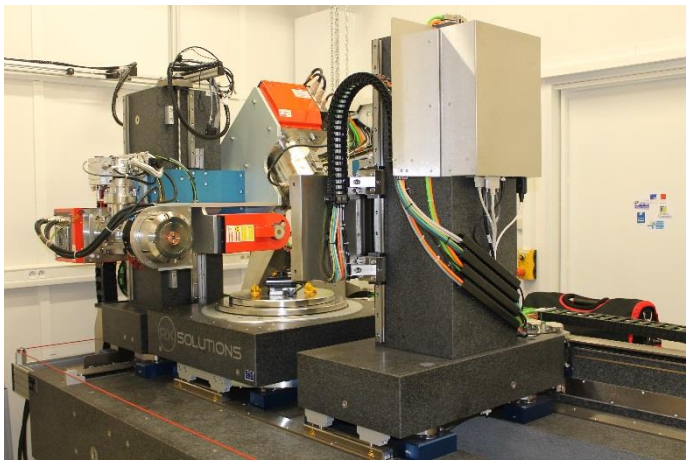

Fig.2. 29 : μCT facility at the PPrime laboratory.

The micro-focus tube Hamamatsu L1216-07 has a maximum power in output of 75 W and an X-ray beam angle (θ referring to *Fig.2. 23*) of 43°. Two devices are available for the X-ray detection: a Charge Coupled Device CCD (resolution 4008x2624 px², pixel size 5.9 μm) and a flat-panel detector Paxscan Varian 2520D (1920x1536 px², pixel size 127 μm). During the test campaign the Varian detector has been used in agreement with the lower received signal to noise ratio of the Varian detector for the range of used photons energies and flux.

For each µCT scan the specimen was mounted on a metallic support and placed on the rotating platen. The specimen dimensions limited the maximal reached spatial resolution. Referring to *Fig.2. 23* , the Source-Object Distance [*SOD*] was 26 mm and the Object-Detector Distance [*ODD*] 354 mm. The acceleration voltage of the electron was fixed in order to avoid detector saturation and at the same time, to have a wide spectrum of X-Rays. The X-Ray beam cone was not enough large to scan entirely the height of the specimen using a single scan. To overcome this problem, two options for the acquisition are existing: a circular tomography or a helical like acquisition (*see Fig.2. 30*). In *Fig.2. 30* the distance between red lines is the beam cone height.

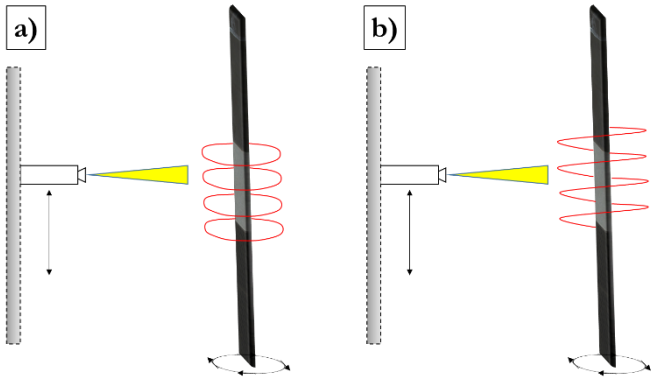

Fig.2. 30 : Acquisition techniques **a)** Circular tomography **b)** Helical tomography.

The helical acquisition was not suitable because the metallic support on which the specimen was mounted on for the scan obstructed the vertical motion of the source toward the bottom side of the specimen. For the circular acquisition, the source was not limited in the lower position because the scan started from a different vertical position, far from the support constrain. These two acquisition techniques are widely used in medical field, and adapted reconstruction methods have been developed to obtain the reconstruction of the entire scanned volume. For the helical acquisition, some adaptations of the Feldkamp algorithm (Feldkamp, Davis and Kress, 1984) are existing. Other adaptations of the same algorithm are created for circular acquisitions as in (Grass, Köhler and Proksa, 2000). For this technique, the most relevant defect is narrowed the transition zones and between two subsequent circular orbits of the source and is due to the conic nature of X-Ray beam. This give an intensity drop along the axial direction (Zhu, Starman and Fahrig, 2008) shown in *Fig.2. 31*.

Concerning the spatial resolution, the specimens was placed at the minimal distance from the source. This was limited to the half width of the specimens. The zoom provided from the positioning of the detector was maximised to deal with the X-Rays attenuation effects. The parameters used for X-Rays generation are reported in *Table 2. 7* with the spatial resolution achieved. The selected parameters are recurrent for this kind of materials, see for example (Straumit, Lomov and Wevers, 2015).

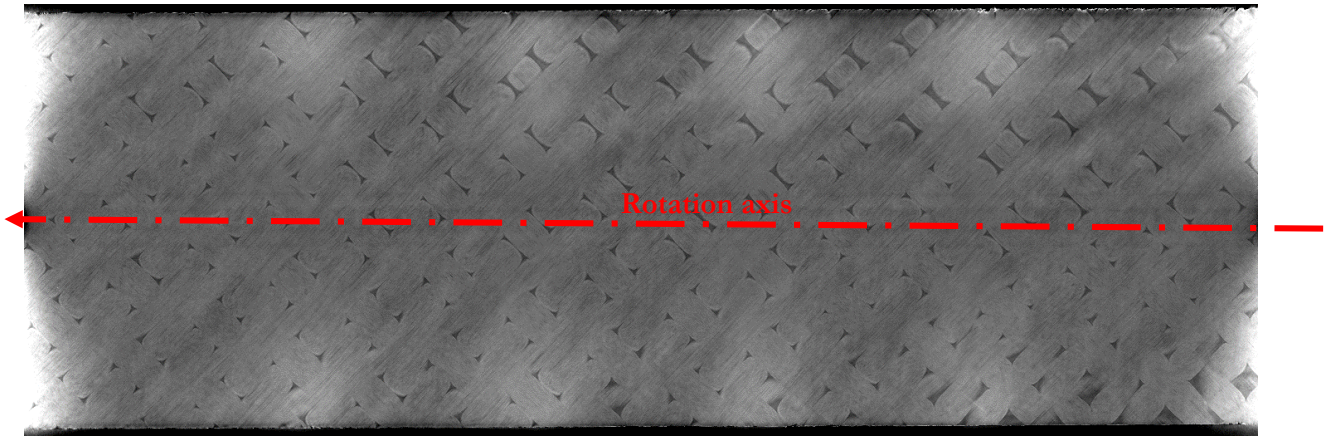

Fig.2. 31 : Slice of µCT scan. Intensity drop along the axial direction at each circular orbit transition.

Parameters	Values
Voltage [kV]	60
Current Intensity [µA]	139
Power [W]	8.34
Averaging	20
Frame Rate [pps]	4.8
Spatial resolution [µm/px]	8.79

Table 2. 7 : Parameter for X-Ray generation

The µCT scans have been performed using the circular acquisition and an anti-ring shift option in order to reduce ring artifact. The duration of each scan was around 11 hours.

The reconstruction stage is performed using X-Act. The 3D image is obtained using the Filter Back-Projection techniques and using some correction tools. One of this allows correcting *beam drift* and another one allows correcting the offset in the reconstruction of some slices due to relative oscillations of the specimen respect to the source or the detector. During reconstruction, an anti-ring filter was applied and a reduction of the noise by using the filter back projection reconstruction algorithm was obtained.

2.4.2 Image segmentation

The image segmentation is a process carried out to split a digital image into several segments. This operation is generally used to highlight edges, pores or inclusion in a bulk material. In the material science, the segmentation is usually performed for two reasons: to quantify damage/porosity and to

extract the real geometry of a sample. A segmentation is the final step of a longer image processing. In this image processing, filters are applied to the initial image to improve the visibility of barely visible elements of the original image, eliminating the noise. It is obvious that for each kind of searched elements in a 3D image there exist different filters sequences applied to the initial image (Iassonov, Gebrenegus and Tuller, 2009). For cracks segmentations, edge detection filters are often applied to 3D images. This category includes the *Canny edge detector*, the *Sorbel filter*, the *Anisotropic diffusion filter*, the *Bilateral filter* and other. A good edge-preserving algorithm should follow two basic principles, that is to preserve geometric edges which represents the structures of an image and to suppress or remove insignificant details in the texture areas (Tang et al., 2016).

Morphological filters

Another class of filters employed for crack detection are the morphological filters. Morphological image processing describes a range of image processing techniques that deal with the shape (or morphology) of features in an image. Morphological operations are typically applied to remove imperfection on a 3D image (Megha Goyal, 2011). D*ilation*, *Erosion*, *Closing* filter and *Opening* filter are the most notorious operations.

The application of a morphological filter to an image requires the definition of a structuring element. This is defined in (Gonzalez, R. C., Woods, 2007) as a *small set or a subimage used to probe an image under study for properties of interest*. For simplicity let consider the case of binary image. A 2D binary image is a $p \times q$ matrix containing a zero or a one in each cell. In this context, a structuring element is a rectangular or square matrix containing in each cell binary numerical values, an example of binary structuring elements is reported in *Fig.2. 32* where one and zero are associated to white and black pixels respectively.

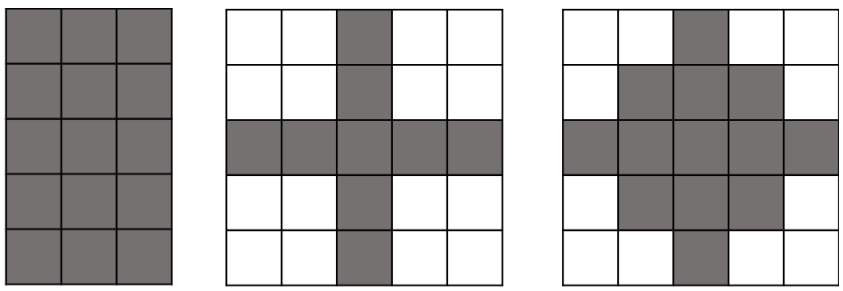

Fig.2. 32 : Different sizes and kind of structuring element: line, cross, diamond.

Dilation and erosion are the most elementary morphological filters; for the erosion filter application, the centre of the structuring element is superimposed to each pixel of the binary analysed image. The eroded image is composed by all the pixels of the initial image in which the structuring element matches the initial image pixels (Mardiris and Chatzis, 2016). The dilation filter is based on the same principle but the resulting dilated images is the union of the initial image pixels and of all the pixels in which the centre of the structural element is placed to have at least one element overlapping the initial image pixels. An example of erosion and dilation is presented in *Fig.2. 33*: in this figure the results of the erosion and of the dilation filter are reported as grey pixels. It should be noted that grey pixels in the eroded image are subtracted from the initial image, while in the dilated image the grey pixel are added.

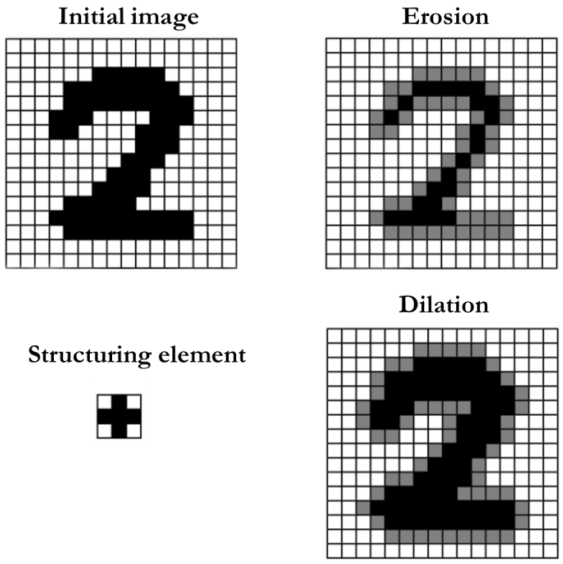

Fig.2. 33 : Erosion and dilation images obtained using the illustrated structural element on the initial image. Grey pixels are new black pixels in the final image (Mardiris and Chatzis, 2016).

Closing and opening are combination of dilation and erosion filter. A detailed mathematical description for closing and opening filter is reported in (Serra and Vincent, 1992). Morphologically, the result of the application of the opening filter is the smooth of the contours, the elimination of thin protrusion and the breaking of narrow isthmuses. A closing filter also tends to smooth the contours of the image, but contrarily to the opening filter, it fuses narrow breaks, eliminates small holes and fills gaps in the contour (Gonzalez, R. C., Woods, 2007). An opening filter correspond to the application of an erosion followed by a dilation of the result using ever the same structuring element. The closing filter is exactly the opposite, hence the application of a dilation filter followed by an erosion on the resulting image. These two filters are widely used in image segmentation, some example are reported in (Vincent, 1994) for medical and materials science fields. The result of an opening and of a closing filter applied on a 2D image of a cracked composite tow is shown in *Fig.2.*

34. The structuring element is a line having a thickness of 4 pixels (4×1 referring to *Fig.2. 32*) and oriented along the -45° direction that is the perpendicular direction of the target crack. Along a line perpendicular to the crack direction, the crack results as a region of black pixels that the closing filter fills as shown in *Fig.2. 34* ***b)***. On the same initial image, an opening filter tends to separate the crack edge, for this reason the target crack appears more pronounced compared to the initial image in *Fig.2. 34* ***c)***.

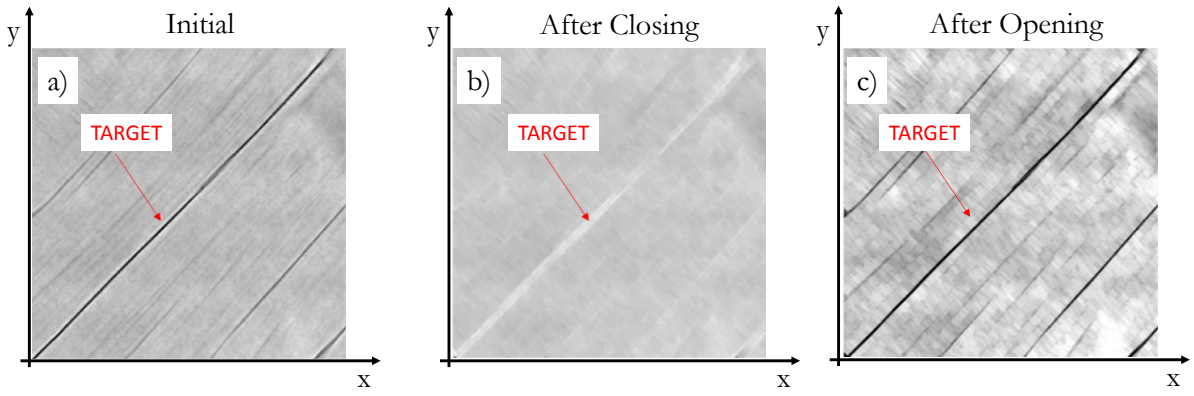

Fig.2. 34 : Cracked tow and closing and opening filter application. The target crack of the initial image **a)** disappears after the application of the closing filter **b)**, while it is more evident after the application of the opening filter **c)**.

Image thresholding

Generally, images are not in binary format, but composed by pixels having several grey shades or grey levels. In a typical μCT image, 16 bit contain the information about the grey level of each pixel, this means that each pixel could assume a value between the 65536 (2^{16}) combination of zeros and ones, keeping in mind that a low value of the pixel corresponds to a grey level close to black, while the highest value represents the white. In the domain of image processing, a standard practice is to report the number of pixel having the same pixel value in a histogram as illustrated in *Fig.2. 35*. The histogram in *Fig.2. 35* shows the grey levels distribution of the image already reported in *Fig.2. 34* ***a)***, that are concentrated in the low grey level zone. A zoom of the native histogram where the grey levels are between 12500 and 15000 allows appreciating the real grey level distribution of the image: having the same number of bins (1024), the native histogram shows a peak of 20000 pixels for a grey levels between 14477 and 14605 that is represented by only 2 bins in the native histogram; in the zoom of the native histogram, the grey levels per bin is increased about 26 times and the result is a better representation of the greyscale of the image. For this reason, in the rest of this chapter, all the native histograms will be reduced to the interesting zone. Furthermore, the histogram of two different

images will have different maximum and minimum values; in consequence of this, for simplicity in the presentation of the segmentation steps and didactic purpose, all the reduced histograms will be converted to 8bit histograms in which the white will be represented by the pixel value 255.

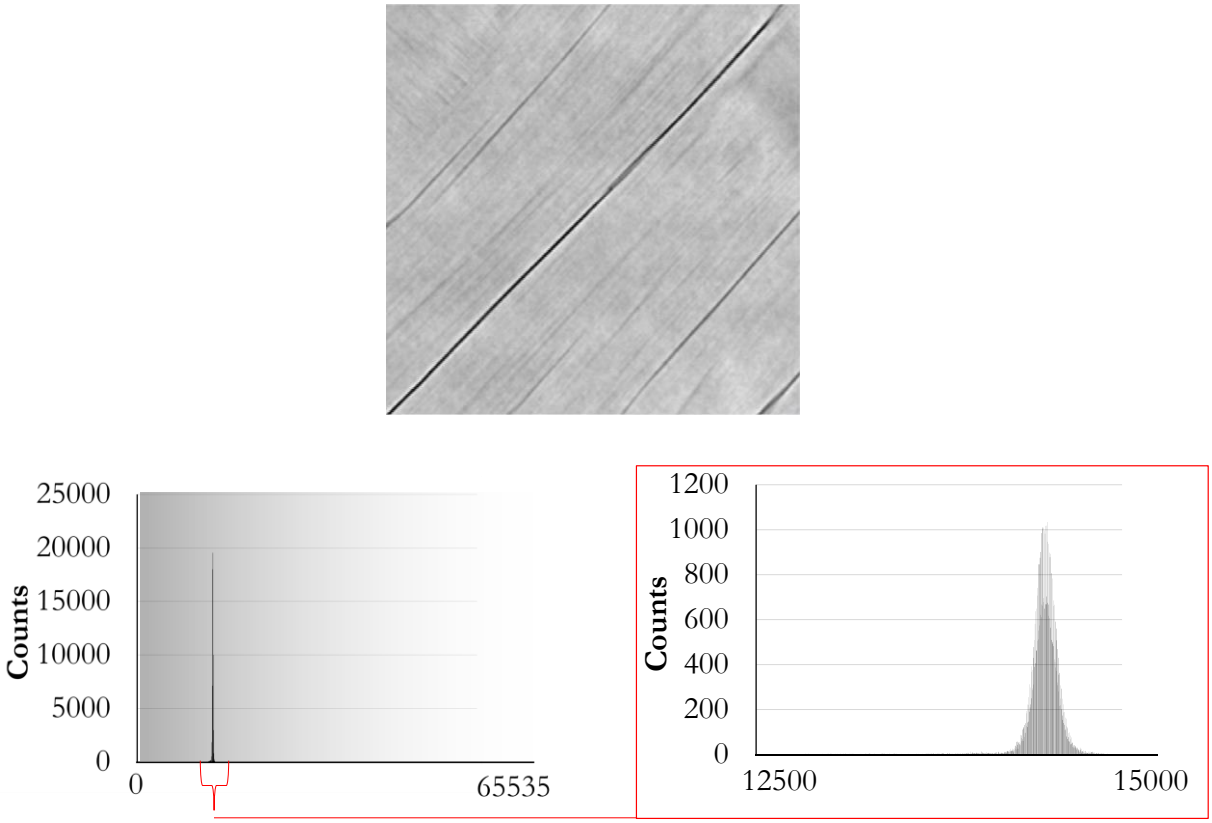

Fig.2. 35 : histogram of a 16bit image. The grey values of the image are concentrated in the low part of the grey levels.

Image thresholding has a great interest in image segmentation because it is the simplest method for the separation of different elements in a µCT image: it requires the imposition of a threshold on the grey level of the image to separate the pixels having a value over the chosen threshold value from the pixels having a value under the threshold.

A µCT slice of an exterior ply of the woven composite is reported in *Fig.2. 36* ***a)***. Resin rich regions, cracks and tows are clearly distinguishable. The original image is segmented using two different threshold values reported on the associated histogram (*Fig.2. 36* ***b)***). In the first case the pixel having a grey value between 0 and 130 are selected (in blue *Fig.2. 36* ***c)***), while in the second case all the pixel having a grey level from 0 to 160 are segmented (in green *Fig.2. 36* ***d)***). Other segmentation methods take into account further information of the image like the grey gradient or the connected zones.

The image processing remains an adaptive method. In (Sket et al., 2014) the Hough transform is used for cracks identification, a Canny edge detector reveals the edges of the cracks that are then segmented by a simple image thresholding. In (Wright et al., 2008; Scott et al., 2012) the edges are detected using the phase contrast information of the 3D image and then segmented by thresholding. In (Chateau et al., 2011) the authors observe that the fluctuations of the greys levels is useful to localize a crack in a SiC_f/SiC composite, and the same idea is employed in (ElAgamy, Laliberte and Gaidies, 2015) for a laminated C/Epoxy.

These papers, and *Fig.2. 36* show that a threshold could be a simple and fast solution (and somewhere enough accurate in a first approximation) for crack detection. The same threshold value is a strong limit for segmentation. In an image where the grey values for cracks and other no-damaged zones are similar, the choice of the *appropriate* threshold is not a simple task. The information provided to the segmentation procedure insert a limit on the detectable features.

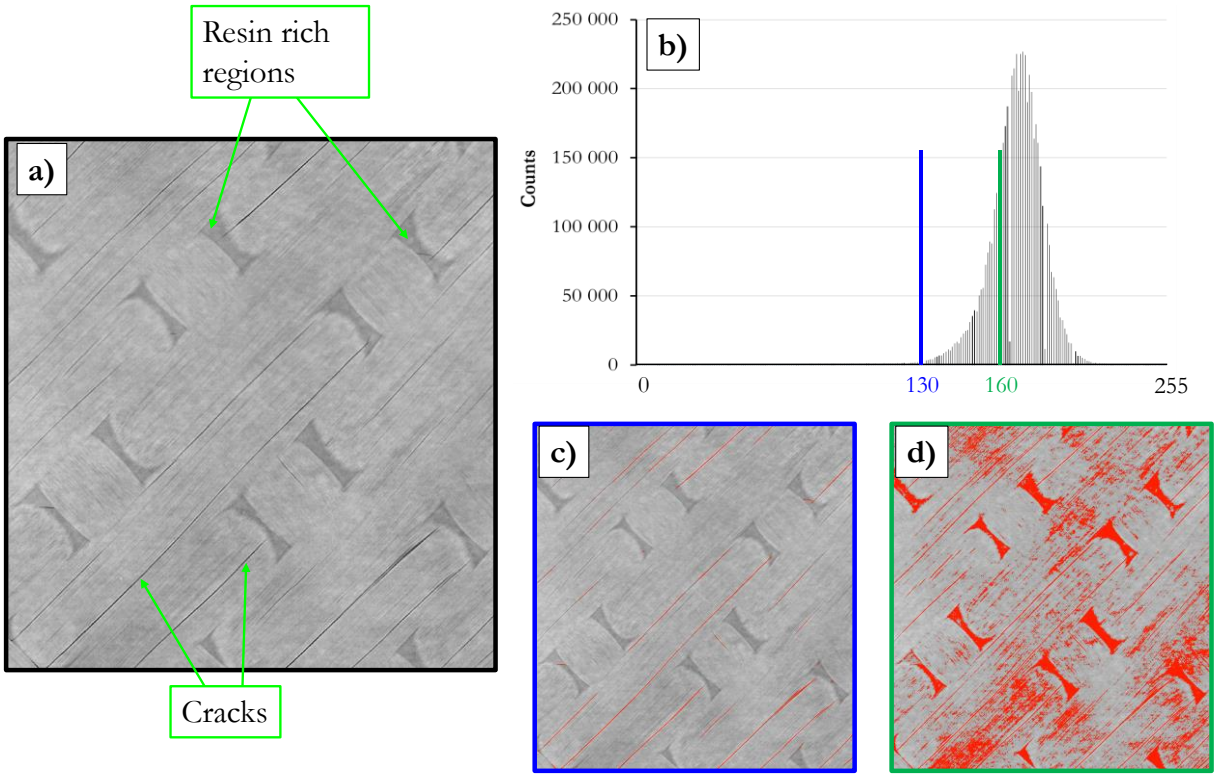

Fig.2. 36 : Threshold segmentation **a)** Original image **b)** Histogram of the initial image **c)** Threshold segmentation using 0-130 as threshold values **d)** Threshold segmentation using 0-160 as threshold values.

The evaluation of quality of a segmentation remains quite subjective, an unwritten rule is to arrive to segment at least the interesting items that are bare eye visible on the 3D image.

For this reason, a crack in the follow is a well-defined element having some specific features and is segmented for each 3D scan using ever the same technique and the same set of parameters. All the image post-processing activities in this work are performed using AvizoFire9®.

2.4.3 Segmentation of woven architecture from µCT scan

An image segmentation has been employed in order to separate resin zones, weft tows and warp tows. The initial image has a resolution reported in *Table 2. 7*. A detailed explanation of the segmentation procedure is given in the following, for each filter application, the result is reported in the corresponding image.

Matrix segmentation

The choice to begin the segmentation of the composite constituents from the matrix is due to the similarity of the parameters defining a warp and a weft zone: grey levels, shapes and contrast are quite similar and the difference of the orientation is 90°. The identification and the exclusion of the matrix zones simplifies the segmentation of warp and weft.

Before the application of segmentation functions, the image is processed by a filter sequence. The first filter is a *closing filter* using a cubic structural element of 26 voxels. The result (in *Fig.2. 37*) is an image where little dark regions embedded in more bright regions are integrated in the latter ones.

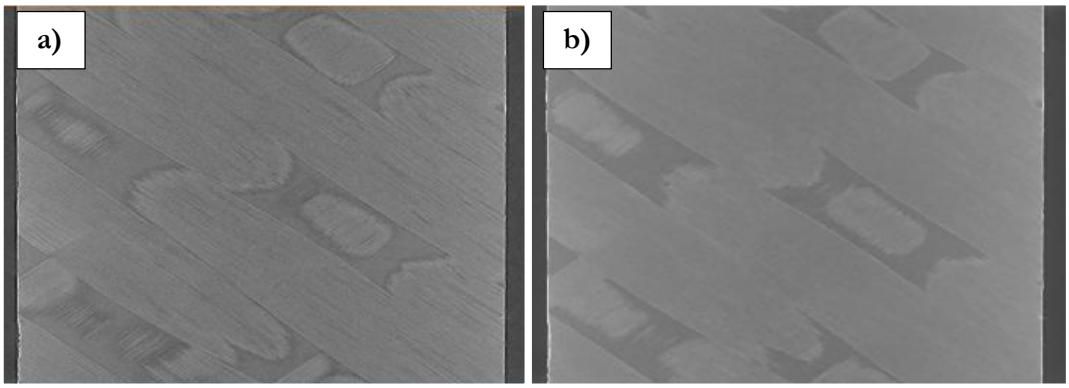

Fig.2. 37 : Closing filter **a)** Original image and **b)** result of a closing filter application.

After this homogenization, the application of an *anisotropic diffusion* allows reducing the noise in the image and at the same time to emphasize the contour lines (*Fig.2. 38*). A contour, from a mathematical point of view, is a small regions in which the levels of grey change suddenly, or in other terms, there is a high value of the gradient of the grey levels.

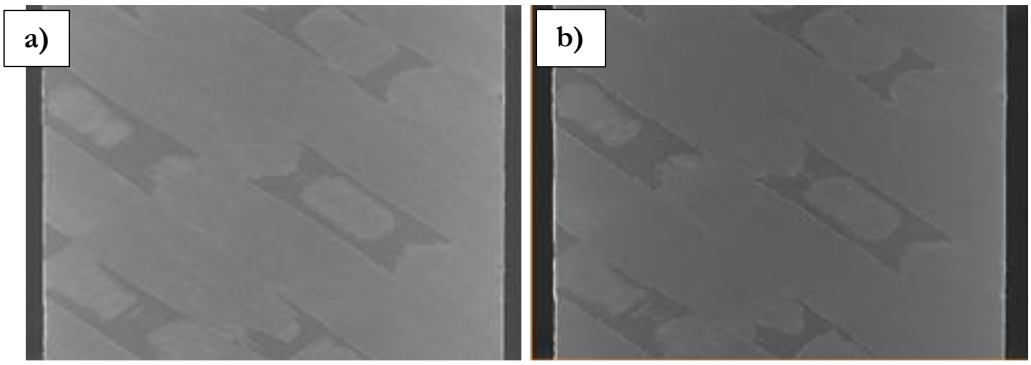

Fig.2. 38 : Anisotropic diffusion **a)** Closing image and **b)** Result of an anisotropic diffusion on the closing image.

A *Sorbel filter*, analysing the gradient values, permits to extract the contours in the images. These contours, are finally segmented (*Fig.2. 39*) by fixing a threshold on the grey levels of the *Sorbel filters* resulting image.

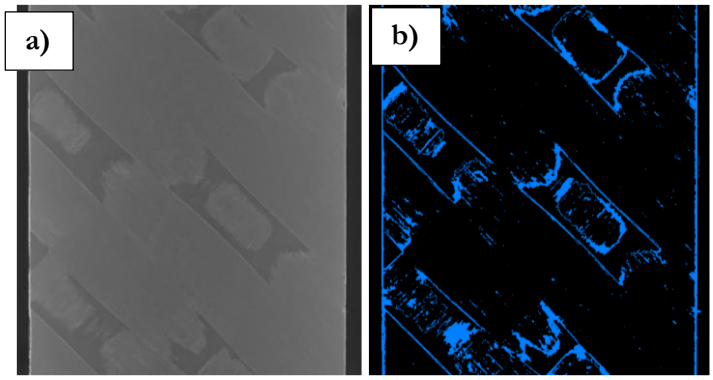

Fig.2. 39 : Segmentation **a)** anisotropic diffusion on the closing image **b)** Contours segmentation result.

The blue regions of the picture on the right side in *Fig.2. 39* are the segmented zones. For this image the pixels may have only two values *i.e.* 1 and 0, and the blue colour is associated to the value 1.

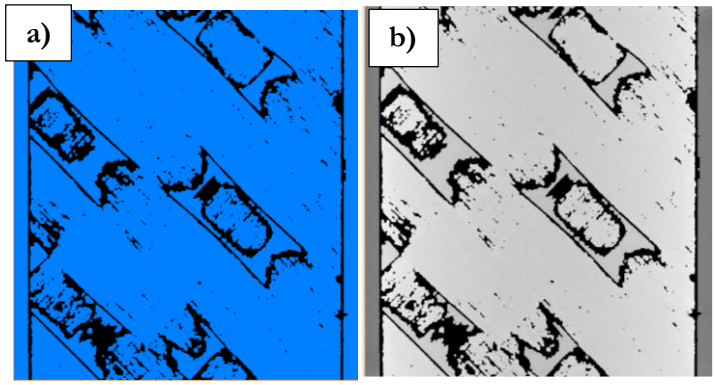

Fig.2. 40 : Segmentation inversion **a)** Inverted segmentation and **b)** result of the multiplication between the inverted segmentation and the original image.

This segmentation is then inverted (the 0 became 1 and *vice versa*) and multiplied for the original image to remove the contours from the initial image *Fig.2. 40*. This operation gives an image containing some border fences, very useful to separate different regions during segmentation.

Starting from the image in *Fig.2. 40* ***b)*** the *Magic Wand* tool in Avizo9® allows selecting the tow regions and defining the appropriate grey levels, obtaining the segmentation of the tow zones (without distinction among warp and weft). Remaining regions are external to the volume (air) or matrix (see *Fig.2. 41* ***b)***).

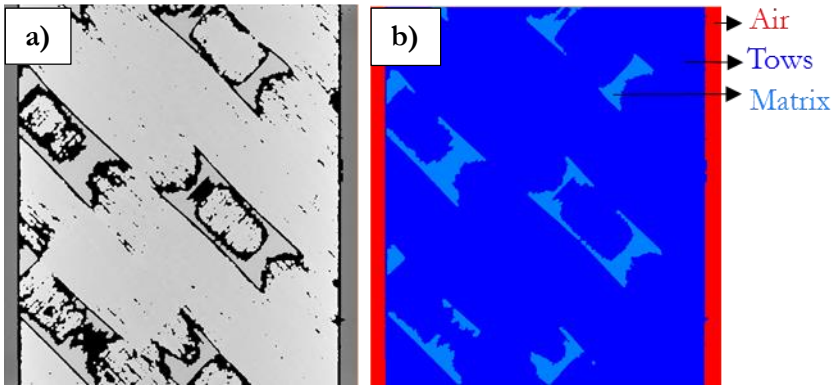

Fig.2. 41 : Segmentation result **a)** Multiplication between the inverted segmentation and the original image and **b)** Air, matrix and tow segmentation.

Tows segmentation

For the segmentation of the tows the most natural technique is to take advantage of their orientation. The resin rich regions are no longer a problem because they have been isolated in the previous step. Starting again from the original image, by the application of *closing* and *opening* filters with an orientation of the structural element along the warp or the weft direction and combining the results, one obtains *Fig.2. 42*.

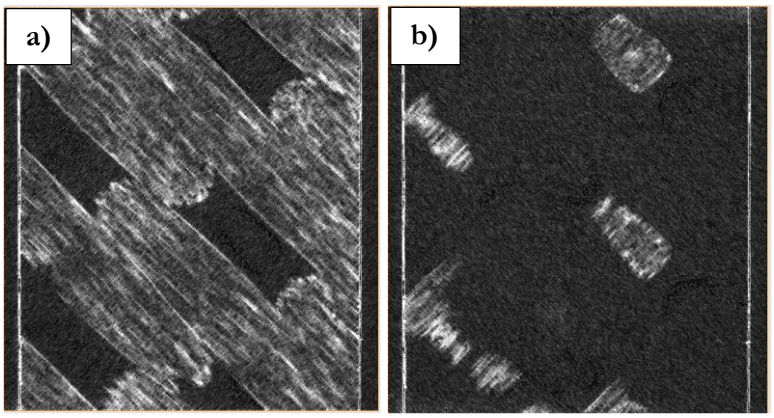

Fig.2. 42 : Combination of *closing* and *opening* filters. Result along the warp (**a)**) and the weft (**b)**) direction.

A new image is then created starting from an arithmetical combination of the two images of *Fig.2. 42*. The value of each pixel of the new image is calculated separately. If *n* is number of pixels composing the two images of *Fig.2. 42*, *i* is the generic pixel and P^i_{warp} and P^i_{weft} are the values of the generic pixel in the image in *Fig.2. 42* ***a)*** and *Fig.2. 42* ***b)*** respectively, the value of the generic pixel of the new image is (P^i_{new}):

$$P^i_{new} = \begin{cases} P^i_{warp} & if\ P^i_{warp} < P^i_{weft} \\ P^i_{weft} & if\ P^i_{warp} > P^i_{weft} \end{cases} \qquad \text{Eq.4. 6}$$

Application of *Eq.4. 6* gives the image of *Fig.2. 43*. Before the finalization of the segmentation a *Gaussian filter* is applied for noise reduction.

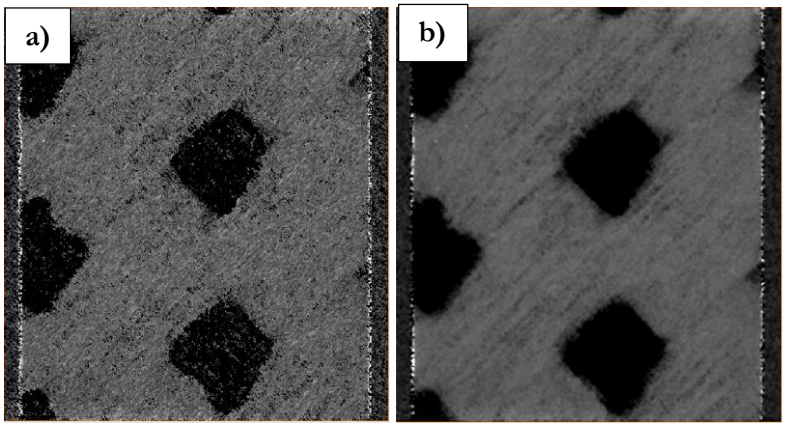

Fig.2. 43 : Warp segmentation obtained by combination of warp and weft image pixel values. Before noise reduction (**a)**) and after noise reduction (**b)**)

In conclusion, ever using the *Magic Wend* tool, the warp and weft regions are segmented. Initial image and segmentation are in *Fig.2. 44*, while a three-dimensional rendering of the results is in *Fig.2. 45*.

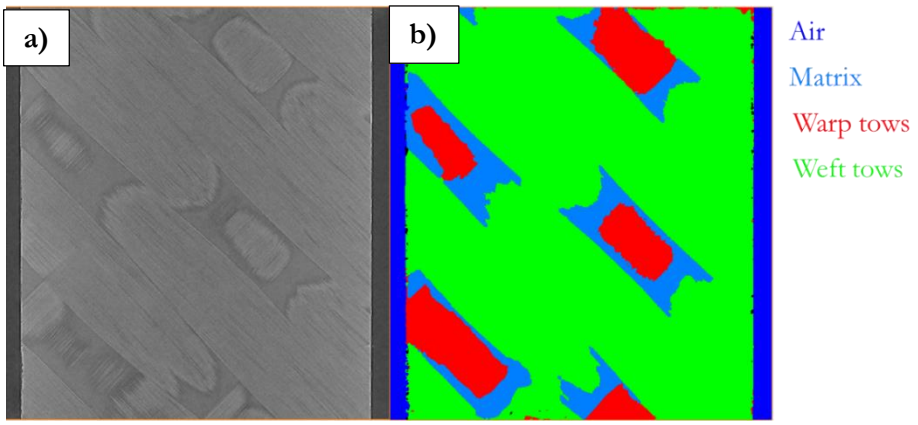

Fig.2. 44 : Complete segmentation. **a)** Initial image **b)** Air, matrix, warp and weft tow segmentation

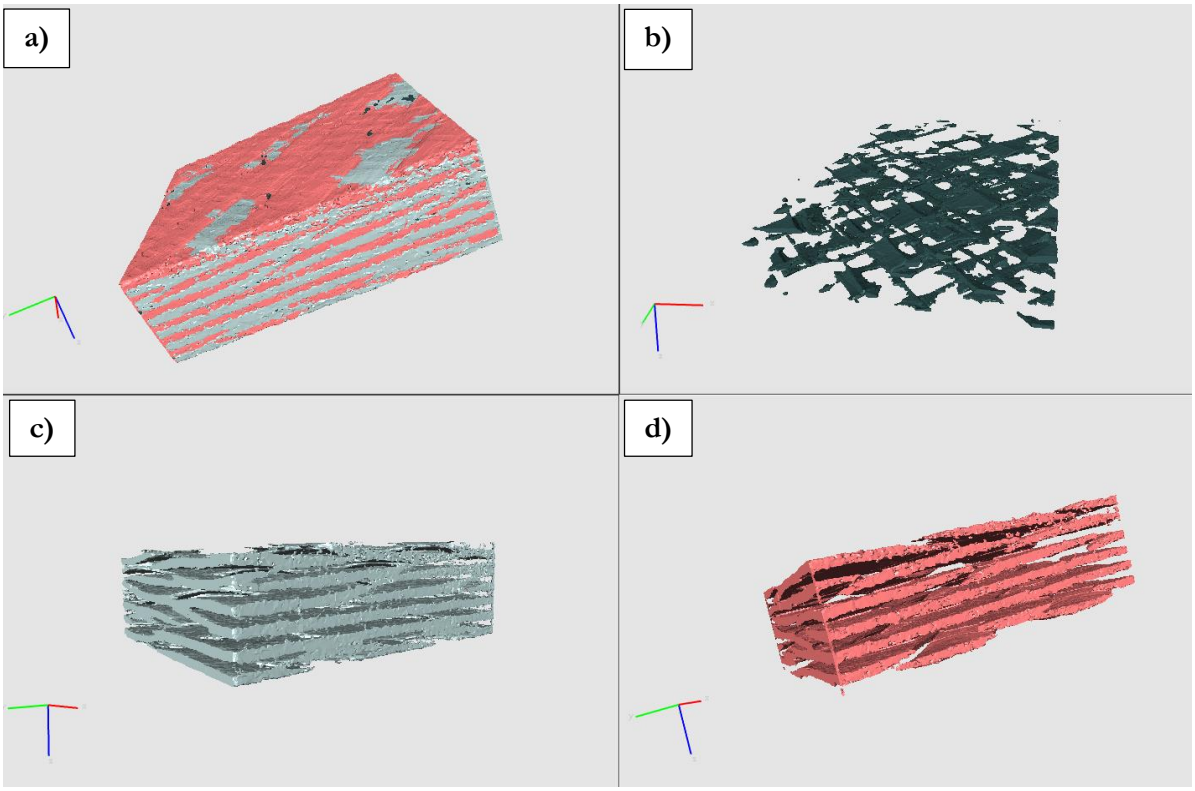

Fig.2. 45 : Three-dimensional segmentation result. **a)** Three-dimensional rendering of the segmented volume **b)** Three-dimensional rendering of the matrix regions **c)** Three-dimensional rendering of warp tows and **d)** Three-dimensional rendering of weft tows.

The visual results are quantified in *Table 2. 8*.

Material Label	Material Name	Total voxel Analysed	Voxel Label Count	Volume Fraction
1	Weft	4.72e+08	2.315e+08	0.49
2	Warp	4.72e+08	2.225e+08	0.47
3	Matrix	4.72e+08	1.8e+07	0.04

Table 2. 8 : Results segmentation.

In conclusion, the fibre volume in the composite, calculated as $V_F \times V_T$ is 0.595 (*cfr* 2.1), equally distributed between warp and weft direction.

2.4.4 Cracks segmentation

Due to image noise, to isolate cracks it is necessary to analyse their morphology for a better choice of the segmentation strategy. A reconstruction of a µCT scan performed on a damaged specimen is shown in *Fig.2. 46*. In the original image (*Fig.2. 46* ***a)***) cracks are clearly visible on the upper surface of

the specimens. These cracks are oriented in the fibre direction and no additional information are derivable from this image. In *Fig.2. 46* ***b)*** the specimen is cut by a plane perpendicular to the upper surface of the coupon. This cut, allows seeing inside the specimen, a zoom of the *slice* parallel to the cutting plane is reported in *Fig.2. 47*.

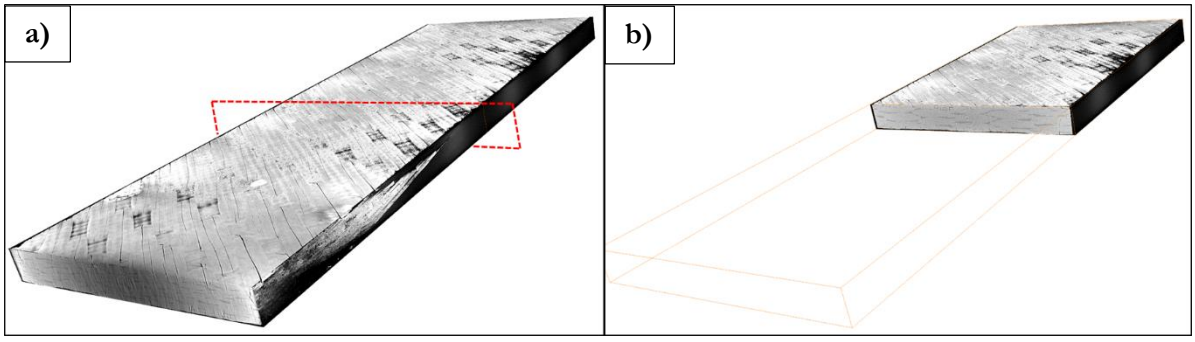

Fig.2. 46 : Damaged specimen µCT scan **a)** Whole specimen **b)** Cut specimen.

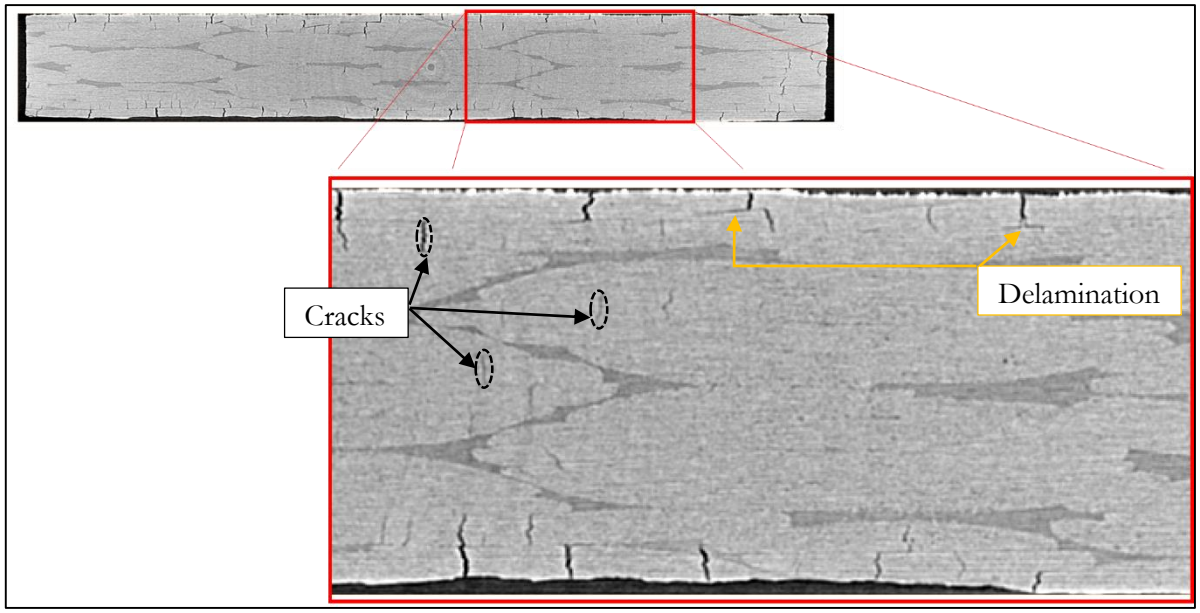

Fig.2. 47 : Zoom of the cutting plane. Crack and delamination along the thickness direction.

Fig.2. 47 shows some common crack properties. Despite the specimen in *Fig.2. 46* - *Fig.2. 47* is widely cracked, delamination, appears as little decohesion that starts from the crack tip and propagates between two differently oriented tows in the same ply. Delamination appears only just before the failure, in the majority of µCT scans this kind of damage is not detectable and the volume related to delamination is quite small compared to crack volume, for this reason delamination will not be taken into account in the presentation of the results in the following discussion.

In *Fig.2. 47* the cracks are condensed close to the edges of the specimen, and only intra-yarn cracks appear. It seems that the crack height is the same than that of the tow in which it is localized. Moreover, the few cracks far from the edge have a width smaller than the cracks placed more close to the external surfaces. This difference brings to operate using different segmentation parameters for the segmentation of more external cracks and for internal cracks.

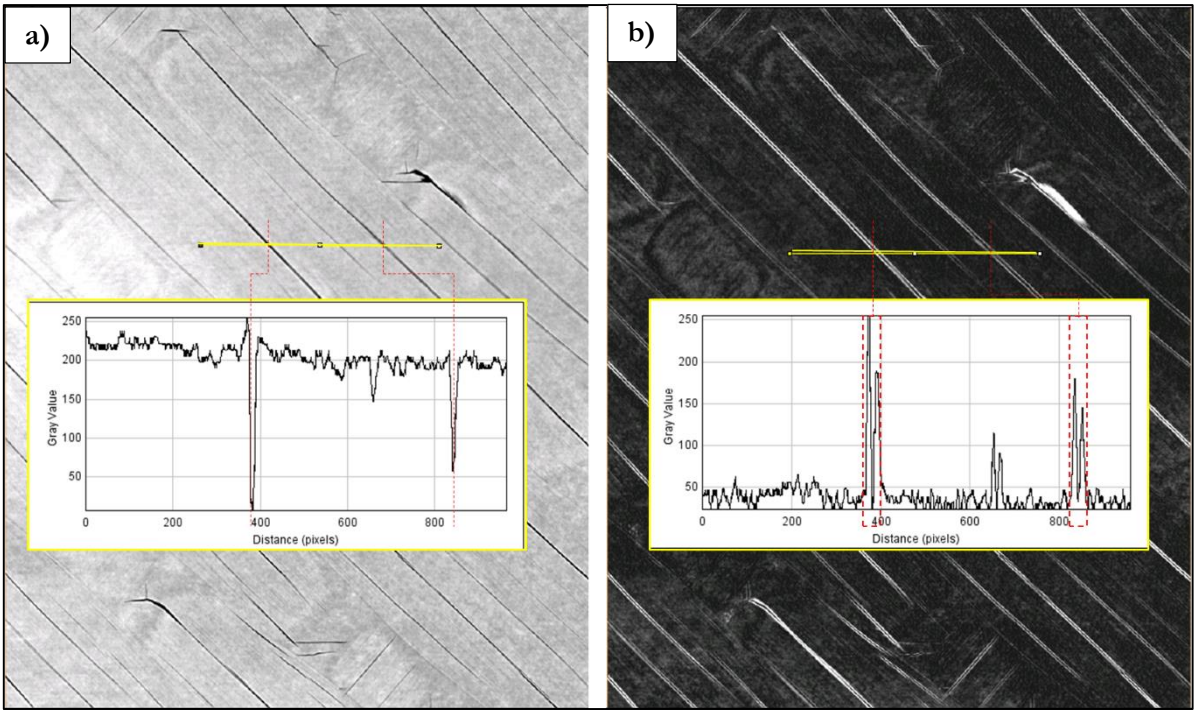

Fig.2. 48 : Pixels values for original (**a)**) and gradient (**b)**) image of an external ply - -45° cracks.

For example *Fig.2. 48* and *Fig.2. 49* show the values of the grey levels for a slice of an external ply (*Fig.2. 48*) and for a slice of an internal ply (*Fig.2. 49*). For each figure are plotted the grey levels of the pixels along the yellow line. In *Fig.2. 48* ***b)*** and *Fig.2. 49* ***b)*** the gradient of each image is calculated and reported in a plot for the pixels belonging to the same yellow line. On the surface, the cracks are more visible because they are extremely open, and the value of a pixel belonging to a crack is quite near to zero. The pixels surrounding the cracks have higher values and so the gradient of the grey scale in proximity of a crack edges is important.

For the internal ply in *Fig.2. 49* the peaks of the grey values in presence of a crack are not pronounced as the crack related peaks of *Fig.2. 48*. This is shown in *Fig.2. 49* ***b)***, where the gradient intensity in proximity of a cracks has a peak magnitude lower than the gradient intensity peaks in *Fig.2. 48* ***b)***. Resin rich regions in *Fig.2. 49* have grey levels close to the grey levels of cracks and in terms of gradient, a resin rich region shows two peaks as for the cracks and the magnitude of these peaks is in

the same range of the peaks correlated to a crack, also if the distance between the two peaks enclosing the resin region is more spaced than two peaks related to the crack edges.

Due to the differences between internal and external plies, for the segmentation a separation of the more external regions from the internal regions is necessary. In order to avoid artificial modifications of the real damage scenario, the simplest choice is a division in plies of the whole specimen image.

Scrolling the slice oriented parallel to the external surface, the transition between the plies is identified and a splitting of the volume in six sub-volumes, each one associated to a ply, is made. For each specimen, the thickness of the ply does not change from one scan to another.

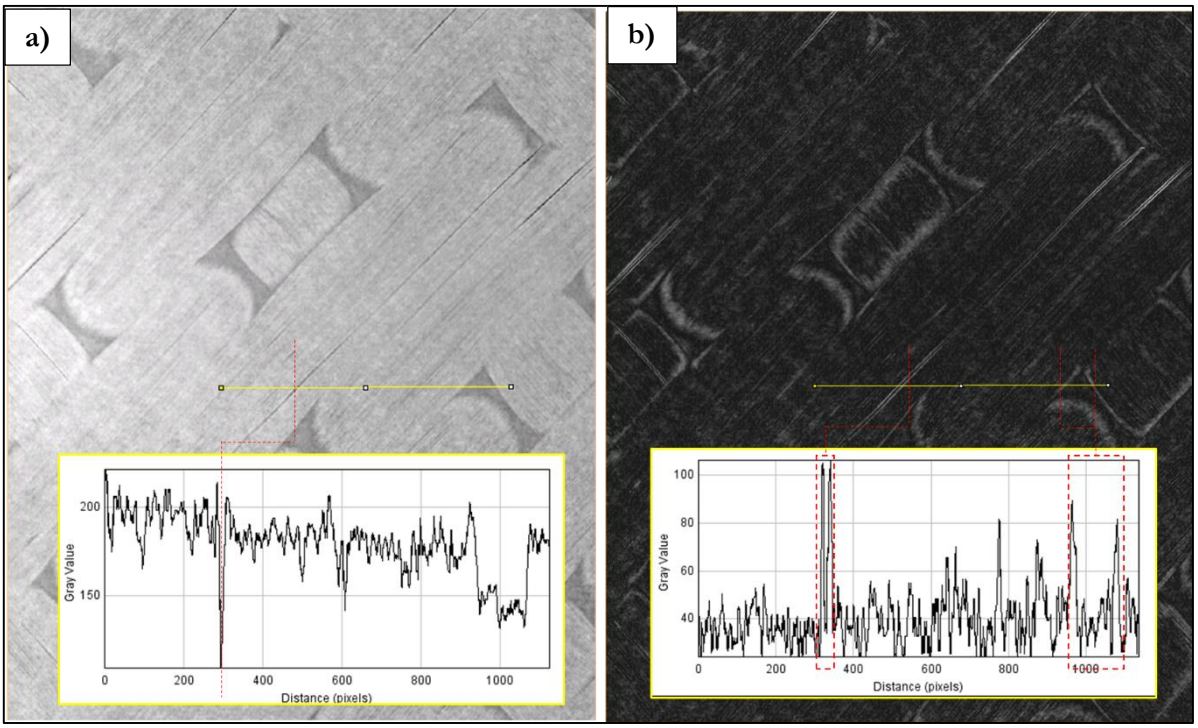

Fig.2. 49 : pixels values for original (**a)**) and gradient (**b)**) image of an internal ply - 45° cracks.

The separation of the plies is manual. Scrolling the slice along the vertical direction, the principal orientation of the tow appears clearly (*see Fig.2. 50*). Each ply is characterised by two subsequent and opposite tow orientations (orange and blue in *Fig.2. 50*) followed by a transition zone (green in *Fig.2. 50*). After this transition zone, another ply begins, and another couple of tow orientations is found (only the first orientation is shown in pink in *Fig.2. 50*).

To prevent the segmentation of undesired elements, as the resin rich regions of *Fig.2. 49*, the original images are filtered. From *Fig.2. 46* - *Fig.2. 50* it could be remarked that the preferential orientation of the cracks is the same of the tow they belong. This characteristic suggests the employment of some *directional/morphological* filters. For a generic ply, the cracks are oriented along the tow directions, so the

segmentation procedure have been applied two times for each ply (one for each tow/crack orientation).

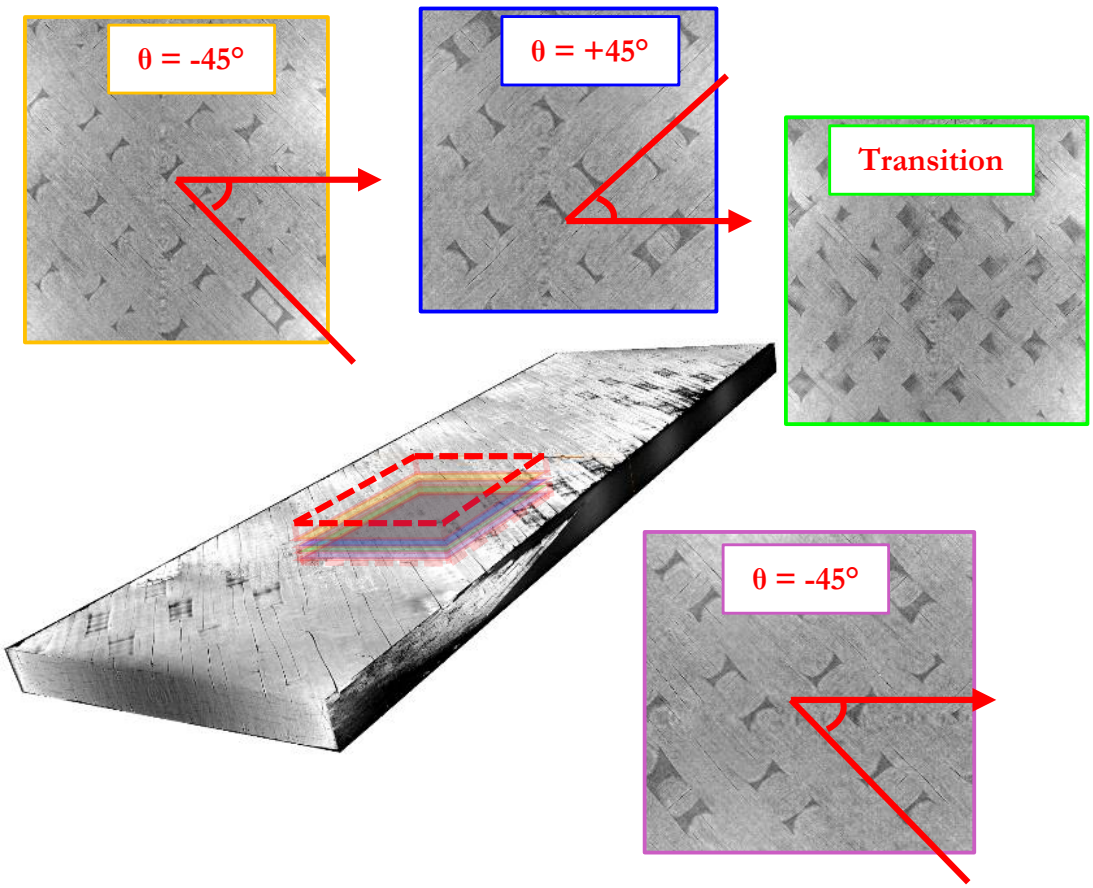

Fig.2. 50 : Plies separation. In the coloured windows, the fibre direction changing along the thickness direction.

For each direction a closing filter using a linear structuring element, oriented along one of the two tow directions is applied. After that, the obtained image is subtracted from the initial image (third step in *Fig.2. 51*).

At this step the cracks are more visible, but some dark pixels could add a noise to the results. Instead of using a simple threshold on the last image in *Fig.2. 51*, a *watershed filter* is applied, in order to avoid, or at least, to reduce the selection of undesired pixels. For this filter, as explained in (Haris et al., 1998), a gradient level and a threshold value for the grey scale must to be fixed. The final results is strongly influenced by the choice of these two parameters. How these two parameters have been chosen is explained in *Fig.2. 52*. In *Fig.2. 52* ***a)*** the grey levels of the filtered image are shown, while in *Fig.2. 52* ***b)*** the gradient intensity is reported. In proximity of a crack both the grey level and the gradient intensity of the filtered image show a peak. A gap separates the mean value of the histograms and the threshold values (in terms of grey scale and gradient intensity) that are used for the watershed filter.

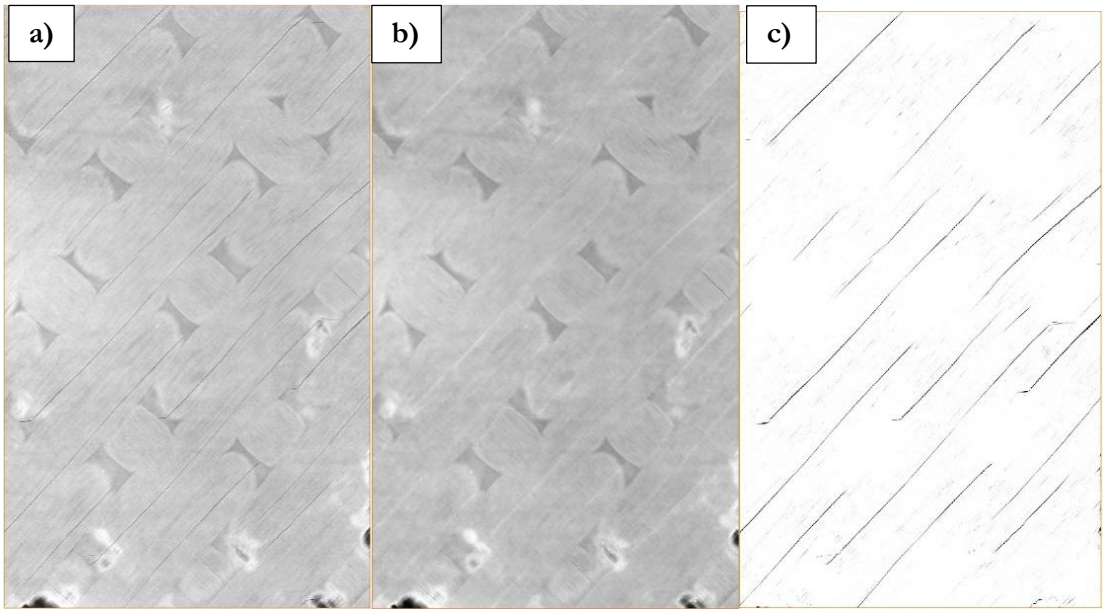

Fig.2. 51 : - 45° cracks crack segmentation. **a)** Initial image **b)** Closing result and **c)** Subtraction result between the images in **a)** and **b)**.

A similar strategy is employed in (Yu et al., 2016), where the grey level of each scan are normalized with a reference scan and the values of the watershed filter are ever the same for all the images. It could be seen that in *Fig.2. 52* all the three cracks crossed by the yellow line will be segmented.

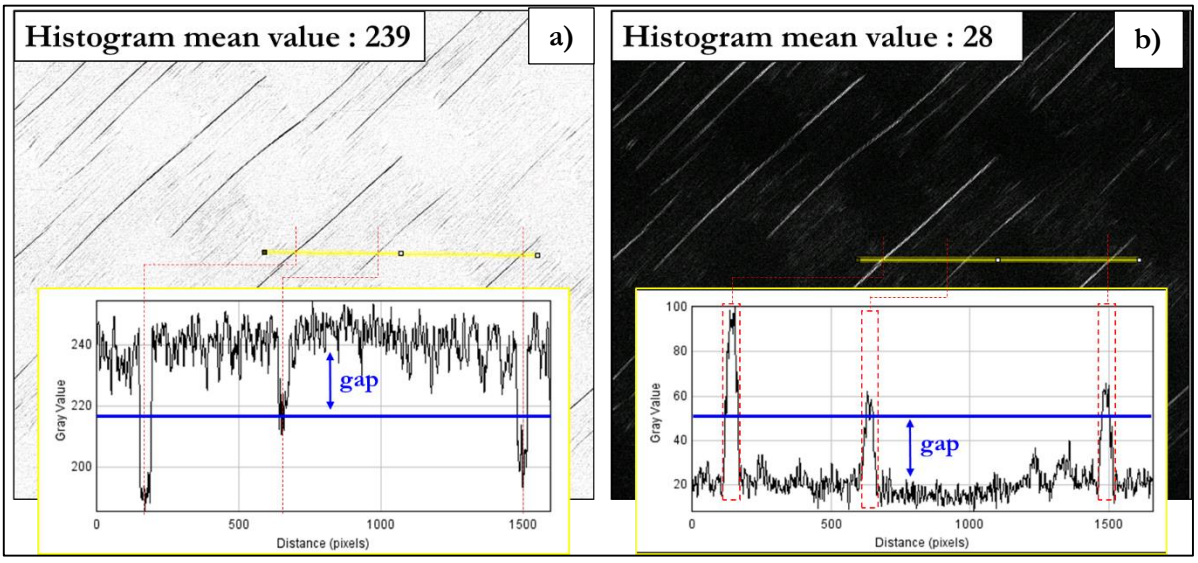

Fig.2. 52 : Grey levels of the image (**a)**) and its gradient (**b)**) – external ply - 45° cracks.

For an internal ply the procedure is the same. The differences highlighted above between an external and an internal ply, affect the choice of the gap values. The choice of the gaps for an internal ply is shown in *Fig.2. 53*. In this case the cracks are not so evident both in terms of grey level and gradient. Resin regions and artefacts especially may be behind these large fluctuations of the grey levels. For this reason, for the internal plies, a couple of gaps different from which of the external plies is taken.

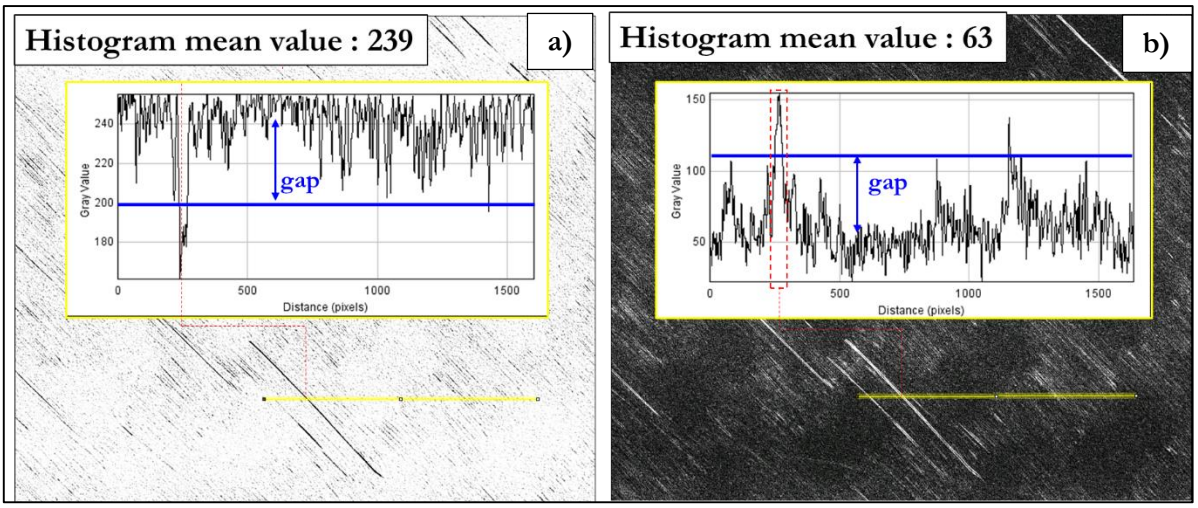

Fig.2. 53 : grey levels of the image (**a)**) and its gradient (**b)**) – internal ply - -45° cracks.

Finally, for a single scan, two combinations of parameters (one for the internal plies and another one for the external plies) allows performing a correct evaluation of the specimen detectable damage.

On the grey levels of the initial images act a large number of factors directly linked to the μCT scan, impossible to take into account (distance specimen-X-ray source, temperature, *etc.*..). Generally, the mean values of the histograms of different images are not the same; however the difference between the mean values of the grey scale and the pixel values of a crack, are spaced in the same manner, so the chosen gap is the same. In conclusion, for two subsequent scans of a specimen the segmentation could be performed using the same couples of gaps, but different filter parameters. The last segmentation step is the application of a *remove island* that allows removing all the segmented regions having a volume lesser than a prefixed values. In the presented segmentations the regions having a volume lesser than 100 vox^3 have not been considered.

The gap choice is performed on visual considerations and after a sensibility evaluation of the segmented volume regarding small variations of these gaps. An example of sensibility evaluation carried out on an external ply, that is generally, affected by an intensive matrix cracking is reported in *Fig.2. 54*. The segmented volume is calculated in terms of ratio between the segmented and the total volume of the 3D image. On the vertical axis is reported the variation of this ratio from a reference condition represented in the graphs by a red point. In abscissa is expressed the gap value as ratio from the reference condition.

To study the variation of the segmented volume as a function of the gap on the gradient level, the segmentation was carried out using three different values of this gap keeping the gap on the grey level fixed to a reference value. The result, in *Fig.2. 54* ***a)***, is that variation up to 35% of the gap on the gradient values does not give large difference in segmented volume, the points remain close to 1 from

each gap ratio. The variation of the segmented volume as a function of the gap on the grey levels is obtained performing the segmentation using three different values of this gap and keeping the gap on the gradient level fixed to the reference value.

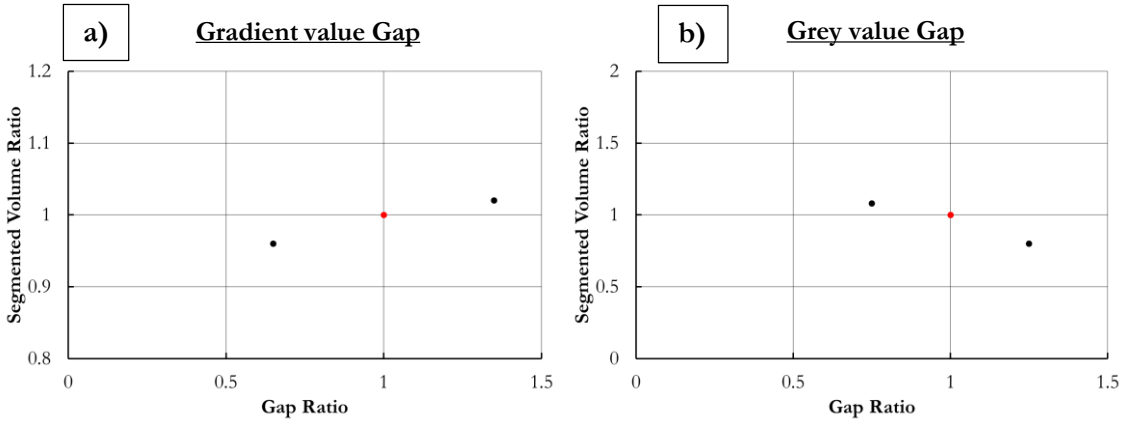

Fig.2. 54 : Sensibility study result of segmented volume regarding a variation on the gap on gradient level and grey level for a watershed segmentation.

The result, in *Fig.2. 54* ***b)*** shows that the choice of the gap for the grey threshold for the watershed segmentation seems to be more critical. Using a gap reduced by 25% from the reference value, the segmented volume is bigger than 10% of the reference value. Going in the opposite direction, increasing of 25% the gap, the segmented volume decreases of about 20%. For the choice of the more suitable gap value, a study on the threshold values on the analysed images is shown in *Fig.2. 55*.

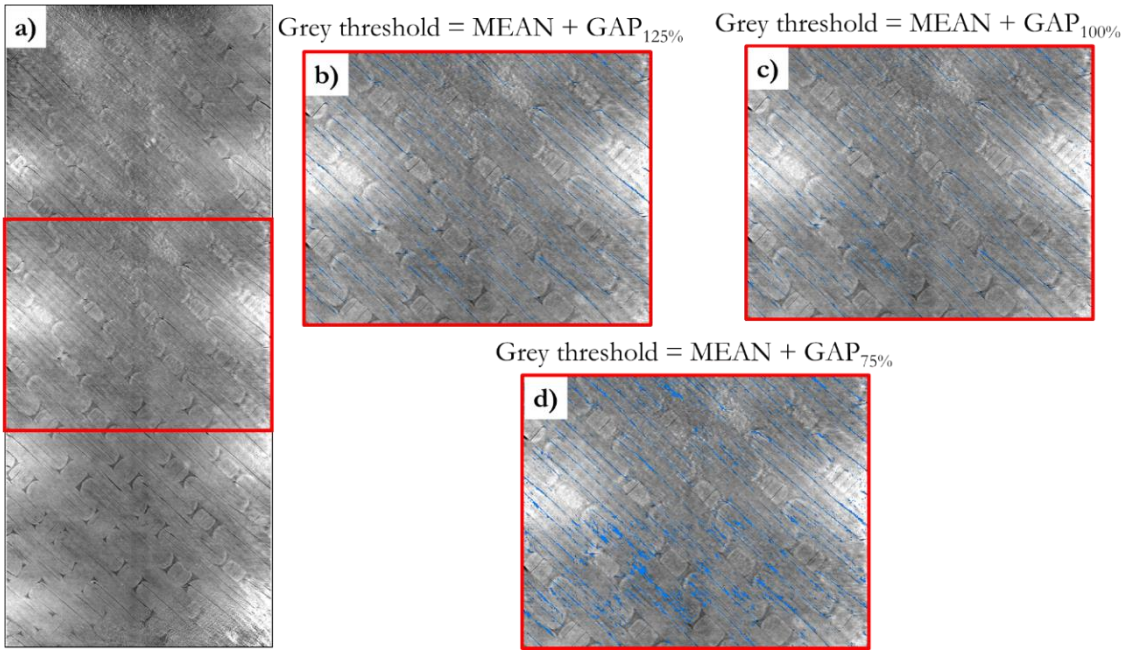

Fig.2. 55 : Choice of grey levels gap. **a)** Initial image **b)** Segmentation using $GAP_{125\%}$ **c)** Segmentation using $GAP_{100\%}$ **d)** Segmentation using $GAP_{75\%}$.

The initial image is segmented using the procedure argued in this paragraph and the three threshold values on the grey levels associated to the three points of the graphs in *Fig.2. 54* ***b)*** are compared. In the segmentation related to the gap raised of 25% ($GAP_{125\%}$) the majority of visible cracks are segmented, but in some regions of long cracks the grey level is lower than for the surrounding pixel (such as bright artifact regions) of the same crack, and are not segmented. For the segmentation related to the gap decreased of 25% ($GAP_{75\%}$) all the cracks are well segmented, but the increase in segmented volume is in part due to the segmentation of zones not related to cracks. Generally, the volume of these elements is very small compared to the volume of a crack because these parasite regions are principally extended on the plane but not so thick (1-3 voxels in the third direction) or even little dispersed pixels. These regions are removed by the *island remove*, by this operation some cracks no correctly segmented (as in drop intensity regions) could disappear (this is the case for $GAP_{125\%}$). $GAP_{75\%}$ leads to a more complete crack segmentation, so a *remove island* allows reducing the parasite segmented volumes.

Generally, little adjustments on the GAPs are performed to include or exclude some pixels. These adjustments are subjective of the operator, but the threshold does not change more than 15% respect to the reference values calculated as explained above. Data in *Fig.2. 54* could be used to evaluate the magnitude of the operator intervention in crack volume quantification: using the same procedure for crack segmentation varying only the GAPs to adjust the watershed thresholds, the crack volume does not change more than 10-15%. This value is an evaluation of the reproducibility of the segmentation procedure: considerations on the crack volume evolution differences between two or more specimens should be done bringing in mind this value.

The result of the watershed filter on the closing/subtracted image is reported in *Fig.2. 56*.

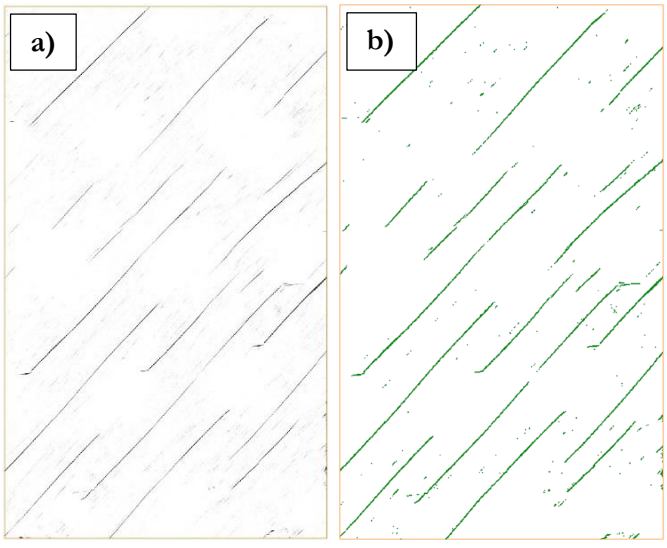

Fig.2. 56 : Crack segmentation. **a)** Closing + subtraction and **b)** Final result - 45° cracks.

The strategy put in use is satisfactory regarding the crack segmentation. Also after the *remove island* some parasite elements not linked to cracks, but rather to artifacts or resin rich regions are visible on the resulting image. However, these elements does not give an important contribution to the total segmented volume.

The described procedure allows segmenting crack oriented along preferential directions known *a priori* that are the tow directions, *i.e.* ±45°. In external regions of the specimens, this procedure has to be adapted to the presence of two more features: speckle pattern and 0° cracks. A detailed description is given in the next paragraph.

External plies segmentation

In the external plies the damage scenario includes little 0° cracks in the resin rich regions (*see Fig.2. 48* for example) not present in the interior plies. The segmentation of those is performed using the same procedure used for +/-45° cracks, but orienting the structural element of the closing filter in the 90° direction.

Another adaptation of the segmentation procedure is required for the ply observed by DIC. The ceramic particles contained in the paint employed for speckle pattern realization are very X-ray absorbent. In the 3D image they appear like white zones, and after the filtering procedure of the images, they become black points having a grey intensity comparable to the grey intensity of the crack pixels. To overcome this problem, before the application of the general procedure for the segmentation, the voxels associated to the speckle pattern are isolated and segmented. At the end of the crack segmentation, from the segmented volume of crack, the speckle pattern volume is subtracted. The speckle dots in the initial image are brighter than all the other elements in the image. The level of grey for those points saturated the pixel value of the rescaled histogram (the grey value in *Fig.2. 57* achieves 255/255), while resin regions, yarn regions and crack are well below this value.

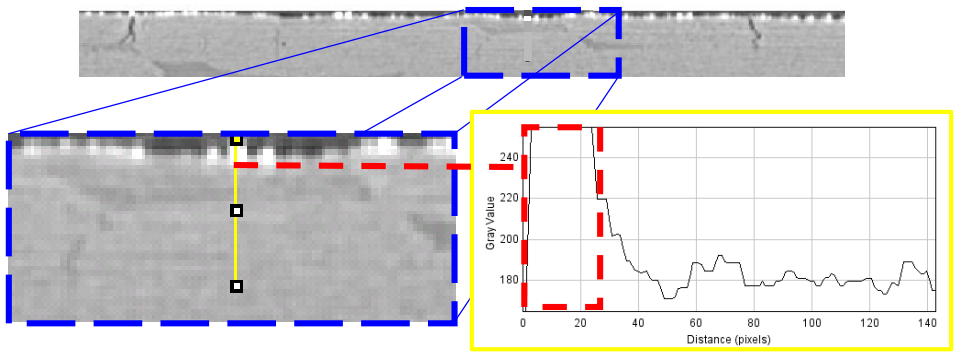

Fig.2. 57 : Speckle pattern grey values.

Summary of crack segmentation

The segmentation procedure detailed in the previous paragraph is summarized in *Fig.2. 58*. The colour of each branch in the block diagram is correlated to the segmented cracks reported on the bottom side of *Fig.2. 58*.

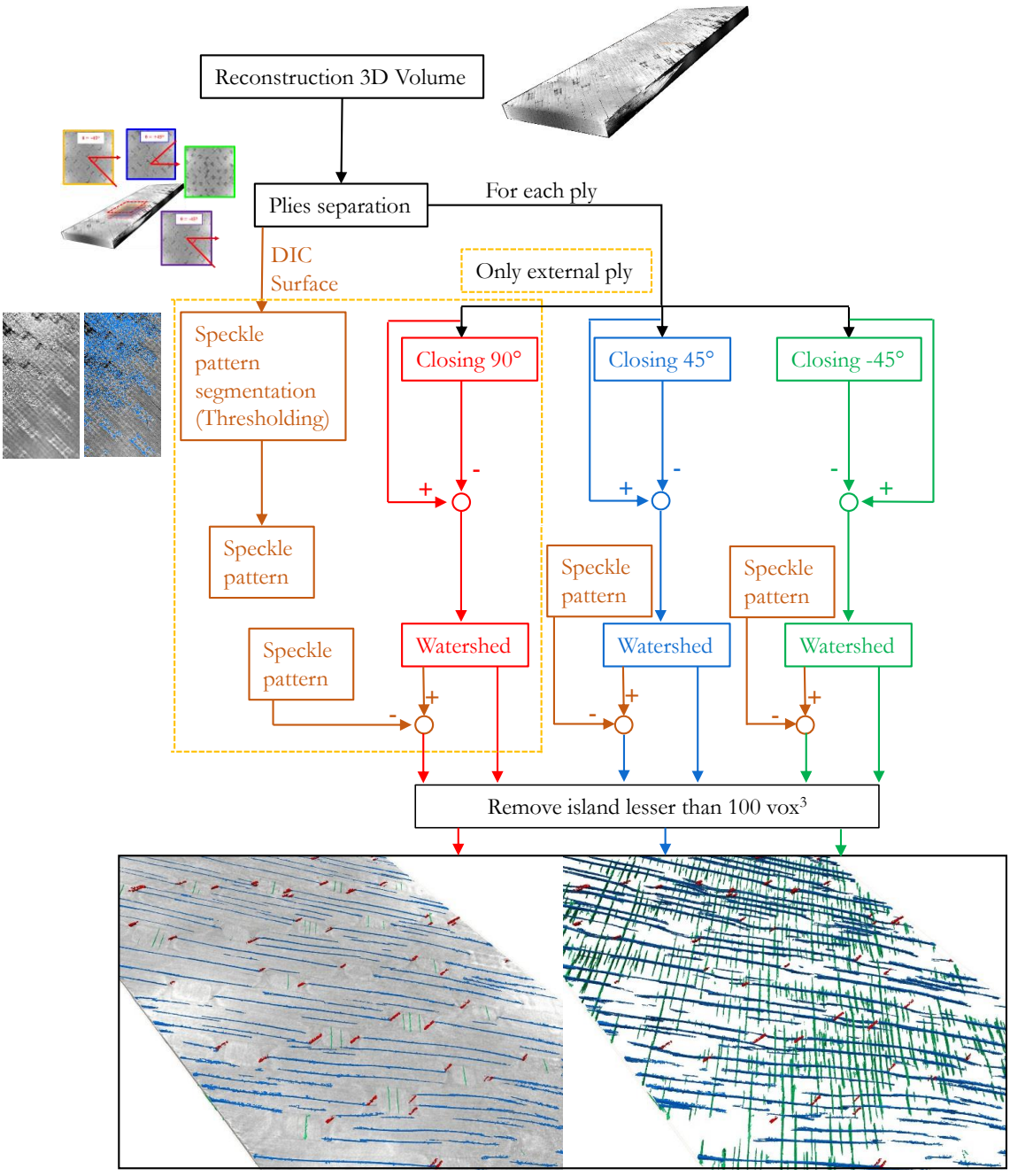

Fig.2. 58 : Summary of segmentation procedure for the woven specimen.

Chapter 3

Environmental effect on fatigue of cross-ply C/epoxy laminated composites

In this chapter the results about the environmental effect on high temperature fatigue for C/epoxy cross-ply UD composites are presented. In early stage of fatigue, these specimens are affected by transverse cracks that onset on the lateral specimens edges. The role of the environment on crack multiplication for these specimens is evaluated and modelled by an existing analytical model. An acceleration of the crack multiplication kinetic is observed during fatigue in severe environmental conditions.

Summary

The aim of this chapter, is the evaluation of the environmental effect during a high temperature fatigue test on a C/epoxy cross-ply laminated composite. During the experimental activity on cross-ply laminated composites, traction tests are carried out in order to choose the test parameters for the fatigue tests. Experimental results are presented in the following paragraphs and an analytical model is introduced to describe the result evolutions and to compare the different tests conditions.

3.1 Cross-ply laminated specimens and test setup

Tested specimens are $[0_2/90_2]_s$ cross-ply carbon/epoxy HTS40/TACTIX742 laminated composites having the dimensions reported in *Fig.3. 1*. The stacking sequence is illustrated ever in *Fig.3. 1*: two 0° layers are located at the external surfaces giving a layer having a thickness of 0.25mm, while four 90° plies, placed at the centre of the specimen thickness, form a layer thick 0.5mm of transversal fibres.

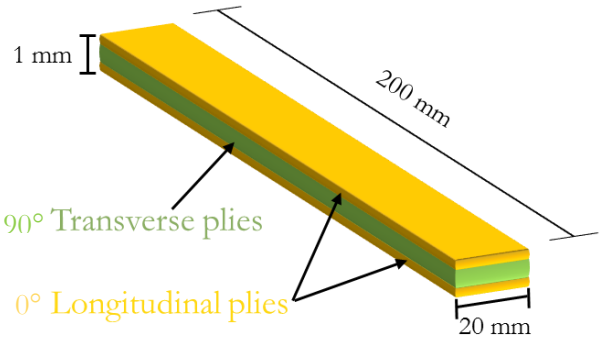

Fig.3. 1 : Specimen dimensions and stacking sequence illustration. Plies in 0° direction, aligned with the load direction, are at the outer faces of the specimen. The 90° plies compose a thick layer at centre of the specimen thickness.

Traction and fatigue tests have been performed using the COMPTINN' multi-physical test machine presented in Chapter 2. During tests, long distance microscope (*cf.* Chapter 2) has been used for damage assessment: the number of transversal cracks on the polished edge was counted in order to study the evolution of the number of cracks as a function of the applied load (for a traction test) or the number of cycles (for a fatigue test).

3.2 Traction test on cross-ply laminated composites

Preliminary traction tests have been performed on two specimens, in order to fix the maximal stress level for fatigue tests. During traction tests, the tensile load gradually increased as the movable head of the testing machine moves. The speed was fixed at 0.5 mm/min and the temperature of the tests

was 150°C, lower than the glass transition temperature (T_G) of the matrix (T_G = 190-250°C). The traction tests were stopped each 0.25mm of head displacement for crack counting. The load levels reported in the graphs are relative to the stress level at instant of the stop. The observed damage scenario has been already described in Chapter 1 (*see* for example in (Siulie Liu and Nairn, 1992; Berthelot et al., 1996; Kashtalyan and Soutis, 2000; Shen et al., 2017). Transverse matrix cracking occurs in the off-axis plies, for example in the 90° plies of a cross-ply laminate, followed by delamination and splitting in the 0° (on-axis direction) plies. In (Lafarie-Frenot and Hénaff-Gardin, 1991) an influence of the 90° layer thickness on transverse crack has been experimentally observed, in detail, for a laminate having a thick 90° layer loaded in fatigue, transverse cracks onset at a lower strain level than a laminate having a thin 90° layer. Moreover, for the former laminate the cracks onset on the specimen edges and rapidly propagate along the specimen width, while this is not the case for the second laminate. Other 90° layer thickness effects are documented for example in (Garrett and Bailey, 1977; A Parvizi and Bailey, 1978) where the authors observe that as the transverse layer thickness increases, the distance between the transverse cracks also increases, and in (A. Parvizi and Bailey, 1978) where the constraint effect on transverse cracking provided by the outer 0° plies is described.

During the traction tests, the number of cracks was counted along the observed region L_0. The crack distribution along the longitudinal direction of the specimen as the tensile load increases is reported in *Fig.3. 2*. Cracks are equally distributed along the longitudinal direction, no particular localization for crack onset has been observed during tensile tests.

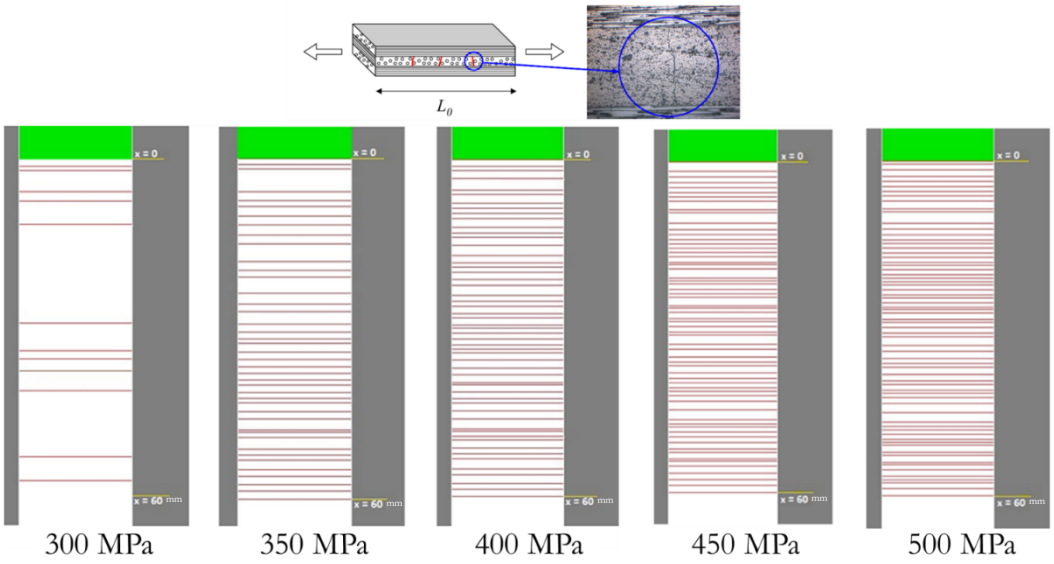

Fig.3. 2 : Representation of the crack distribution on the polished edge of the specimens during a traction test.

A µCT scan performed on a reduced zone of the specimen after the tensile tests confirms that the crack counted on the specimen edge span the whole specimen width. The results, in terms of reconstructed 3D image and volume segmentation, are reported in *Fig.3. 3* (resolution $12^3 \mu m^3$/vox). Cracks in the transversal direction span the whole specimen width and have the same height of the 90° layer. Longitudinal cracks are discontinuous and less numerous than the transversal ones, these cracks have the same height of the 0° layers and onset along the two 0° faces of the specimen.

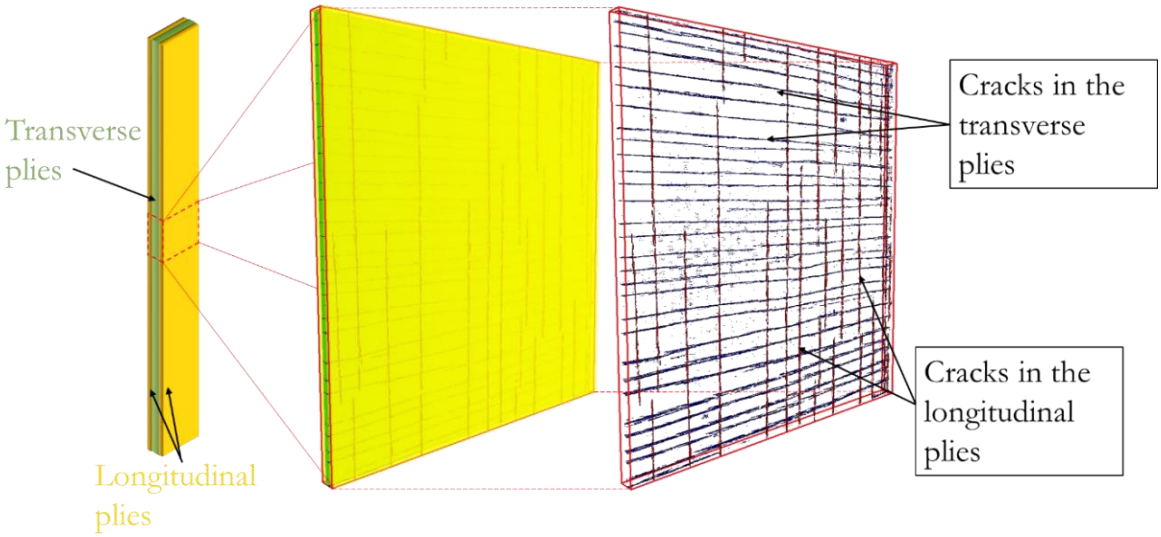

Fig.3. 3 : Segmentation results on a tested specimen after tensile test (studied volume 20x20x1 mm^3). The segmentation shows transverse cracks in the 90° plies spanning over the whole specimen width and longitudinal splitting on the exterior 0° plies.

In order to quantify the damage in the specimen during the tensile tests, from the number of cracks on the polished edge of the specimens N_{cracks}, a crack density D has been defined as:

$$D = \frac{N_{cracks}}{L_0} \qquad \text{Eq.3. 1}$$

where L_0 is the length of the observed region (L_0 = 60mm). The evolution of the crack density as a function of the applied load is shown in *Fig.3. 4*.

The first consideration is on the reproducibility of the traction tests, the cracks density values obtained on the two specimens are quite close for each stress value. A general trend of D can be remarked in *Fig.3. 4* : the initial value of D is null as the load increases until a threshold stress (σ_{TH}) where D starts to grow up.

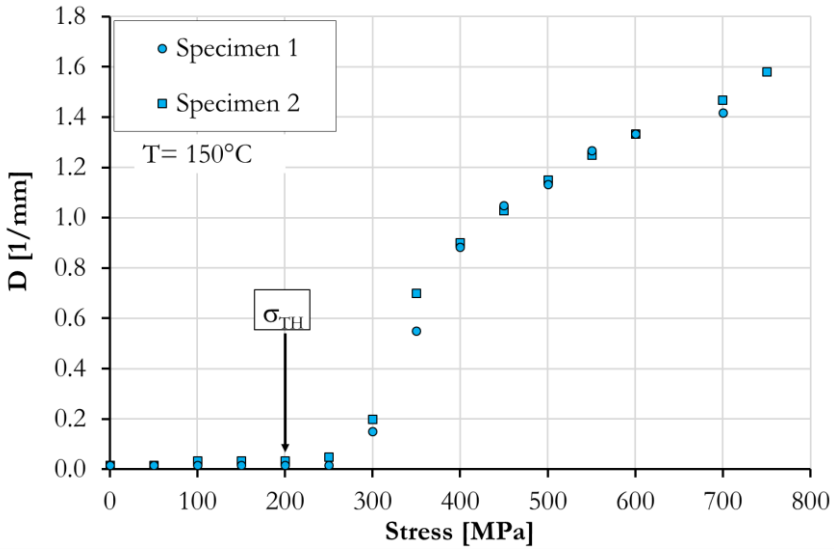

Fig.3. 4 : Evolution of the crack density D as a function of the applied traction load. An increasing of D is recorded only for traction loads higher than a threshold load value σ_{TH} = 200MPa.

The growth ends when a saturation value is achieved for *D*, in this case an increasing in applied load does not give an increase in *D*. This last step is not visible in *Fig.3. 4* because the tests were stopped before the saturation of the crack density. As reported in the graph of *Fig.3. 4* the threshold stress for crack multiplication on the tested specimens is around 200 MPa.

3.3 Fatigue test on cross-ply laminated composites – Environmental effects

Previous paragraph provided several useful elements for the evaluation of the environmental effect on fatigue of cross-ply laminated composites. First of all, the existence of a threshold traction load under which transverse matrix cracks do not multiply. In other words, transverse cracks are detected for traction loads higher than 200 MPa for the tested specimens. The following fatigue tests have been performed using a maximum fatigue load lesser than this threshold value in order to exclude the static load effect on transverse crack multiplication.

A second founding issued from the traction tests is the geometry and the distribution of the transverse cracks along the longitudinal direction. All the transverse cracks span over the whole width of the specimens: this is visually documented by the μCT scan reported in *Fig.3. 3* and from an analytical point of view, by the good agreement between the experimental results and the shear-lag model presented in the paragraph 3.4 and *Fig.3. 11*. Moreover, transverse cracks are not concentrated in a particular location, but are homogeneously distributed along the longitudinal direction.

From these two assumptions, three fatigue tests have been performed under three different environmental conditions. The test temperature was 150°C, representative of the employment temperatures of aeronautical components realized using this kind of material, while the gas in the climatic chamber changes for each specimen to test the effects of a variable oxygen concentration. The gases are: 2 bar Nitrogen, 1 bar air and 2 bar Oxygen. In the first atmosphere the oxygen concentration is null, while in the second one is at 20%; finally in 2 bar of Oxygen the oxygen concentration is 10 times greater than the oxygen concentration in air. Traction-traction fatigue tests (R=0.1) have been carried out using a frequency *f* of 1Hz and a maximum fatigue load (σ^f_{max}) of 190MPa (lesser than the threshold tensile load for crack multiplication) as shown in *Fig.3. 5*.

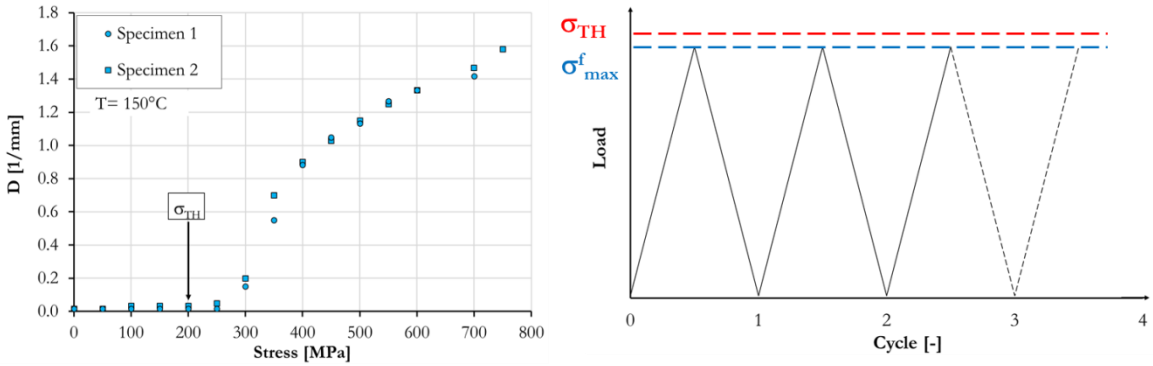

Fig.3. 5 : Fatigue test cycle. Fatigue tests are carried out at R=0.1, *f* = 1Hz and a maximum fatigue load (σ^f_{max}) lesser than the threshold tensile load for crack multiplication (σ^f_{max} = 190MPa).

Periodically the tests were stopped in order to count the cracks on the polished edge using the QUESTAR long-distance microscope. Fatigue tests have been conducted until 1 million of fatigue cycles, this test duration was sufficient to see an environmental effect on crack multiplication kinetic and at the same time, allows obtaining results in a reasonable time lapse.

As for the tensile tests, a µCT scan followed by an image processing (segmentation) performed on fatigued specimens allows characterizing the fatigue damage scenario. The results of image segmentation on the 2 bar O_2 specimen at the end of the fatigue test, are shown in *Fig.3. 6*. As for the traction tests, transverse cracks are located in the transverse layer and cross the entire width of the specimen. Longitudinal cracks in the two on-axis layers are also visible, but less numerous than the transverse ones. Contrarily to the µCT scan performed on the traction specimens, the scanned zone for the fatigue specimens was 60×20×2 mm^3 (resolution $12^3 \mu m^3$/vox) that is the whole region observed for crack density quantification. As clearly shown in *Fig.3. 6*, crack quantification by µCT is strongly conditioned by image resolution. The central-low region of the specimen in *Fig.3. 6* seem not affected by transverse cracks, but the crack observation made using the QUESTAR microscope

(resolution 1.2µm/px, *cf* Chapter 2) confirms the presence of transverse cracks in this region as well as in the upper region of the specimen.

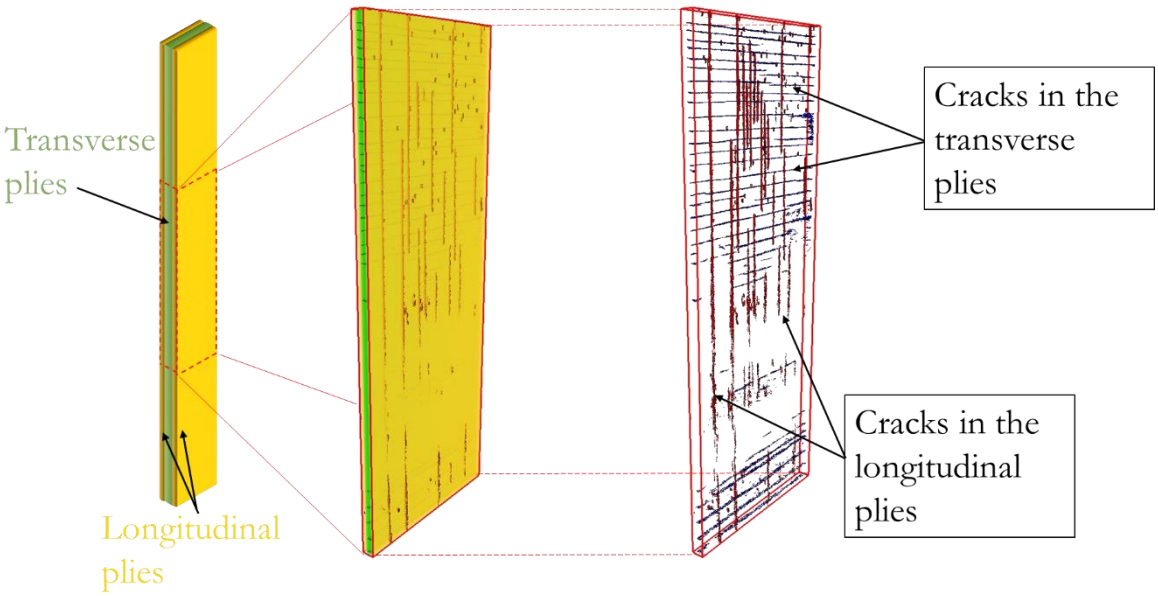

Fig.3. 6 : Segmentation results for the µCT scan performed at the end of fatigue test on 2 bar O_2 specimen. The analysed volume has a length L_0 =60mm, the same length used for crack quantification by QUESTAR Microscope.

Spatial resolution could be the mainly reason but, as explained in (Böhm et al., 2015) also a crack closing effect could result in a gap between *in-situ* (QUESTAR) and *ex-situ* (µCT) evaluations.

The transverse crack density evolution as a function of the number of the cycles is reported in *Fig.3. 7*. A dashed line is drawn on the experimental data reported in *Fig.3. 7* to describe a hypothetical evolution for crack density between subsequent stops. The crack density remains zero for the 2 bar N_2 specimen until 10k cycles; after that a quasi-linear evolution for D is observed until the end of the test. The air specimen shows a similar behaviour until 650k cycles, after that a sudden increase in crack multiplication rate is noticeable. Finally, the crack multiplication kinetic for the 2 bar O_2 specimen is quite different from the two previous specimens. After an initial rapid evolution, a quasi-linear trend from 10k cycles and until the end of the test is observed for D. In the late stages of fatigue the evolution of D for the 2 bar O_2 specimen is not clear, possibly due to crack saturation.

From the graph in *Fig.3. 7* the crack multiplication kinetic results strongly affected by the test environment. The evolution obtained under 2 bar N_2 is related to the fatigue load effect alone. The specimens tested in air shows evidences of environmental damage acceleration only in the late stage of fatigue, where the value of D for air and 2 bar N_2 specimens is quite different.

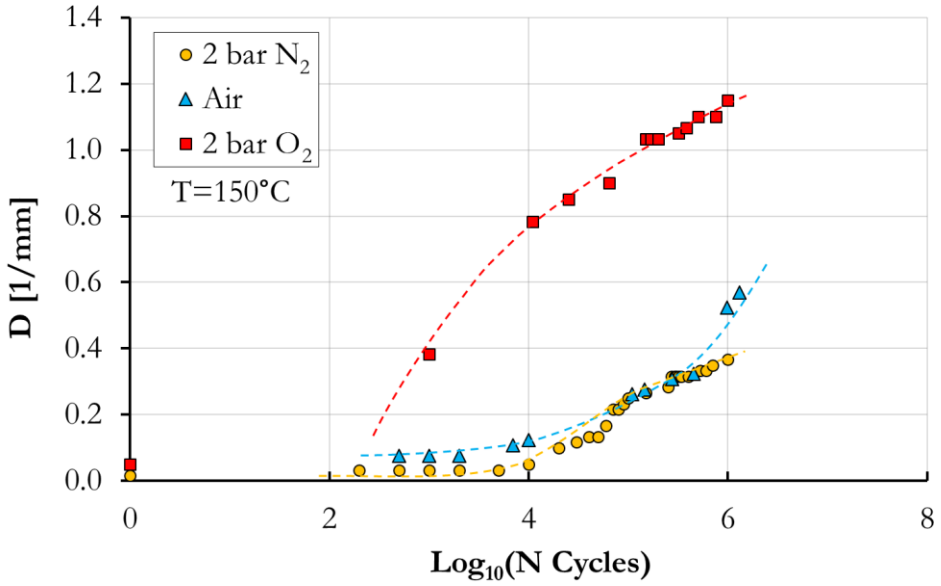

Fig.3. 7 : Crack density D evolution as a function of the number of cycles (semi-logarithmic graph) for fatigue specimens tested in 2 bar N_2, air and 2 bar O_2.

The damage evolution encountered for the 2 bar O_2 specimen proves the high oxygen concentration effect during fatigue, showing an accelerated evolution for crack multiplication from the early fatigue stage.

3.4 Energy release rate based analytical model for transverse cracking

For the tested cross-ply laminated specimens, the longitudinal plies, aligned with the load direction, give a global purely elastic response. The sample response could be modelled neglecting the viscous effects related to the resin and considering only the damage effects. As explained in (Huchette, Lévèque and Carrère, 2005), in a cross-ply laminate the damage kinetics is dependent on the transverse layer thickness: a stress based criterion is forecast to describe damage evolution for thin transverse plies, while for thicker transverse plies an energy based criterion is more appropriate. The analysis of the stress distribution in the laminate after the apparition of the first transverse micro-crack in the off-axis plies is widely studied in the literature. In (Garrett and Bailey, 1977) the authors use a shear-lag modified analysis to describe the stress transfer between longitudinal and off-axis plies. A basic concept of this analytical model is that the maximum stress and hence a preferential site for the onset of a new transverse crack, is a midway between two existing cracks. The shear–lag analysis captured the interest of a large number of researchers. In the following publications some assumptions have been modified as explained in (Laws and Dvorak, 1988) where the authors resume the evolution of the basic shear lag-theory. In the same publication, the authors exploit the concept of *energy release rate* (G) as a parameter governing the onset of a new transverse crack that does not lie

necessarily at the midway of the existing cracks. In (Nairn, 1988) the shear-lag model and the energy release rate are used to describe the evolution of longitudinal and transverse midway cracks, in (Nairn and Wedgewood, 1991) also the fibre bridging is considered and in (Siulie Liu and Nairn, 1992; Nairn, Hu and Bark, 1993) the thermal residual stress are included in the model. Stress distributions description in cracked cross-ply laminated using modified shear-lag models are numerous in the literature (*see for example* (Hahn and Johannesson, 1983; Han, Hahn and Croman, 1988; Lee and Daniel, 1990; John A Nairn, 1997)) and an adaptation for the case of $[0_n/90_m]_s$ laminates is reported in (Nairn and Mendels, 2001) and here briefly invoked.

The stress distribution along the thickness of the laminated is expressed as:

$$\frac{d^2\tau_{xz}^*(x)}{dx^2} - \beta^2\tau_{xz}^*(x) = 0 \qquad \text{Eq.3. 2}$$

where, referring to *Fig.3. 8*, $-L \leq x \geq +L$, τ^*_{xz} is the shear stress at the interfaces between longitudinal and transversal plies and β is the shear-lag parameter, generally calculates by *Eq.3. 3*.

$$\beta^2 = \frac{\frac{1}{E_{22}h_1} + \frac{1}{E_{11}h_2}}{\frac{k_r h_1}{G_{23}} + \frac{k_l h_2}{G_{13}}} \qquad \text{Eq.3. 3}$$

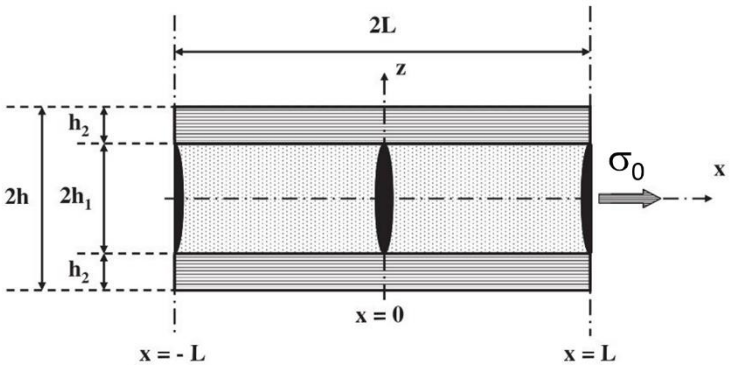

Fig.3. 8 : Notation used for the shear-lag model. The fibres in the exterior and in the interior plies are oriented along the load direction and along the direction perpendicular to the load direction respectively.

In *Eq.3. 3* E_{11}, E_{22}, G_{13} and G_{23} are the ply mechanical properties calculated in Appendix-A, h_1 and h_2 are the thickness of the plies (*see Fig.3. 8*), while k_r and k_l are the parameters of the shape function describing the shear stress variation in all the plies. For a linear variation of the shear stress in the plies, these two parameters have the same value $k_r=k_l=0.33$ (Nairn and Mendels, 2001), but in the same publication is explained as $k_r=0.330$ and $k_l=0.307$ are more appropriate values for a $[0/90_2]_s$ laminated.

The energetic approach is used as failure criterion. As argued in (Vu, Gigliotti and Lafarie-Frenot, 2013), the following analytical formulation is limited to the elastic case. Moreover, it is supposed that new cracks onset at the midway of two existing cracks and instantaneously propagate across the specimen thickness and width. It is implicit that the cracks span over the entire specimen width, hypothesis confirmed by the μCT scan presented in *Fig.3. 3*. The following analysis refers to an elementary cell between two matrix cracks (see *Fig.3. 8*) and on the assumption that a new crack onsets, at the middle of two existing cracks, when a critical value for the release energy rate (G_c) is reached.

The formulation of the energy release rate used in (Hashin, 1996; J A Nairn, 1997) is based on concept of discrete fracture mechanics, the energy release rate is calculated as:

$$G = -\frac{\Delta E}{\Delta A} \qquad \text{Eq.3. 4}$$

where E is the total potential energy of the plate taking into account residual thermal stress due to the curing process; ΔA is the discrete variation of damaged area (the area of a new crack) (Vu, Gigliotti and Lafarie-Frenot, 2013). From the solution of the shear-lag differential equation reported in *Eq.3.2*, the expression of G, dependent on the applied stress σ_0 and the crack density D, could be written as (Vu, 2011):

$$G(\sigma_0, d) = G_{max}(\sigma_0) f_d(d) \qquad \text{Eq.3. 5}$$

$$G_{max} = \frac{E_T(1+h_{12})}{\beta E_c E_L}\left[\sigma_0 - \frac{E_L \Delta\alpha_{TL}\Delta T}{1+h_{12}}\right]^2 \qquad \text{Eq.3. 6}$$

$$f_d(d) = 2\tanh\left(\frac{\beta}{4d}\right) - \tanh\left(\frac{\beta}{2d}\right) \qquad \text{Eq.3. 7}$$

$$E_C = \frac{E_L + h_{12}E_T}{1+h_{12}} \qquad \text{Eq.3. 8}$$

$$h_{12} = \frac{2h_1}{2h_2} \qquad \text{Eq.3. 9}$$

$$\Delta\alpha_{TL} = \alpha_T - \alpha_L \qquad \text{Eq.3. 10}$$

$$d = \frac{1}{2D} \qquad \text{Eq.3. 11}$$

where ΔT is the difference between the curing temperature (free stress temperature) and the test temperature, while α_T and α_L are the transverse and the longitudinal thermal expansion coefficients of the off-axis ply respectively. Initially a constant value could be taken for the critical energy release rate G_c such as intrinsic properties of the material, that is not dependent on the accumulation of transverse cracks. This is expressed from a criterion in the form:

$$G(\sigma_0, d) = G_c \qquad \text{Eq.3. 12}$$

The results obtained by this formulation are not in good agreement with the experimental data for low values of D (Vu, Gigliotti and Lafarie-Frenot, 2013). As experimentally remarked in (Hahn and Johannesson, 1983; Han, Hahn and Croman, 1988) the G_c of a cracked material is generally higher than the G_c of the virgin material. A possible explanation of this phenomena is in (Nairn, 2000; Thang, 2009): several fabrication defects are situated on the edge of the plies, and the G_c has different values locally, an average of these values could be taken as G_c for the whole specimen. The firsts cracks will onset close the bigger defects, where locally a G_c lower than the average value of the specimen is sufficient for crack initiation. Next cracks will onset where the defect size is minor than the first ones, hence the average value of G_c for the specimen grows up during matrix cracking. This is noticeable also looking the experimental results obtained on the two tested specimens. The values of G_c calculated using the experimental measures on D and using *Eq.3. 4*-*Eq.3. 10* and the parameters in *Table 3. 1* are reported in *Fig.3. 9*.

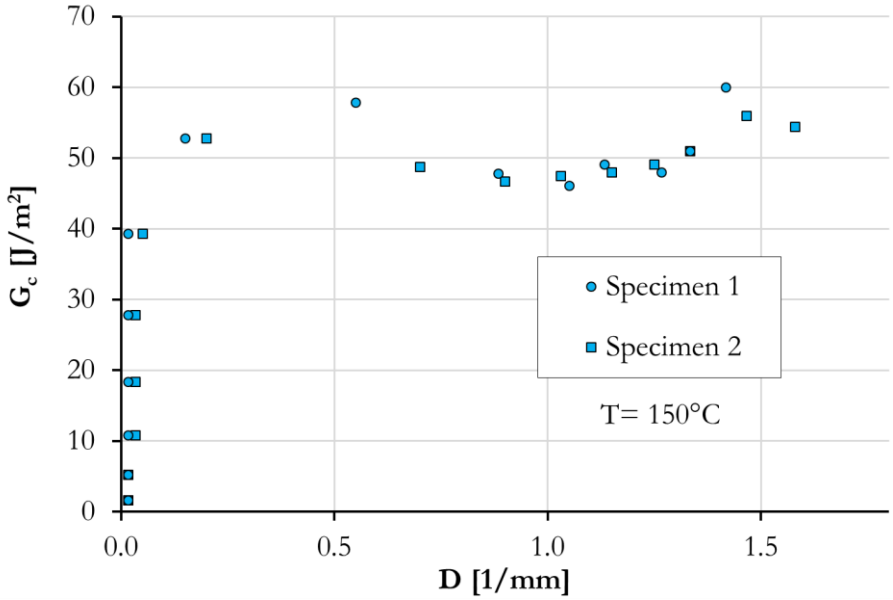

Fig.3. 9 : Evolution of the critical energy release rate G_c as a function of the crack density during fatigue.

Variable	Value
Transverse Young's modulus $E_T = E_{22}$	13.8 GPa
Longitudinal Young's modulus $E_L = E_{11}$	159 GPa
Thickness of transverse plies h_2	0.25 mm
Thickness of longitudinal plies h_1	0.25 mm
Transverse shear modulus $G_{TT} = G_{23}$	5.85 GPa
Longitudinal shear modulus $G_{LT} = G_{13}$	7.6 GPa

Table 3. 1 : Mechanical ply properties for the HTS40/Tactix $[0_2/90_2]_s$ laminated at **150°C**.

For the lowest values of D, an increasing of G_c is observed. When D assumes values higher than 0.5 G_c has a quasi-constant value kept until the end of the tests. Also in *Fig.3. 9* the reproducibility of the tests can be remarked.

The random nature of defect sizes and defect locations, has brought some authors to use probabilistic (Ogi and Takao, 2001; Vinogradov and Hashin, 2004) or empirical (Han, Hahn and Croman, 1988; Vu, 2010; Vu, Gigliotti and Lafarie-Frenot, 2013) approaches to describe the evolution of G_c as a function of the crack density.

The empirical formulation reported in (Vu, 2010) is used in this work. This formulation describes an initial evolution of the G_c followed by a constant value, that theoretically should be equivalent to the G_c of the material without defects. Other damage forms (*e.g.* delamination) taking place after the crack saturation are not taken into account. The apparition of other damage forms represents a limit in the utilization of the presented model. The proposed formulation for G_c is (Vu, 2010):

$$G_c = G_{c0}\,\frac{\exp\left(\frac{d^k}{C^k}\right)}{B - \exp\left(\frac{d^k}{C^k}\right)} \qquad \text{Eq.3. 13}$$

In this description, the evolution of G_c is defined by the 4 parameters C, k, B and G_{c0} representing the G_c of the material without defects, while *d* is defined in *Eq.3. 11*. The failure criterion become hence:

$$G(\sigma_0, d) = G_c(d) \qquad \text{Eq.3. 14}$$

where the terms on the right side is calculated by *Eq.3. 13*. The same graphs of *Fig.3. 4* and *Fig.3. 9* with the superposition of the evolution of G_c as a function of D and the evolution of D as a function

of the applied stress calculated using *Eq.3. 5* - *Eq.3. 11* and the parameters listed in *Table 3. 2* are shown in *Fig.3. 10* and *Fig.3. 11*. The approximation of G_c evolution illustrated in *Fig.3. 10* is in good agreement with the experimental data: the parametric curve describes the initial increase of G_c until the asymptotic value is reached. The values issued from the parametric interpolation are used for the failure energetic criterion and the results of this analytical model are shown in *Fig.3. 11*.

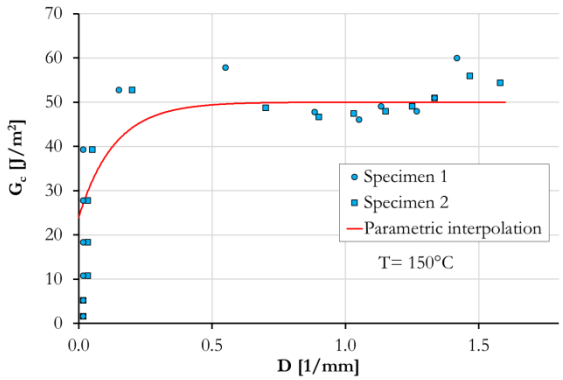

Fig.3. 10 : Evolution of G_c as a function of D obtained using the parametric interpolation for G_c.

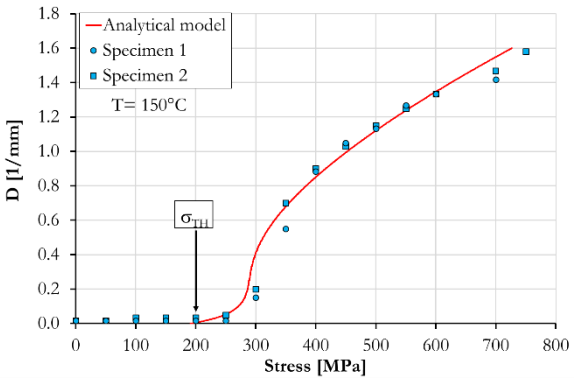

Fig.3. 11 : Evolution of D as a function of the tensile load obtained using the shear-lag model and the energetic failure criterion.

Variable	Value
Shape parameters k_l, k_r	0.33,0.33
ΔT	-60 °C
$\Delta\alpha_{TL}$	1.4 10^{-5} K^{-1}
C	0.01
k	1
B	1
G_{c0}	50 J/m²

Table 3. 2 : Parameters for the application of the energetic failure criterion using the shear - lag model for stress distribution description inside a $[0_n/90_m]_s$ laminated.

All the assumptions made for the stress analysis are validated by the good agreement between the analytical model results and the experimental data on crack multiplication. The tensile tests have been interrupted before the physical separation of the specimen ends, however the saturation level for D has been achieved. This is noticeable in *Fig.3. 11* where the increasing rate for D slightly changes after 600MPa. Other forms of damage taking place at this load level are not considered in the used model. For these reasons experimental data and model predictions are not perfectly superposed after 600 MPa.

The energetic criterion based on the energy release rate could be applied also for the description of the fatigue test results. The stress distribution does not change because the applied load has ever the same direction. The equations *Eq.3. 5* - *Eq.3. 11* could be applied for the quantification of G_c during fatigue. The results obtained from the experimental data on D and substituting the maximal fatigue load σ^f_{max} to σ_0, are reported in *Fig.3. 12*.

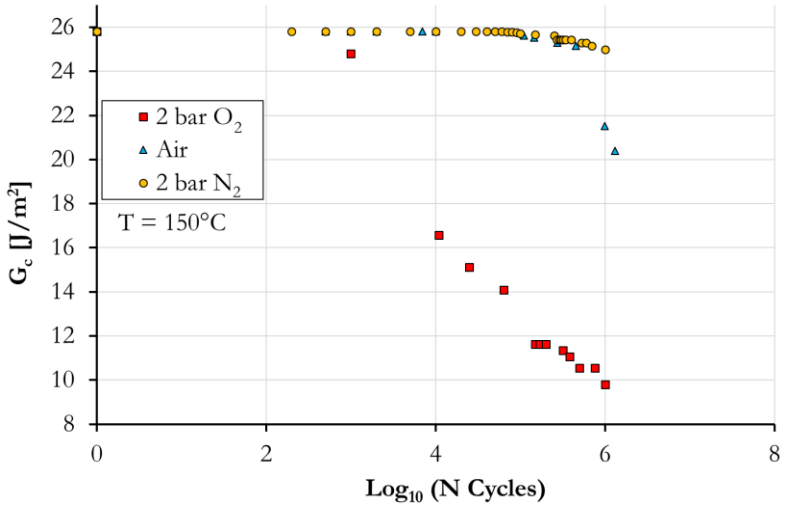

Fig.3. 12 : Critical energy release rate calculated using the shear lag equations for the laminate fatigue specimens tested in 2 bar N_2, air and 2 bar O_2.

As one can see, the initial value of G_c is the same for all the specimens and it is the same initial value of the interpolation model of *Fig.3. 10*. The most relevant difference between the evolution of G_c during tensile test and fatigue test is that in the former case, an increase until a stationary value is observed as the applied load increases; in the case of fatigue test the G_c decreases as the number of cycles increases. This effect is not so visible for the 2 bar N_2 specimen, but quite pronounced for 2 bar O_2 specimen. The air specimen has an intermediate behaviour: except for the last two points, the G_c evolution is the same of the 2 bar N_2 specimen.

The interpolation of the G_c values (as made for the traction test in *Fig.3. 10*) allows describing the crack evolutions as a function of the number of the cycles. The existing model for the description of the G_c evolution during a fatigue tests, are not numerous. One of these models is described in (Vinogradov, 2002) and successfully used in (Thang, 2009). The model developed by Vinogradov is interesting also because gives an explanation for the decreasing of G_c as the number of cycles increases. A schematic evolution of G_c during a fatigue test issued from (Thang, 2009) is reported in *Fig.3. 13*. During fatigue, little defects become larger or in terms of energy release rate, the energy asked for crack onset decreases. When a transverse crack onsets and propagates instantaneously, the bigger defects no longer exists, hence a brutal rise of G_c is observed, followed by a gradual decreasing

until the next crack onset. The G_c decrease during fatigue has been observed also in (Lafarie-Frenot and Hénaff-Gardin, 1991) during a fatigue test campaign on $[0_n/90_m]_s$ laminated.

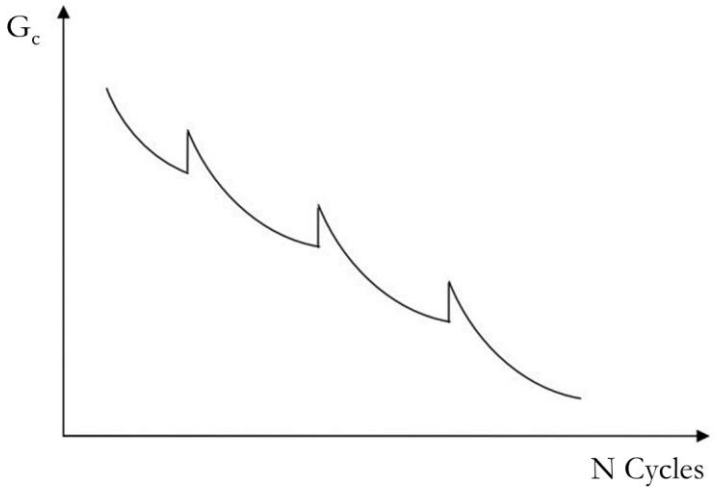

Fig.3. 13 : Schematic evolution of the critical energy release rate (G_c) during fatigue of cross-ply laminate specimens. The value of G_c decreases gradually. (Vinogradov, 2002)

For the test campaign presented in this chapter a bilinear analytical model is used for G_c evolution description and for crack density calculation. The cited bilinear interpolation for G_c describes the variation of G_c with a constant value (G_c^{init}) until a number of cycle at which the G_c decreasing becomes important (N_{TH}).

$$G_c = \begin{cases} G_c^{init} & \text{for } N \leq N_{TH} \\ G_c^{init} + \varphi \, \mathrm{Log}_{10}(N - N_{TH}) & \text{for } N > N_{TH} \end{cases} \qquad \text{Eq.3. 15}$$

The interpolation on G_c performed using *Eq.3. 15* by substituting the parameters in *Table 3. 3* and the results in terms of crack density evolution as a function of the number of cycles are reported in *Fig.3.14* and *Fig.3. 15* respectively. In *Fig.3. 14* the approximation of G_c using the bilinear model gives a good fitting for the description of the G_c evolution for the specimens tested under 2 bar N_2 and 2 bar O_2. The last two points relative to the air specimen are not well described. This imperfect description of G_c for the air specimen has an implication in *Fig.3. 15* for the prediction of D evolution during fatigue. For the specimens tested in 2 bar O_2 and 2 bar N_2 indeed, the model prediction satisfactorily fits the experimental data.

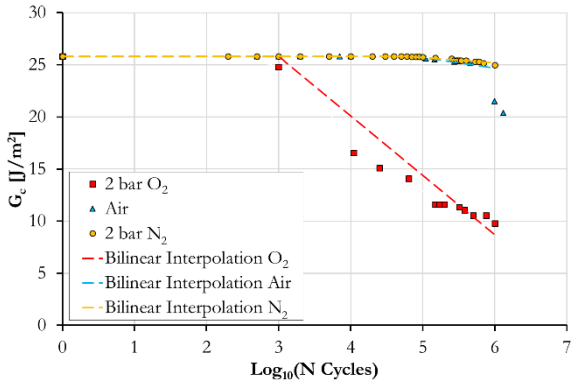

Fig.3. 14 : Evolution of G_c as a function of fatigue cycles. Superposition of G_c values obtained by experimental data and shear-lag equations and bilinear interpolation.

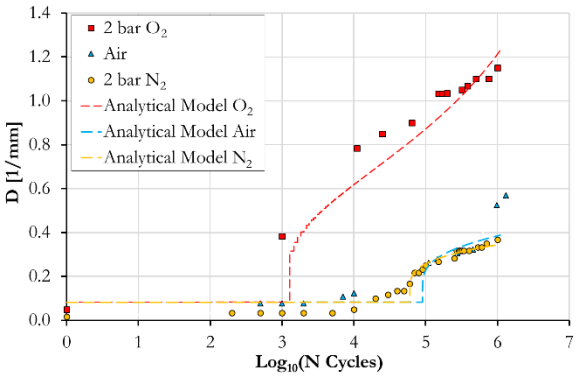

Fig.3. 15 : Evolution of D as a function of the fatigue cycle obtained using the shear-lag model and the energetic failure criterion issued by bilinear interpolation.

	G_c^{init}[J/m²]	N_{TH} [cycle]	φ [J/(m²*Log_{10}N)]
2 bar N_2	25.8	60000	-0.5
Air	25.8	90000	-1
2 bar O_2	25.8	1000	-5.7

Table 3. 3 : Parameters for bilinear interpolation on G_c for the three tested specimens.

The values reported in *Table 3. 3* give the weight of the environmental effect on crack multiplication rate evolution. At the beginning of the tests, the value for G_c is the same for the three specimens, after that a degradation for G_c is observed from N_{TH}. The N_{TH} values, which could be considered as an index of the beginning of oxidation effects, are quite different for the three specimens: the order of magnitude for N_{TH} of the 2 bar O_2 specimen is quite little if compared to N_{TH} of the air and the 2 bar N_2 specimens that have similar values. The severity of the environmental effect is quantified by the slope of the linear part of the model (φ). For the 2 bar O_2 the slope is six times greater than the air specimen, despite this the two last points of the air specimen seem to be better described by a linear model having a slope similar to that of the 2 bar O_2 specimen.

The observed environmental dependent phenomenological behaviour has its origin at the microscopic scale. As noted in Chapter 1, thermo-oxidation phenomena lead to the development of mechanical property changes, matrix shrinkage and embrittlement in the polymer matrix of the composite starting from the surfaces directly exposed to the environment and along a thin thermo-oxidized layer: this may in turn promote localized damage/debonding at fibre/matrix interfaces (*Fig.3. 16*) and facilitate the fatigue induced onset and instantaneous propagation of transverse cracks

in the 90° off-axis layers of the [0/90] samples, with a direct impact on the critical energy release rate for matrix micro cracking (*Fig.3. 16*).

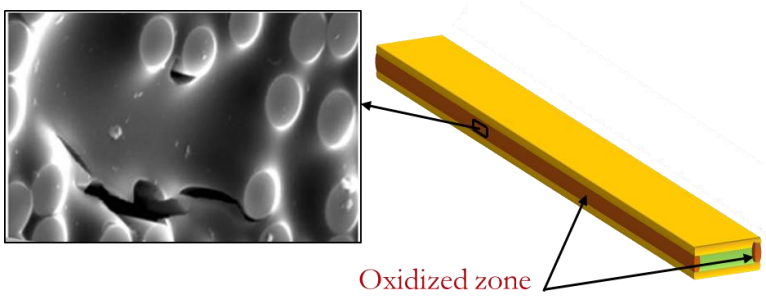

Fig.3. 16 : Oxidized regions of the cross-ply laminate specimens during fatigue and micro scale damage due to environmental ageing.

As put in evidence in (Gigliotti et al., 2016), a good indicator of the environmental degradation of the external surface of a thermo-oxidized composite material is represented by the local measure of the elastic indentation modulus (EIT_{MAX} or its equivalent adimensional value γ_{MAX}), since this value correlates well with matrix shrinkage and fibre/matrix debonding onset phenomena taking place at the same surface. The hypothesis can be formulated is that the environmental degradation of the surface directly exposed to the environment is the main factors affecting the observed environmentally-assisted fatigue behaviour.

To corroborate this hypothesis the idea is thus to correlate the measured environmentally-assisted fatigue damage phenomena (D, G_c …) with the thermo-oxidation tracer γ_{MAX}. This will be the object of the next section.

3.5 Ageing behaviour for the TACTIX 942 matrix

The results presented in this Section concerning the thermo-oxidation behaviour of the TACTIX 942 resin are issued from the PhD thesis (Minervino, 2013) and reported also in (Gigliotti et al., 2016).

Fig.3. 17 presents the profile of the ageing parameter γ, as defined by *Eq.3. 16*, along the thermo-oxidized layer, starting from the external surface directly exposed to the environment.

$$\gamma = \frac{EIT(t)}{EIT_0} - 1 \qquad \text{Eq.3. 16}$$

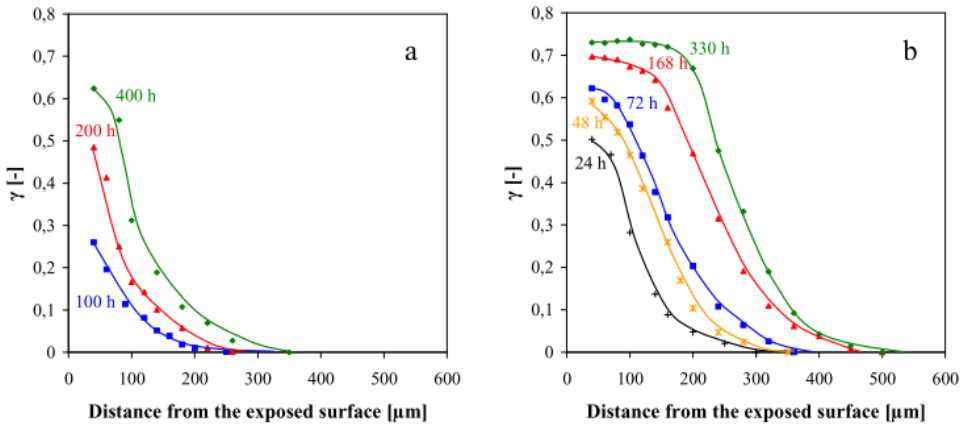

Fig.3. 17 : Evolution of the ageing parameter (γ) as a function of the distance from the exposed surfaces for the specimens aged in air (**a)**) and in 2 bar O_2 (**b)**) at 250°C.

where *t* is the ageing time and EIT_0 is the indentation module of the virgin resin. The evolution of γ_{MAX} as a function of the ageing time for the specimens aged in air and in 2 bar O_2 is reported in *Fig.3. 18*. The interpolation function shown in *Fig.3. 18* is the same for the two ageing conditions:

$$\gamma_{MAX}(150°C, p, t) = 0.75 - 0.6\exp\left(-\frac{t}{\tau_1(p)}\right) - 0.15\exp\left(-\frac{t}{\tau_2(p)}\right) \qquad \text{Eq.3. 17}$$

where τ_1 and τ_2 are characteristic times linked to the oxygen partial pressure *p*, reported in *Table 3. 4*.

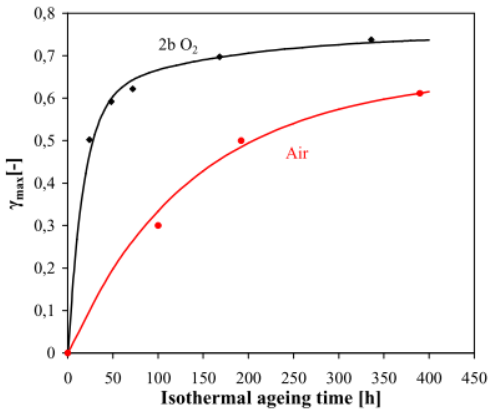

Fig.3. 18 : Evolution of the ageing parameter measured at 40µm from the exposed surface (γ_{max}) as a function of the ageing time in 2 bar O_2 and air at 150°C.

	Air	**2 bar O_2**	**Air/2 bar O_2**
τ_1	130 h	17.5 h	7.33
τ_2	1200 h	164 h	7.32

Table 3. 4 : Characteristic times for γ_{max} description at T=150°C.

As discussed in (Tsotsis et al., 1999) the oxidizing process of a polymer could be accelerated using a moderate oxygen pressure (2 bars), without the generation of parasite *phenomena*. An acceleration of the ageing process for the tested specimen at 150°C of a factor λ=7.3 clearly appears by the observation of the characteristics times reported in *Table 3. 4*. This suggests the use of a reduced time (t^*) to describe the γ_{MAX} evolution as a function of the ageing time as proposed in *Eq.3. 18* and *Eq.3.19*.

$$t^* = t \cdot \lambda(p) \qquad \text{Eq.3. 18}$$

$$\gamma_{MAX}(150°C, p, t) = 0{,}75 - 0{,}6 \exp\left(-\frac{t^*}{130}\right) - 0{,}15 \exp\left(-\frac{t^*}{1200}\right) \qquad \text{Eq.3. 19}$$

The results issued from *Eq.3. 18* and *Eq.3. 19* are illustrated in *Fig.3. 19*. The master curve traced using in abscissa the reduced time t^* describes the γ_{MAX} evolution for both air and 2 bar O_2 specimens. By this parameter, the oxidation effects in a bulk matrix coupon could be quantified for each ageing condition eliminating the time scale.

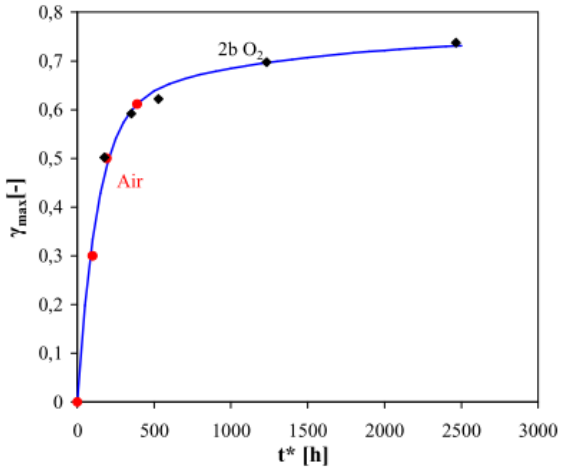

Fig.3. 19 : Master curve for the evolution of γ_{max} as a function of the ageing time at 1 bar and 150°C in air.

The values of γ_{MAX} issued from the graph of *Fig.3. 19* are used in abscissa in *Fig.3. 20* to plot the evolution of the G_c for the fatigue specimens tested under the same environmental conditions used to characterize the matrix ageing behaviour (air and 2 bar O_2 at 150°C). The data points relative to the two specimens belong to a master curve. For low values of γ_{MAX} the critical energy release rate does not change, and the initial value is kept. Starting from values of γ_{MAX} between 0.3-0.4, G_c decreases until the end of the test. The transition value for γ_{MAX} is reached after 800k cycles for the air specimen and after 1000 cycles for the 2 bar O_2 specimen. This value represents the frontier between

two distinct kinds of behaviour: the first one follows the crack multiplication kinetic observed also in 2 bar N_2 specimen and mainly related to pure fatigue phenomena; the second one is specific to air and 2 bar O_2 samples, and testifying the synergy between the environment and the fatigue behaviour.

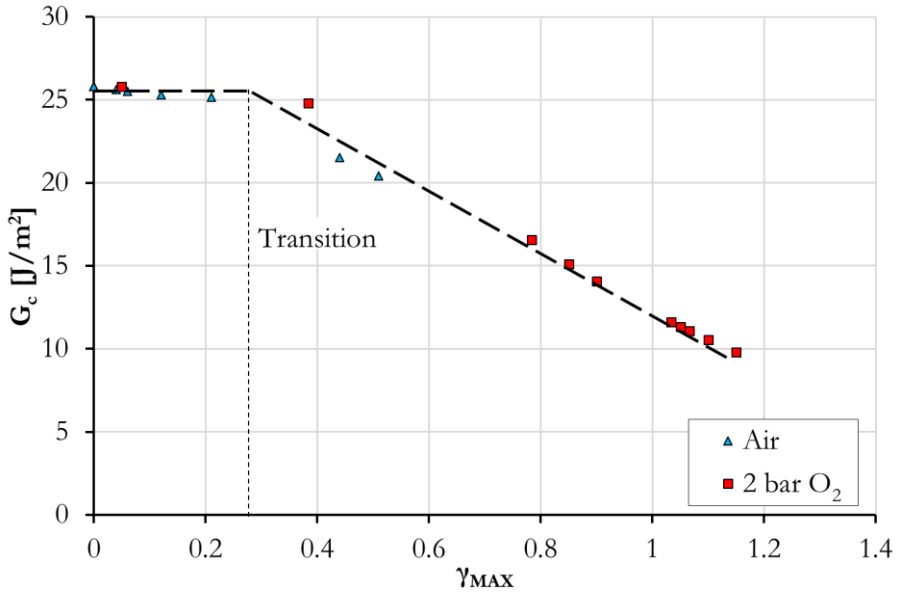

Fig.3. 20 : Evolution of the critic energy release rate as a function of the aging parameter γ_{MAX} for air and 2 bar O_2 specimen. A master curve is plotted as black dotted line.

Fig.3. 21 shows the evolution of D as a function of γ_{MAX}. In this graph the change in crack multiplication rate before and after the transition value of γ_{MAX} is clearly shown. Again, the evolution follows two distinct regimes, one related to pure fatigue, the other showing the synergy between fatigue behaviour and the environmental effect.

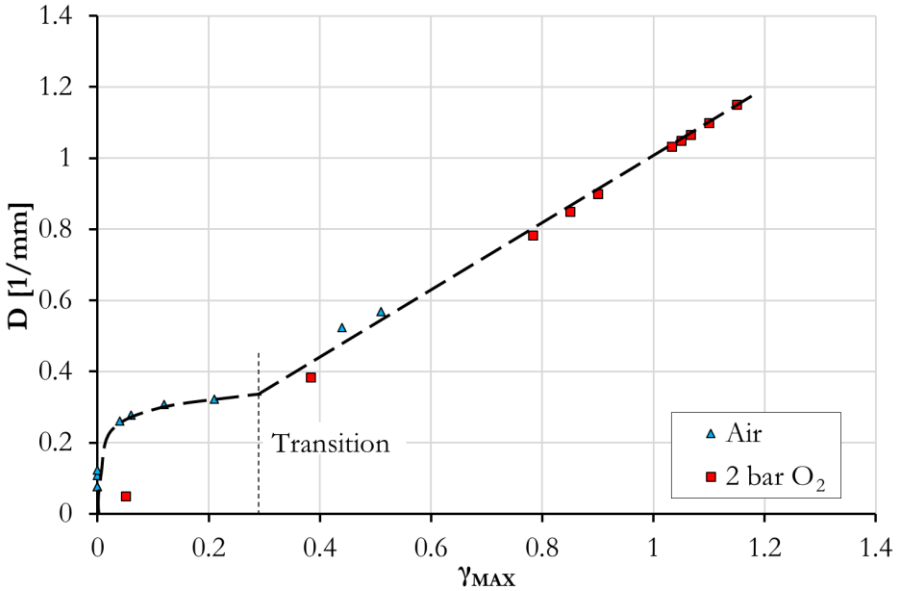

Fig.3. 21 : Crack density D evolution as a function of the aging parameter γ_{MAX} for air and 2 bar O_2 specimen. A master curve is plotted as black dotted line.

By the good correlation observed in *Fig.3. 20* and *Fig.3. 21*, the aging parameter γ_{MAX} proves to be a suitable parameter to link the ageing conditions to the mechanical properties and to the damage evolution for the fatigue tested specimens.

In this particular case, the use of a high partial oxygen pressure leads to an acceleration of a factor 7 compared to ordinary fatigue tests (air specimen) that is the same acceleration factor obtained from the ageing tests on pure resins samples.

Based on this result, a test protocol for accelerated environmentally-assisted fatigue can be proposed. The protocol consists of two phases, namely:

- identification of the ageing parameter evolution (γ_{MAX}) from UMI tests on the surface of pure resin samples under different environmental conditions: a reference condition, under air at atmospheric pressure, and an accelerated condition, under a certain pressure of pure oxygen. This tests allow identifying the scale factor between the reference and the accelerated environmental condition;
- realization of environmentally-assisted fatigue tests under the same accelerated environmental conditions. This allows obtaining the same results as those obtained under reference environmental conditions, in less experimental time.

Moreover, fatigue data can be employed to develop a damage tolerant approach in part design as detailed in Appendix-B.

3.7 Conclusion

The environmental effects on the degradation of a $[0_2/90_2]_s$ laminate have been analysed in this chapter. It has been observed that in the tested model specimens, the main damage forms are transversal cracks. During a tensile test, no crack onset under a threshold stress, this stress value has been chosen as maximum fatigue load for fatigue tests.

High temperature fatigue tests under different environmental conditions reveal that the presence of oxygen in the testing environment strongly affects the transversal crack multiplication kinetic. By using an existing analytical model describing the specimen degradation in terms of transversal crack multiplication, it has been shown that an oxidizing environment leads to a decrease of the critical energy release rate G_c for the onset of transversal cracks on the exposed lateral specimen edges,

consequently a more rapid crack accumulation has been observed for the specimen tested in 2 bar O_2 if compared to air and 2 bar N_2 specimens. The reduction of the G_c depends on the thermo-oxidation process progression that is defined by the ageing parameter value measured on the exposed surface. In the plot G_c vs. γ_{MAX}, a master curve describing the G_c decrease for the air and 2 bar O_2 specimens, confirms that the acceleration factor measured for the thermo-oxidation of the pure resin (7 between air and 2 bar O_2 at 150°C for this resin) is also an index of the G_c decrease for the transverse crack onset on the composite lateral edges.

For these model specimens, it has been demonstrated that results issued from the thermo-oxidation of the pure resin can be employed to predict the acceleration in crack multiplication (or material degradation) of the composite laminate.

This result has been obtained for a model composite architecture, in the next chapters the same strategy has been adapted to study the thermo-oxidation process of woven laminates.

Chapter 4

Environmental effect high temperature on fatigue of C/polyimide woven composites

Multi-physical fatigue results obtained on woven laminated composites are presented in this chapter. Observation means as Digital Image Correlation and μ-Computed Tomography are employed for damage detection and quantification at the macro and micro-scale respectively. It is shown that the environment affects the damage accumulation rate as well as the global damage scenario. At the end of this chapter, a paragraph is devoted to a deeper investigation about the creep and creep/fatigue interactions during fatigue of the tested woven specimens.

Summary

After the presentation of the specimens and the explanation of the test parameters for the experimental campaign, the results of *multi-physical fatigue* tests are exposed. As in the Chapter 3, in order to understand how the environment affects fatigue test results, woven specimens have been tested under three different environmental test conditions.

4.1 Woven specimens

The plates of 8-harness satin woven carbon fibre/polyimide matrix composite (*see* Chapter 2 for further material details) have been cut to obtain specimens with the fibres in off-axis direction in order to enhance the resin role during fatigue. The dimensions of the specimens and the notation that is used in the following paragraphs are reported in *Fig.4. 1*. Longitudinal and transverse directions are labelled as Y and X respectively, while the direction parallel and the perpendicular to the fibres is labelled as 1 and 2 respectively. The θ angle gives the orientation of the observed ply (-45° in *Fig.4. 1*).

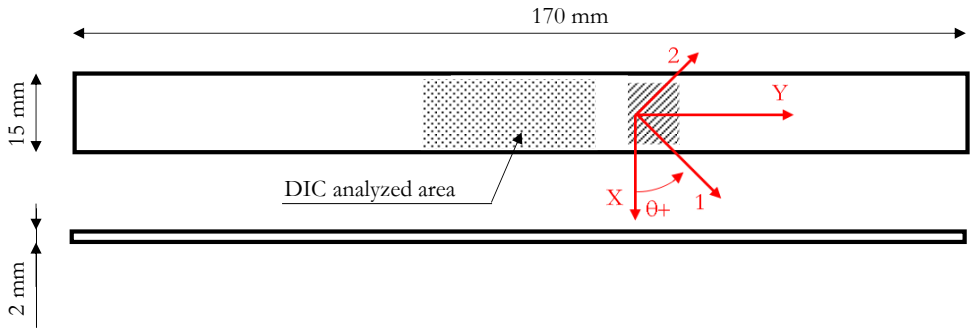

Fig.4. 1 : Specimen dimensions and notation used for the woven composite plies. Longitudinal direction is denoted by Y and the transversal one by X.

Using the angle θ to characterize the fibre direction in the specimens, in a generic woven ply, for an half of the ply thickness, the fibres are oriented mainly along the -45° direction and in the second half thickness along the +45° direction. These specimens are called in the following paragraphs [45_6] specimens without any sign distinction. The DIC speckle pattern location, deposed in order to measure strain fields, is represented in *Fig.4. 1*.

4.2 Identification of the tensile behaviour of non-aged woven specimens

Monotonic traction tests have been performed to characterize the non-aged specimen behaviour at 250°C. During traction tests, DIC has been used to measure surface strain field using the DIC

parameters reported in Chapter 2. The tested specimen dimensions are shown in *Fig.4. 1* and the tensile test results are illustrated in *Fig.4. 2*. The tensile test results, are used in Appendix-C to identify the matrix properties of the tested woven specimen by an FE model.

4.2.1 Tensile test results

Only one of the two tensile test results is reported in *Fig.4. 2* being the results obtained on the second specimen quite similar to the first one. The stress values have been calculated by dividing the applied force by the cross section area of the virgin specimen, while the strain values plotted in the graph are the mean values issued from the DIC strain fields, as explained in Chapter 2.

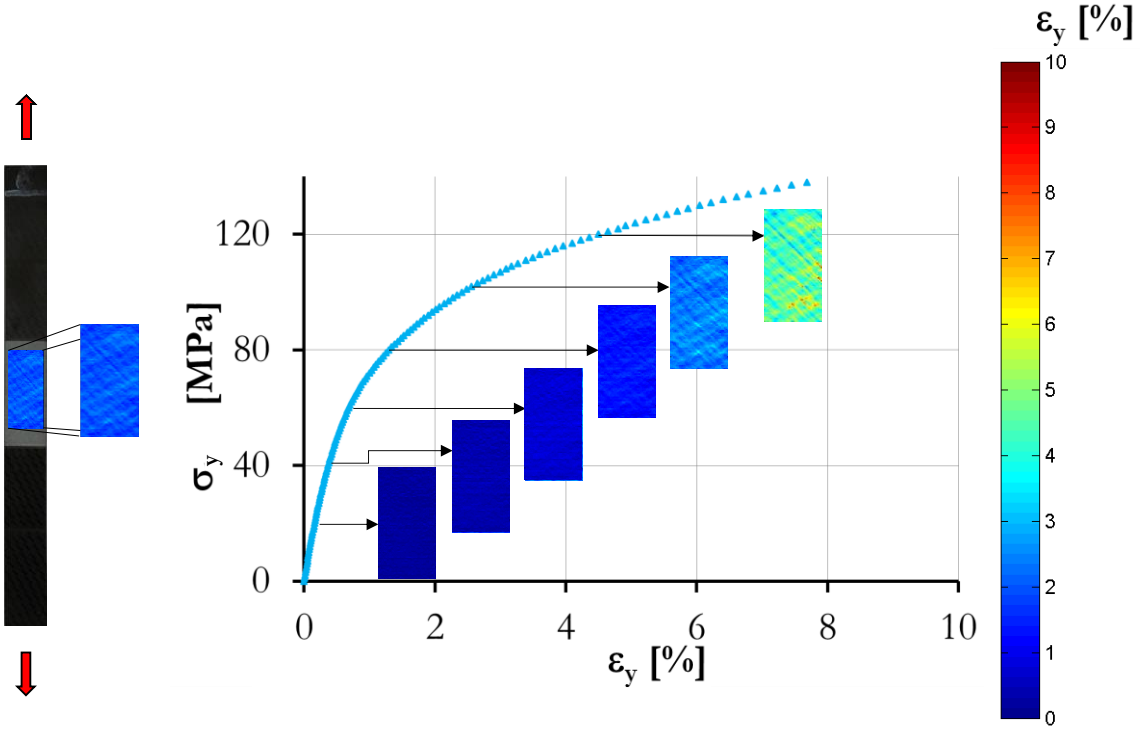

Fig.4. 2 : Traction test results on 8HS carbon fibre/polyimide matrix specimen. Stress-strain curve and DIC strain fields during the test.

The stress/strain curve of *Fig.4. 2* clearly shows that during traction the non-linearity in the material response increases as the applied load increases. At σ_y=130MPa the test has been interrupted because the strain grows up without significant load increasing (not reported in *Fig.4. 2*), this load is used as failure load for the specimens. Some DIC strain fields, calculated during the traction test, are illustrated in *Fig.4. 2* on the traction stress/strain curve. As the load increases, high strain zones appear in the strain field. These regions tend to coalesce forming straight lines oriented in the direction parallel to the -45° tows (or the direction parallel to the axis 2 in *Fig.4. 1*). The high strain values could be correlated, as explained in Chapter 2, to the woven architecture or to cracks, the spatial resolution of the strain field does not allow separating these two features.

The presented tensile test has been used in Appendix-C for matrix properties identification by using an FE model.

4.3 Fatigue tests description

All fatigue tests have been performed using the COMPTINN test machine. As in the tests on the cross-ply laminated composites, this machine allows testing specimens under three environmental conditions: air, 2 bar N_2 and 2 bar O_2. All the tests were load-piloted and the fatigue test cycle is reported in *Fig.4. 3*. Tensile-tensile fatigue tests (R=0.1) have been performed for a predetermined maximum number of cycles. The fatigue test was then interrupted to conduct intermediate quasi-static load/unload cycles as in (Montesano et al., 2012). At the end of the quasi-static load/unload cycle, fatigue was restarted until the next interruption. Two kind of fatigue tests have been performed during the presented experimental campaign:

- *Continuous fatigue test*: during this kind of test the specimens are not removed from the test rig. The tests are periodically stopped just to perform static load/unload cycle.

- *Discontinuous fatigue test*: in order to perform μCT scans, other specimens have been tested using the same test cycle of *Fig.4. 3* but this time the fatigue tests were periodically completely interrupted and the specimen removed from the test rig. After the μCT scan, the specimens were replaced on the test machine and the fatigue test restarted.

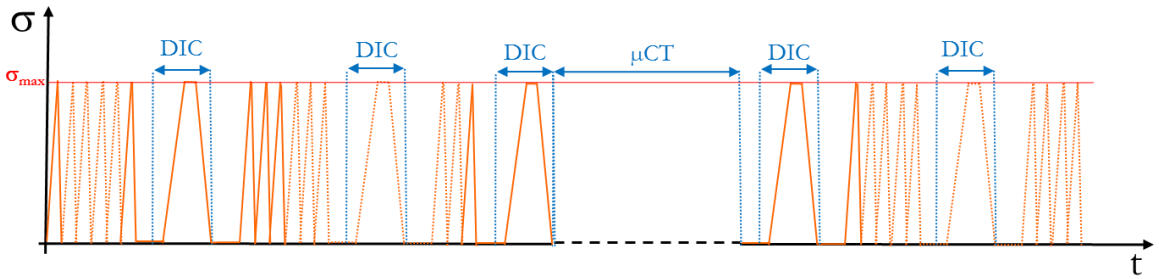

Fig.4. 3 : Schematic test cycle. Continuous fatigue tests are interrupted to perform DIC measures, while for the discontinuous fatigue tests, stops for μCT scans are carried out in addition to DIC stops.

Fatigue test parameters are reported in *Table 4. 1*, as one can see, these are identical to those used for the fatigue tests on UD cross-ply laminated composites except for the temperature and the maximum fatigue stress. The temperature is a function of the resin type, the polyimide matrix of the tested woven specimens can withstand temperatures higher than the epoxy matrix of the cross-ply laminated specimens of the Chapter 3. The maximum stress is chosen to have fatigue damage after a reasonable time-lapse; on the other hand, to avoid failure of the specimen before the apparition of remarkable environmental effects, the maximum fatigue stress level has been taken far from the failure stress value seen during traction tests.

Parameter	Value
Stress Ratio **R**	0.1
Max Stress σ_{max} [MPa]	75 (~55% σ_{fail})
Frequency **f** (Hz)	2
Maximum Cycles to end	10^6
Temperature	250°C

Table 4. 1 : Fatigue test parameters

During the quasi-static load/unload cycles, DIC has been employed to measure the specimen strain field. The stress rate for these tensile tests was chosen weighting the limits on the acquisition system of the camera, the number of data points needed to have an adequate stress/strain graph, and finally, in order to reduce creep effects on measured strains. A mean stress rate about 1.25 MPa/sec has been used both for the load and the unload step. Adopting this stress rate, ten data points for each step have been collected.

Typical longitudinal strain fields observed during load/unload cycles are shown in *Fig.4. 4* and *Fig.4.5*. The strain fields in *Fig.4. 4* are quite different from the *Fig.4. 5* ones. For the same stress levels, the strain fields during the load stage of the quasi-static load/unload cycle are similar between the two figures in terms of mean strain values.

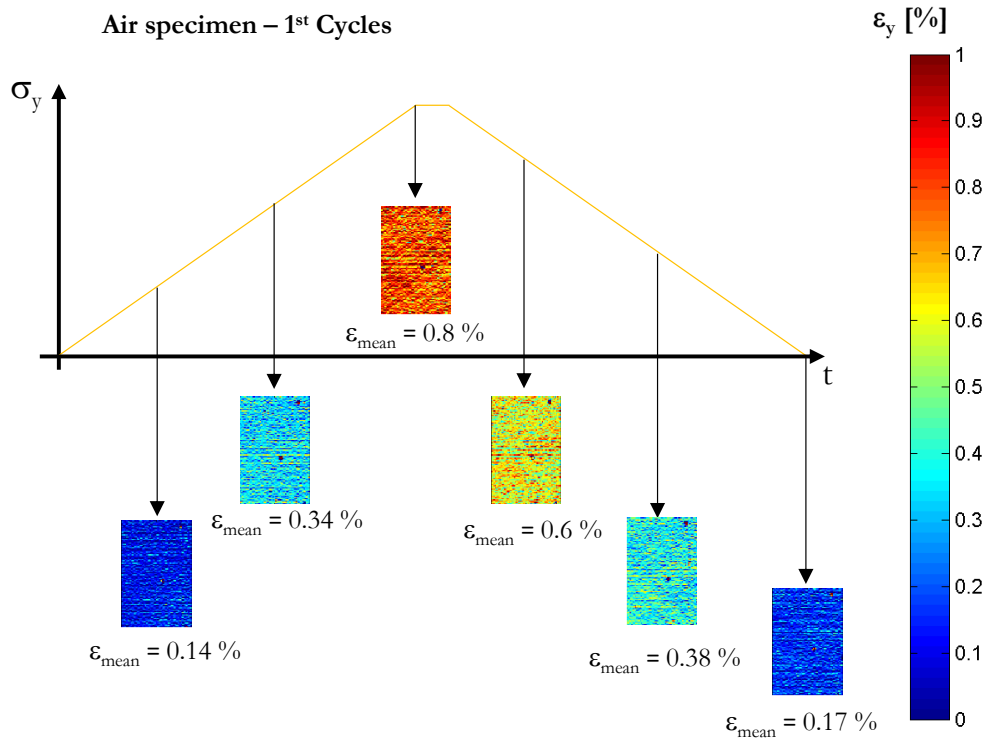

Fig.4. 4 : DIC strain fields during a load/unload cycle for the air specimen before to start fatigue.

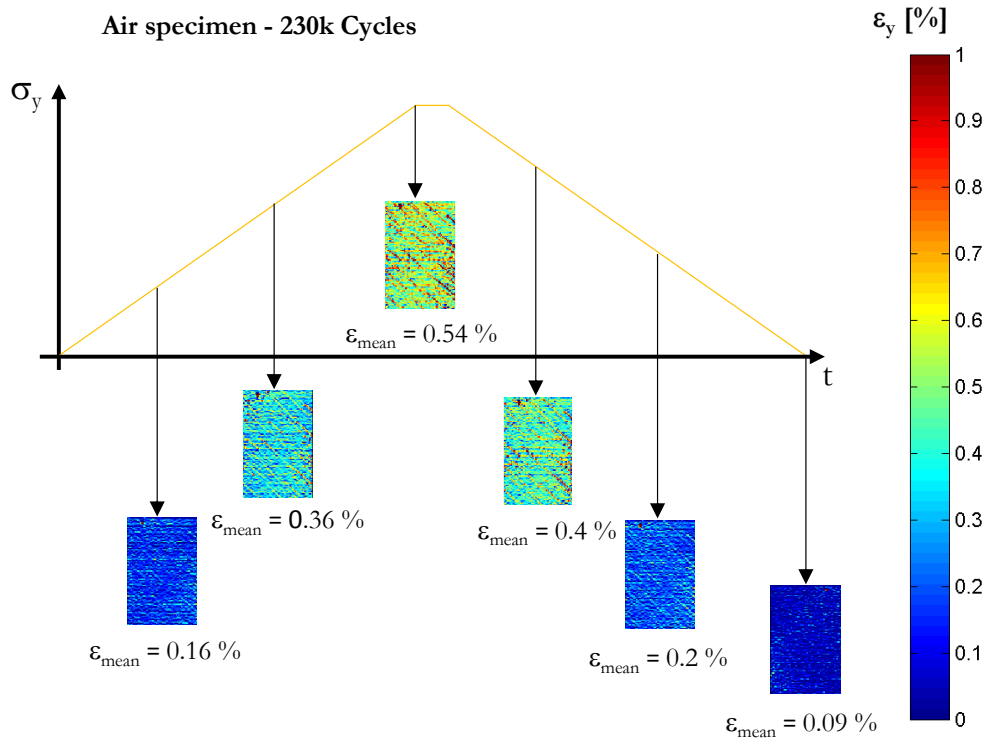

Fig.4. 5 : DIC strain fields during a load/unload intermediate stop for the air specimen after 230k cycles.

At the maximum stress level, the mean strain value encountered in the virgin specimen is higher than the value observed for the same specimen after 230k fatigue cycles. The same consideration could be made for the strain field relative to the end of the unload stage. The heterogeneity sources in the strain fields in *Fig.4. 4* are due to DIC algorithm errors and to the woven architecture, while in the case of the load/unload cycle reported in *Fig.4. 5* a further source of heterogeneity is related to cracks. As already explained in the Chapter 2, for mechanical properties calculation, only the mean value of each strain field is plotted as a function of the applied stress in graphs like *Fig.4. 6*. The first two graphs reported in *Fig.4. 6* show a shear stress/shear strain curve (plotted as explained in Appendix-D) recorded at the beginning of the fatigue test and after 170k cycles respectively. The maximal value of the shear strain is quite different between the two graphs and this difference is well described by the variation of the secant shear *modulus* G_{12}^{sec}. DIC data points have been interpolated using second degree polynomials to smooth the strain along time. Load and unload curves have been interpolated using two different polynomials and finally the area enclosed by the interpolating polynomials has been calculated (*see Fig.4. 6*).The area enclosed in the hysteresis loop of the first load/unload cycle is relatively extended if compared to the area of the load/unload cycle carried out after 170k cycles.

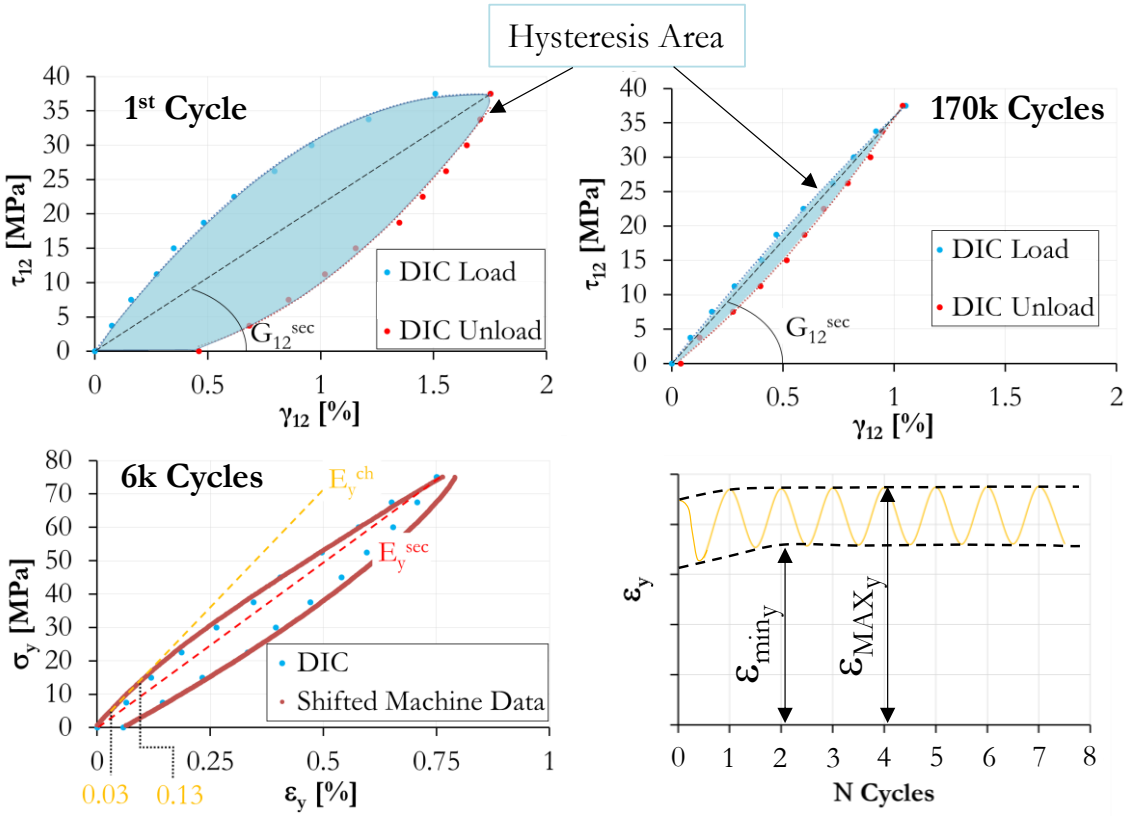

Fig.4. 6 : Hysteresis loops area from DIC data along shear direction, secant and chord modulus along load direction and minimum and maximum fatigue strain.

During fatigue tests, stress/strain data have been used to evaluate the following quantities:

- Hysteresis area *A*, is used to characterize the load/unload cycles in full, while the following properties characterize only the load stage. In the first three graphs reported in *Fig.4. 6*, a residual strain could be remarked at the end of the unload stage. The resulting hysteresis loop is not completely closed in the bottom side of the stress/strain graph. During fatigue, the magnitude of this residual strain decreases and in the quasi-static load/unload cycle performed after 170k cycle, the hysteresis loop seems to be perfectly closed.
- Secant shear *modulus* G_{12}^{sec}, has been calculated using the maximum shear strain and the maximum shear stress values in the fibre direction for each load/unload cycle;
- The longitudinal secant *moduli* E_y^{sec}, have been calculated using the maximum longitudinal strain and the maximum longitudinal stress values for each load/unload cycle.
- The longitudinal elastic *moduli* E_y^{ch}, is defined from the data points of the first stages of traction using the method reported in (Topal et al., 2015): a chord modulus is calculated as the slope of a straight line fitting the corrected machine data points over the strain range 0.03%-0.13%. The secant properties are generally strongly affected by creep effects, so

corrected data on movable head displacement have been used for "elastic" properties calculation.

- The fatigue maximum strain ε_{MAXy} (fourth graph in *Fig.4. 6*) is plotted for the *continuous fatigue test* in the next paragraph. This strain allows quantifying the creep/fatigue interaction during fatigue.

A description of the evolution of the listed quantity during *continuous* and *discontinuous* fatigue is given in the next paragraph.

4.4 Fatigue test results

This paragraph is split in two parts: firstly the results issued from the continuous fatigue tests are presented, after that the damage at the micro-scale is described thanks to μCT scan analysis of the specimens tested in discontinuous fatigue.

4.4.1 Continuous fatigue results

The first remarkable result of the continuous fatigue test is the failure of the 2 bar O_2 specimen at 330k cycles that is less of the half of the prefixed duration of the test, while the air and the 2 bar N_2 specimen arrive to the prefixed end of fatigue test (1M of cycles) without failing.

The evolution of the hysteresis area during fatigue is reported in *Fig.4. 7* in which dotted lines are manually drawn to show a general trend of A.

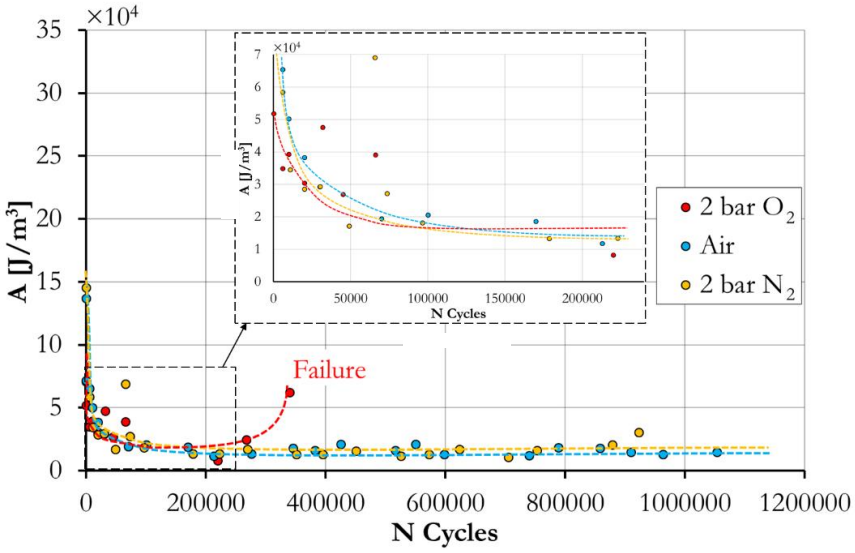

Fig.4. 7 : Evolution of the hysteresis area as function of the number of cycle during continuous fatigue tests.

The hysteresis area starts from a value of 10-15×10⁴ J/m³ at the beginning of fatigue and decreases until 2-5×10⁴ J/m³ after 6k-50k cycles. This last value is kept until the end of the test for the air and 2 bar N_2 specimen, while a slightly rise is seen for the 2 bar O_2 specimen just before the failure. This final rise just before the failure of the 2 bar O_2 specimen, could be due to the stick-slip frictional sliding (Kristofer Gamstedt, Redon and Brøndsted, 2002; Topal et al., 2015).

The secant shear *modulus* trend (G_{12}^{sec}) is shown in *Fig.4. 8*. After an increase from 2 to 3.5-4 GPa in the first thousands cycles, the shear secant *modulus* does not evolve for the air and 2 bar N_2 specimen, while a gradual decrease from ~200k cycles is observed for the 2 bar O_2 specimen until the end of the test.

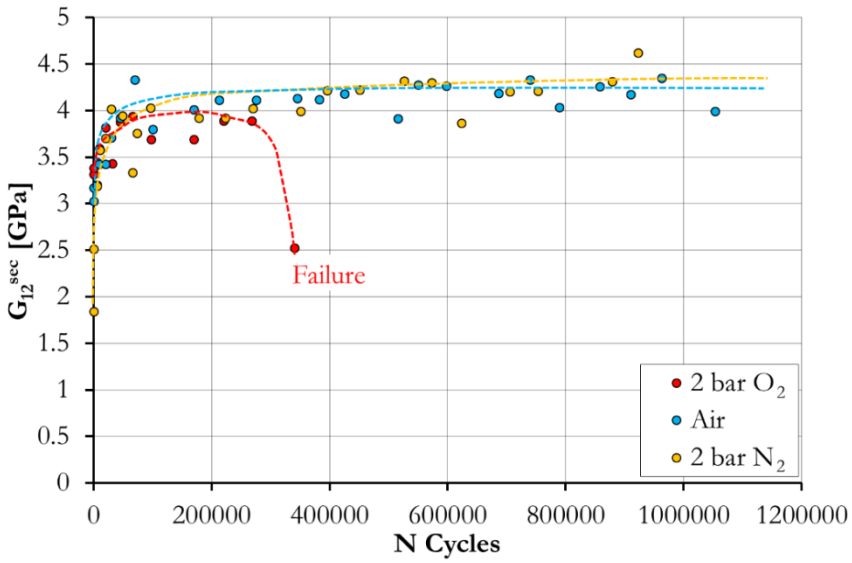

Fig.4. 8 : Evolution of the secant shear modulus as function of the number of cycle during continuous fatigue tests.

Fig.4. 9 shows the evolution of the chord longitudinal modulus (E_y^{ch}) as a function of the number of cycles. For the three tested specimens the initial value is around 14 GPa, after 30k cycles E_y^{ch} decreases to 11-12 GPa, after that a slightly continuous reduction is observed for the three specimens until the end of the test. Dotted lines in *Fig.4. 9* represent the trend of the experimental data. These lines show a decrease rate different for the E_y^{ch} of the three specimens. The 2 bar O_2 specimen has the highest decrease rate, while the decrease rates of the 2 bar N_2 and air specimen are quite similar. On the initial value of the chord *modulus* a scatter is observed for the three specimens, besides only three specimen have been tested (one for each environmental condition) in continuous fatigue because the complexity and the duration of the tests, it follows that a statistical analysis on the obtained results is not practicable.

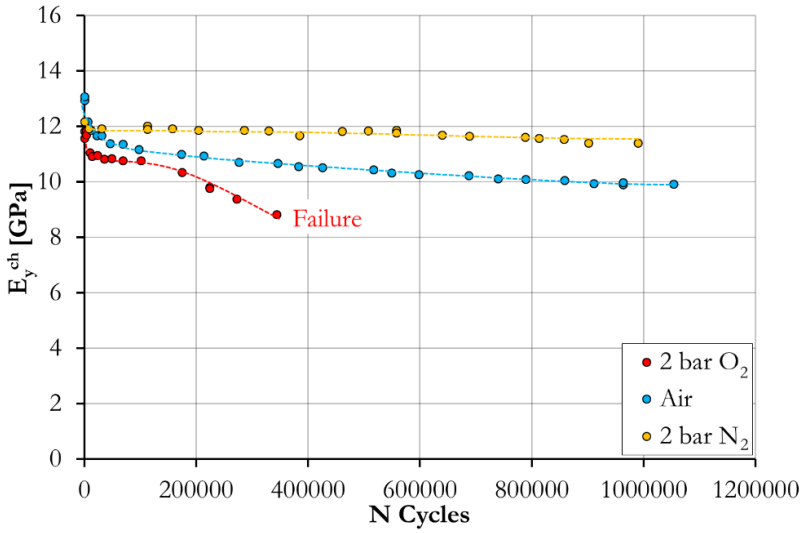

Fig.4. 9 : Evolution of the chord longitudinal modulus as function of the number of cycle during continuous fatigue tests.

The evolution of the secant longitudinal *modulus* (E_y^{sec}) as function of the number of cycle is reported in *Fig.4. 10*. As for G_{12}^{sec}, an increase of this property is observed in the early stage of fatigue and for the rest of the test a constant degradation rate is observed for the three tested specimens. In detail, the 2 bar O_2 specimen seems to start the degradation before to arrive to the stabilized value.

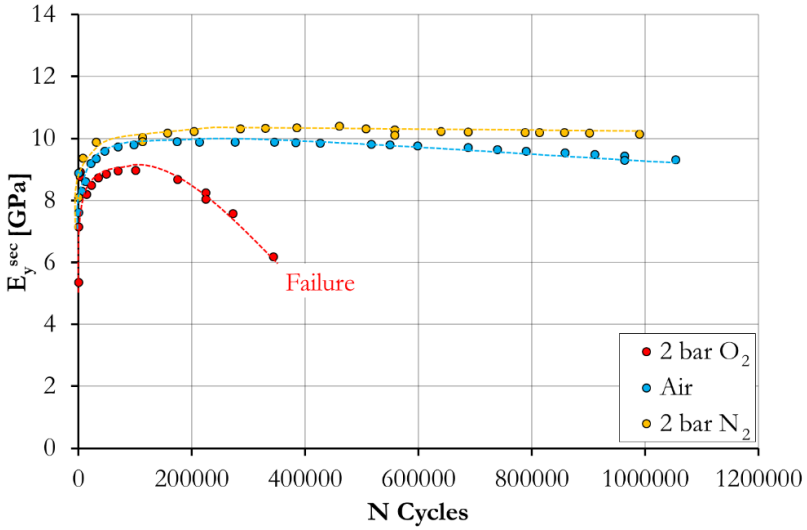

Fig.4. 10 : Evolution of the secant longitudinal modulus as function of the number of cycle during continuous fatigue tests.

The difference between elastic and secant *moduli* is a measure of the non-linearity in the tensile longitudinal coupon response. The chord *modulus* reduction and the secant *modulus* increase in the first stage of fatigue could be linked to a damage development that does not give a rise in terms of non-linearity in the tensile response of the specimen, on the contrary the longitudinal response becomes more *linear* and this is also supported by the decreasing of the hysteresis area. The stiffness degradation in the second stage of fatigue results in a rise of the difference between chord and secant

moduli suggesting that damage introduces a non-linearity in the longitudinal direction that however is not detectable on the hysteresis curves. The first evolution stage of the chord and secant *moduli* may be mainly due to two phenomena that could act together.

The former is fibre reorientation: for a woven composite material, loaded along an off-axis direction, a stiffening of the specimens could be present as a result of fibre rotation, as in (Albouy, Vieille and Taleb, 2014) where the test temperature was higher than T_g of the composite's matrix. In (Montesano et al., 2012) the same stiffening effect has been observed at test temperature lower than T_g for a carbon fibre/bismaleimide woven composite. For the authors the increase in stiffness was about 20%, and the magnitude of the fibre rotation, indirectly calculated from the permanent longitudinal deformation, was around 0.15°. In the graphs reported above, a stiffening of the materials is noticeable only on the secant properties. The chord modulus decreases from the beginning to the end of the tests. Two reasons could clarify this evolution. The first is the major effect of the damage on the evolution of the chord *modulus* in the first stage of fatigue, so, despite the stiffening due to fibre rotation, the softening effect linked to damage is more important. This could results in the *linearization* of the tensile longitudinal response seen in this fatigue stage (*i.e.* the secant *modulus* tends toward the value of the chord *modulus*). The second is that the fibre rotations take place only after a threshold stress, so only in the high zone of the stress-strain curve there is a change (*i.e.* the secant *modulus*).

A second kind of phenomena taking place in the first step of fatigue, could be linked to the viscous nature of the matrix: the stiffening of the specimens could be due to a kinematic hardening of the matrix, as explained in (Da Costa Mattos and Martins, 2013) for an epoxy matrix during cyclic load. Recently, the fatigue data analysis of some authors focused on the *ratcheting strain*. This is the progressive accumulation of deformation while the materials are subjected to cyclic loading, especially under stress controlled mode with a non-zero mean stress (Zhang, Chen and Wang, 2010). Further details on the r*atcheting strain* during fatigue test are given in Appendix-E.

The two discussed phenomena could be linked: as explained ever in (Albouy, Vieille and Taleb, 2014), a plasticization of the resin regions results from the rotation of the fibre bundles that at a macroscopic level should be give the same effect of a matrix hardening.

These phenomena are here introduced to give a possible interpretation of the general evolution of the obtained curves but will be no longer investigated. In fact, all these evolutions are seen at the beginning of the tests when the environmental effect are not yet visible on properties evolution.

Some authors characterize the degradation of the tested specimens during fatigue studying the evolution of longitudinal strains (minimal, mean or maximal). The evolution of the maximum strain (ε_{MAXy}) throughout the fatigue tests, issued from the data about the displacement of the movable part of the test machine, is reported in *Fig.4. 11*.

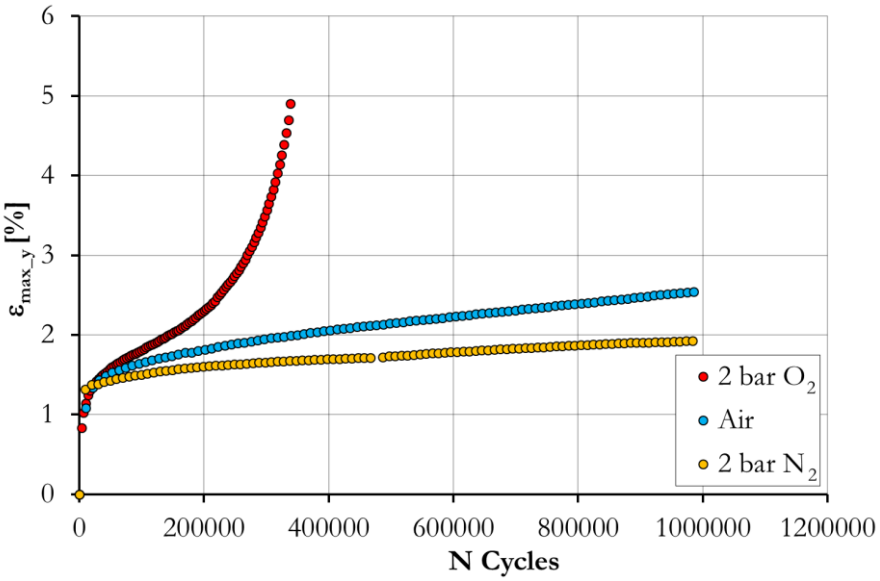

Fig.4. 11 : Evolution of the maximal strain as function of the number of cycle during continuous fatigue tests.

The environmental effect is remarkable in *Fig.4. 11*, where in the early stage of fatigue, the ε_{MAXy} trend is the same for the three specimens. After an initial increase, the environment begins to affect the response of the specimens and the three specimens take three different evolutions. For the air and 2 bar N_2 specimen, a slightly increase of the maximum strain is observed until the end of test. For the 2 bar O_2 specimen, after the initial evolution, the maximum strain grows up rapidly up to the specimen failure. The evolution of the ε_{MAXy} during fatigue can be view as the sum of a contribution linked to damage development during fatigue, a second terms related to creep during fatigue and a third term related to the elasto-plastic deformation dependent on the maximum fatigue load.

In the graphs in *Fig.4. 7* -*Fig.4. 11* three evolution stages are discernible, as detailed in 4.6:

- Firstly, a rapid evolution toward a steady state, clearly remarkable for E_y^{sec}, G_{12}^{sec}, A and ε_{MAXy};
- A steady state that, for the 2 bar N_2 and air specimen, persists until the end of the fatigue test;
- Finally, a gradual evolution of the properties from the end of the second stage up to the end of fatigue. This last evolution stage is clearly visible looking at the 2 bar O_2 specimen related graphs.

The most important evidence issued from these graphs is the role of the environment on fatigue behaviour. In fact, after the first evolution stage, completed within 70k cycles (*i.e.* ~10 hours), the evolution of the three specimen properties begins to differ from each other, especially for the graphs in *Fig.4. 9*, *Fig.4. 10* and *Fig.4. 11*. In particular for the 2 bar N_2 specimen, after the initial evolution, the longitudinal chord *modulus* slightly decreases, while the secant *modulus* does not change until the end of the test. For the air specimen a degradation is observed for both chord and secant *moduli* and finally, for the 2 bar O_2 the second stage of fatigue is not easy to detect on the graphs, a continuous loss of longitudinal properties is detected until failure but, until 100k-150k cycles to failure, the hysteresis area evolution does not suggest an increase in specimen energy dissipation.

4.4.2 Discontinuous fatigue results

The differences between the three environmental test conditions during discontinuous fatigue tests are reported in the follow. The first and more evident effect is the failure of the 2 bar O_2 specimen after 550k cycles, while the air and 2 bar N_2 specimen reach 1M of fatigue cycles without fail.

The evolution of A during fatigue is reported in *Fig.4. 12* and the evolution of G_{12}^{sec} during discontinuous fatigue is shown in *Fig.4. 13*.

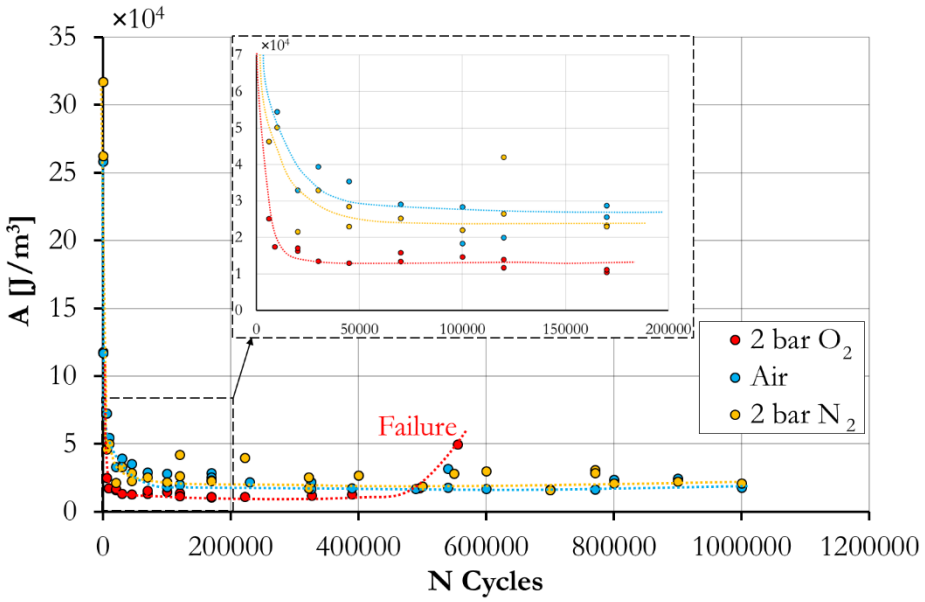

Fig.4. 12 : Evolution of the hysteresis area as function of the number of cycle during discontinuous fatigue tests.

In *Fig.4. 12* a rapid decrease from 30-25×10⁴ to 2-5×10⁴ J/m³ is recorded during the first 50k cycles. After this reduction, for the air and 2 bar N_2 specimen a stationary stage is observed until the end of the test, while for the 2 bar O_2 specimen *A* increases just before the specimen failure.

The secant shear *modulus* in *Fig.4. 13* increases from 2 GPa to 3.5-4 GPa over 100k cycles. This value persists until the end of the test for the air and 2 bar N_2 specimen, while decreases just before the failure for the 2 bar O_2 specimen.

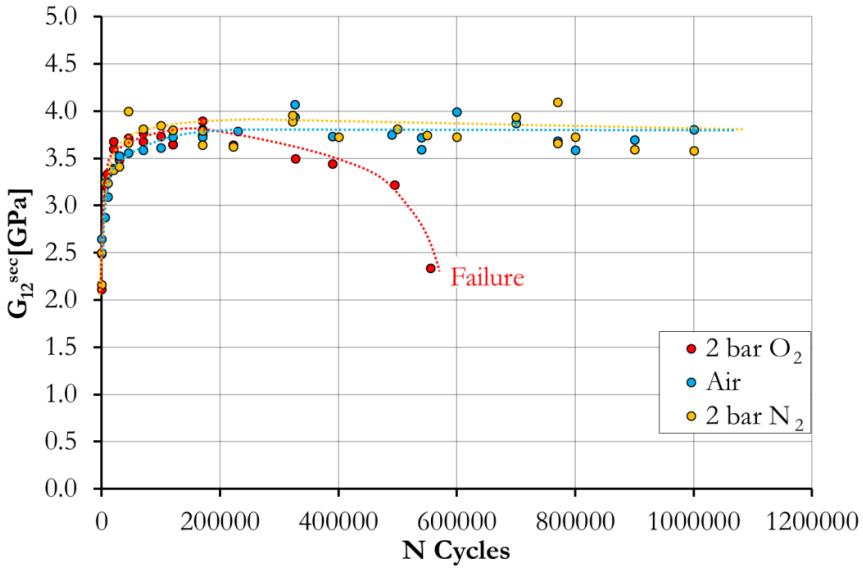

Fig.4. 13 : Evolution of the secant shear modulus as function of the number of cycle during discontinuous fatigue tests.

Longitudinal properties are illustrated in *Fig.4. 14* and *Fig.4. 15*.

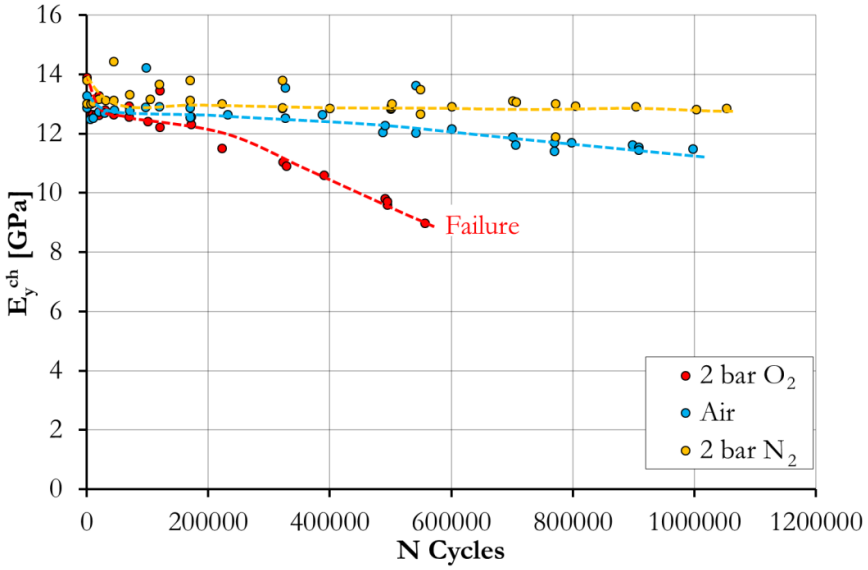

Fig.4. 14 : Evolution of the chord longitudinal modulus as function of the number of cycle during discontinuous fatigue tests.

For the chord longitudinal *modulus* a rapid degradation is observed in the early stage of fatigue for the three specimens; after this stage, E_y^{ch} shows a constant decreasing rate for the air and the 2 bar N_2 specimen until the end of fatigue. For the 2 bar O_2 specimen, E_y^{ch} has three different degradation rates: the former until 70k cycles, a second until 200k cycles and the third between 200k cycles and the end of the test.

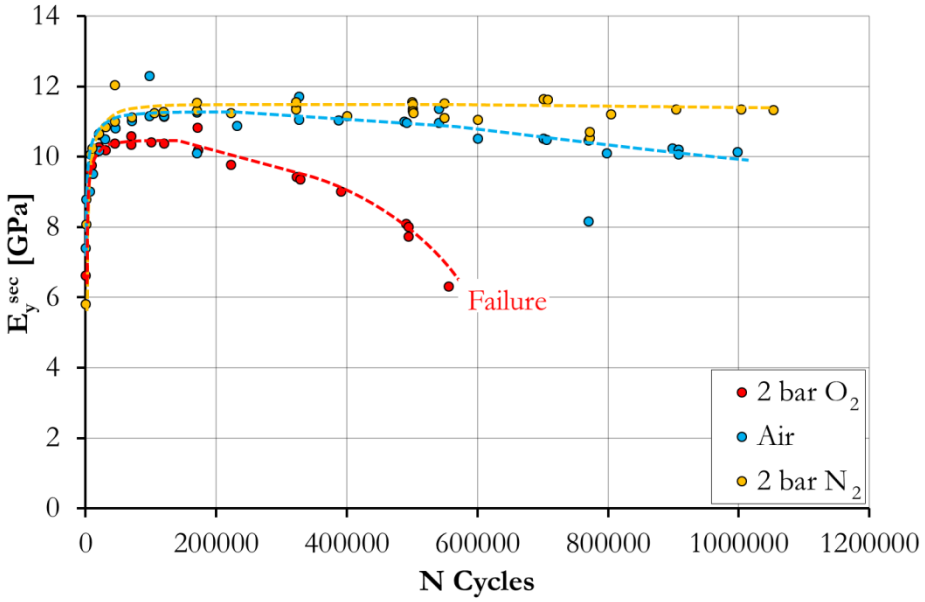

Fig.4. 15 : Evolution of the secant longitudinal modulus as function of the number of cycle during discontinuous fatigue tests.

The secant longitudinal *modulus* in *Fig.4. 15* rises in the first stage of fatigue for the thee specimens achieving 11 GPa for the air and 2 bar N_2 specimen and 10.5 GPa for the 2 bar O_2 specimen. The achieved value seems to be kept until the end of the test for the 2 bar N_2 specimen, while a decreasing is observed for the air and the 2 bar O_2 specimen. The decreasing observed for these two specimens is quite different: the air specimen has a constant decreasing rate until the end of the test, instead the 2 bar O_2 specimen shows an acceleration of the degradation from 400k cycles.

The general trend of the macroscopic properties evolution seen during discontinuous and continuous fatigue is quite similar. As said above, the number of tested specimens is not adequate to perform a statistical analysis of the results, so the difference in values between discontinuous and continuous fatigue tests both at the beginning and during the tests, is attributed to the experimental scatter.

As could be remarked comparing the graphs resuming the results obtained during continuous and discontinuous fatigue, the failure of the 2 bar O_2 specimen during continuous fatigue arrives after 330k cycles that is quite lower than the life of the 2 bar O_2 specimen tested in discontinuous fatigue. This difference could be due to a preload effect: as reported in (Vieille, Albouy and Taleb, 2014) the

effects of a preload on a C/PPS laminates is a longer fatigue life. If each interruption and removal of the specimen for μCT scans is viewed as a preload stage, a preload effect could appear on the tested specimens. To confirm this, the specimens tested in continuous and discontinuous fatigue have been tested up to failure. The life of each specimen is reported in *Table 4. 2* and *Fig.4. 16*.

Fatigue / Test conditions	**Continuous**	**Discontinuous**
2 bar O_2	330000	550000
Air	1699205	2045900
2 bar N_2	1925000	1312000

Table 4. 2 : Fatigue life for specimens tested under three different environmental conditions and in continuous and discontinuous fatigue.

From the histograms in *Fig.4. 16* and *Table 4. 2* does not appear a clear preload effect, on the other hand the number of tested specimens does not allow performing a statistical analysis. The specimen tested in discontinuous fatigue in 2 bar N_2 specimen fails before the analogous specimen tested in continuous fatigue. Furthermore, the difference in life seen for the 2 bar O_2 specimens is much higher than the difference observed for the air specimens. However, an important result issued from *Fig.4. 16* and *Table 4. 2* is the life-reduction effect during fatigue in strongly oxidizing environmental test conditions for an organic composite specimen.

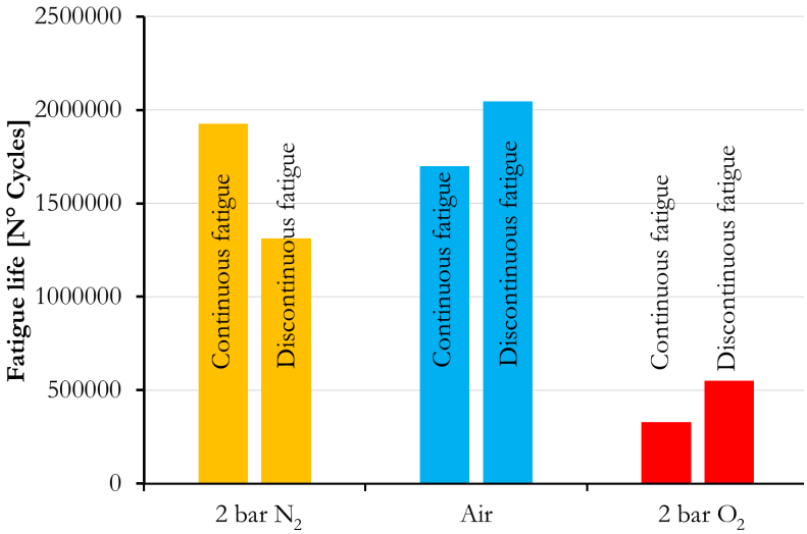

Fig.4. 16 : Fatigue life for specimens tested under three different environmental conditions and in continuous and discontinuous fatigue.

Finally, from the graph in *Fig.4. 12*-*Fig.4. 15* it can be concluded that the interruptions of the fatigue tests for μCT scans does not affect the macroscopic properties evolution, no preload effect seems to affect the obtained results.

µCT scan segmentation results

Discontinuous fatigue tests have been performed in order to investigate damage at the micro-scale by µCT scan segmentation. The µCT results are now presented and discussed, after that a link between the macroscopic properties evolution and the damage observations made by µCT scan segmentation is proposed.

An exterior ply and the relative segmentation are illustrated in *Fig.4. 17*. The non-segmented image is shown on the left; in this image cracks in the tows oriented along the -45° direction are clearly visible as little cracks in 0° direction and, uniquely in the crossover regions, cracks in the tows oriented along the +45° direction.

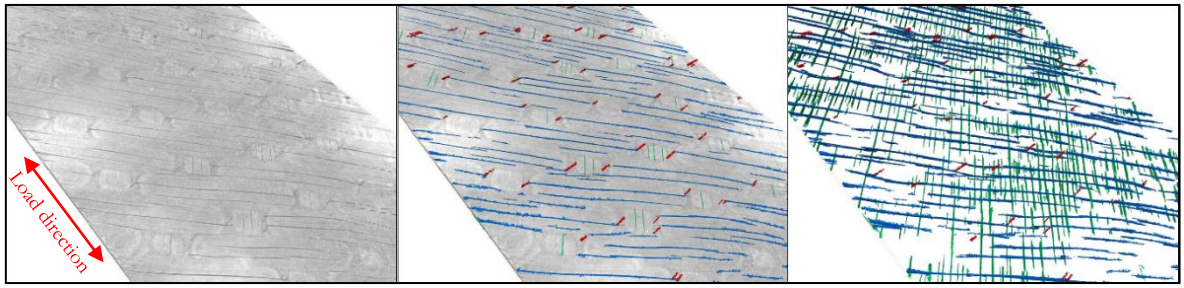

Fig.4. 17 : Segmentation of an external ply. In the reconstructed image ply, cracks are segmented and the segmentation result is reported in the last image. Red segments are 0° cracks, the blue and green ones are associated to -45° and +45° cracks respectively.

Using the segmentation procedure described in Chapter 2, the cracks are segmented, and the result is reported in the central image of *Fig.4. 17*, where the 0° cracks are in red, -45° cracks in blue and finally, +45° cracks in green. The segmented cracks are illustrated in the right side of *Fig.4. 17*, where the 3D ply reconstruction is not reported. The majority of blue cracks on the right side in *Fig.4. 17* are continuous cracks and not all the cracks reach the lateral edges of the ply. Observing the surface of the specimen it is not possible to know if, in the crossover regions, the cracks in the -45° tows are interrupted or not. A zoom of the segmentation proposed in *Fig.4. 17* is reported in *Fig.4. 18*.

In *Fig.4. 18* +45° cracks are shorter than the -45° ones and concentrated where the -45° cracks are more developed or close to the lateral edges of the ply. Three regions where the +45° crack density is high are zoomed and enclosed in dotted lines. Chronologically, the formation of +45° cracks far from the edges, is subsequent to the formation -45° cracks for the external ply in *Fig.4. 18*.

The segmentation allows following the path of these cracks. A complete description of the crack location inside the woven is reported in *Fig.4. 19*.

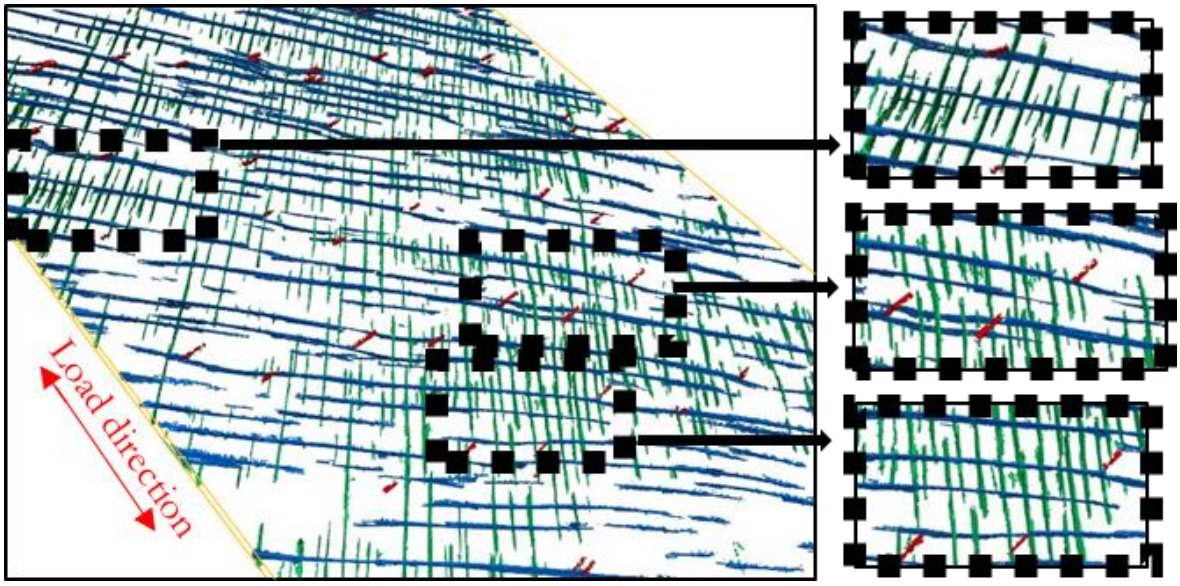

Fig.4. 18 : Zoom of the segmentation reported in Fig.4. 17. Detail of the cracks in the 45° direction. Red segments are 0° cracks, the blue and green ones are associated to -45° and +45° cracks respectively.

Fig.4. 19 shows a representative region of a damaged external woven ply. The damage scenario described in these pictures is the same for all the tested specimens. In *Fig.4. 19* ***a)*** 4 tows are identified using dotted lines: the tows from 1 to 3 are surface tows aligned along the -45° direction, while the tow 4 is a +45 tow belonging to the same external ply.

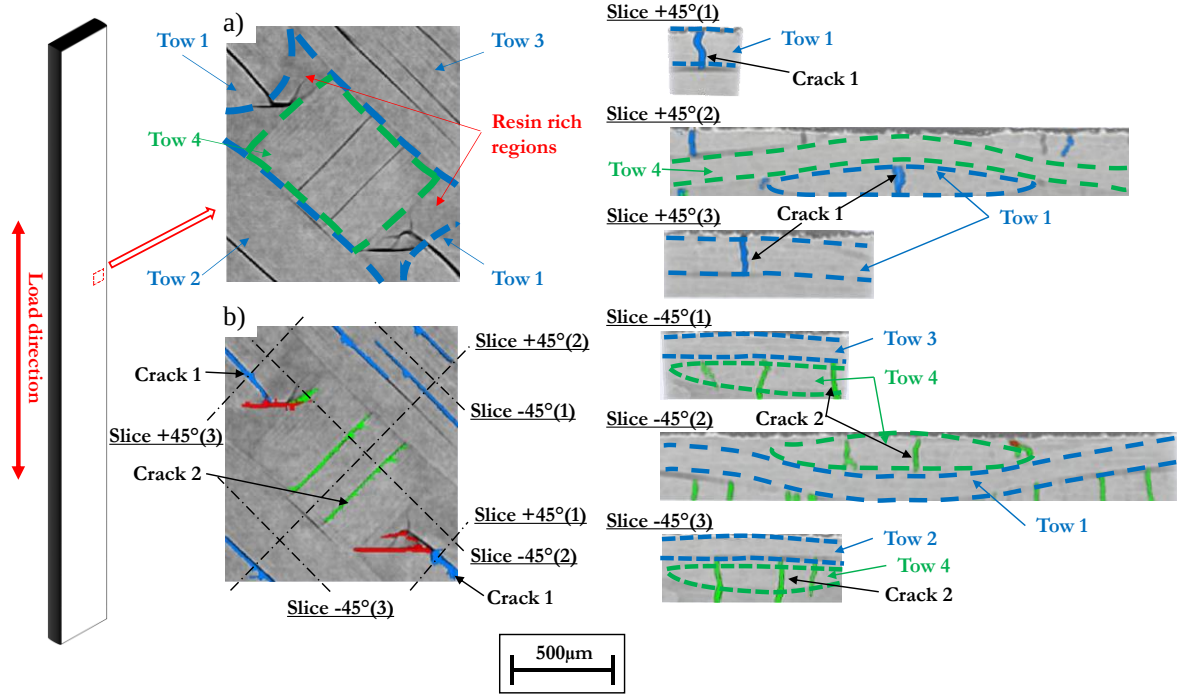

Fig.4. 19 : Representative region of a damaged external woven ply. In **a)** the external slice of the ply shows tows in -45° and +45° direction, resin rich regions and cracks. The segmentation results are in **b)** and the whole crack paths are shown using the cutting planes in +45 and -45° direction.

The segmented cracks are illustrated in *Fig.4. 19* ***b)***, this figure clearly shows three different kind of crack:

- 0° cracks (in *red*) are located in the resin rich regions and the direction of these cracks is normal to the direction of the applied load;

- -45° cracks (in *blue*) are aligned along the -45° direction and are located inside the -45° tows. In *Fig.4. 19* the path of the -45° crack named C*rack1* is shown: by using the cutting planes *slice +45°* from 1 to 3 one can see that this intra-tow crack propagates in the *Tow1* also across the crossover region, where *Tow1* passes under *Tow4;*

- +45° cracks (in *green*) are aligned along the +45° direction and are located inside the +45° tows. In *Fig.4. 19* the path of the +45° crack named C*rack2* is shown: by using the cutting planes *slice -45°* from 1 to 3 one can see that this intra-tow crack propagates in the *Tow4* across the crimp region and has a propagation also in the tow regions that are not on the visible surface. This is shown by the *slice-45°(1*) and *slice-45°(3)* where C*rack2* propagates also under *Tow3* and *Tow2* respectively.

A potential conclusion issued from the analysis of *Fig.4. 19* and *Fig.4. 18* is that in the external plies the -45° cracks propagate in the crimp region only after an extensive propagation in the straight zone of the tow between two crimp regions, while +45° cracks onset after the apparition of -45° cracks.

A chronological description of the crack onset and propagation is now presented for the three test conditions. For simplicity only an internal ply and only an exterior ply are presented for each specimen, bearing in mind that for each specimen the damage process of all the internal plies is the same as the same is the damage process for the two external plies.

The conclusions issued from the observation of the segmentation results are detailed in the following sub-paragraphs. The environmental conditions affect both damage scenario and damage extension. The presence of regions, in the observed specimens, where the damage is less or more extended than other ones, highlights the heterogeneous nature of the damage distribution and hence the importance in analysing and study a large specimen region to correctly characterize the damage process.

2 bar N_2 specimen

Damage scenario for the 2 bar N_2 specimen is depicted in *Fig.4. 20* and in *Fig.4. 21* for an external ply and an internal ply respectively. In *Fig.4. 20* -45° and 0° matrix cracks appear from 170k cycles. As

said above, 0° cracks are localized in resin rich regions. -45° intra-tow cracks are situated in the centre of the tows, between two crossover regions preferentially. During fatigue 0° pre-existing cracks do not propagate, but new cracks appear in the resin rich regions not already cracked. The -45° intra-tow cracks propagate along the belonging tow and new cracks onset and propagate in the other surrounding tows. For the +45° cracks the multiplication mechanism appears to be predominant on the propagation mechanism. This multiplication of cracks occurs especially in the region affected by the early -45° cracks.

The scenario for the internal ply in *Fig.4. 21* is quite different. In the first segmentation the damage level is very low, hence the gradient in proximity of cracks and the crack grey values are close to the values calculated near the edges of the tows, or the image artifact. When damage is more important, the segmentation is less noisy. After 170k cycles only some -45° cracks are observable. The propagation of these cracks is not so clear, it could be that longer cracks are in reality short cracks situated in the same tow. +45° cracks are ever placed where the volume of -45° cracks is more important.

Air specimen

On the exterior ply reported in *Fig.4. 22* the -45° cracks are spread on the whole observed volume. With respect to the 2 bar N_2 specimen, the noise affecting air specimen segmentation is less important, maybe due the better quality of the μCT scan. Discontinuous cracks between the crossover regions appear clearly from the first scan. As in the previous case, 0° cracks multiplication is observed during fatigue.

The +45° cracks are not linked to the -45° crack presence in the first half test (until 550k cycles), these cracks onset on the lateral edges of the specimen and the longitudinal distance between these cracks seems to be the same (clearly visible on the left side of the scan at 170k cycles).The early +45° cracks propagate toward the centre of the specimen during the entire test. In the second half of test, the diffuse cracking in -45° direction promotes the apparition of short +45° cracks near the oldest -45° cracks.

An internal ply of the air specimen is reported in *Fig.4. 23*. As for the 2 bar N_2 specimen, the extremely low damage level and the consequently uncertainty of the segmentation parameters, make the results noisy for the first half test. However, some items for the description of the damage scenario are identifiable. The -45° and the +45° cracks appear separately, and no 0° cracks are detected. The main onset location for both -45° and +45° crack direction, are the lateral edges of the specimen. During fatigue, new cracks appear while the oldest ones propagate toward the centre of the specimen.

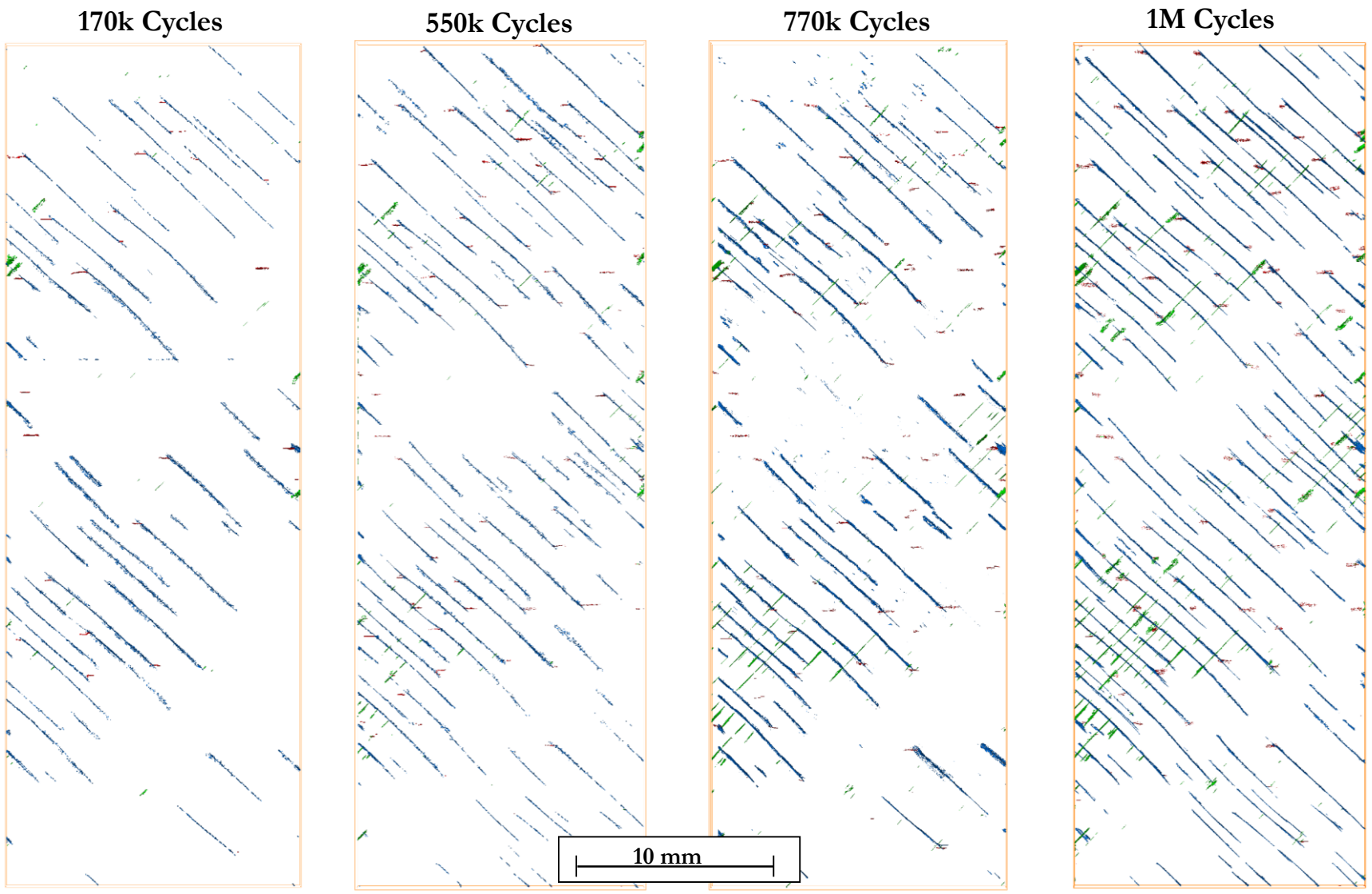

Fig.4. 20 : External ply cracks during fatigue in 2 bar N_2. Red segments are 0° cracks, the blue and green ones are associated to -45° and +45° cracks respectively.

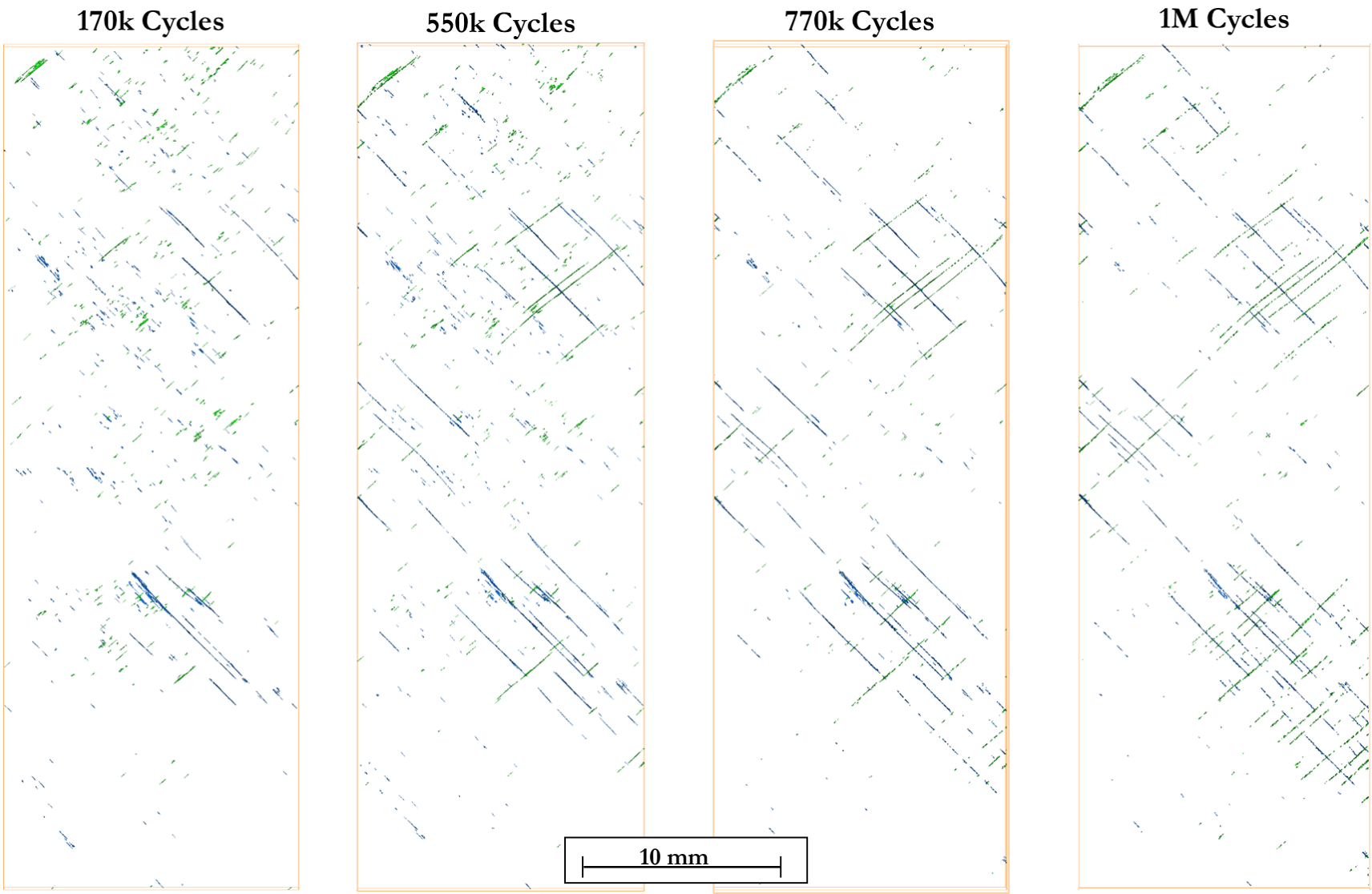

Fig.4. 21 : Internal ply cracks during fatigue in 2 bar N_2. Blue and green segments are associated to -45° and +45° cracks respectively.

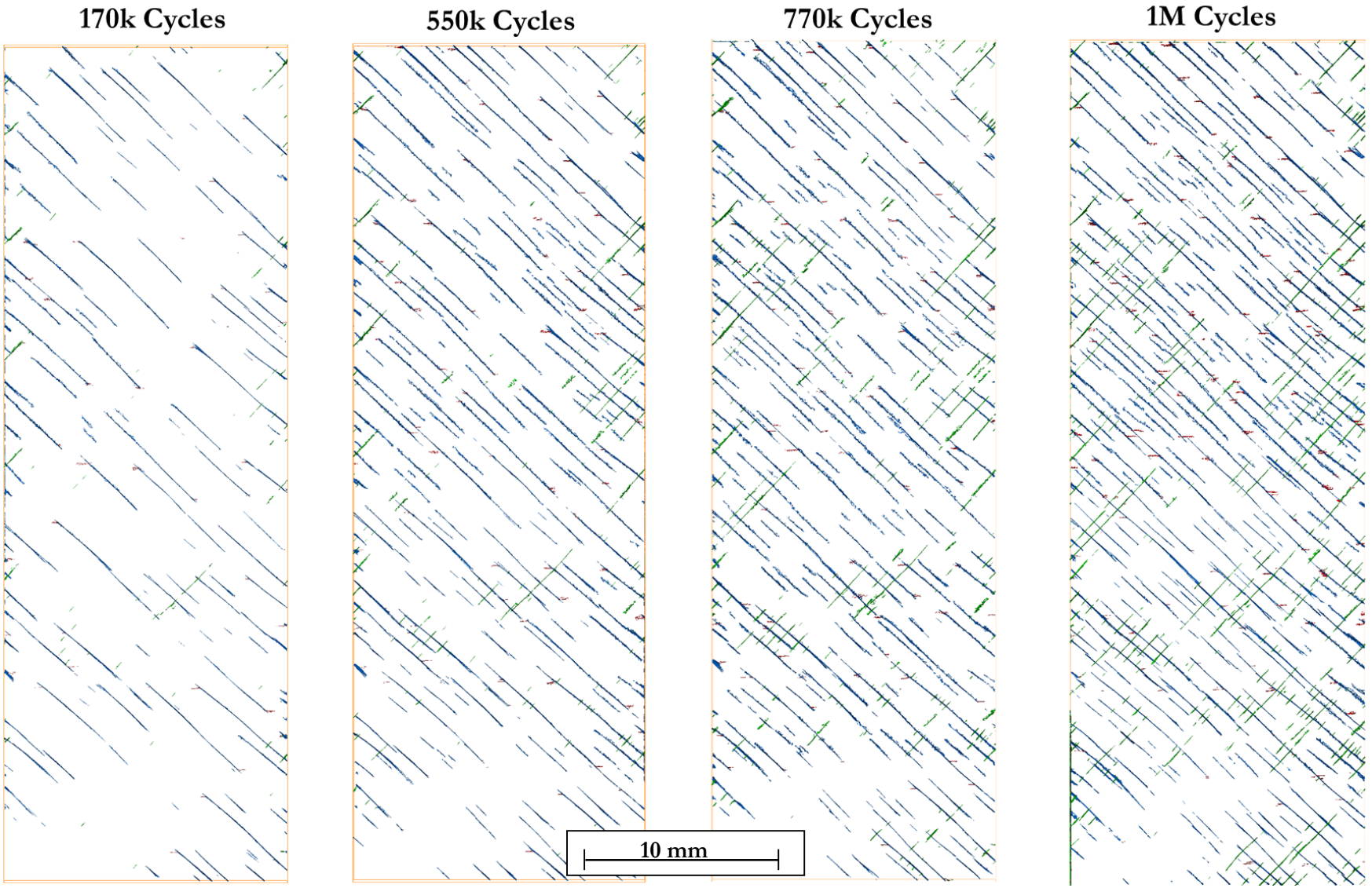

Fig.4. 22 : External ply cracks during fatigue in air. Red segments are 0° cracks, the blue and green ones are associated to -45° and +45° cracks respectively.

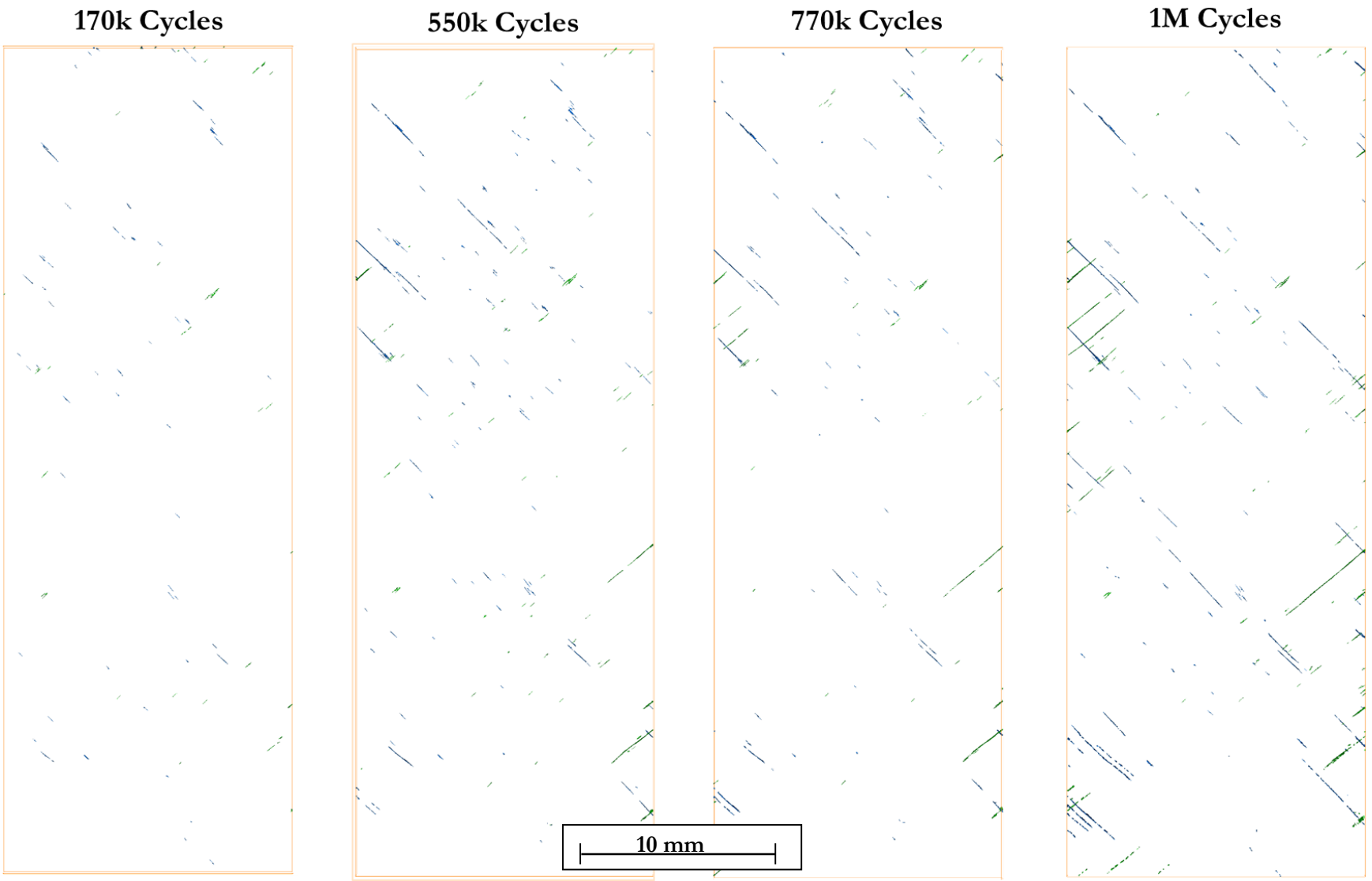

Fig.4. 23 : Internal ply cracks during fatigue in air. Blue and green segments are associated to -45° and +45° cracks respectively

2 bar O_2 specimen

The segmentations of an external ply belonging to the 2 bar O_2 specimen are reported in *Fig.4. 24*. Due to the severity of the expected environmental effects during the test of this specimen, the first μCT scan has been performed after 20k cycles. The opening of small 0° cracks is observed from this first scan. As for the previous specimens, these cracks do not propagate outside the resin rich regions, but rather a multiplication of these cracks is noted until saturation of the resin rich regions. -45° cracks are located between two crossover regions of the tows oriented along the -45° direction. These cracks appear as multiple cracks between crossover regions of the same tow and during fatigue they tend to join in a long single crack. +45° cracks are not widely extended in the first scan, the majority of the segmented regions could be associated to noise. At 170k cycles some +45° cracks appear under the oldest -45° cracks. At 550k cycles, where the specimen has failed, +45° cracks are largely distributed in the ply in the form of little discontinuous cracks, some of which arrive to form a single crack.

For the internal ply shown in *Fig.4. 25* the noise is very important at 20k cycle where, apparently, no damage is detected. At 170k cycle, some little -45° and +45° cracks are segmented close the lateral specimen edges, but only between 170k and 550k cycles the damage evolution is significant. In the scan performed after 550k cycles, the lateral edges become the most damaged regions of the internal plies. The majority of these cracks are short and do not propagate towards the centre of the specimen. Other cracks onset at the centre of the ply without apparent propagation/contact with the edge cracks. As for the previous two specimens, for the internals plies no 0° cracks have been detected.

Looking at the μCT results, two mainly aspects of the damage could be remarked. The former is the specific damage evolution in the different plies of each specimen. In all the external plies, the first damage form are the cracks in the surface tows direction of the plies. These appear in the specimens as multiple cracks in the same tow and tend to coalesce in a single crack. The early crack development in the exterior ply is already reported in (Yu et al., 2016); for the authors this could be due to the major undulation of the exterior tows respect the inner ones or, to the better deformability of the exterior plies if compared to the interior ones, during load.

The presence of +45° cracks is often related to the presence of -45° ones and rarely they onset from the lateral edges of the specimens. In the internal plies the damage is less important than an external ones. The presence of cracks in -45° is important as the presence of cracks in +45° direction and no 0° cracks are detected.

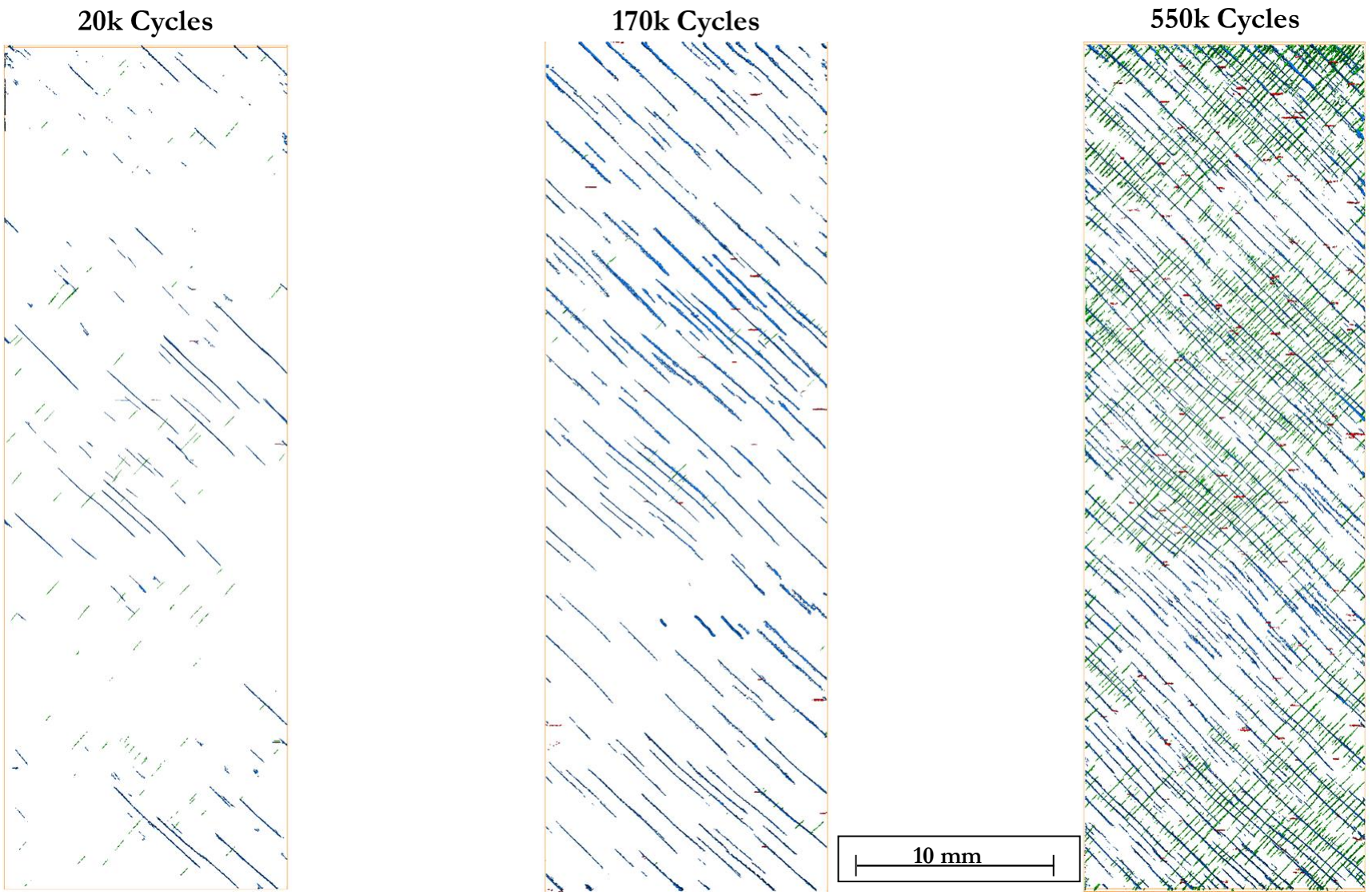

Fig.4. 24 : External ply cracks during fatigue in 2 bar O_2. Red segments are 0° cracks, the blue and green ones are associated to -45° and +45° cracks respectively.

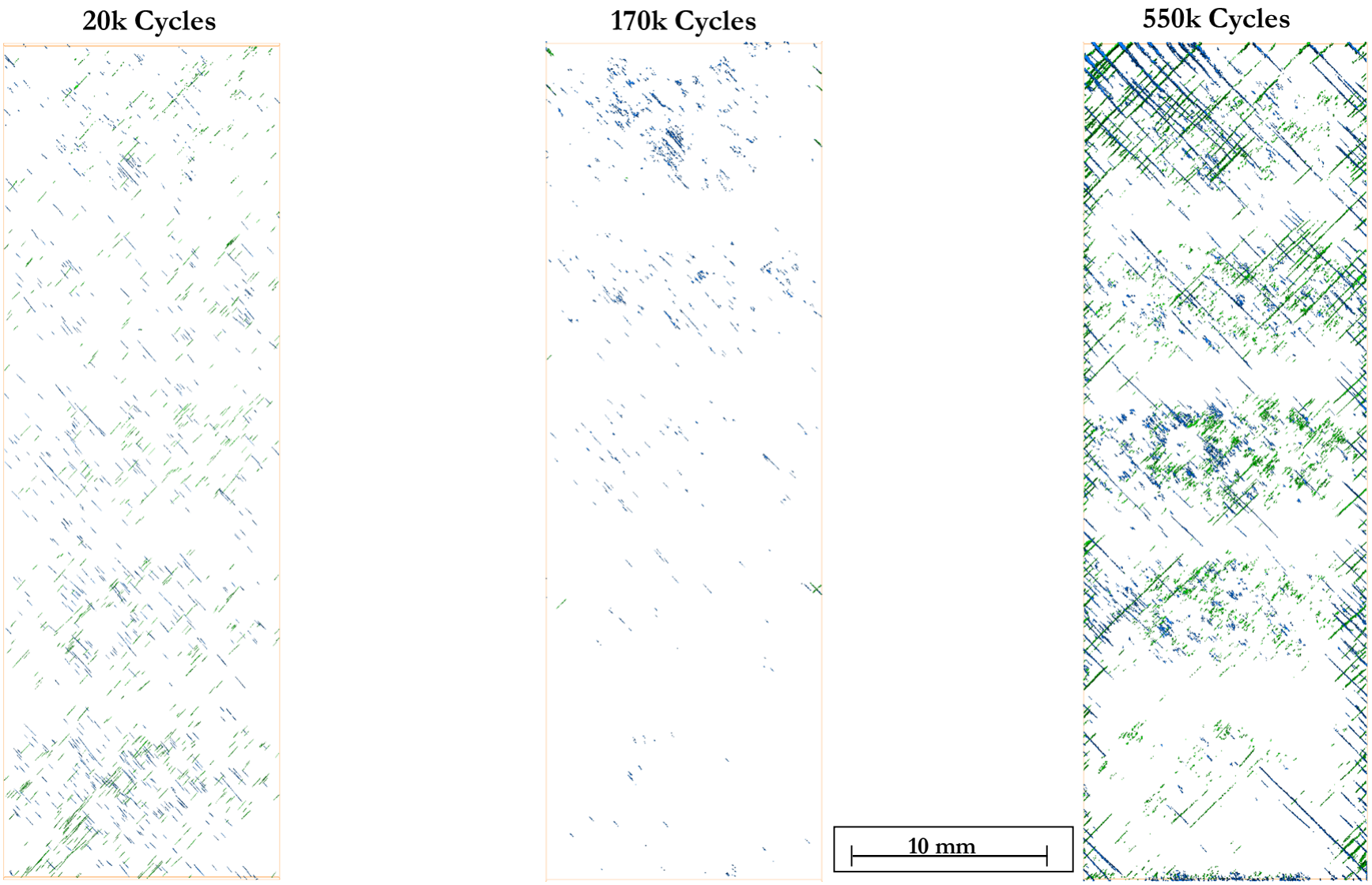

Fig.4. 25 : Internal ply cracks during fatigue in 2 bar O_2. Blue and green segments are associated to -45° and +45° cracks respectively.

The second and the most relevant aspect of μCT results, is the observation of the differences in damage scenario for the three environmental conditions. In the external plies the formation of +45° cracks is strongly dependent on the test conditions: in terms of +45° crack volume, after 170k cycles the difference for the three specimens is not relevant, while at 550k cycles there is a great gap for the external plies damaged volume. Since the formation, propagation/multiplication of -45° cracks in an exterior ply seems to be affected by the environmental test conditions, and the presence of +45° cracks related to the presence of -45° cracks, under severe environmental conditions (2 bar O_2) the +45° cracks are more numerous compared to +45° cracks in the external plies of the air and 2 bar N_2 specimen. For the internal plies, an important environmental effect is the preferential location for crack onset: for the 2 bar N_2 specimen the cracks presence seem to be linked to internal defects and/or stress concentration zones. For air and 2 bar O_2 specimen the cracks onset mainly on the lateral edges *i.e.* the surfaces directly exposed to the environment.

In order to compare the detected cracks, a global quantitative evaluation of the volumetric crack density during fatigue is proposed. For each μCT scan, the specimen volume (V^{TOT}) and the segmented cracks volume (V^{CRACKS}) are calculated using the *label analysis* tool in Avizo9®. The volumetric crack density $D^{\mu CT}$ is hence defined from *Eq.4. 1*:

$$D^{\mu CT} = \frac{V^{CRACKS}}{V^{TOT}} \qquad \text{Eq.4. 1}$$

The evolution of $D^{\mu CT}$ during continuous and discontinuous fatigue is reported in *Fig.4. 26*.

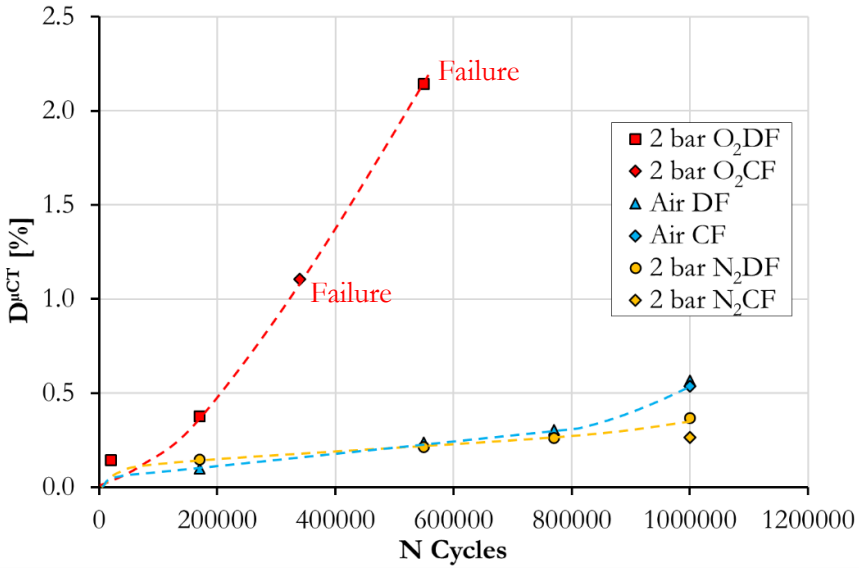

Fig.4. 26 : Evolution of the volumetric crack density $D^{\mu CT}$ during continuous (CF) and discontinuous (DF) fatigue.

The segmentation results of the specimens tested in continuous fatigue are reported in the graph in *Fig.4. 26* with the results obtained for the discontinuous fatigue tests. As one can see, for air and 2 bar N_2 specimen tested in continuous fatigue the damaged volume is quite similar to the analogous specimen tested in discontinuous fatigue. This brings to the conclusion that the interruptions performed for μCT scans during discontinuous fatigue, has not an impact on the results in terms of damaged volume. For the 2 bar O_2 specimens there is a remarkable difference because the specimen tested in continuous fatigue fails at 330k cycle and at the failure the damaged volume is 1.1% of the total specimen volume. In discontinuous fatigue the specimen fails at 550k cycles with 2.1% of damaged volume. An important evidence is that the ratio between the numbers of cycle at failure of the two 2 bar O_2 specimens is 1.6, while the ratio between damaged volumes at failure is 1.9. This similarity could be due to a direct environmental effect on the damage evolution, the specimen more exposed to environmental condition is more damaged than the specimen less exposed. If the damage level in the specimen is not an indicator of the health of the specimen, some other phenomena are correlated to the failure of the specimens such as fatigue-creep interaction.

Microscopic damage effects on macroscopic properties

The results obtained by DIC and μCT scan segmentation are here correlated in order to verify the existence of a direct link between matrix crack volume and macroscopic properties evolution. The evolution of the hysteresis area is reported in *Fig.4. 27* as a function of $D^{\mu CT}$.

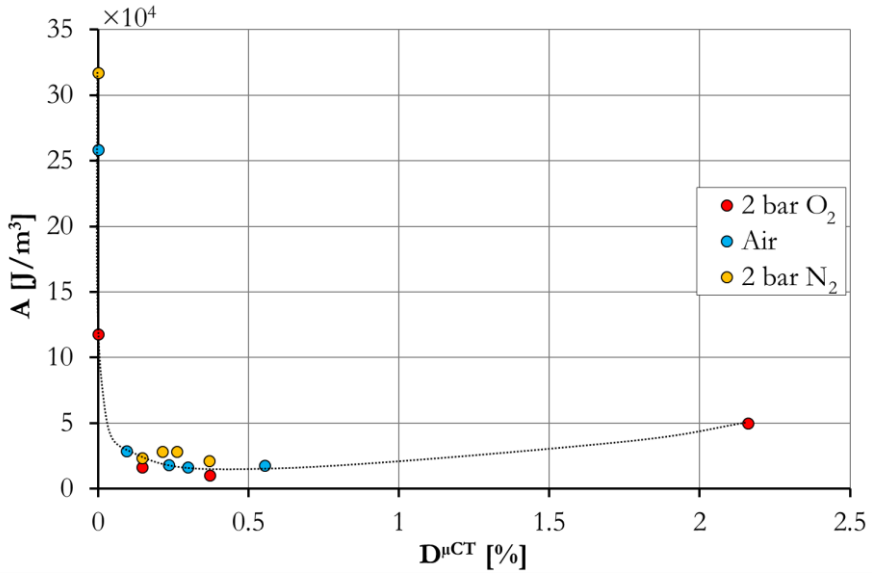

Fig.4. 27 : Evolution of the hysteresis area as a function of the volumetric crack density for the tested specimen in 2 bar O_2, air and 2 bar N_2 during discontinuous fatigue.

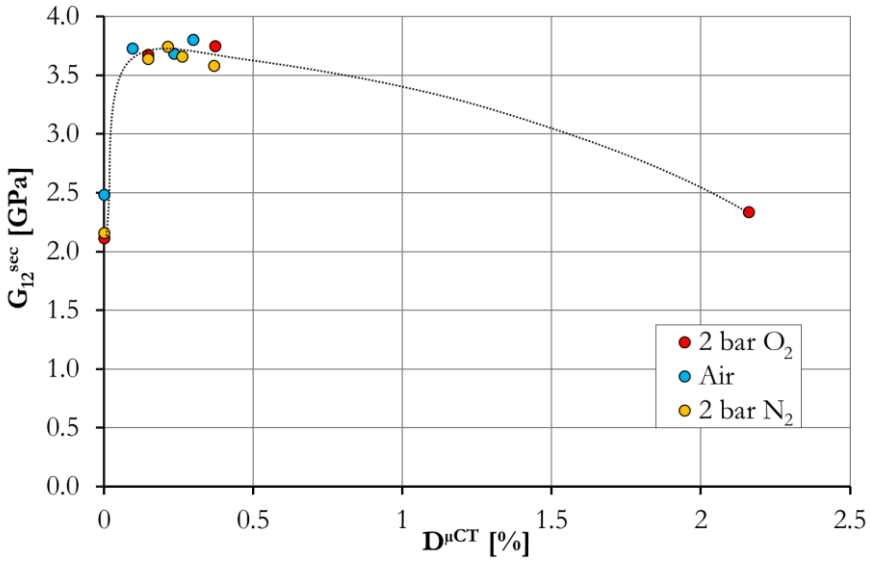

Fig.4. 28 : Evolution of the secant shear modulus as a function of the volumetric crack density for the tested specimen in 2 bar O_2, air and 2 bar N_2 during discontinuous fatigue.

As $D^{\mu CT}$ increases, no noticeable evolution of A is seen. Only for the 2 bar O_2 specimen a slight rise of A occurs when $D^{\mu CT}$ is higher than 2%. *Fig.4. 28* shows the evolution of the secant shear modulus as a function of $D^{\mu CT}$. As for the previous graph, no apparently link exists between G_{12}^{sec} and $D^{\mu CT}$, only for the 2 bar O_2 specimen an important degradation of G_{12}^{sec} is seen when $D^{\mu CT}$ is higher than 2%.

The evolution of the longitudinal chord modulus E_y^{ch} as a function of $D^{\mu CT}$ is reported in *Fig.4. 29*. A continuous degradation of the chord modulus is observed as the $D^{\mu CT}$ increases.

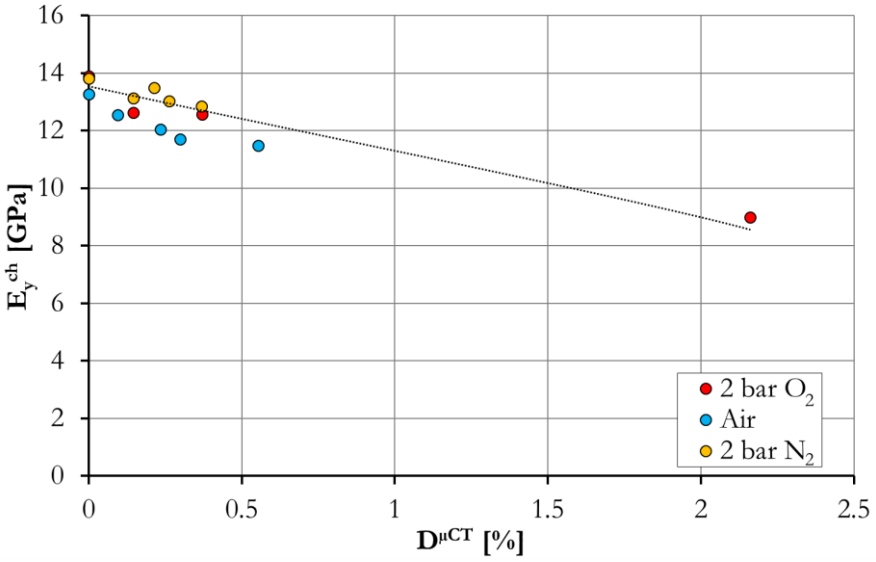

Fig.4. 29 : Evolution of the longitudinal chord modulus as a function of the volumetric crack density for the tested specimen in 2 bar O_2, air and 2 bar N_2 during discontinuous fatigue.

The three data series seem to lie to the same straight, the proposed trend in dotted line in *Fig.4. 29* resumes the supposed linear evolution. Despite this, the points of the three specimens are not perfectly aligned on this straight; in Chapter 5, results issued from further investigation concerning this dispersion are reported.

Finally, the evolution of the longitudinal secant modulus E_y^{sec} is illustrated in *Fig.4. 30* as a function of $D^{\mu CT}$. As for A and G_{12}^{sec} there is not a clear evolution of this properties as the cracked volume increases.

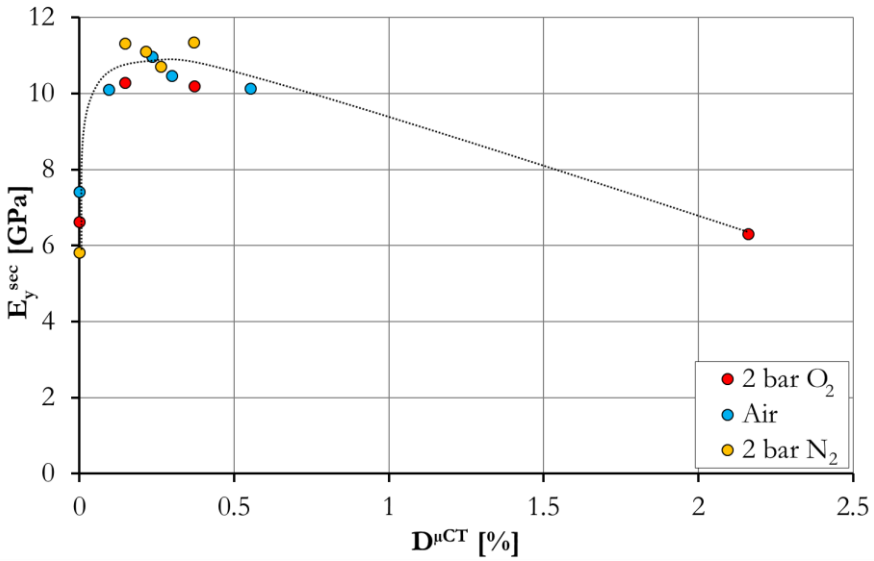

Fig.4. 30 : Evolution of the longitudinal secant modulus as a function of the volumetric crack density for the tested specimen in 2 bar O_2, air and 2 bar N_2 during discontinuous fatigue.

In the graphs in *Fig.4. 27*-*Fig.4. 30* a not clear evolution is depicted for all the specimen properties that are affected by creep effects at the beginning of fatigue. Elastic *modulus* E_y^{ch} is less affected by the non-linearity in the material behaviour, hence could be directly linked to the $D^{\mu CT}$ evolution. After the stabilisation of the material behaviour, a linear degradation as the damaged volume increases could be assumed also for E_y^{sec} and G_{12}^{sec}.

The link between the μCT scan segmentation results and the macroscopic properties degradation needs further investigations, the result of these investigations is reported in Chapter 5.

As noted in Chapter 3, the observed environmentally-assisted fatigue behaviour has its origin from the phenomena taking place at the micro-scale, in turn affected by the environment. In fact (*Fig.4. 31*) the exterior plies of the woven specimens represent two large surfaces potentially degraded by the thermo-oxidation process, in which matrix degradation may promote the acceleration of damage evolution and have a strong impact on the off-axis samples mechanical behaviour. In this case,

contrarily to the cross-ply laminated specimens of Chapter 3, the degradation of the specimen lateral edges, also affected by oxidation phenomena, do not involve important consequences on mechanical behaviour of the whole specimen.

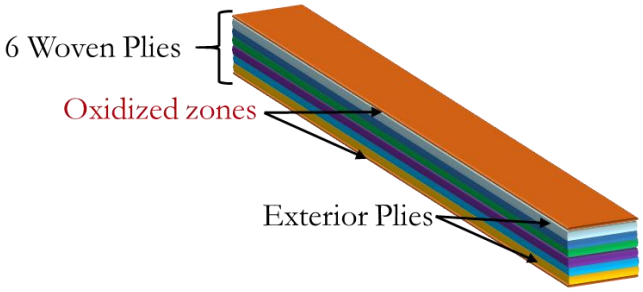

Fig.4. 31 : Schematization of a 6 plies woven specimen. The main oxidized regions are located in the external plies.

Since environmental phenomena can be essentially considered as surface phenomena, again the kinetic of the adimensional indentation modulus measured on the external resin surface, γ_{MAX}, is of interest for the rest of the analysis.

4.5 Environmental effects

The experimental procedure explained in the Chapter 3 for the characterization of the ageing effects on the TACTIX942 matrix, has been used for the characterization of the ageing effects on the resin MVK-14; in this paragraph, only the obtained results are presented in order to introduce how the environment acts on the woven specimens.

The indentation modulus profile is plotted as function of the distance from the exposed pure resin specimen edge in *Fig.4. 32* for two different ageing conditions. *Fig.4. 32**a)*** shows the evolution of EIT for a specimen aged in air at 250°C, while in *Fig.4. 32**b)*** the evolution of EIT for an ageing in 2 bar O_2 at 250°C is reported. These results are issued from (Minervino, 2013), and the general evolution is the same of the TACTIX942 matrix: the EIT of the oxidized surface is higher than the EIT of the virgin resin. Moreover, for the aged specimens, the EIT decreases in the oxidized thickness to achieve the value of the unaged resin at a distance from the exposed edges that grows up with the exposure time. Thus, the oxidized thickness grows up with the ageing time: compared to the characteristic dimensions of the studied woven ply, after 100h in air (less than 24h in 2 bar O_2) the oxidized thickness is bigger than the tow thickness (*cf.* 2.1). The EIT results shown in *Fig.4. 32* for the two ageing conditions are converted in terms of the ageing parameter γ defined in Chapter 3 and the values that this parameter has at 40µm from the exposed surface (γ_{MAX}) are reported in the graph in *Fig.4. 33*.

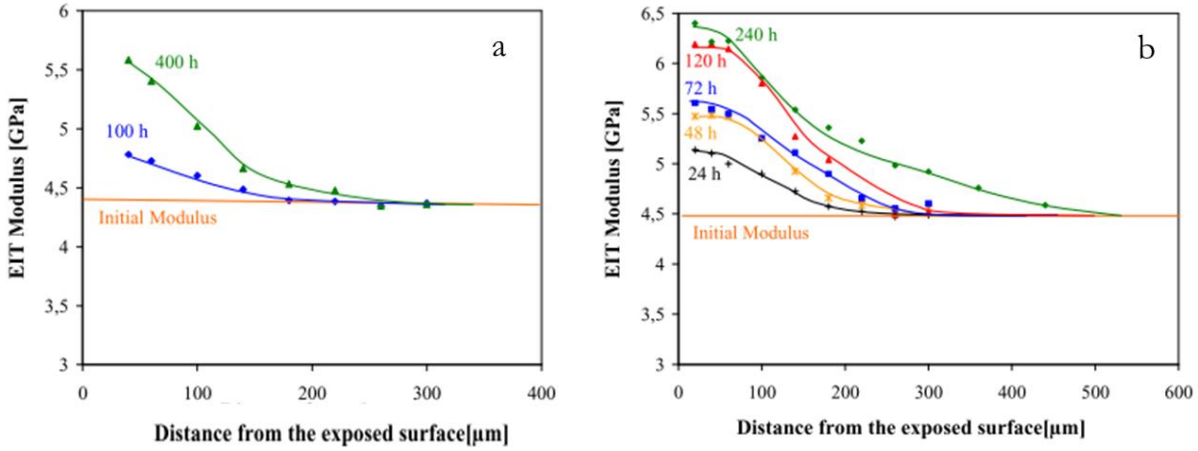

Fig.4. 32 : Indentation modulus evolution as a function of the distance from the exposed surface for pure resin specimens aged under different environmental conditions: ageing in air at 250°C **a)** and ageing in 2 bar O_2 at 250°C **b)**.

As for the TACTIX942 matrix, an interpolation function has been used to fit experimental data, this curve, having the form reported in *Eq.4. 2* is plotted as a line for each ageing condition in *Fig.4. 33* , by substituting the characteristic times reported in *Table 4. 3*.

$$\gamma_{max}(250°C, p, t) = 0.75 - 0.4\exp\left(-\frac{t}{\tau_1(p)}\right) - 0.35\exp\left(-\frac{t}{\tau_2(p)}\right) \qquad \text{Eq.4. 2}$$

	Air	**2 bar O_2**	**Air/2 bar O_2**
τ_1	7000 h	1200 h	5,83
τ_2	310 h	50 h	6,2

Table 4. 3 : Characteristic times for γ_{max} description at T=250°C.

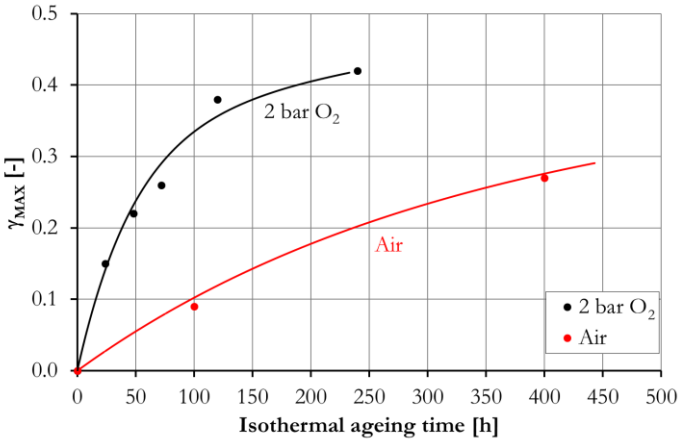

Fig.4. 33 : Evolution of the ageing parameter measured at 40µm from the exposed surface (γ_{MAX}) as a function of the ageing time in 2 bar O_2 and air at 250°C.

The acceleration of the oxidizing process obtained using 2 bar O_2 can be quantified using a scaling factor λ=6, that is an average value between the two characteristic time ratios in *Table 4. 3*. By using a reduced time, as already proposed in Chapter 3, the *Eq.4. 2* becomes:

$$\gamma_{max}(250°C, p, t) = 0.75 - 0.4\exp\left(-\frac{t^*}{7000}\right) - 0.35\exp\left(-\frac{t^*}{310}\right) \quad \text{Eq.4. 3}$$

The obtained master curve is reported in *Fig.4. 34*.

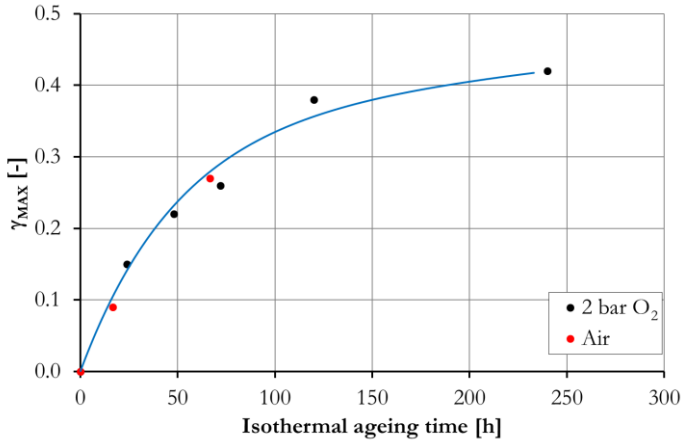

Fig.4. 34 : Master curve describing the evolution of γ_{MAX} as a function of the ageing time in ambient pressure at 250°C for the MVK-14 resin.

The macroscopic properties evolution during fatigue are now re-plotted for the air and the 2 bar O_2 specimen as a function of the ageing parameter values on the exposed surfaces, calculated by substituting to the exposure time, the fatigue test duration taking into account the acceleration factor.

The evolution of the hysteresis area as a function of ageing parameter γ_{MAX} is reported in *Fig.4. 35*.

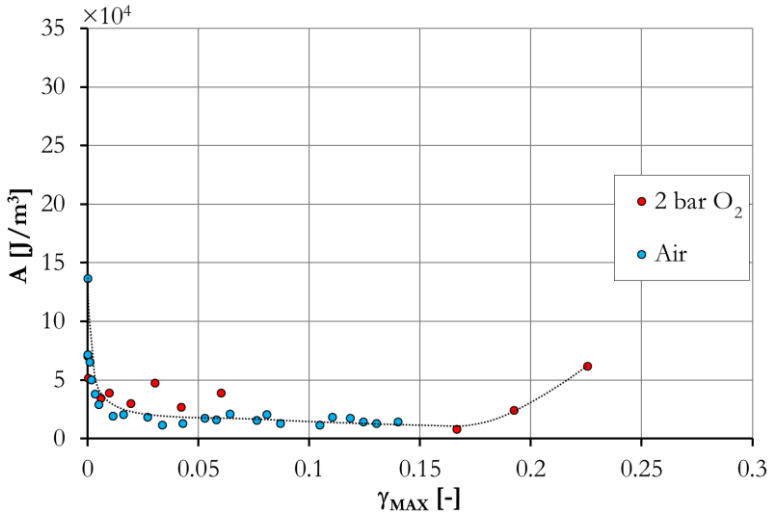

Fig.4. 35 : Evolution of A as a function of the ageing parameter during continuous fatigue tests.

Air and 2 bar O_2 data points are quite close and a master curve is proposed in *Fig.4. 35* to fit the two data series. The existence of a master curve could be also deducted by the graph in *Fig.4. 36* showing the evolution of the secant shear *modulus* as a function of γ_{MAX}.

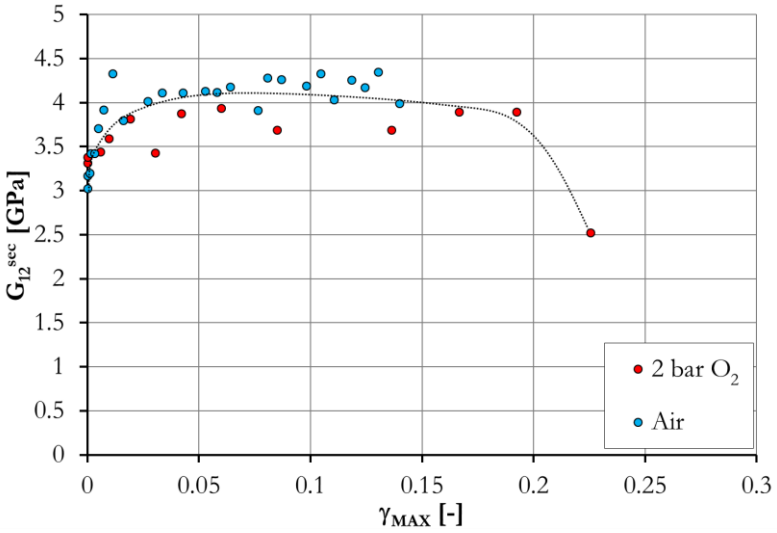

Fig.4. 36 : Evolution of G_{12}^{sec} as a function of the ageing parameter during continuous fatigue tests.

Fig.4. 37 shows the evolution of E_y^{ch} as a function of γ_{MAX}. A quite good correlation is encountered for this mechanical property for the two test conditions. The master curve plotted in the graphs gives a satisfactory description of E_y^{ch} evolution for the two test conditions.

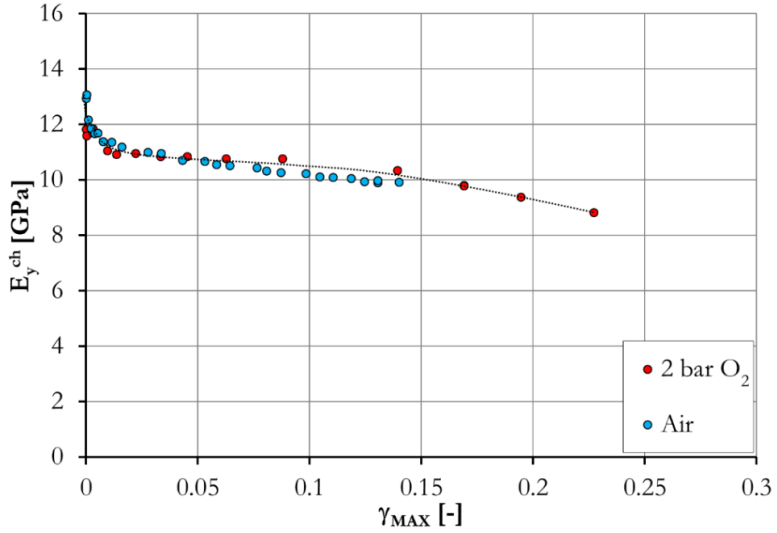

Fig.4. 37 : Evolution of E_y^{ch} as a function of the ageing parameter during continuous fatigue tests.

The secant longitudinal *modulus* evolution described by the master curve illustrated in *Fig.4. 38* is not satisfactory as in the previous graph. The evolution of E_y^{sec} is similar for the two specimens, but, on the other hand, the values are not the same. This could be due to a different material properties

evolution in the first stage of the test, where environment does not have the time to affect material behaviour.

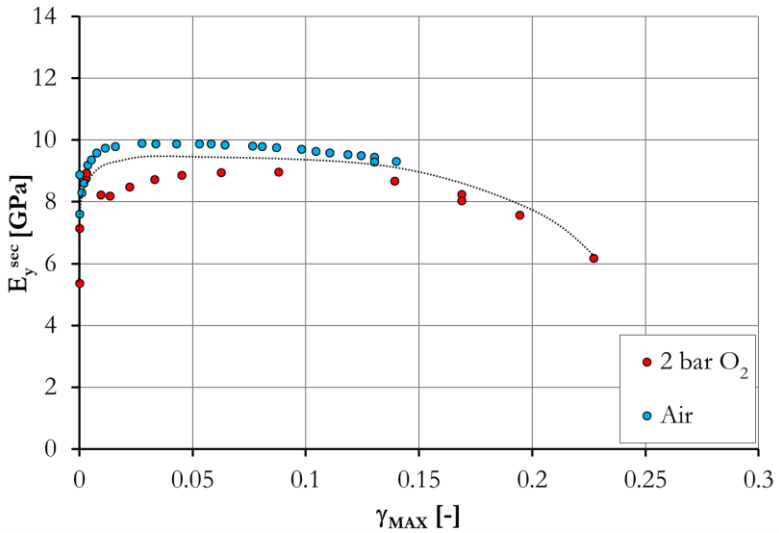

Fig.4. 38 : Evolution of E_y^{sec} as a function of the ageing parameter during continuous fatigue tests.

The fatigue test acceleration performed using aggressive environmental conditions can be quantified looking the evolution of the maximal fatigue strain ε_{MAXy}. This parameter, often used as a degradation index, allows to take into account also creep effects during fatigue. The maximal fatigue strain ε_{MAXy} as a function of γ_{MAX} is reported in *Fig.4. 39*.

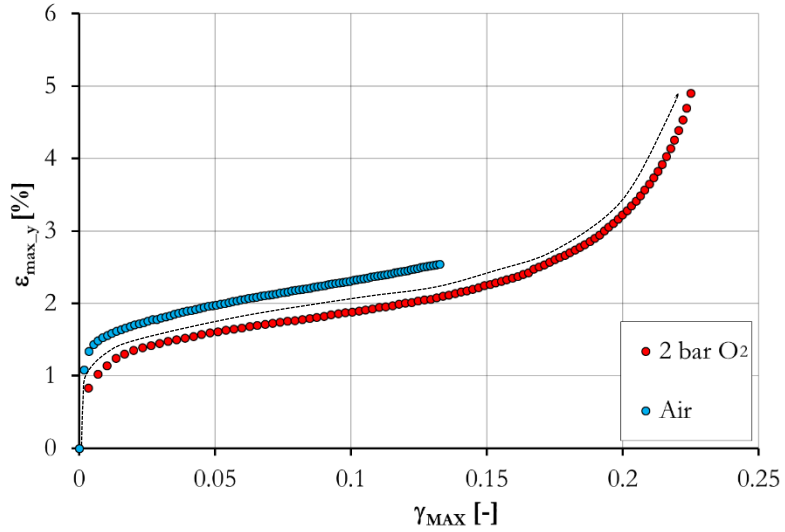

Fig.4. 39 : Evolution of ε_{MAXy} as a function of the ageing parameter during continuous fatigue tests.

The evolution of ε_{MAXy} for the two specimens is similar, but an initial gap between the two point series is visible from the first stage of fatigue and this gap increases as γ_{MAX} increases. Despite this, a

master curve describing the evolution for the two data series is reported in *Fig.4. 39*, but to explain the origin of the highlighted gap, the creep/fatigue interaction has to be take into account.

Crack volume evolution as a function of the ageing parameter γ_{MAX} is shown in *Fig.4. 40*. As for E_y^{ch} the two point series seem to belong to the same master curve.

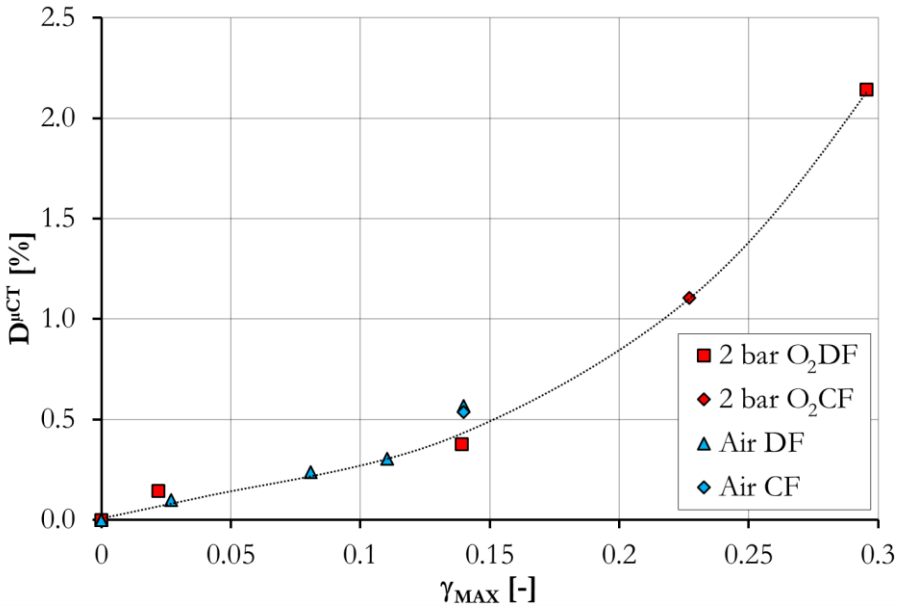

Fig.4. 40 : Evolution of $D^{\mu CT}$ as a function of the ageing parameter during continuous (CF) and discontinuous (DF) fatigue tests for the air and 2 bar O_2 specimen.

The master curves presented in this paragraph show that the ageing parameter can be used as an index to describe the oxidation effects on the woven composite. This scaling parameter, in particular, perfectly matches the evolution of the elastic longitudinal *modulus* and the damage evolution $D^{\mu CT}$. Consequently, an acceleration of the fatigue test performed in air can be obtained by testing specimens in 2 bar O_2. Looking the master curves in the graphs *Fig.4. 35* - *Fig.4. 40* could be concluded that the thermo-oxidation process of the resin promotes the damage development on the exposed surfaces accelerating the specimen degradation.

The graph in *Fig.4. 39* shows a link between the maximal longitudinal strain and the ageing parameter. A deeper investigation on the creep/fatigue interaction of the tested specimens is proposed in the next section to study separately the creep effects and the environmental effects on fatigue. A good comprehension of these aspects leads to a detailed explanation of the not clear maximal strain evolution shown in *Fig.4. 39*.

The link between damage accumulation and ageing parameter suggests a test protocol for the woven specimens similar to the test protocol developed for the cross-ply UD laminates in the Chapter 3 to perform accelerated fatigue tests:

- identification of the ageing parameter evolution on pure resin samples for different environmental test conditions;
- realization of environmentally-assisted fatigue tests fatigue tests under the same environmental conditions.

4.6 Creep-fatigue-environment interaction

In this paragraph, the results of the investigation on the evolution of the *maximum* longitudinal strain ε_{MAX_y} (*see Fig.4. 11*) during fatigue is presented. During fatigue, the evolution of the longitudinal strain is strongly affected by the creep/fatigue interaction; this is highlighted also looking at *Fig.4. 39*, where the environmental effect on the evolution of the ε_{MAX_y} is not adequately described using only the ageing parameter γ_{MAX}.

In the literature the creep effect during fatigue is well known, for example in (Petermann and Schulte, 2002) the interaction fatigue-creep is evaluated discerning the maximum fatigue strain in two parts: a contribution due to creep dependent on the time and on the mean fatigue stress, and a second part, strictly correlated to fatigue that is a function of the mean fatigue stress, of the fatigue load amplitude and of the number of cycles *N*.

In the analysis proposed in this paragraph, if no damage is detected during creep tests, the maximum fatigue strain ε_{MAXy} can be considered as the sum of three contributions:

- a contribution linked to the visco-elasto-plastic part related to test duration and mean fatigue load (ε_{creep_y});
- a second contribution taking into account fatigue damage and dependent on the maximum fatigue load (σ^{f}_{max}), the number of cycles (*N*) and the environmental conditions (ε_{D_y});
- a third contribution ($\varepsilon^{f}_{vep\_y}$) related to the visco-elasto-plastic strain cumulated during fatigue and dependent on the maximum fatigue load (σ^{f}_{max}) and the number of cycles (*N*).

$$\varepsilon_{MAX\_y} = \varepsilon_{creep\_y} + \varepsilon_{D\_y} + \varepsilon^{f}_{vep\_y} \qquad \text{Eq.4. 4}$$

Creep tests have been performed on $[45_6]$ specimens under the same three environmental conditions used for fatigue tests. The duration and the temperature of the creep tests is the same used for the fatigue tests and the applied load is the mean fatigue load as shows *Fig.4. 41*.

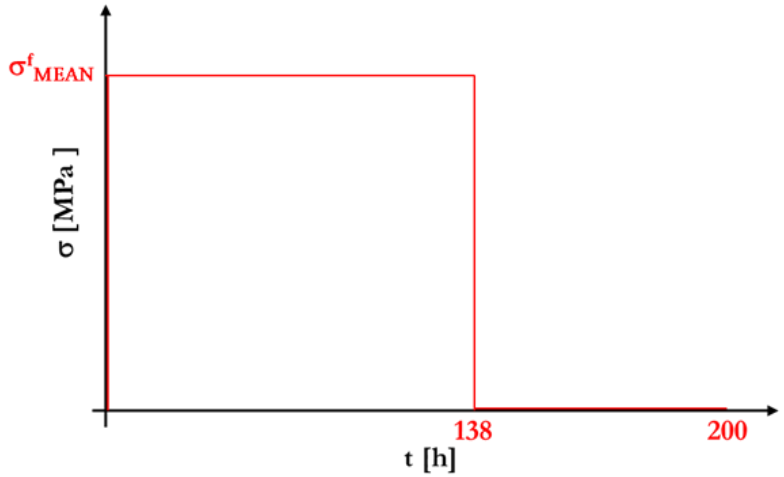

Fig.4. 41 : Creep test cycle. The maintain time is the same of the fatigue tests, while the maintain stress is the mean fatigue stress.

During the tests, the strain values have been obtained by DIC using the mean values of the strain fields as explained in Chapter 2. Results of creep tests are illustrated in *Fig.4. 42*.

For the three specimens, an instantaneous strain is recorded as the load is applied and the longitudinal deformation increases until the end of the maintain stage. In *Fig.4. 42*, one can see that after 12h the 2 bar O_2 specimen behaviour differs from the other two specimens. In the same manner, after 30h, also the air and the 2 bar N_2 specimen show a slight different behaviour. After load removing, all the specimens exhibit an instantaneous strain reduction followed by a slower recovery stage. Some relevant strain values of the creep tests are in *Table 4. 4*.

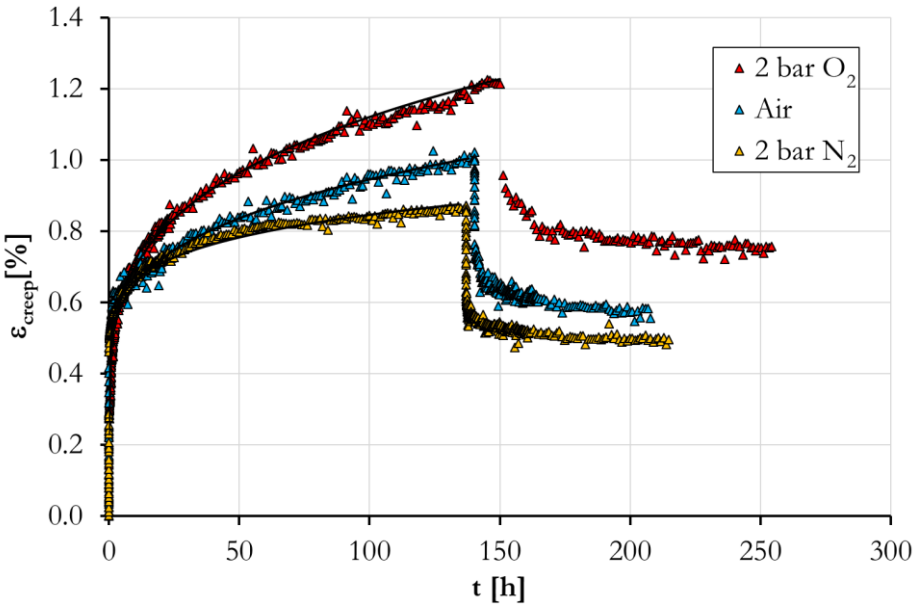

Fig.4. 42 : Creep results at 250°C on woven $[45]_6$ specimens under 2 bar N_2, air and 2 bar O_2.

	Instantaneous strain on loading [%]	Total cumulated strain [%]	Instantaneous strain recovered on unloading [%]	Time under recovery [h]	Residual strain after recovery [%]
2 bar O_2	0.23	1.21	0.26	103	0.75
Air	0.34	1.02	0.28	66	0.58
2 bar N_2	0.27	0.87	0.27	77	0.49

Table 4. 4 : Creep test values at 250°C on woven [45_6] specimens under 2 bar N_2, air and 2 bar O_2.

The environmental effects are not visible in the first stage of creep. In the first column of *Table 4. 4* the response of the specimens loaded in traction is almost the same for all the environmental conditions. A relevant difference in total strain at the end of the maintain stage is appreciable looking the second column in *Table 4. 4*. After 138/150h the total strain for the 2 bar O_2 specimen is higher than the total strain of the air specimen which in turn is higher than the total strain of the 2 bar N_2 specimen. The response of the three specimens during the unloading stage seems to be not affected by environment, the differences between the residual strains at the end of the recovery have the same magnitude of the differences at the end of the maintain time. In conclusion, the visco-elastic response of the specimens is not affected by the environmental conditions, while is not the same for the permanent part of the strain. The permanent deformation in 2 bar N_2 specimen is not due to environmental effects, but is linked to the material response and to the specimen architecture. Fibre rotation and matrix micro-cracking due to initial traction load could take part to the longitudinal deformation of the specimens, and these effects are present in all the three tested specimens.

The data-points in *Fig.4. 42* give a clear evolution of the strain as function of the maintain time, but a mathematical function describing this evolution may be useful in terms of temporal smoothing. The creep curves could be approximated using the Nutting's parameters (Nutting, 1921) allowing describing the evolution of creep strain using a simple power law function during the maintain time:

$$\varepsilon_{creep\_y}(\sigma, t) = \varepsilon_0(\sigma) + K\,\sigma^m t^n \qquad \text{Eq.4. 5}$$

where ε_0 is the instantaneous strain on loading and *K*, *m* and *n* are function parameters. For the creep results reported in *Fig.4. 42* the best-fit parameters are reported in *Table 4. 5* and the interpolating functions are shown in black lines in *Fig.4. 42*.

	ε_0	K	m	n
2 bar O_2	0.23	3.34×10^{-9}	5	0.278
Air	0.34	2.18×10^{-9}	5	0.287
2 bar N_2	0.27	3.59×10^{-9}	5	0.167

Table 4. 5 : Nutting's parameters for interpolation of creep data during maintain time.

No damage on the tested specimens has been detected after creep tests. This validate the use of *Eq.4.4*, allowing to continue with the identification of the two remaining terms of *Eq.4. 4*.

Data in *Table 4. 5* have been employed for the calculation of the $\varepsilon_{D\_y}+\varepsilon^f_{vep\_y}$ for each specimen tested in continuous fatigue starting from the ε_{MAX_y} obtained during fatigue (*see Fig.4. 11*) and using *Eq.4. 4*. The results are reported in *Fig.4. 43*. In *Fig.4. 43* ***a)*** the ε_{MAX_y}, the ε_{creep_y} and $\varepsilon_{D\_y}+\varepsilon^f_{vep\_y}$ are reported for the 2 bar N_2 specimen. As already explained, $\varepsilon_{D\_y}+\varepsilon^f_{vep\_y}$ is obtained by subtracting to ε_{MAX_y} the longitudinal strain due to creep ε_{creep_y}. In *Fig.4. 43* ***b)*** the $\varepsilon_{D\_y}+\varepsilon^f_{vep\_y}$ evolution for the three tested specimens has been plotted.

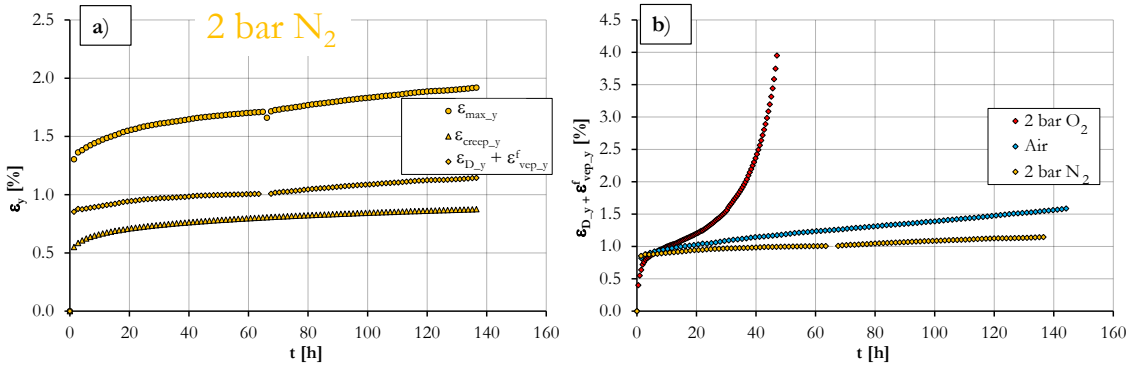

Fig.4. 43 : Evolution of the longitudinal strain due to creep, fatigue and fatigue damage under 2 bar N_2 (**a**)) and evolution of the longitudinal strain due to fatigue damage for the three specimens tested in continuous fatigue (**b**)).

In order to separate the two contributions $\varepsilon_{D\_y}+\varepsilon^f_{vep\_y}$ for the three specimens, the evolution of the $\varepsilon_{D\_y}+\varepsilon^f_{vep\_y}$ as a function of the global volumetric crack density measured on the *discontinuous fatigue* specimens is plotted in *Fig.4. 44*. The initial value on the graph could be related to an instantaneous strain accumulation linked to the maximum fatigue load and not to damage. Starting from this initial strain value, a linear relation can be assumed between the μCT measured damage and the macroscopic longitudinal strain evolution. A master curve having the form reported in *Eq.4. 6* can be plotted to describe the evolution of the strain $\varepsilon_{D\_y}+\varepsilon^f_{vep\_y}$ independently on the test environment.

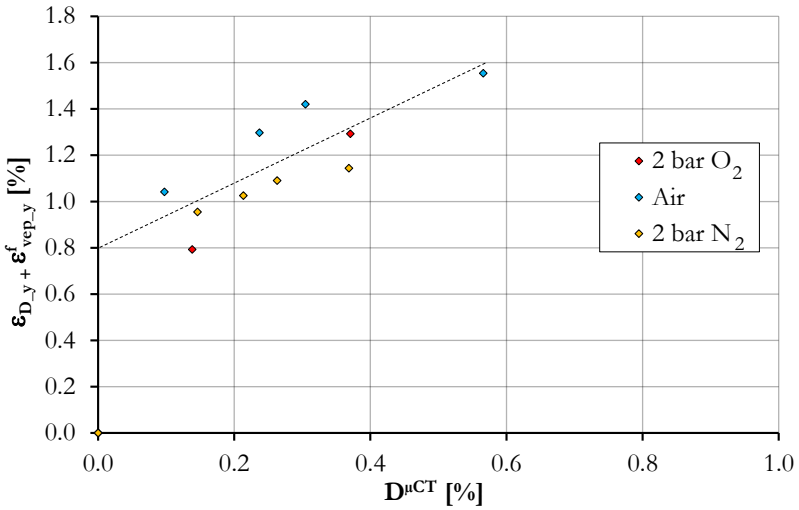

Fig.4. 44 : Evolution of the longitudinal strain ε_{D_y} for the 2 bar N_2 air and 2 bar O_2 specimens.

The value on the vertical axis for $D^{\mu CT}=0$ could be associated to the terms $\varepsilon^f_{vep\_y}$ in the presented analysis, it is supposed to not evolve during fatigue and its value is $\varepsilon^f_{vep\_y}=0.8\%$. The slope of the straight in *Eq.4. 6*, B, gives the weight of the volumetric crack density on the damage related strain. This slope is not dependent on the environmental conditions and for the graph in *Fig.4. 44*, its value is B= 1.34.

$$\varepsilon_{D\_y} + \varepsilon^f_{vep\_y} = B \times D^{\mu CT} + 0.8 \qquad \text{Eq.4. 6}$$

The terms ε_{D_y} is dependent only on the volumetric crack density measured on the specimen; being the volumetric crack density evolution for the air and the 2 bar O_2 specimen, linked to the environmental conditions by the ageing parameter γ_{MAX} (*see Fig.4. 40*), independently from the test conditions, the ageing parameter γ_{MAX} can be used to rescale the results concerning the ε_{D_y} evolution. The plot in *Fig.4. 45* has been obtained by rescaling the evolution of ε_{D_y} as a function of the ageing parameter. The superposition of the ε_{D_y} for the two specimens confirms the environmental effect in damage development during fatigue. In *Fig.4. 45*, the evolutions of ε_{D_y} for the air and the 2 bar O_2 specimen are superposed until the end of the test, the maximal difference seen in the graph between the air strain and the 2 bar O_2 strain is under the cumulated DIC measurement accuracy. Comparing this result with the damage scenario shown in 4.4.2, the air specimen reaches γ_{max} = 0.13 after 970k cycles, while the 2 bar O_2 specimen, after 140k cycles; the damage scenarios illustrated in *Fig.4. 22* - *Fig.4. 25* for air and 2 bar O_2 specimen are quite similar until 170k cycles, while for the following stops, the damage scenario considerably changes: for the air

specimen the cracks lie mainly to the external layers, while for the 2 bar O_2 specimen, little cracks appear also in the more interior layers.

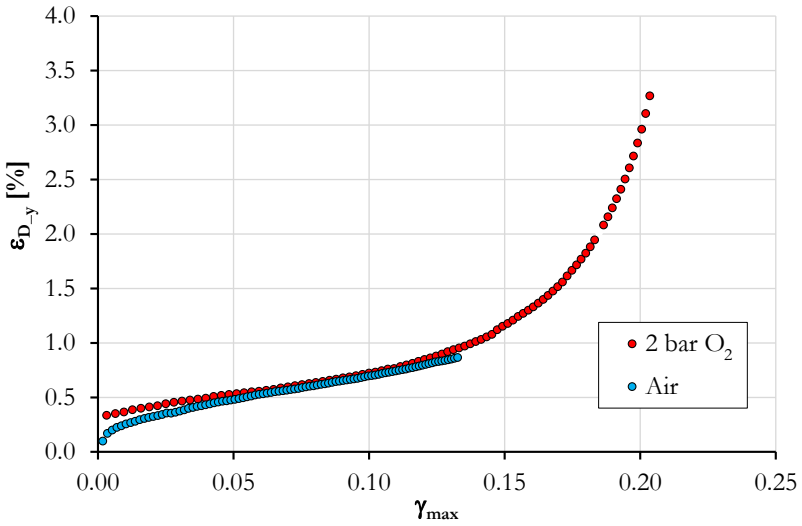

Fig.4. 45 : Evolution of ε_{D_y} as a function of the aging parameter γ_{MAX}.

On the other hand, the superposition of ε_{D_y} for the air and the 2 bar O_2 specimens in *Fig.4. 45* proves that, for the presented experimental campaign, interactions between creep and fatigue damage during fatigue tests is negligible: the environmental role and the creep response of the specimens during fatigue can be decomposed as sum of the various effects. The strain ε_{D_y} could be associated to the deformation related to opened crack that, due to friction, cannot re-close.

The schematization employed demonstrates that during fatigue in oxidizing environment, the ageing parameter allows having a time rescaling of the macroscopic properties evolution and of the volumetric crack density. Alternatively, an evaluation of the specimen degradation by using the maximum fatigue strain, has to take into account the viscous nature of the material. This last can be not rescaled using the ageing parameter because is a function of the test duration.

To conclude the evolution of the maximum fatigue strain ε_{MAX_y} can be written as:

$$\varepsilon_{MAX\_y} = \varepsilon_0(\sigma) + K\,\sigma^m t^n + \varepsilon^f_{vep\_y} + B \times D^{\mu CT} \qquad \text{Eq.4. 7}$$

In *Eq.4. 7* some terms are linked to material properties, fibre architecture and test parameters (stress, time …). These terms are the same for the three tested specimens: from *Table 4. 5* one can see that ε_0 and m are material dependent parameters as well as the coefficient B in *Eq.4. 6* that link the volumetric crack density to the accumulation of plastic strain. The remaining parameters are

associated to the environmental test conditions, in particular the presence of oxygen accelerates at the same manner the evolution of the creep and of the maximum fatigue strain as proved looking at *Fig.4.45*.

4.7 Conclusion

The environmental effects on the behaviour of a woven specimen have been observed and quantified in this chapter. DIC has been used to measure strain field during fatigue test at 250°C in controlled environment and the analysis of the load and strain data allowed evaluating some mechanical elastic (E_y^{ch}) and secant (E_y^{sec}, G_{12}^{sec}) specimen properties as well as the area (A) of the hysteresis loops, while data issued from the test machine allowed tracing the evolution of the maximum strain (ε_{MAX_y}) during fatigue for the continuous fatigue tests.

Creep/fatigue interaction affects the response of the tested specimens during fatigue. This can be observed looking at the evolution of the hysteresis loops of the load/unload cycles performed stopping the fatigue test at predefined number of cycles or equally from the evolution of the secant properties at the beginning of fatigue. Moreover, during fatigue a degradation of the mechanical properties is observed for the 2 bar O_2 specimen that fails before the predefined maximum test duration, while only longitudinal properties show a clearly degradation for air and 2 bar N_2 specimen.

Fatigue tests have been repeated for the analysis of the environmental effect at the micro-scale. For this purpose fatigue tests have been periodically interrupted in order to perform μCT scans. It has been shown that fatigue test interruptions do not involve parasite effects on the macroscopic specimen response. Image segmentations performed on the μCT scans reveal a different damage scenario of the 2 bar O_2 specimen compared to air and 2 bar N_2 specimen: after 170k cycles little cracks onset on the lateral specimen edges, while for the other two specimens the damage remains narrowed in the external plies. μCT scan segmentation allows establishing that the main damage forms for the tested specimens are intra-tow matrix cracks: these cracks are oriented as the belonging tow and does not propagate in the surrounding tows. A global evaluation of the damaged volume is proposed by using a volumetric crack density: the evolution of the volumetric crack density during fatigue highlights the strong environmental role in damage apparition for the tested specimens, it has been shown that during fatigue the cracking rate for the 2 bar O_2 specimen is greater than the cracking rate observed for the air and 2 bar N_2 specimen.

From the macro-scale properties plotted as a function of the volumetric crack density is difficult to evaluate the micro-scale damage effect on the macro-scale properties evolution. Except the elastic

longitudinal *modulus*, the macroscopic properties show an evolution in which the creep affects the measured values, followed by a stage where the degradation can be associated to damage. Only for the 2 bar O_2 a significant evolution is remarked, while a not evident evolution appears for the specimen tested in the other two environmental conditions. The elastic longitudinal *modulus* shows a constant decrease rate, but for a given value of the volumetric crack density, the elastic *moduli* of the three specimens have not the same values.

As made for the cross-ply laminated composite of the Chapter 3, the ageing parameter, resuming the thermo-oxidation effects on the composite resin, has been used to correlate air and 2 bar O_2 results in terms of macro scale properties evolution and micro scale damage development. Mechanical properties evolution as well as micro scale damage accumulation for air and 2 bar O_2 specimen lie to the same master curve when plotted as a function of the ageing parameter: excluding the initial evolution (no environmental effect expected in early stage of fatigue), the ageing parameter describes in a satisfactory manner the remaining part of the graphs in terms of environmental effects.

A not clear evolution has been depicted for the maximum strain accumulated during fatigue. The knowledge of the evolution of this parameter is necessary to realize structural parts using the tested material. Consequently, a more detailed study about the environment-creep-fatigue interaction has been proposed in the last part of the chapter. It has been shown that the maximum strain cumulated during fatigue is a sum of three contributions: one strictly linked to the creep load during fatigue, a second one that is a function of the damage accumulation during fatigue and a third, dependent on the maximum fatigue load. The dependence of these terms on the material properties, test conditions and test environment has been investigated.

Finally, to describe the behaviour of the specimens up to failure it should be remarked that:

- the hysteresis area A, decreases during the early stage of fatigue until a value kept until the end of the test, except close to specimen failure (*see* 2 bar O_2 specimens);
- after the initial evolution, the observed macroscopic properties decrease as the volumetric crack density increases;
- the evolution of the *maximum* fatigue strain during fatigue is related to the creep load during fatigue and to damage accumulation during fatigue.

Consequently, an analytical model describing the tested specimen behaviour should include:

- an elasto-damage response of the specimens that can be identified by the knowledge of the elastic response of the virgin specimen, the crack volume and the micro-scale damage effect on the macroscopic properties;

- the visco-elasto-plastic strain evolution during fatigue test. From creep tests it has been remarked that this term can be split in a part affected by the damage development (and consequently by the environmental conditions), and a second one, representing the visco-elasto-plastic strain evolution due to fatigue load.

For a deeper understanding of the damage effect on the macro-scale response of the specimen, in the next chapter, an analytical model has been developed to describe the elasto-damage behaviour of the tested material. Consequently, the model will be not able to describe the creep/fatigue interaction.

Chapter 5

A deeper damage investigation: towards an analytical model for macroscopic properties degradation

A different damage representation is presented in this chapter: the global volumetric crack density is replaced by a damage matrix taking into account the crack orientations and the *through the thickness* crack distribution. From a detailed damage description, given in the first part of the chapter, the damage matrix is obtained and the degraded properties of the specimens are calculated via an existing analytical model. In this model, the damage is introduced as a directly measured crack volume and not using internal damage variables. The presented elasto-damage model is then employed in the development of a possible way for a damage tolerant approach in a part design. The end of the chapter is consecrated to the presentation of a damage quantification technique via DIC optimised for the tested material.

Summary

As shown in the previous chapter, the evolution of the macro-scale properties, after a stabilization stage, can be described using an elasto-damage model. This kind of model could give a description of the specimen properties degradation, but is not able to predict the failure that, as shown in Chapter 4, is dependent also on the creep/fatigue interaction. The volumetric crack density $D^{\mu CT}$ introduced in Chapter 4 gives a global quantification of the crack volume for each specimen. This description does not provide information about crack location, shape and orientation and for this reason is not suitable for an appropriate micro scale damage quantification in an analytical model. In the next paragraph, a more detailed description of the specimen damage is proposed in order to obtain a damage description useful in an elasto-damage analytical model.

5.1 Crack shape and distribution

In order to obtain a more useful damage characterization than the volumetric crack density, some information as the crack shape, orientation and position are needed. *Fig.5. 1* shows a 3D μCT reconstructed image of a damaged woven specimen. The zoom on the XZ and on the XY planes shows that the main damage form is intra-tow cracks and the cracks are principally narrowed in the external tows, as already observed in the previous chapter.

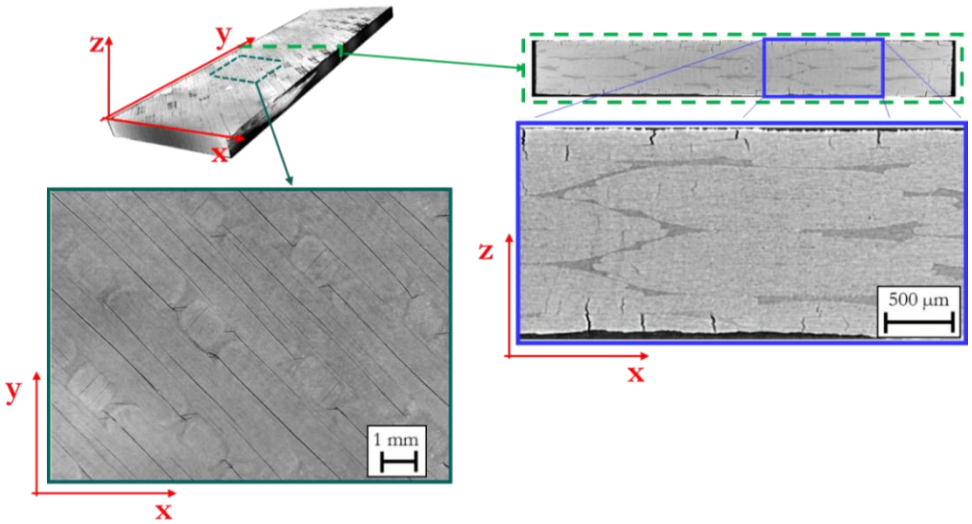

Fig.5. 1 : 3D image reconstruction. Two cut planes show typical intra-tow crack shape, location and dimensions: the cracks are oriented in the same direction of the belonging tow, furthermore cracks in surface tows are more opened than internal cracks.

Further information issued from *Fig.5. 1* are related to cracks shape: each crack is preferentially oriented in the belonging tow direction, and does not propagate through the specimen thickness. The segmentation procedure adopted for crack segmentation allows separating the crack volume for each tow direction and for each ply. This separation, taking into account the through the thickness damage distribution, leads to a more detailed damage quantification. As illustrated in *Fig.5. 2* each ply of the

woven is split in two semi-plies and for each semi-ply the tows are oriented along a preferential direction. In *Fig.5. 2* the woven plies are enumerated from one to six. The first and the sixth plies are the external plies, while the plies from two to five are internal plies. Moreover, in the first ply, the semi-ply oriented along the -45° direction is the semi-ply directly exposed to the environment, while, for the sixth ply, is the +45° semi-ply to be exposed to the environment.

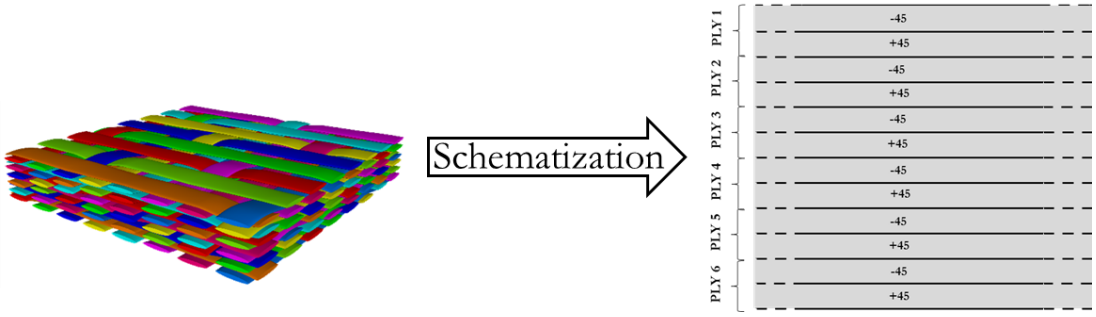

Fig.5. 2 : Woven architecture schematization. Each ply is split in two semi-plies having the tows oriented in one direction. For the tested specimens each ply is divided in -45° and +45° semi-plies.

This schematization of the woven specimen in twelve semi-plies is used in *Fig.5. 3* to represent the damage volume evolution along the z (*through the thickness*) direction of the specimen.

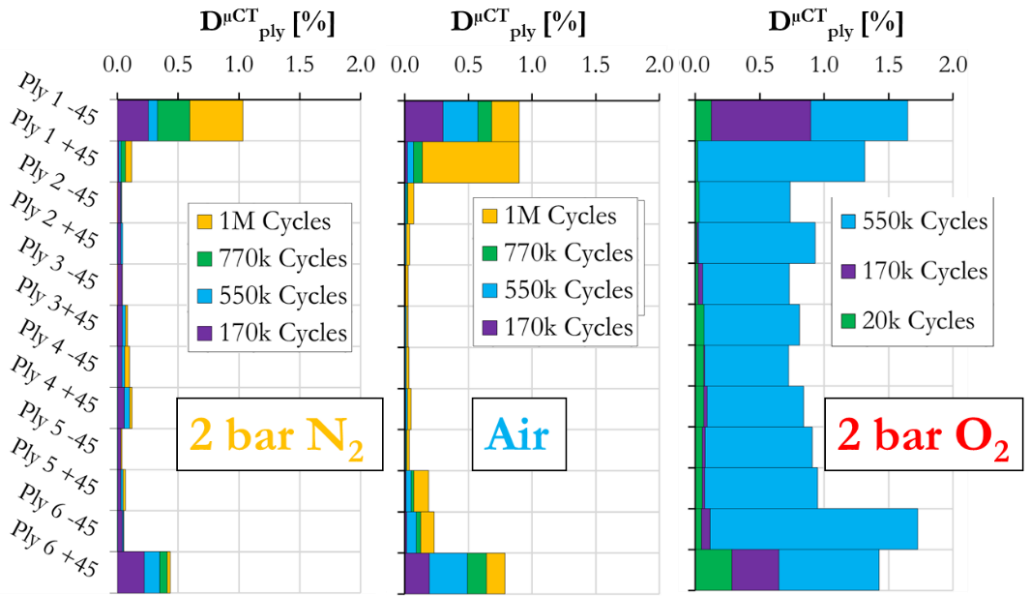

Fig.5. 3 : Through the thickness crack distribution for the three environmental test conditions. The vertical axis represents the vertical position of each ply.

On the vertical axis of the histograms in *Fig.5. 3* the volumetric crack density for each single semi-ply calculated as in *Eq.5. 1* is reported.

$$D_{ply}^{\mu CT} = \frac{V_{semi-Ply}^{CRACKS}}{V_{Ply}^{TOT}} \qquad \text{Eq.5. 1}$$

where $V^{CRACKS}_{semi\text{-}Ply}$ is the crack volume in one of the two main ply fibre directions and V^{TOT}_{Ply} is the volume of the whole ply. The damage distribution along the through the thickness direction resumed in the histograms of *Fig.5. 3* confirms the considerations made for *Fig.5. 1*: for each test condition, the damaged volume is concentred in the tows directly exposed to the environment. For the 2 bar N_2 and air specimen the cracks are mainly confined on the external semi-plies until the end of the test, while for the 2 bar O_2 specimen, the last μCT scan reveals that a consistent crack volume is located also in the internal plies.

Fig.5. 4 shows a typical intra-tow crack shape. The tow dimension (t_T and w_T) are reported in *Table 2.2*. The crack height generally corresponds to the tow thickness, in other words, an intra-tow crack separates the tow in two parts.

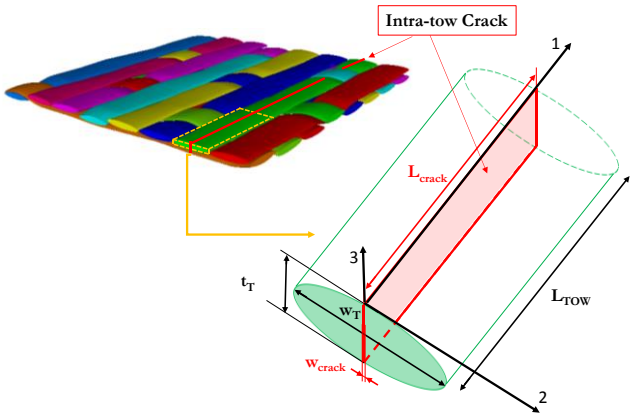

Fig.5. 4 : Schematic representation of crack shape. The elliptical tow is divided in two parts by a crack.

The crack width (w_{crack}) is strictly correlated to the scan resolution and the image contrast. The μCT scan resolution and the image processing allow identifying crack having a width two/three times the μCT image resolution (17.5/26.3 μm). Consequently, cracks having a width smaller than the detectability threshold could exist, but the observation mean resolution is not enough to see them. The crack length (L_{crack}) is different for each crack and grows up during fatigue until its maximum value *i.e.* the tow length (L_{TOW}). The crack shape of the internal plies of the 2 bar O_2 specimen after 550k cycles is slightly different from the surface cracks: internal ply cracks have the same width and height of a surface crack, but their length is generally smaller than a surface crack, as shown in *Fig.4.25*. Internal ply cracks are generally narrowed the lateral edges of the specimen, only few cracks have been detected far from the lateral specimen edges.

The damage at the ply-scale quantified by μCT scan segmentation has been observed by optic microscope to understand which could be the driving forces. Two surface observations are shown in *Fig.5. 5*. The pictures in *Fig.5. 5* are referred to an air and a 2 bar O_2 specimen. Little matrix cracks in resin regions between two adjacent fibres onset and propagate in the direction perpendicular to the

applied load direction. This micro crack propagation is limited by the fibre presence, hence the increasing damage is related to micro cracks multiplication. When the micro crack density reaches a critical value, they coalesce forming a single meso crack oriented in the fibre direction.

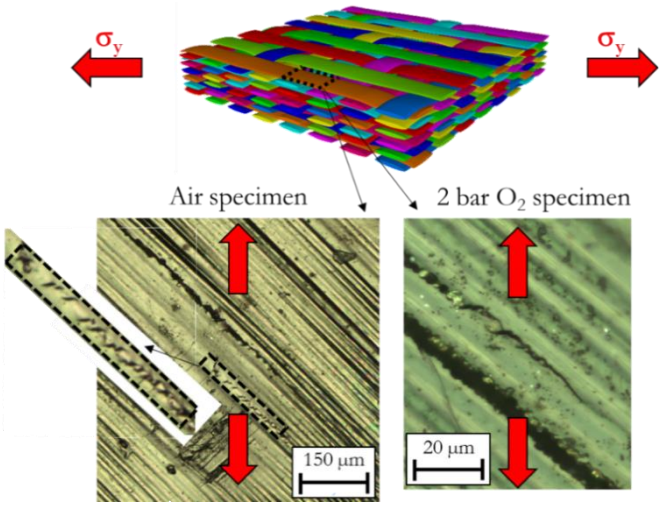

Fig.5. 5 : Intra-tow cracks in air and 2 bar O_2 specimen. Resin micro cracks onset in the matrix region between fibres, then coalesce to form a single meso crack oriented as the tow fibres.

The crack apparition driving forces seem to be the same in both the cases: as explained in (Talreja, 1981) the three damage forms of each ply are the fibre failure, the matrix cracking and the fibre/matrix debonding; the latter two mechanisms are difficult to separate, but the driving force are the same: the transverse and the shear stresses. The micro crack multiplication has been already described in (Quaresimin, Carraro and Maragoni, 2016) where the driving force is a combination of the transverse and the shear stresses in the ply. The crack coalescence mechanism is described in the same publication and also in (Sket et al., 2015). These work jointly with the observations in *Fig.5. 5* suggest the introduction of a new damage representation including the damage orientation information. A damage matrix D_{UD} is thus proposed as reported in *Eq.5. 2*, where D_{22} and D_{66} link the crack volume oriented along the direction normal to the axis 2 (see *Fig.5. 4*) to the loss of transverse and shear rigidity of the tow respectively. Along the fibre direction, crack do not affect the longitudinal stiffness, thus $D_{11}=0$.

$$D_{UD} = \begin{bmatrix} 0 & 0 & 0 \\ 0 & D_{22} & 0 \\ 0 & 0 & D_{66} \end{bmatrix} \qquad \text{Eq.5. 2}$$

The volumetric crack distribution detailed in this paragraph and the presented new damage description, are employed in the next paragraph to develop an analytical model allowing calculating the specimen mechanical properties starting from the measured crack density. The aim of this analysis is the interpretation of the link between the crack density evolution and the elastic properties degradation. In

the next paragraphs the scalar damage quantification has been replaced by a matrix taking into account the crack orientation. Moreover, the *ply-by-ply* damage quantification allowed to introduce information about the crack localization in the analytical model.

5.2 Analytical model for macro scale properties degradation

This paragraph is devoted to the presentation of the analytical model describing the sample properties evolution starting from the knowledge of the crack volume measured by μCT scan segmentation. The specimen constitutive law can be written as:

$$\boldsymbol{\sigma} = \mathbf{Q}(\mathrm{D})(\boldsymbol{\varepsilon} - \boldsymbol{\varepsilon}_{cf} - \boldsymbol{\varepsilon}_{th}) \qquad \text{Eq.5. 3}$$

where in $\boldsymbol{\varepsilon}_{cf}$ are included all the creep/fatigue interaction strain contributions already analysed in 4.6 while, $\boldsymbol{\varepsilon}_{th}$ take in account the thermal residual strain due to the forming process of the specimens. In this paragraph the discussion is focused on the terms $\mathbf{Q}(\mathrm{D})$, to describe the elasto-damage behaviour of the specimens observed for a large part of the fatigue tests. The proposed strategy is to split the woven specimens in 6 virtual woven plies. Each ply is in turn divided in two semi-plies, as made for the damage description in the *trough the thickness* direction in *Fig.5. 3*. In each semi-ply all the fibres are oriented in the same direction and so locally, a semi-ply can be considered as an UD lamina having the mechanical properties calculated as follows.

Woven virtual ply

The lamina local coordinate system is reported in *Fig.5. 6*: the direction 1 is aligned with the fibre direction, the direction 2 is the transversal to the fibre direction and the third direction is the out-of-plane direction.

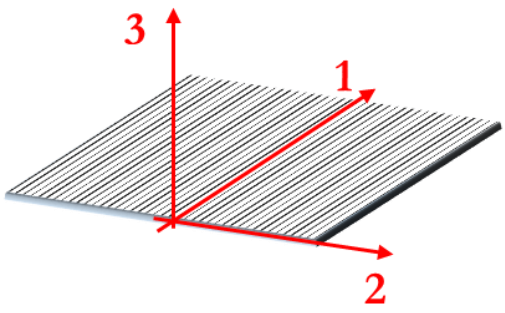

Fig.5. 6 : UD lamina and principal coordinate system.

The stiffness matrix for the lamina in *Fig.5. 6* can be expressed in the principal material coordinates, using the plane stress condition as:

$$Q_{UD} = \begin{bmatrix} Q_{11} & Q_{12} & 0 \\ Q_{12} & Q_{22} & 0 \\ 0 & 0 & Q_{66} \end{bmatrix} \quad \text{Eq.5. 4}$$

where:

$$Q_{11} = \frac{E_1}{1 - \upsilon_{12}\upsilon_{21}} \quad \text{Eq.5. 5}$$

$$Q_{22} = \frac{E_2}{1 - \upsilon_{12}\upsilon_{21}} \quad \text{Eq.5. 6}$$

$$Q_{12} = \frac{\upsilon_{21}E_1}{1 - \upsilon_{12}\upsilon_{21}} = \frac{\upsilon_{12}E_2}{1 - \upsilon_{12}\upsilon_{21}} \quad \text{Eq.5. 7}$$

$$Q_{66} = G_{12} \quad \text{Eq.5. 8}$$

$$\frac{E_2}{\upsilon_{21}} = \frac{E_1}{\upsilon_{12}} \quad \text{Eq.5. 9}$$

Mechanical properties of the lamina have been calculated using the homogenization equations reported in Appendix-A using the fibre volume fraction in the tows (V_F), calculated via statistical approach in Chapter 2. The fibre properties have been taken from the literature, while the matrix properties have been obtained by using the FE model presented in Appendix-C. Fibre and matrix properties are reported in Appendix-F.

In the proposed analytical model, the tow properties are used as lamina properties to employ for the woven architecture simplification proposed in (Thollon and Hochard, 2009) and resumed in *Fig.1.21*. Briefly, each woven ply could be studied as superposition of two virtual UD plies in plane stress state. The warp and the weft tow fraction in the woven ply are n_{+45} and n_{-45} respectively, their values are reported in *Table 2. 8*. The stiffness matrix of the UD ply Q_{UD} is transformed by using a rotation matrix to obtain the re-oriented UD stiffness matrix Q_{UD}^{+45} and Q_{UD}^{-45}. The ply stiffness matrix is then obtained by *Eq.5. 10*:

$$Q_{ply} = n_{+45}Q_{UD}^{+45} + n_{-45}Q_{UD}^{-45} \quad \text{Eq.5. 10}$$

The behaviour of the specimens is finally obtained as sum of the different plies contributions using the classical lamination theory and by *Eq.5. 10*. To have the specimen mechanical properties the presented procedure is repeated for the 6 woven plies composing the laminated.

To describe the degradation of the specimen mechanical properties, the damage volumes calculated by μCT scan segmentation are used to introduce the damage matrix in the presented model. The generic form of this damage matrix is in *Eq.5. 2*. The damage coefficients in the damage matrix D_{UD} are calculated directly from the μCT segmentation results. For each virtual UD ply composing the specimen, the damage values are issued from the damaged volume representation reported in *Fig.5. 3*. The damaged virtual UD ply stiffness matrix is calculated by using the degraded elastic ply properties that are introduced in the next paragraph.

Damaged woven virtual ply

In accord with the observation reported in *Fig.5. 5*, two damage variables are used to describe the damage evolution inside the tow. These variable are introduced in the analytical model by *Eq.5. 11* and *Eq.5. 12*.

$$E_{2_{UDsemi-ply}} = E_2^{in}(1 - D_{22_{UDsemi-ply}}) \quad \text{Eq.5. 11}$$

$$G_{12_{UDsemi-ply}} = G_{12}^{in}(1 - D_{66_{UDsemi-ply}}) \quad \text{Eq.5. 12}$$

where the damage variables is defined from the volumetric crack density in each ply by:

$$D_{22_{UDsemi-ply}} = \beta \frac{D_{ply}^{\mu CT}}{D_{MAX\_ply}^{\mu CT}} \quad \text{Eq.5. 13}$$

$$D_{66_{UDpsemi-ply}} = cD_{22_{UDsemi-ply}} \quad \text{Eq.5. 14}$$

In *Eq.5. 13* and *Eq.5. 14*, β and c and are model parameters taking into account the transverse and shear damage effect on the transverse and shear elastic properties respectively. These parameters are the same for all the specimens being "interaction" parameters.

In *Eq.5. 13* the volumetric crack densities are normalised using the maximal crack volume in the ply calculated supposing that each tow in the ply is cracked and each crack has the characteristic crack dimensions shown in *Fig.5. 4*.

The *ply-by-ply* mechanical behaviour description is in agreement with the observation made in (Quaresimin, Susmel and Talreja, 2010) where the authors argue that a composite laminate subjected to cycling loading undergoes fatigue in individual plies; each ply could be viewed having a plane stress state and a proper damage evolution. Due to damage accumulation, the reduced ply stiffness will eventually cause the ply to shed its load to the other plies. Also for this reason a ply-by-ply failure analysis can be a suitable method to describe specimen failure by critical stiffness reduction, for this reason has been employed by other authors, see for example (Lee, Allen and Harris, 1989; Adden and Horst, 2010).

Eq.5. 13 shows that in the present damage model, no internal variables are used, but the damage is introduced in the mechanical model directly from the μCT results. The damage parameter D_{22} is hence directly linked to the ply μCT segmentation results, used as diffused damage index like, by a linear equation and an interaction parameter β. The accumulation of the shear damage D_{66} is correlated to the development of the transverse damage by the linear relation in *Eq.5. 14* (Hochard, Miot and Thollon, 2013) because the crack are parallel to the fibres, then their effect on the transverse and shear modulus is the same. The graphs in *Fig.5. 7* and *Fig.5. 8* show the degradation of E_y^{ch} and G_{12}^{sec} for a woven ply as a function of the damaged volume in the -45 semi-ply or the warp virtual UD ply.

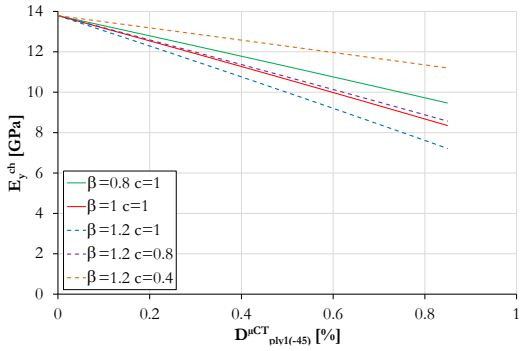

Fig.5. 7 : Evolution of E_y^{ch} in a woven ply as a function of the crack density in a semi-ply for different values of β and c.

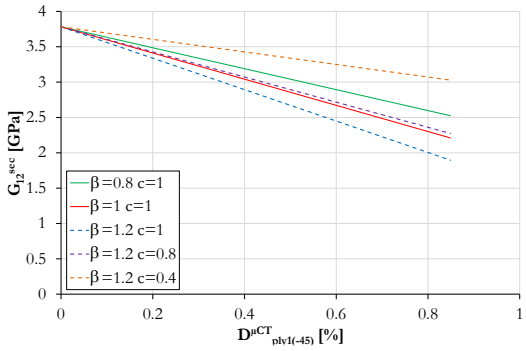

Fig.5. 8 : Evolution of G_{12}^{sec} in a woven ply as a function of the crack density in a semi-ply for different values of β and c.

For both the elastic longitudinal *modulus* and the secant shear *modulus*, a higher value of β and c results in a faster degradation rate. The value for c is chosen in accord to the values seen in literature, for example in (Burgarella, Lahellec and Charles, 2015) this coefficient is fixed to 0.26 by a linear regression

on the results obtained in terms of comparison between model and experimental data; while in (Montagnier et al., 2015) the same coefficient is 1. The exact values for c and β have been calculated fitting the results of the ply-by-ply damage model and the experimental results obtained for the tested specimens. The two parameters have been fixed by a best fit in graphs of *Fig.5. 9* and *Fig.5. 10* for the 2 bar N_2 data. The parameter values used for all the specimens are β=1.2 and c=1.

In *Fig.5. 10* the degraded elastic *moduli* calculated by the presented analytical model is quite close to the experimental results, except for the value obtained for the 2 bar O_2 specimen at 550k cycles. This decreases with a constant rate for the 2 bar N_2 specimen, while for the air and 2 bar O_2 specimen two decrease rates could be remarked. In detail, an acceleration of the degradation is observed from 170k cycles and 800k cycles for 2 bar O_2 and air specimen respectively.

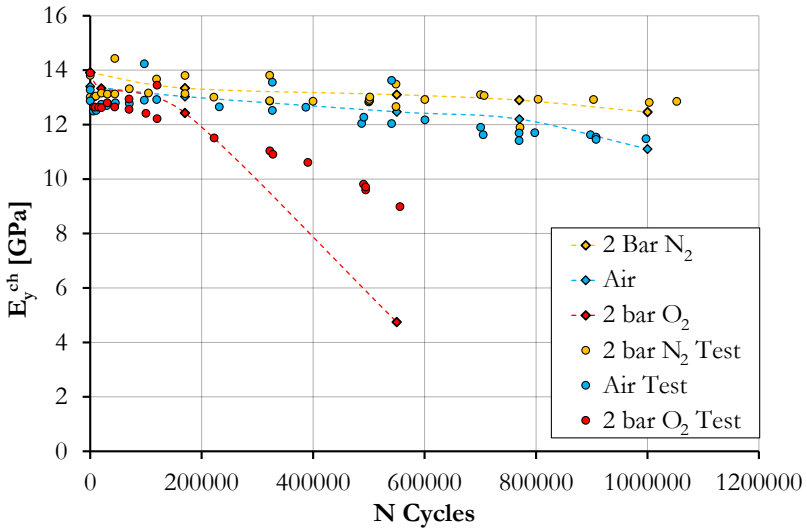

Fig.5. 9 : Elastic *modulus* evolution as a function of number of fatigue cycles. Test results and model result obtained for the three specimens tested in discontinuous fatigue.

The evolution of the secant shear *modulus* calculated by the analytical model is plotted on the graph in *Fig.5. 10*. The secant shear *modulus* degradation described by the analytical model is not really confirmed by the experimental results. In fact, the analytical model application does not give the same experimental G_{12}^{sec} values observed for air and 2 bar N_2 specimen: by the model a slight decrease is seen until the end of the test for both air and 2 bar N_2 specimen and this is not the case for the experimental values. This trend, is encountered also for the 2 bar O_2 specimen resulting in a faster degradation rate. In fact at 550k cycles, the maximal distance between experimental values and model results is observed.

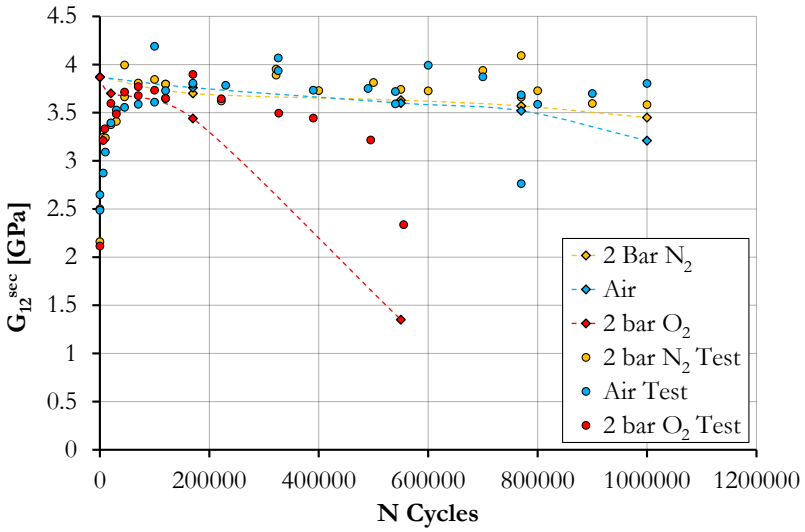

Fig.5. 10 : Secant shear module evolution as a function of number of fatigue cycles. Test results and model result obtained for the three specimens tested in discontinuous fatigue.

To explain the unmatched point for the 2 bar O_2 specimen different items are considered. As explained in (Hochard, Aubourg and Charles, 2001) delamination is a 3D *phenomena* requiring a 3D model to be described. In other words, at high damage levels some delaminations could appear inside the specimens. These delaminations produce a re-distribution of the stresses between the plies invalidating the plane stress and the iso-strain hypothesis within the virtual unidirectional plies.

Fig.5. 11 shows an example of delamination observed in the 2 bar O_2 specimen after 550k cycles. The delamination appears at the crack root and propagate between two superposed tows. Delamination remains narrowed close the crossover region. These intraply/inter-tow delaminations are generally located near the most cracked regions. In the concerned specimen, at 550k cycles, the most damaged regions are the external surfaces and the edges of the internal plies, consequently delaminations affect the first and the sixth ply and the interior plies, but only close to the exposed surfaces.

The segmentation procedure described in Chapter 2, is not able to quantify this kind of element due to their particular shape/orientation, the total damaged volume hence is underestimate for the 2 bar O_2 specimen after 550k cycles. As said above, these damage evaluation errors concern only some regions of the specimen, in particular, between the affected regions, the more important are the two external plies. If the stress redistribution inside the specimen changes, the DIC observed surface might no longer be representative of the behaviour of the whole specimen.

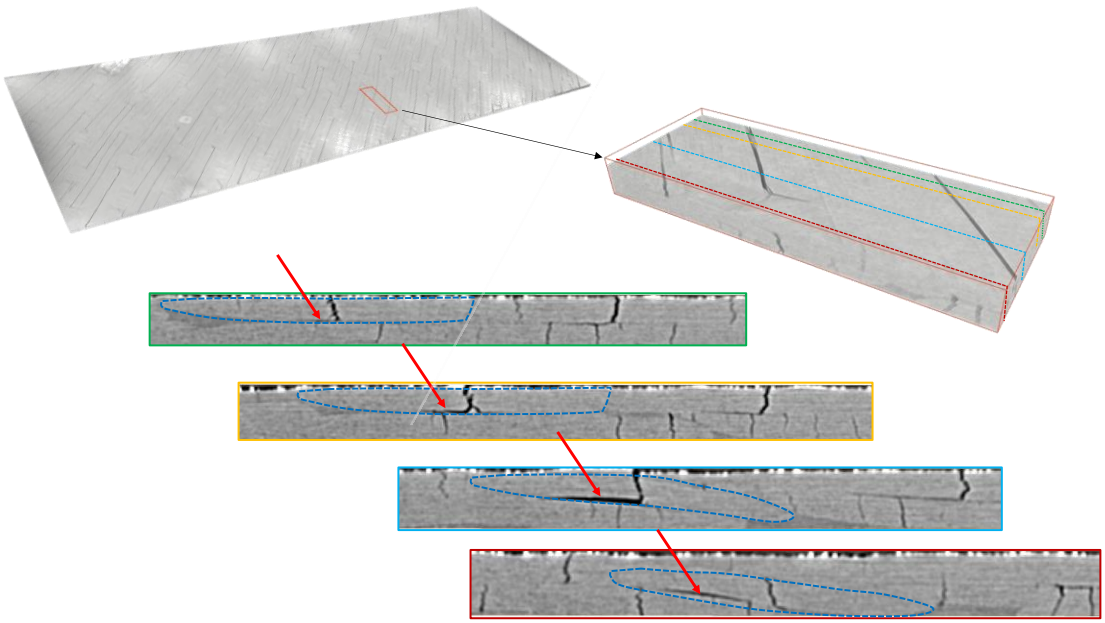

Fig.5. 11 : Delamination. In the upper region of the picture is illustrated the first ply of the 2 bar O_2 specimen after 550k cycles. The zoomed region is cut by four planes and the corresponding views are reported in a sequence. A tow is marked by dotted blue line. A crack in the marked tow generate an intra-ply/inter-tow delamination that remains narrowed close the crossover region.

A third consideration is on the morphology of the damage scenario. The internal plies of the 2 bar O_2 specimen after 550k cycles are damaged mainly close the exposed edges, while the internal regions of the same plies is far less damaged. The employment of a diffused damage parameter to describe this kind of damage scenario is not appropriate.

This effect is quantified in the following manner: from the segmentation results concerning the internal plies, the crack volume contribution of the regions near the lateral surfaces is suppressed. The damaged volume obtained excluding these contributions is heterogeneously distributed inside each internal ply and justifies the use of a global damage parameter (like smeared crack distribution).

The analytical model results obtained applying the modified damage index is reported in *Fig.5. 12* and *Fig.5. 13*. For the air and 2 bar N_2 specimen the evolution obtained by the analytical model is the same as the evolution seen in *Fig.5. 9* and *Fig.5. 10*. The same observation goes also for the first points relative to the 2 bar O_2 specimen, moreover a more close value between experimental and analytical calculation is seen for the point at 550k cycles.

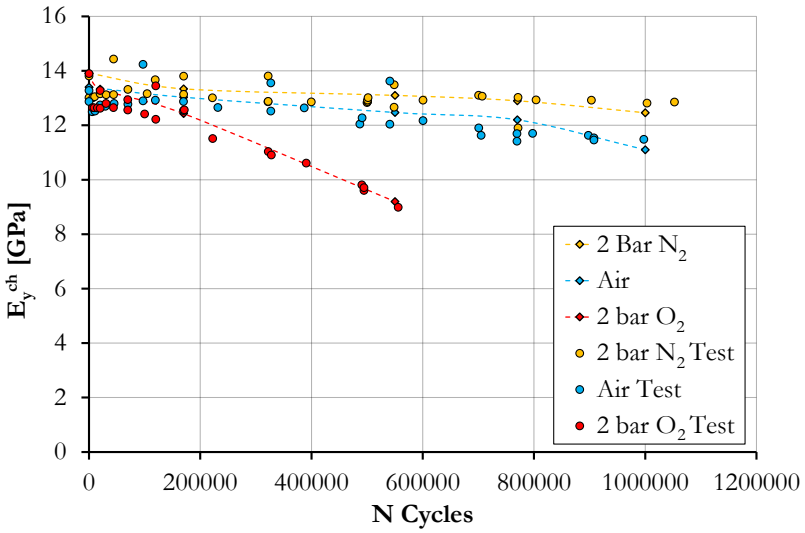

Fig.5. 12 : Elastic *modulus* evolution as a function of number of fatigue cycles. Test results and model result obtained for the three specimens tested in discontinuous fatigue excluding the internal plies damage close to the specimen lateral edges.

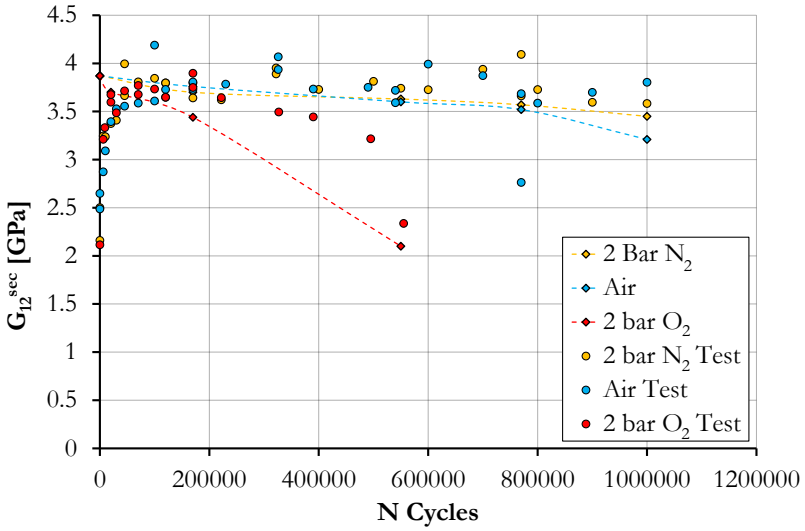

Fig.5. 13 : Secant shear *modulus* evolution as a function of number of fatigue cycles Test results and model result obtained for the three specimens tested in discontinuous fatigue excluding the internal plies damage close to the specimen lateral edges.

The presented results show that the lateral edge cracks of the internal ply does not affect the longitudinal mechanical response of the specimens during traction. Moreover, the global volumetric crack density give a good description of the *damage state* of the specimens. The calculated evolution of G_{12}^{sec} does not match experimental data as well as for E_y^{ch}, maybe for the limited number of µCT data, especially between 200k and 500k.

The good agreement between experimental values and model results confirms the accuracy in using DIC surface measures for specimen response characterization. The model gives a satisfactory description of specimen properties degradation using a matrix damage description. On the other hand,

the model hypothesis seem to be fully respected. This means that the plane stress assumption, the *no plies interaction* as well as the adequately of damage description in the analytical model are validated.

Damaged-material strain energy

The presented analytical model is useful for results interpretation and to understand the importance of using a matrix to describe damage instead of a global volumetric crack density. As made for the cross-ply UD based laminate, the described analytical model allows plotting an energy parameter as a function of the ageing parameter in order to develop a damage tolerant approach also for the woven specimen. Following the presented analytical model, the damaged-material strain energy E^{ps}_D can be written as *Eq.5. 15* for a ply under the plane-stress hypothesis(Ladeveze and Ledantec, 1992):

$$E_D^{ps} = \frac{1}{2}\left[\frac{\sigma_{11}^2}{E_{11}^0} - \frac{2\nu_{12}^0}{E_{11}^0}\sigma_{11}\sigma_{22} + \frac{\sigma_{22}^2}{E_{22}^0(1-D_{22})} + \frac{\sigma_{22}^2}{E_{22}^0} - \frac{\sigma_{12}^2}{2G_{12}^0(1-D_{66})}\right] \quad \text{Eq.5. 15}$$

where the index "0" are referred to the initial value of the mechanical properties. The thermodynamic forces associated with the two damage variable are obtained by deriving the damaged-material strain energy.

$$Y_{D22} = \frac{1}{2}\frac{\partial E_D^{ps}}{\partial D_{22}} = \frac{\sigma_{22}^2}{E_{22}^0(1-D_{22})^2} \quad \text{Eq.5. 16}$$

$$Y_{D66} = \frac{1}{2}\frac{\partial E_D^{ps}}{\partial D_{66}} = \frac{\sigma_{12}^2}{2G_{66}^0(1-D_{66})^2} \quad \text{Eq.5. 17}$$

The stress values in *Eq.5. 16* and *Eq.5. 17* have to take into account the thermal residual stress. The stress levels due to the application of the maximal fatigue load to the specimen as well as the thermal stress are issued from the FE model presented in Appendix-C. The stress fields has been calculated simulating a cooling (from the free stress temperature - T_G=330°C - to the test temperature) of the repetitive unit cell followed by a mechanical load application along the longitudinal direction with a $\sigma=\sigma^f_{MAX}$. The two thermodynamic forces are employed as the energy release rates governing damage development in Chapter 3: also if the meaning of these introduced thermodynamic forces is quite different from the energy release rate introduced in the Chapter 3, for different environmental conditions, the evolution of the critical values of these two forces is only dependent on the measured crack volume. The evolution of these two forces for three semi-plies is reported in *Fig.5. 14*.

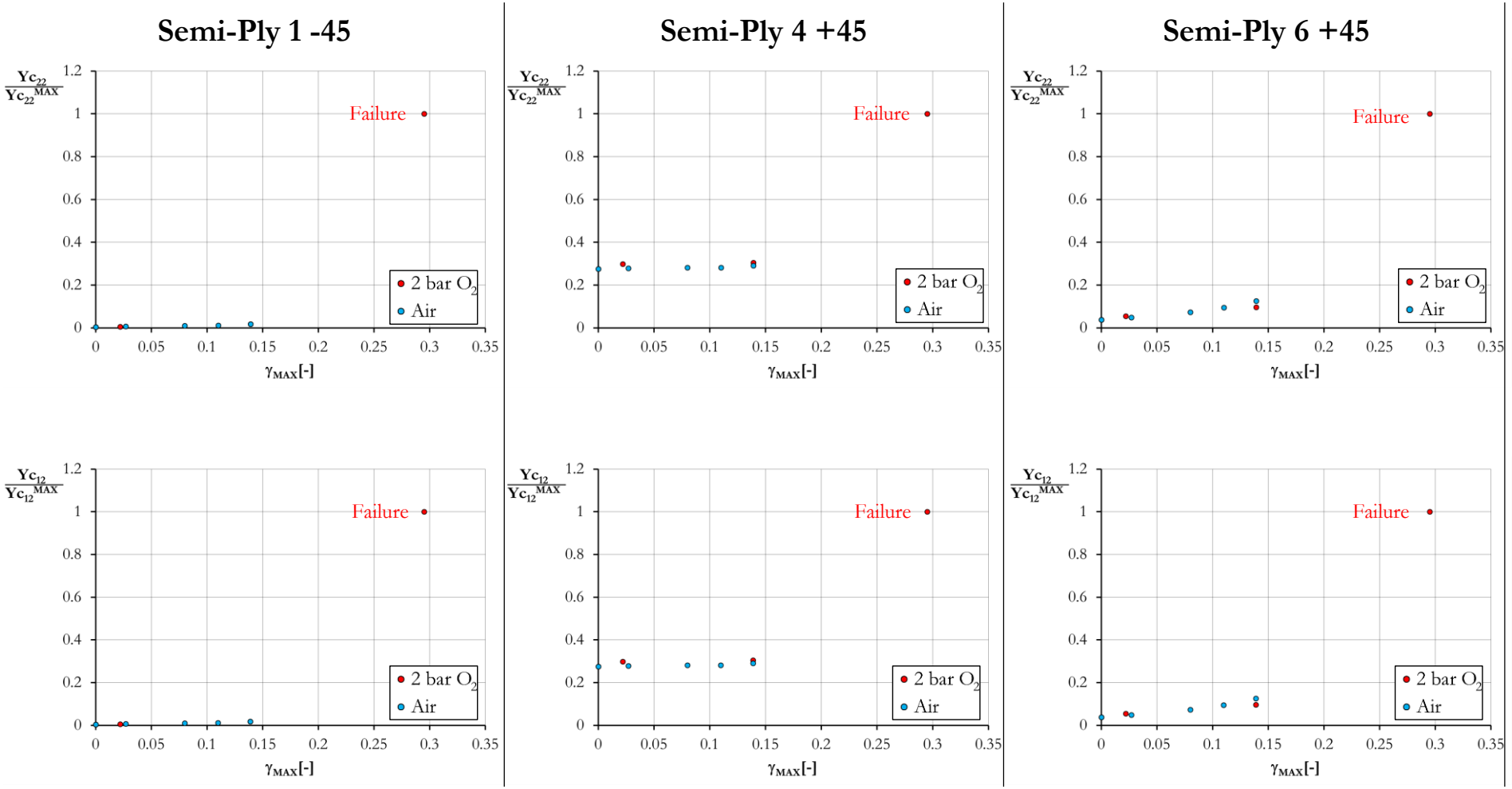

Fig.5. 14 : Evolution of the critical thermodynamic forces as a function of the ageing parameter for the semi-plies.

The evolution of the critical values of the thermodynamic forces (Yc_{22} and Yc_{12}) could be used to define a predictive strategy to fix the maintenance intervals for a component realised using the tested material as already made for the cross-ply UD laminate in Chapter 3 (*see* Appendix-B). In such a way, a Paris like law as *Eq.5. 18* can be used to describe the damage evolution during cycling associated to a discrete variation of a generic thermodynamic force ΔY.

$$\frac{\Delta D}{\Delta N} = A \times \Delta Y^{p} \qquad \text{Eq.5. 18}$$

The volumetric crack values used for mechanical properties calculation are mainly referred to external plies (PLY1 and PLY6). The external surface of PLY1 is generally one of the most damaged regions of the tested specimens and it is, at the same time, the surface observed by DIC. The next paragraph is devoted to the presentation of an in-situ damage assessment technique performed using DIC. As is explained in the following paragraph, a more detailed properties evolution could be plotted by the application of the presented analytical model by using DIC crack detection.

5.3 *In-situ* damage assessment by DIC

During fatigue tests, slow load/unload cycles are performed to observe by DIC the specimen degradation in terms of loss of the elastic properties and in terms of damage development. This latter result is obtained using the procedure described in *2.3.3*. The specimen surface observed by DIC is one of the two most damaged surfaces of the specimen, which is the -45° tow direction belonging to the first ply. *Fig.5. 15* illustrates a segmentation result of a damaged specimen first ply in the -45° direction. The zoom of the μCT segmentation results shows the cracks situated on the DIC observed zone of the same surface. Longest cracks are clearly visible using both μCT scan segmentation and DIC, while shortest crack are detectable only using the segmentation procedure.

In this case the μCT scan segmentation method has a detectability threshold better than the DIC method. On the other hand, the DIC damage quantification is performed when the specimen is loaded at maximum fatigue load, this means when the cracks are open. As argued in (Böhm et al., 2015), the cracked volume quantification by μCT scan of the same specimen is lower for an *ex-situ* scan than for an *in-situ* scan due to the crack opening effect, consequently some cracks could be not detected also by μCT scan segmentation.

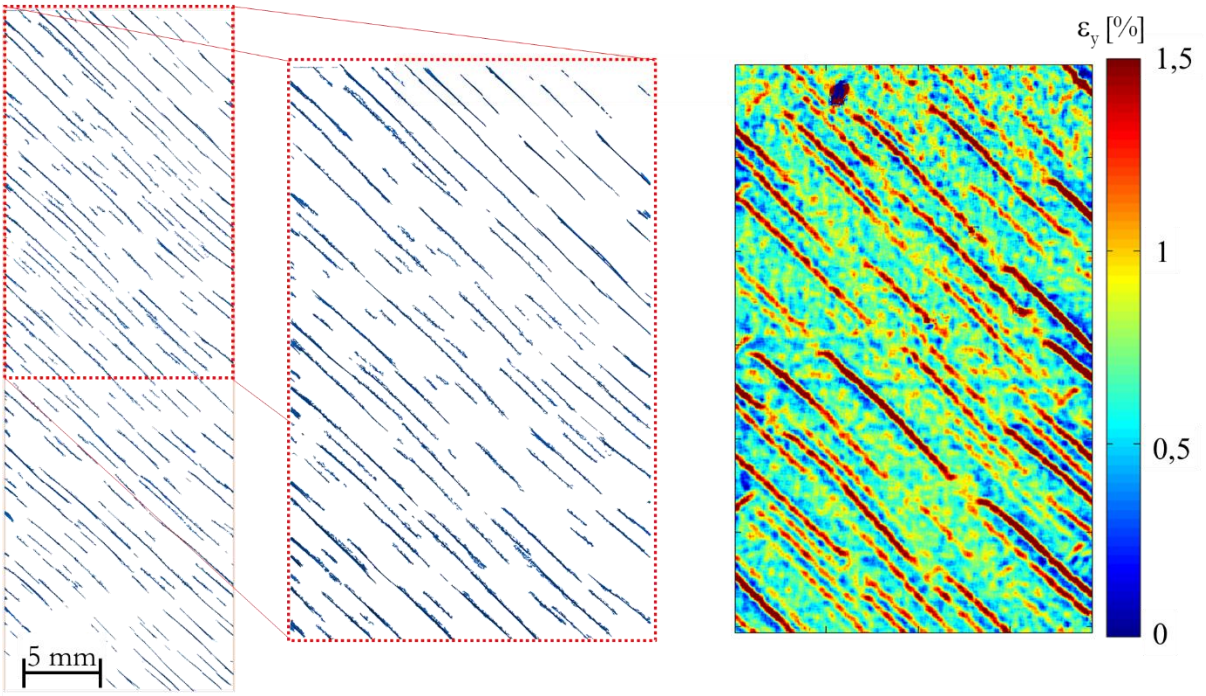

Fig.5. 15 : Segmentation results obtained for a first ply segmentation (only -45° cracks are shown) and DIC longitudinal strain field. High stain regions match with crack in the zoomed portion of the segmentation.

The results of crack detection by DIC for specimens tested in discontinuous fatigue are shown in *Fig.5. 16*. The evolution of the total crack length for the three specimens is quite similar to the µCT results shown in Chapter 4 in terms of crack volume evolution under the different environmental conditions: the 2 bar O_2 specimen exhibits an evolution of the total crack length faster than the air specimen, while the crack evolution for the 2 bar N_2 specimen is quite slow compared to the 2 bar O_2 and air specimen.

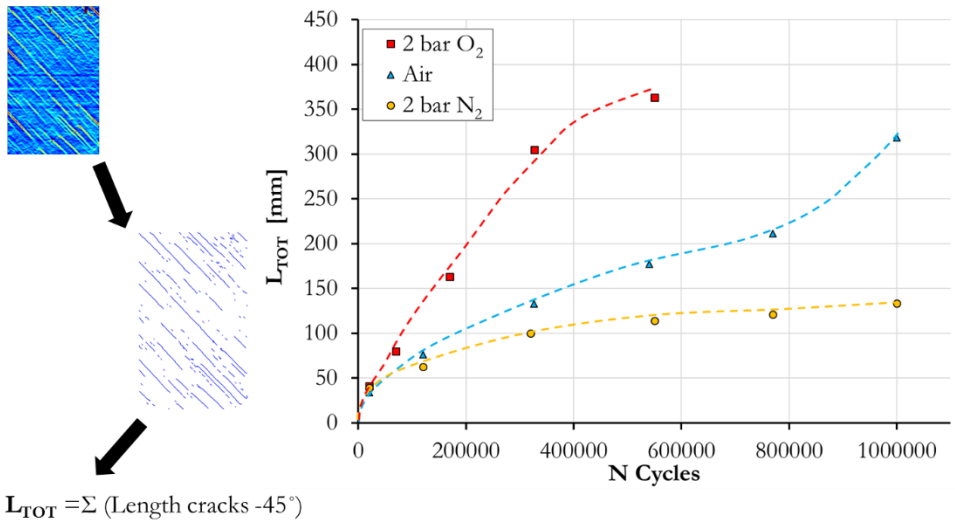

Fig.5. 16 : -45° crack length evolution measured by DIC on PLY1 for during discontinuous fatigue in 2 bar O_2, air and 2 bar N_2.

A comparison between the damage in the -45° tows of the first ply measured by µCT and by DIC is reported in *Fig.5. 17*. Each graph in *Fig.5. 17* has a double vertical axis: in the former, the total crack length is reported, while the second one represents the first ply damaged volume along the -45° direction calculated by *Eq.5. 1*. The scaling factor between the two ordinates is calculated considering that an entirely cracked tow, approximating the crack shape as reported in *Fig.5. 4*, results in a $D^{\mu CT}_{ply1}$ between 0.08% and 0.12% depending from the crack width. The relatively most important results concern damage evolution. The µCT scans are limited in number during the fatigue test due to the complexity in remove/mounting the specimens to perform the scans. DIC stops are more numerous, hence the data points obtained allow tracing a more detailed evolution for elastic properties and first ply damage during fatigue. The good agreement between DIC and µCT data illustrated in *Fig.5. 17* confirms that DIC is useful for surface damage characterization.

The graphs in *Fig.5. 17* compare two kind of damage characterization that finally give similar information. The damage parameter $D^{\mu CT}_{ply1}$ gives a volumetric description of the damage that is a volumetric ratio representing the damage state of the whole specimen. DIC gives a surface evolution/quantification of damage obtained studying a smaller region compared to µCT (*see Fig.5. 15*).

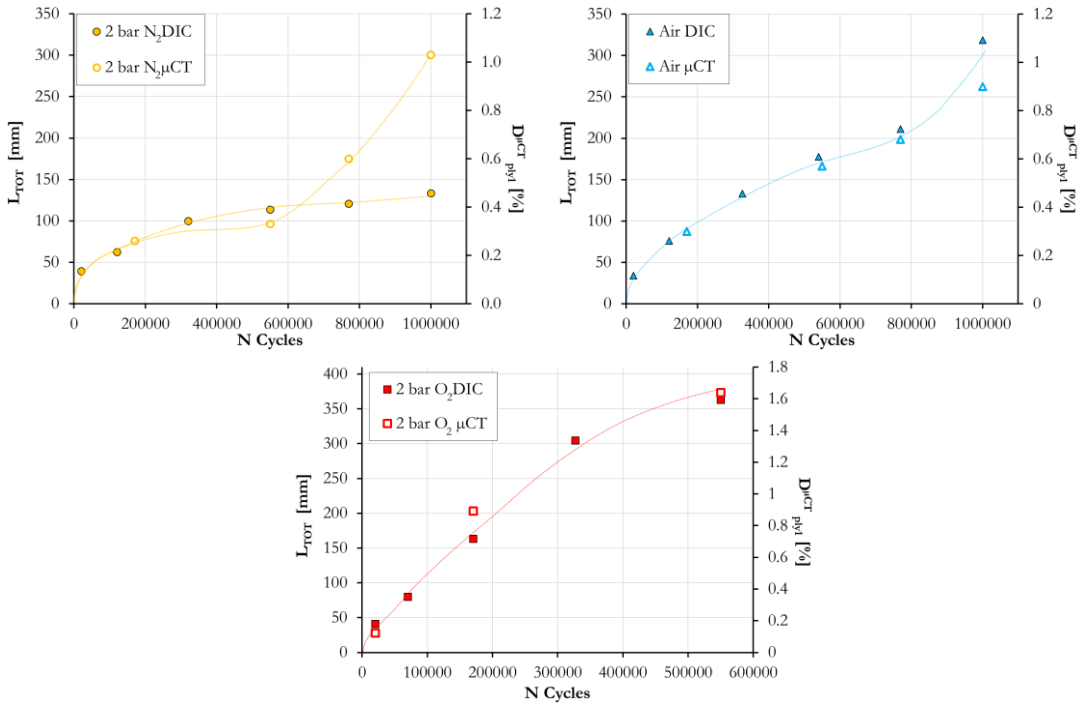

Fig.5. 17 : Damage on the first ply quantified using DIC and µCT scan segmentation for woven fatigue specimens tested in 2 bar O_2, air and 2 bar N_2.

For a very heterogeneous damage scenario as was observed for the 2 bar N_2 specimen, the DIC results are quite far from the µCT ones, proving the importance to scan a large region of the specimen to have an appropriate average mean damage characterization.

The crack opening effect above cited and the dimension of the observed region (heterogeneity of damage distribution) could justify the difference in data points reported in the graphs of *Fig.5. 17*.

The information provided by DIC on the first ply could be used to describe the damage development of the whole specimen keeping in mind that for a consistent part of fatigue tests the damage is narrowed the external surfaces. Considering the volume of the whole specimen, the scaling factor will be 6 times the scaling factor used for comparison of the two measurement methods employed for *Fig.5. 17*. Furthermore, to plot the graphs relative to the whole volume, the crack length measured by DIC has been multiplied by a factor 2, taking into account that the damage observed on the surface tows of the first and the sixth ply should be the same; consequently the ordinate L_{TOT} is named $2L_{TOT}$. The resulting graphs are reported in *Fig.5. 18*. The scaling factor and the assumption on the evolution of the damage for the sixth ply seem confirmed by the experimental segmentation results. For the graph relative to the 2 bar N_2 the distance between the points obtained after 1M cycles could be justified as previously done by the heterogeneous distribution of the damage. The DIC results for the 2 bar O_2 specimen are close to the µCT results until 170k cycles. The scan performed after 550k cycles shows an important damage volume also for the internal plies, and no additional information on the damage development for these plies are available.

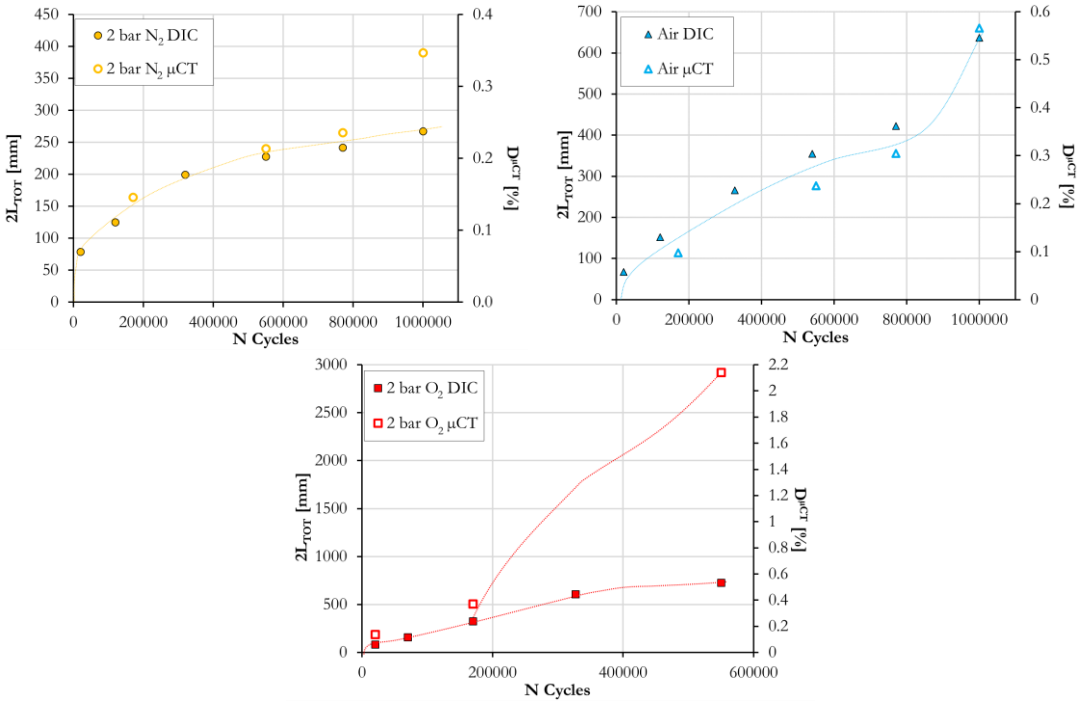

Fig.5. 18 : Damage on the whole specimen volume quantified using DIC and µCT scan segmentation for woven fatigue specimens tested in 2 bar O_2, air and 2 bar N_2.

This uncertainty in damage evolution for the 2 bar O_2 specimen is represented in *Fig.5. 18* by a split of the dotted line describing the damage evolution. The factor 2 used to take into account DIC damage

in the sixth ply includes also the slow increasing of the damage in the internal plies: the damage in the sixth ply is ever around the 80% of the damage in the first ply and apparently the remaining 20% is distributed in the internal plies. For the air specimen the damage development in first and sixth ply is quite similar, for this reason in the graph of *Fig.5. 18* related to air specimen, DIC tends to overestimate damage development if compared to μCT results.

The damage assessment performed by DIC for the tested material is a powerful method, it allows obtaining a more detailed damage evolution using a larger number of data point than the μCT derived method. The limit of the explained method, clearly highlighted in the graph relative to the 2 bar O_2 specimen in *Fig.5. 18*, is the undetectability of the damage distribution along the *through the thickness* direction. However, for the 2 bar N_2 and air specimens, crack are located mainly on the external surfaces, consequently damage evaluation by DIC and global volumetric crack density have the same trend. The scaling factor used to plot the graph in *Fig.5. 17* is used to convert DIC crack length evaluations in μCT volumetric crack density results. The DIC damage measurements are used to describe the degradation of the semi-plies directly exposed to the environment (PLY1-45 and PLY6+45). The mechanical properties degradation calculated by the analytical model above presented and using the damage evaluation obtained by DIC is illustrated in *Fig.5. 19* and *Fig.5. 20*.

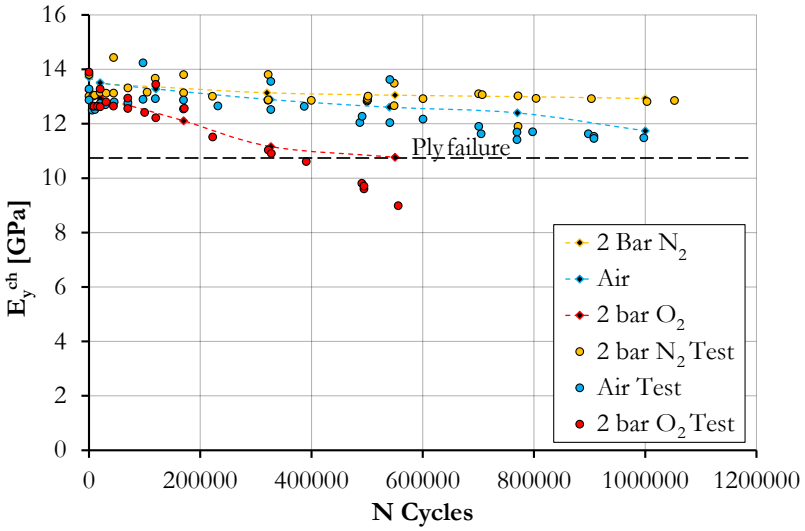

Fig.5. 19 : Elastic *modulus* evolution as a function of number of fatigue cycles. Test results and model result obtained for the three specimens tested in discontinuous fatigue using damage data issued by DIC crack detection.

The mechanical properties evolution obtained using the analytical model and the damage detected by DIC are in agreement with the experimental data for the 2 bar N_2 and the air specimens because the matrix crack are mainly located on the external surfaces. For these two specimen, DIC and μCT give

the same results confirming that DIC could be used as *in-situ* damage monitoring allowing a faster damage evaluation by suppressing the μCT scans and the associated image post-processing.

A second benefit in using DIC for crack detection is the more accurate degradation description due to the more numerous data points if compared to μCT.

The limitation of this method clearly appear for the 2 bar O_2 data. An extensively cracking of the surface semi-ply leads to a whole ply failure (reported in black dotted line in *Fig.5. 19*). After this value, DIC cannot be used to evaluate crack volume in the specimens.

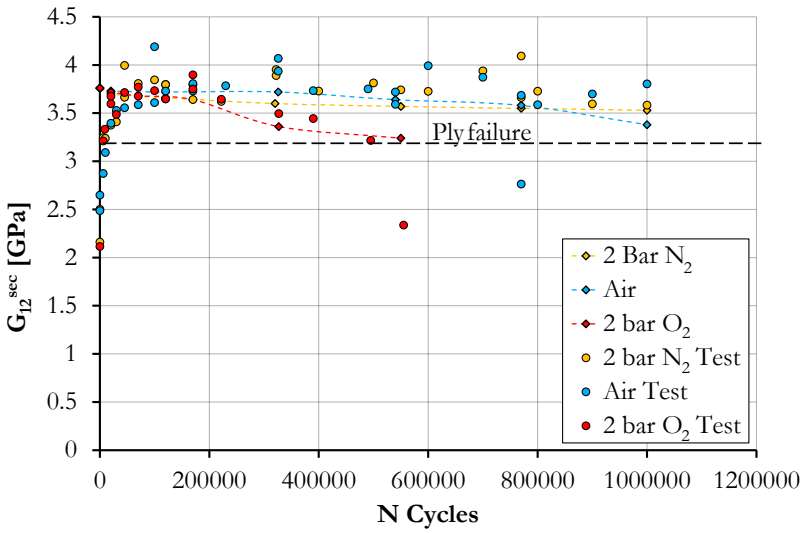

Fig.5. 20 : Secant shear *modulus* evolution as a function of number of fatigue cycles. Test results and model result obtained for the three specimens tested in discontinuous fatigue using damage evaluation by DIC crack detection.

The evolution of G_{12}^{sec} for the air and 2 bar N_2 specimens remains unclear, but the DIC data allow plotting the evolution of G_{12}^{sec} for the 2 bar O_2 specimen in the range 200k-500k cycles, where the μCT did not give details on the general trend. The ply failure effect is appreciable already in this plot. On the two graph a saturation of the cracked region on the external semi-plies seems to take place at about 400k cycles. The same conclusion could be issued looking at *Fig.5. 17* and *Fig.5. 18*.

DIC crack detection allows having a satisfying damage evaluation for the tested specimen. The major advantage of this method is that is an *in-situ* monitoring technique, the damage characterization could be carried out without removing the specimen from the test rig and this gives a faster and simpler fatigue tests. Other fundamental founding of this paragraph are related to the surface crack effect on the macroscopic specimen response. For the air and 2 bar N_2 specimen, the surface cracks are the main damage form resulting in a reduction of the mechanical properties. Until the first ply failure, this goes

for the 2 bar O_2 specimen too. In abscissa of the graph in *Fig.5. 21* are reported the ageing parameter values calculated for the air and the 2 bar O_2 specimen, while on the vertical axis is reported the sum of the damaged volume on the surface semi-plies (PLY1 -45° and PLY6 +45° referring to *Fig.5. 3*). Data point obtained for air and 2 bar O_2 specimens lie to the same master curve that is, in this particular case a straight, reported in the graph as dotted black line.

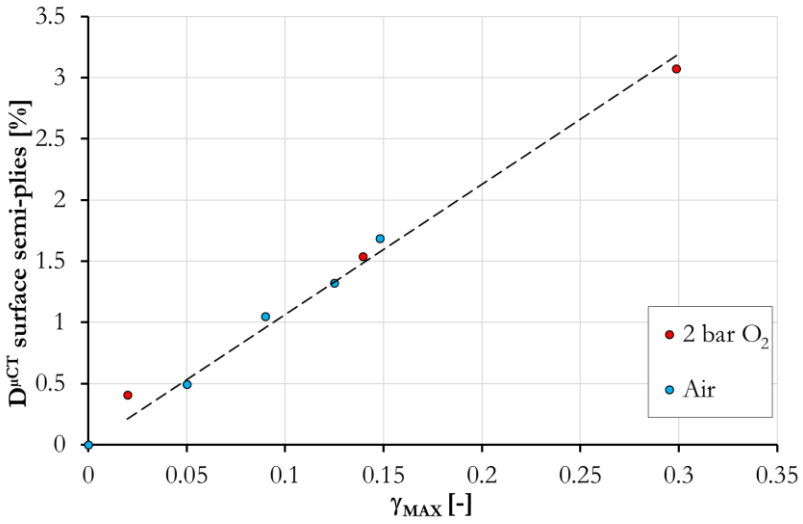

Fig.5. 21 : Volumetric crack density on the external surfaces of the specimens as a function of the ageing parameter γ_{MAX} for the air and 2 bar O_2 specimen tested in discontinuous fatigue.

The evidence issued from *Fig.5. 21* is the direct link between the ageing parameter and the volumetric crack density in the most important locations. This has a clear effect on the elastic *modulus* degradation illustrated in *Fig.5. 12*. This involves the link between the ageing parameter and the reduction in longitudinal elastic *modulus* reported in *Fig.4.37*.

The phenomenological explanation of the master curve existence in *Fig.5. 21* was not accurately investigated in this work. However, in (Asp, Berglund and Talreja, 1996a, 1996b) the authors define an energetic failure criterion for a composite material. In this criterion, a matrix crack onsets when a critical energy value is crossed. The general form of the volumetric energy density criterion is:

$$U_v = \frac{1-2\nu}{6E} f(\boldsymbol{\sigma}) = U_v^{crit} \qquad \text{Eq.5. 19}$$

where $f(\boldsymbol{\sigma})$ is a function of the stress state and ν and E are the Poisson coefficient and the Young *modulus* of the material and U_v^{crit} is the critical volumetric energy density. The matrix Young *modulus* is function of the ageing parameter (*see* Chapter 4), consequently as the oxidizing time increases, the matrix becomes more stiff and consequently, a matrix less strained results in a lesser energy density. On the

other hand, in the term f(**σ**), in addition to mechanical loads, matrix shrinkage between fibres could superposes an additional stress state to resin regions having an intensity dependent on the ageing parameter. This phenomena, directly linked to γ_{MAX}, may give an acceleration of the matrix cracking described in *Eq.5. 19* by a decrease of the critical value U_v^{crit} as for the G_c of the cross-ply laminated in Chapter 3.

5.4 Conclusion

The damage description given in this chapter allows a better understanding of the environmental effects on the fatigue of the tested woven composites. In particular, the perfect rescaling of the elastic *moduli* in *Fig.4.37* has been explained using an analytical model and a detailed damage description.

The evaluation of the environmental effect on the global damage scenario has been obtained by a ply-by-ply volumetric crack density description, highlighting that the cracked volume in the surface plies is bigger than that in the interior plies. Moreover the volumetric crack density in the interior plies is negligible for the tested specimens, except for the 2 bar O_2 specimen at 550k cycles, where an important cracked volume is noticeable also for the interior plies. The majority of these cracks onset on the lateral specimen edges and do not propagate far from the onset location.

The detailed ply-by-ply crack description has been employed to identify a damage matrix where each terms is related to the directly measured damaged volume. The identified damage matrix has been used in a ply-by-ply analytical model describing the elastic behaviour of the specimen, in order to obtain an elasto-damage model.

By this model has been shown that the cracks on the lateral edges of the internal plies do not affect the longitudinal specimen response. Consequently, the global specimen longitudinal response is dependent on the damage on the surface plies. Moreover, delamination (observed only in the late fatigue stage of the 2 bar O_2 specimen) do not affect the stress distribution in the tested specimen until failure. The analytical model has been employed for a proposition of a damage tolerant approach for a part design. In the proposed approach, the environmental effect (represented by the ageing parameter) becomes an intrinsic parameter, as made for the cross-ply laminated composite in Appendix-B.

DIC crack detection has been presented in the following as a mean allowing characterizing the damage on the specimen surface during fatigue without remove the specimens from the test machine. Being the cracks narrowed essentially on the external surfaces, DIC crack measurements have been used to evaluate the whole specimen damage. The DIC damage evaluations have been employed in the

proposed analytical model to describe the mechanical properties degradation, confirming that DIC crack detection can be used as a novel *in-situ* damage assessment method for the tested specimens until the first ply failure. This alternative method for damage evaluation, in this work, allowed plotting a more detailed evolution of the mechanical properties calculated by the analytical model.

The last part of the chapter is devoted to the study of the environmental effect on the damage development on the external surfaces. The straight master curve observed plotting the volumetric crack density of the surface semi-plies as a function of the ageing parameter confirms that the damage volume on the external semi-plies, and consequently, the longitudinal mechanical properties, are dependent on the testing environment.

Conclusion & Perspectives

In these general conclusions are summarized the proposed approaches for damage assessment and the *multi-physical fatigue* test results issued from this thesis work.

In order to characterize properly the thermo-oxidation effect during fatigue of composites a specially developed test machine has been employed to perform *multi-physical fatigue* tests. This innovative test setup has been presented, highlighting the need to propose some appropriate methods and techniques for the evaluation of the specimen integrity during the tests.

Results of *multi-physical fatigue* tests on C/epoxy $[0_2/90_2]_s$ samples have been shown that degradation during fatigue in air at 150°C could be accelerated by 7 times performing the same fatigue test in 2 bar O_2 at the same temperature. For this model composite architecture, the fatigue degradation has been evaluated by the transversal cracks counting on the lateral specimen edges. It has been observed that crack multiplication kinetics is strongly affected by the thermal-oxidation processes, taking place on resin regions on the lateral (exposed) specimen edges. By the employment of an analytical model it has been shown that thermo-oxidation leads to a decrease of the critical energy release rate G_c of the lateral specimen edges, facilitating transverse crack onset. The evolution of G_c during fatigue in air and 2 bar O_2 plotted as function of the ageing parameter reveals the existence of a master curve supporting that the acceleration of the thermo-oxidation process seen on the pure resin is exploitable to describe the cracking kinetic of the $[0_2/90_2]_s$ samples.

The time scaling factor (7 between air and 2 bar O_2 at 150°C for this resin) is the same acceleration factor identified during ageing of the pure resin samples. This suggests that the time-scaling factor can be defined *a priori*, before starting fatigue test on composite, characterizing the thermo-oxidation process of the pure resin by environmental ageing (gas and temperature).

C/polyimide 8HS woven laminated composites are more interesting from an industrial point of view. *Multi-physical fatigue* tests have been performed on C/polyimide $[45_6]$ 8HS woven specimens to develop a fatigue test acceleration procedure also for this architecture. Due to a more complex damage scenario, the degradation has been evaluated using an adjusted fatigue test cycle including interruptions to use Digital Image Correlation (DIC) and μ-Computed Tomography (μCT). The

adaptation of these two techniques to the required observations represents important progress issued from this thesis work.

μCT was used to perform a 4D damage assessment: this is a 3D damage evaluation in a specimen over the entire test duration (the time provides the fourth dimension). From the μCT images, a quantitative damage evaluation has been done by a segmentation procedure. This segmentation procedure, adapted for the tested specimens, gives the basis for the development of similar segmentation strategies as the use of directional filters and the determination of a set of parameters, characterizing the image post-processing, kept for all the specimen segmentations, giving the reproducibility of the obtained results. The 3D damage description has been essential for the identification of the most critical regions of the samples tested in *multi-physical fatigue*.

The main drawback of the damage evaluation by μCT is that the specimens have to be removed from the test rig to perform the μCT scan. For this reason, to carry out *multi-physical fatigue* tests in a reasonable time-lapse, the μCT interruptions have been limited. A more continuous damage assessment during fatigue has been provided by DIC.

A procedure for the high temperature speckle pattern application has been developed and presented. The macroscopic mechanical properties degradation during fatigue have been characterised using the mean values of the strain fields measured by DIC during slow load/unload cycles. DIC strain fields have been analysed using a particular procedure to evaluate the damage extent.

The μCT scan segmentation reveals that for all the environmental conditions, matrix intra-tow cracks is the main damage form. These onset principally in the more external tows, where thermo-oxidation occurs, promoting a faster damage process. No important damage have been observed for the internal plies, except for the 2 bar O_2 specimen after 550k fatigue cycle at 250°C. For this specimen short cracks onset on the lateral specimen edge and propagate toward the specimen centre. It has been demonstrated that a correct evaluation of the *damage state* of the specimens has to take into account the damage morphology (damage form, localization, extension), arriving to the conclusion that for the tested specimens, only the cracks in the external tows produce a degradation in terms of longitudinal elastic *moduli*. This result, quite important, allows explaining the time rescaling degradation observed for the longitudinal elastic *moduli* for the specimen tested in air and 2 bar O_2 at 250°C: the ageing of the resin accelerates the crack onset kinetics and consequently the loss of longitudinal elastic *modulus*. The time rescaling identified by environmental ageing on the polyimide pure resin sample, can be used to rescale the degradation, in terms of loss of longitudinal elastic *moduli*, for the tested woven specimens.

It has been shown that cracks are mainly concentrated on the exposed surfaces, DIC has been used also as a satisfactory mean for damage extent evaluation. This represents a powerful *in-situ* damage evaluation method, especially for *multi-physical fatigue* on the tested woven composite, allowing to avoid the test interruption for μCT scans. By this technique a more detailed evolution of the cracked volume has been plotted as a function of the fatigue cycles. This method, refined in this thesis, could be used in future work on this material to evaluate the "health" of the specimens during *multi-physical fatigue* without removing the specimen from the testing machine, reducing the testing time.

Looking at the creep/fatigue interaction during fatigue, a relevant visco-elasto-plastic strain has observed on the tested woven specimen. These viscoplastic/viscoelastic deformations were negligible for the $[0_2/90_2]_s$ specimens, while they have been deeply analysed for the woven ones. It has been shown that the maximum fatigue strain can be split in three contributions: the first one is related to the visco-elasto-plastic response to the application of a no-zero mean traction load during fatigue that make creep the specimen; the second one is a strain evolution due to the damage accumulation, being the volumetric crack density affected by the environmental conditions, it has been shown that also the damage related strain can be rescaled with the ageing parameter; the third term is related to the visco-elasto-plastic strain due to the application of the maximum fatigue load.

The time-rescaling of the fatigue maximum strain after the subtraction of the viscoelastic and viscoplastic strain due to creep and fatigue load showed that no synergistic effects take place for the tested specimens during *multi-physical fatigue*. This means that high temperature fatigue tests could be accelerated by using a moderate high partial pressure of oxygen also for woven composites. The acceleration factor identified on the pure polyimide resin has been used to rescale the fatigue result in terms of loss of elastic properties and in terms of maximal fatigue strain. At the same time DIC is a further time-saving and powerful method to monitor the specimen integrity during tests.

An analytical model has been introduced in the last chapter of this work to describe the elasto-damage behaviour of the woven specimens. Starting from a different damage description employing a damage matrix, the ply-by-ply characterization of the damage scenario performed by μCT, the woven architecture has been simplified using two virtual superposed and orthogonal unidirectional laminates. The degradation of this virtual woven laminate has been directly linked to the crack density measured by μCT in each semi-ply. Being the external surfaces the most damaged regions, DIC data have been used similarly to μCT data to describe the specimen degradation during fatigue: the presented analytical model has been employed to describe mechanical properties degradation by using the crack lengths issued by DIC evaluations.

Perspectives

The perspectives concerning this work are mainly related to the characterization of the environmental effect of woven specimens, but also to the evaluation of the same environmental effect on the specimen response under different load conditions, development of analytical model and finally damage characterization/representation.

A more complete understanding of the environmental conditions on the fatigue life of the tested specimens can be obtained only testing specimens until failure and monitoring the damage accumulation during cycling. The life of the specimens tested in this work has been has been employed just to highlight the strong effect of the environmental conditions, but the damage accumulation from 1M of cycle up to failure has been not investigated.

Different fatigue test conditions may lead to the apparition of some synergistic creep/fatigue/environment effects, not observed in the presented test campaign. Moreover, the plastic strain observed during the presented creep tests could be due to matric micro-cracking multiplication and this multiplication can be affected by the environment. A damage observation technique having a resolution better than that obtained for the images shown in this work, can reveal the presence of these micro-cracks.

The analytical model presented in Chapter 5 to describe the elasto-damage behaviour of the specimens can be improved, for example, including the evolution of the elasto-plastic strain to obtain a model to predict the specimen failure; on the other hand, a more detailed damage characterization/representation including in a damage matrix all the crack information as shape, orientation, position,… can lead to an improving of the elasto-damage behaviour description/prediction and to the development of same tools as the proposed damage tolerant approaches, very useful in part design.

The *multi-physical fatigue* test campaign performed during this work is only meant to characterize the acceleration of the fatigue degradation of OMC. A reference working cycle (mechanical load and temperature) was not available to compare accelerated and real time test results. The acceleration of e real reference cycle could require the application of thermal cycling jointly to mechanical fatigue (in oxidizing environment) to be representative of the real conditions; also the test frequency is an important parameter as well as the value of the partial oxygen pressure needed to correctly accelerate the test.

Appendix A - Homogenized mechanical properties for laminated composites

The knowledge of the mechanical properties of the tested specimens is fundamental for the understanding of damage kinetics. The calculation of the mechanical properties for a composite materials requires the employment of some calculation strategies. A common feature for all these methods is the computation of a structural component properties starting from the mechanical properties of a *Representative Volume Element* (RVE) that is a sample structurally entirely typical of the whole mixture on average having macroscopically uniform moduli values (Hill, 1963). For all the RVE based methods, the global mechanical properties are calculated starting from a local level, in other words, from the analysis of the microstructural details (Hollister and Kikuehi, 1992). Starting from the fibre and matrix properties, several methods exist in the literature for the calculation of the average properties of an RVE and therefore of the global structure. These methods are listed and criticized in (Chamis and Sendeckyj, 1968); in practice four main categories are existing: numerical techniques, mechanics of material approach, variational or bounding approaches and the self-consistent field methods. Between these methods, the mechanics of material approaches are the most commonly encountered methods, the *rule of mixture* results from the mechanics of materials approach. The most relevant drawback of this method is the dependence of the transversal properties of a composite *laminae* on the assumptions on fibre geometry, fibre packing and fibre spacing (Whitney and McCullough, 1990; Li, 2001). The calculation of the mechanical properties by the self-consistent field model is not dependent on geometry (Hill, 1965). The basic method is based on the representation of the fibre as a phase embedded in a medium having the mechanical properties equivalent to the studied composite material. Being the results of the basic model applicable for composite materials with low fibre concentration, a new formulation of this model has been developed in (Whitney, 1967) to adjust the general theory to high fibre volume composites. The "doubly embedded" model developed by the author results more realistic and mathematically tractable.

For an unidirectional ply having a longitudinal direction "L" that is parallel to the fibre direction, and a transversal direction "T", perpendicular to the fibre direction, the relationship between the constituent mechanical properties and the RVE properties are the followings:

Longitudinal Young's Modulus (E_L)

$$E_L = E_f v_f + E_m(1 - v_f) + \frac{4\left(v_{LTm} - v_{LTf}\right)^2 k_{Tf} k_{Tm} G_{TTm}(1 - v_f) v_f}{\left(k_{Tf} + G_{TTm}\right)k_{Tm} + \left(k_{Tf} - k_{Tm}\right)G_{TTm} v_f} \qquad \text{Eq. A 1}$$

Poisson's Ratio (υ_{LT})

$$\upsilon_{LT} = \upsilon_{LTf} v_f + \upsilon_{LTm}(1 - v_f) + \frac{(\upsilon_{LTm} - \upsilon_{LTf}) \quad (k_{Tm} - k_{Tf}) G_{TTm}(1 - v_f) v_f}{[(k_{Tf} + G_{TTm}) k_{Tm} + (k_{Tf} - k_{Tm}) G_{TTm} v_f]} \qquad \text{Eq. A 2}$$

Plane strain bulk modulus (k_T)

$$k_T = \frac{(k_{Tf} + G_{TTm}) k_{Tm} + (k_{Tf} - k_{Tm}) G_{TTm} v_f}{(k_{Tf} + G_{TTm}) - (k_{Tf} - k_{Tm}) v_f} \qquad \text{Eq. A 3}$$

In-Plane shear modulus (G_{LT})

$$G_{LT} = G_{LTm} \frac{[(G_{LTf} + G_{LTm}) + (G_{LTf} - G_{LTm}) v_f]}{[(G_{LTf} + G_{LTm}) - (G_{LTf} - G_{LTm}) v_f]} \qquad \text{Eq. A 4}$$

Transverse shear modulus (G_{TT})

$$G_{TT} = \frac{G_{TTm}[k_{Tm}(G_{TTm} + G_{TTf}) + 2 G_{TTf} G_{TTm} + k_{Tm}(G_{TTf} - G_{TTm}) v_f]}{[k_{Tm}(G_{TTm} + G_{TTf}) + 2 G_{TTf} G_{TTm} - (k_{Tm} + 2 G_{TTm})(G_{TTf} - G_{TTm}) v_f]} \qquad \text{Eq. A 5}$$

Transverse Young's Modulus (E_T)

$$E_T = E_m \left[\frac{1}{4 k_T} + \frac{1}{4 G_{TT}} + \frac{E_L}{{\upsilon_{LT}}^2}\right]^{-1} \qquad \text{Eq. A 6}$$

Transverse Poisson's Ratio (υ_{TT})

$$\upsilon_{TT} = \left[\frac{2 E_L k_T - E_L E_T - 4 E_T k_T {\upsilon_{LT}}^2}{2 E_L k_T}\right] \qquad \text{Eq. A 7}$$

In *Eq. A 1*-*Eq. A 7* the subscripts indices *f* is relative to fibre properties, while *m* is for matrix properties. The previous equations allow calculating longitudinal and transversal mechanical properties from the constituents properties and the fibre volume v_f in the composite ply. For the calculation of the thermal properties as well as the expansion coefficients in transverse and longitudinal directions, the equations proposed in (Schapery, 1968) have been employed:

Thermal expansion coefficient in the longitudinal direction (α_L)

$$\alpha_L = \frac{\alpha_f E_f v_f + \alpha_m E_m (1 - v_f)}{E_f v_f + E_m (1 - v_f)} \qquad \text{Eq. A 8}$$

Thermal expansion coefficient in the transverse direction (α_T)

$$\alpha_T = \alpha_f v_f(1+\upsilon_f) + \alpha_m(1-v_f)(1+\upsilon_m) - \alpha_L\left[(1-v_f)\upsilon_m + v_f\upsilon_f\right] \quad \text{Eq. A 9}$$

For the calculation of properties in longitudinal and transverse direction for a composite ply having a volume fraction of v_f = 0.66 (*cf.* Chapter 2), the fibre are considered perfectly isotropic and the mechanical and thermal properties are issued from (Berthelot, 1999) and reported in *Table A. 1*. Also the matrix is considered as isotropic and a value for the Poisson's ratio of υ_m=0.3 and thermal expansion coefficient of α_m=5·10^{-5} K^{-1} in accord to (Minervino, 2013) have been used for composite properties calculus. Finally, the Young's *modulus* of the matrix issued from the DMA tests reported in Chapter 1 at 150°C (E_m=2.32GPa) have been employed. All the matrix properties are resumed in *Table A. 2*.

From the constituent's properties and using the relations of *Eq. A 1* - *Eq. A 9* the homogenised mechanical and thermal properties of the ply are calculated and the results reported in *Table A. 3*.

Properties	**Value**
Young's Modulus $\mathbf{E_f}$ [GPa]	240
Shear Modulus $\mathbf{G_f}$ [GPa]	100
Poisson's Ratio $\boldsymbol{\upsilon_f}$	0.2
Thermal expansion coefficient $\boldsymbol{\alpha_f}$ [°K^{-1}]	-0.1·10^{-6}

Table A. 1 : Mechanical and thermal properties for HTS40 carbon fibres

Properties	**Value**
Young's Modulus $\mathbf{E_m}$ [GPa] **(T=150°C)**	2.32
Shear Modulus $\mathbf{G_m}$ [GPa]	1.67
Poisson's Ratio $\boldsymbol{\upsilon_m}$	0.3
Thermal expansion coefficient $\boldsymbol{\alpha_m}$ [°K^{-1}]	5·10^{-5}

Table A. 2 : Mechanical and thermal properties for TACTIX742 matrix at **T=150°C.**

	Longitudinal direction (plane LT)	**Transverse direction (plane TT)**
Young's Modulus **E** [GPa]	159.2	13.8
Shear Modulus **G** [GPa]	7.6	5.85
Poisson's Ratio **υ**	0.22	0.18
Thermal expansion coefficient **α** [$°K^{-1}$]	$1.5 \cdot 10^{-7}$	$1.4 \cdot 10^{-5}$

Table A. 3 : Mechanical and thermal homogenized properties for a composite ply HTS40 carbon fibre/TACTIX742 epoxy matrix at **T=150°C.**

Appendix B – Fatigue test on laminated composites - A damage tolerant approach

Crack multiplication kinetic is quite affected by the environment, thus a plot of the crack multiplication rates in the different test conditions as a function of the energy release rate related to actual specimen *damage state* (in terms of crack density) and the applied solicitation ΔG(σ,d), could be used in a potential damage tolerant approach where the (aging)-time becomes an intrinsic parameter.

In *Fig.B. 1* the crack multiplication rate and the ΔG are calculated by the *Eq. B 1* and *Eq. B 2*:

$$\Delta G(\sigma\ ,D)_i = G\left(\sigma^f_{MAX}, D_i\right) - G(\sigma^f_{min}, D_i) \qquad \text{Eq. B 1}$$

where σ^f_{min} is the minimum fatigue stress.

$$\left(\frac{\Delta D}{\Delta N}\right)_i = \frac{D_i - D_{i-1}}{N_i - N_{i-1}} \qquad \text{Eq. B 2}$$

The data reported in *Fig.B. 1* show a common feature: as the ΔG decreases, the crack multiplication rate also decreases. High values of ΔD/ΔN are associated to the early steps of the test and to the more high values of ΔG. the proposed method is based on a Paris like description of crack multiplication.

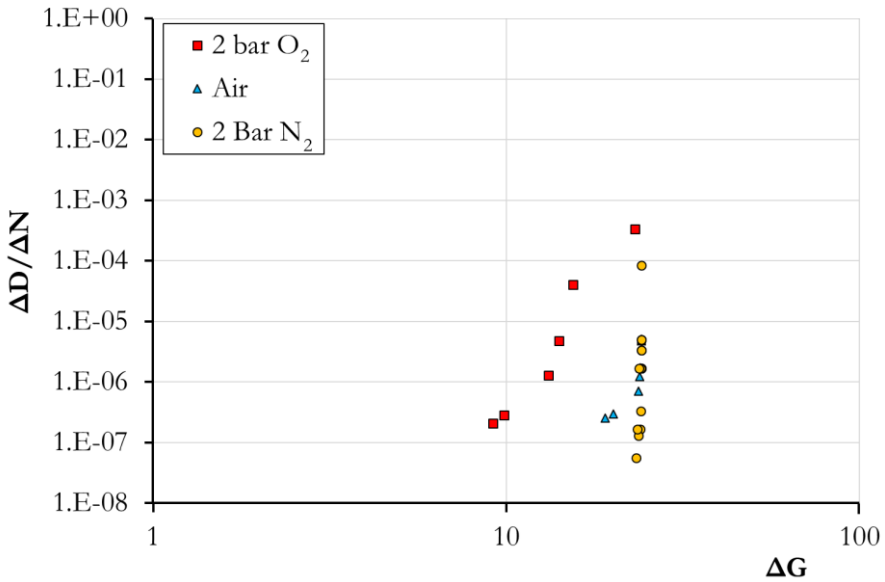

Fig.B. 1 : Crack multiplication rate as a function of the fatigue energy rate (semi-logarithmic graph). The higher values for ΔG are associated to the higher crack multiplication rate.

As for the classical application of this formula, it is excluded here the description of the saturation step for crack multiplication. The Paris approach is resumed in *Eq. B 3*.

$$\frac{\Delta D}{\Delta N} = C \times (\Delta G)^n \qquad \text{Eq. B 3}$$

The values for the two coefficients *C* and *n* for the three tested specimens are reported in *Table. B 1*, these parameters are chosen to fit data in the graph of *Fig.B. 1*. The results of the interpolation are reported in *Fig.B. 2*, while the evolution of the D as a function of the fatigue cycles for the three tested specimens, obtained by integration of *Fig.B. 1*, is reported in *Fig.B. 3*.

	C	**n**
2 bar O_2	2×10^{-15}	8.2
Air	2×10^{-27}	15.32
2 bar N_2	1.48×10^{-230}	161.9

Table. B 1 : Parameters for the description of crack multiplication for the three tested specimens during fatigue.

The interpolation parameters chosen for the 2 bar N_2 and 2 bar O_2 specimens give a good description of the evolution of $\Delta D/\Delta N$ and consequently of the evolution of D as a function of the number of cycles. For the air specimen, the interpolation in *Fig.B. 2* fits only the points relative to the beginning and the end of the test, but despite this the resulting description in terms of damage evolution is satisfactory also for the points relative to the acceleration of damage evolution detected after 800k cycles. The coefficients used to describe the air specimen behaviour are similar to the parameters used for the 2 bar O_2 specimen, testifying that for long test durations, the oxidation effect is remarkable also for a fatigue test in air. Fatigue data plotted as made in *Fig.B. 2* and *Fig.B. 3* do not allows evaluating the environment impact during fatigue of UD cross-ply composite. However the curves plotted in *Fig.B. 2* could be used in a damage tolerant approach to fix the maintenance interval for components exposed to the tested environmental conditions.

The same approach could be proposed for the woven specimen by using the evolution of the damaged-material strain energy instead of the energy release rate employed for the cross-ply UD based laminates.

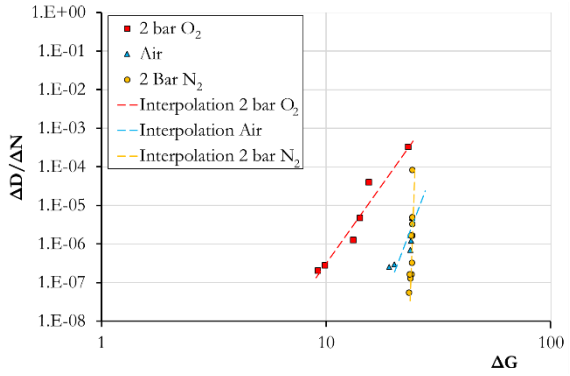

Fig.B. 2 : Crack multiplication rate as a function of the fatigue energy rate (logarithmic graph). Data interpolation using a Paris like function.

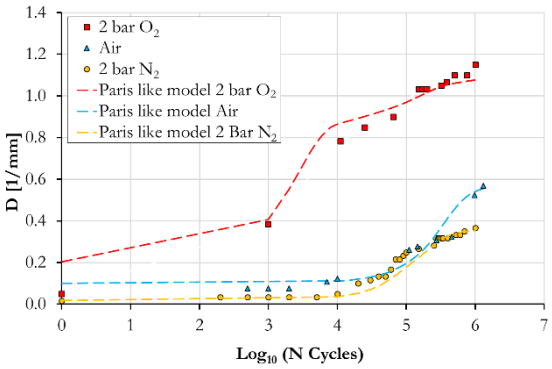

Fig.B. 3 : Evolution of D as a function of the fatigue cycle obtained by integration of the Paris like law.

Appendix C – Woven composite mechanical properties - Finite Element model

In this appendix the segmentation result of matrix, warp and weft tows detailed in Chapter 2 have been employed to extract the geometrical model from a 3D image. A voxel-like meshing is used to obtain a FE model from segmentation results. The segmentation resolution is decreased by 8 times to reduce the voxel number in the FE model, without any important modification of the tow and resin ratios in the composite at the meso-scale. Further details about the FE model employed in this work are reported in (Sinchuk et al., 2017) and *Fig.C. 1*. Simulations have been carried out on a unit cell model of the woven composite, the dimensions of the segmented unit cell were 9.8×8.7×1.73 mm^3 giving a FE model including 206×182×36 (1349712) elements. The tows are supposed orthotropic and the homogenized mechanical properties are calculated using the homogenization equations reported in Appendix-A, while the matrix is supposed a homogeneous material.

The Young *modulus* of the matrix has been chosen by simulating a traction test on the woven unit cell. The linear region of the stress-strain curve reported in *Fig.4 2* has been fit from 0 to 0.1% of longitudinal strain using an elastic *modulus* of the matrix E_m=2.5GPa and a Poisson coefficient ν_m=0.3.

In default of more information on the resin mechanical response, the FE model is the only way to have a Young *modulus* for the resin to use as input for the homogenised property calculation step for the analytical model presented in Chapter 5. FE values presented in this paragraph represent the initial values for the elastic longitudinal *modulus* and stabilized values for the shear secant *modulus* issued by the experimental activity. A comparison between experimental, numerical and analytical specimen properties is proposed in Appendix-D.

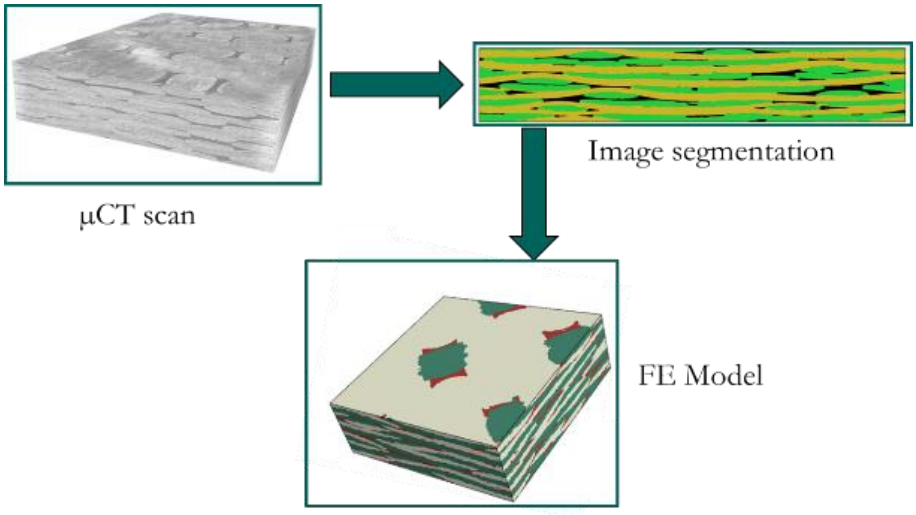

Fig.C. 1 : FE model issued by a µCT scan of a composite unit cell. A mesh is directly created using the image segmentation.

A first simulation have been carried out on the [45_6] woven unit cell in order to characterize the stress distribution in the tows. A cooling from the free stress temperature (T_G=330°C) to the test temperature (T=250°C) followed by the application of a traction load $\sigma=\sigma^f_{MAX}$ have been simulated. The results are in *Eq. C. 1* for the weft and the warp tows (average values for all the weft and warp tow in the unit cell).

$$\boldsymbol{\sigma} = \begin{bmatrix} \sigma_{11} \\ \sigma_{22} \\ \sigma_{33} \\ \sigma_{12} \\ \sigma_{13} \\ \sigma_{23} \end{bmatrix} \quad \sigma_{warp} = \begin{bmatrix} 45 \\ 16 \\ 0.4 \\ -40 \\ 0 \\ 0.2 \end{bmatrix} \quad \sigma_{weft} = \begin{bmatrix} 62 \\ 12 \\ 0 \\ 40 \\ 0 \\ -0.2 \end{bmatrix} \qquad \text{Eq. C. 1}$$

For the application of the analytical model in the Chapter 5, the knowledge of the thermal strains in the composite is needed. These are reported in *Eq. C. 2*.

$$\boldsymbol{\varepsilon}^{th} = \begin{bmatrix} \varepsilon_{11} \\ \varepsilon_{22} \\ \varepsilon_{33} \\ \varepsilon_{12} \\ \varepsilon_{13} \\ \varepsilon_{23} \end{bmatrix} \quad \varepsilon^{th}_{warp} = \begin{bmatrix} -9 \\ -42 \\ -170 \\ 0.9 \\ -0.3 \\ 2 \end{bmatrix} \times 10^{-5} \quad \varepsilon^{th}_{weft} = \begin{bmatrix} -5 \\ -62 \\ -170 \\ 1.9 \\ -0.8 \\ -1.4 \end{bmatrix} \times 10^{-5} \qquad \text{Eq. C. 2}$$

The same unit cell model has been used to extract the stiffness matrix of the woven specimens along the fibre direction. The numerical homogenization of the elastic properties (Young and shear *moduli* and Poisson coefficient) has been implemented using periodic boundary condition (PBC) constrains. The "classical" form for the displacement on the boundary surface using PBC equations is in *Eq. C.3*:

$$u_i^{k+} - u_i^{k-} = \varepsilon_{ij}^0 (x_j^{k+} - x_j^{k-}) \qquad \text{Eq. C. 3}$$

where indices *k*+ and *k*- identify the k^{th} pair of two opposite parallel boundary surfaces of the FE model, ε^0_{ij} is the global (average) strain tensor, x_j are the Cartesian coordinates of a material point and u_i are the displacements, finally *i* and *j* are the index 1, 2 and 3 corresponding to the directions X, Y and Z (*see Fig.4 1*). Applying 6 different value for ε^0_{ij} (3 for pure normal and 3 for pure shear strains), 6 average stresses are obtained. From the applied strain and the resulting average stresses, the complete stiffness matrix **C** for the [0_6] woven unit cell is obtained.

$$\boldsymbol{C} = \begin{bmatrix} 68.7 & 3.1 & 3.5 & 0 & 0 & 0 \\ 3.1 & 57.8 & 3.4 & 0 & 0 & 0 \\ 3.5 & 3.4 & 9 & 0 & 0 & 0 \\ 0 & 0 & 0 & 3.7 & 0 & 0 \\ 0 & 0 & 0 & 0 & 2.9 & 0 \\ 0 & 0 & 0 & 0 & 0 & 2.9 \end{bmatrix} \text{GPa} \qquad \text{Eq. C. 4}$$

The terms corresponding to the normal shear strain coupling are quite small compared to the other coefficients. Assuming the orthotropic conditions and plane stress state, the reduced stiffness matrix for the 45° woven allows calculating the material mechanical properties.

Appendix D – Shear properties for woven composites

In order to plot stress/strain curve in the shear direction, the stress state of the woven specimens is calculated using an analytical model. In the following description, each woven ply is approximated by the superposition of two layers of unidirectional plies. By these approximation, the stress state in the woven could be studied in the same way as the stress state for an angle ply laminate. The stress along the fibre direction in an angle ply laminate can be calculated from the stress transformation equations giving the relationship between stresses expressed in global coordinates and principal material coordinates for an unidirectional layer (C.T. Herakovich, 1998):

$$\sigma_x = c^2\sigma_1 + s^2\sigma_2 - 2cs\tau_{12} \quad \text{Eq. D. 1}$$

$$\sigma_y = s^2\sigma_1 + c^2\sigma_2 + 2cs\tau_{12} \quad \text{Eq. D. 2}$$

$$\tau_{xy} = cs\sigma_1 + cs\sigma_2 + (c^2 - s^2)\tau_{12} \quad \text{Eq. D. 3}$$

where c and s are $cos(\theta)$ and $sin(\theta)$ respectively. When an angle ply laminate is loaded along the Y direction, the $+\theta$ and $-\theta$ layers should respect the following equilibrium condition:

$$0 = c^2\sigma_1 + s^2\sigma_2 - 2cs\tau_{12} \quad \text{Eq. D. 4}$$

$$\sigma_y = s^2\sigma_1 + c^2\sigma_2 + 2cs\tau_{12} \quad \text{Eq. D. 5}$$

From *Eq. D. 4* and *Eq. D. 5* using the trigonometric identity $s^2+c^2=1$:

$$\sigma_y = \sigma_1 + \sigma_2 \quad \text{Eq. D. 6}$$

Finally the stresses in the $+\theta$ layer are function also of the strains in the $-\theta$ layer. The procedure, well detailed in (C.T. Herakovich, 1998), gives:

$$\sigma_1 = B\sigma_y \quad \text{Eq. D. 7}$$

$$\sigma_2 = (1 - B)\sigma_y \quad \text{Eq. D. 8}$$

$$\tau_{12} = -\frac{1}{2cs}[B(1 - 2c^2) + c^2]\sigma_y \quad \text{Eq. D. 9}$$

where B is a parameter combining material properties (Young *moduli* in two principal material directions E_1 and E_2 and the Poisson coefficient υ_{12}) and trigonometric identities. For $\theta=45$ it is:

$$B = \left[\frac{\frac{E_2}{E_1}\upsilon_{12} + 1}{2\frac{E_2}{E_1}\upsilon_{12} + \frac{E_2}{E_1} + 1}\right] \qquad \text{Eq. D. 10}$$

that for $E_1>>E_2$ (as for a $\theta=45$ layer) is $B\rightarrow 1$. Referring to *Fig.4. 1*, on the DIC surface, the stress state could be obtained from *Eq. D. 7* - *Eq. D. 9* in which the stresses are expressed in principal material coordinates (*see Fig.4. 1*) and are:

$$\boldsymbol{\sigma} = \begin{bmatrix}\sigma_1 \\ \sigma_2 \\ \tau_{12}\end{bmatrix} = \begin{bmatrix}\sigma_y \\ 0 \\ -\sigma_y/2\end{bmatrix} \qquad \text{Eq. D. 11}$$

The stress state of *Eq. D. 11* is valid when σ_x and τ_{xy} are zero, consequently, to measure the plane shear *modulus* G_{12}, a tensile test on a $[45_6]$ woven specimen is enough. In fact the shear strain γ_{12} is given by transformation of the measured axial (ε_y) and transversal strains (ε_x). The strain transformation from the laminate theory gives:

$$\gamma_{12} = (\varepsilon_x - \varepsilon_y) \qquad \text{Eq. D. 12}$$

hence:

$$G_{12} = -\frac{\sigma_y}{2(\varepsilon_x - \varepsilon_y)} \qquad \text{Eq. D. 13}$$

DIC strain data points for the quasi-static intermediate tensile load/unload cycles do not allow evaluating material properties in the early stages of traction, hence only the secant shear *modulus* (G_{12}^{sec}) is used to characterize transversal behaviour.

Appendix E – Ratcheting strain

The evolution of the minimal fatigue strain (ε_{min_y} see *Fig.4. 6*) obtained by the test machine head displacement of the air specimen during fatigue from the start of the test to the first specimen removal for μCT scan is shown in *Fig.E 1*. The evolution of ε_{min_y} for the air specimen of *Fig.E 1* is representative of the ε_{min_y} evolution seen also for the 2 bar N_2 and 2 bar O_2 specimen.

The trend seen in *Fig.E 1* is the same of (Bouvet et al., 2013) where two domains are identified for the ratcheting strain evolution. In the former, as the ratcheting strain increases the ratcheting strain rate decreases. In the second stage, the ratcheting strain rate remains constant and while the ratcheting strain increases and generally the ratcheting strain levels attained at the end for this stage are more important than for the previous stage. In the same article, this ratcheting strain is directly linked to the deformation of the amorphous ligaments of the polymer and consequently to a plastic deformation of the specimen. As explained in (Lin, Chen and Zhang, 2011), the ratcheting is load history dependent and the magnitude of the strain increases as the temperature increases (Zhang, Chen and Wang, 2010).

In the timeframe of *Fig.E 1*several stops for quasi-static load/unload cycles have been performed and for each interruption, a recovery stage is present. In the dotted square of *Fig.E 1* the red dots report the minimal strain values at the restart of fatigue just after the quasi-static cycle. To better see this effect, after 100k cycles, the fatigue test was stopped for 10 hours.

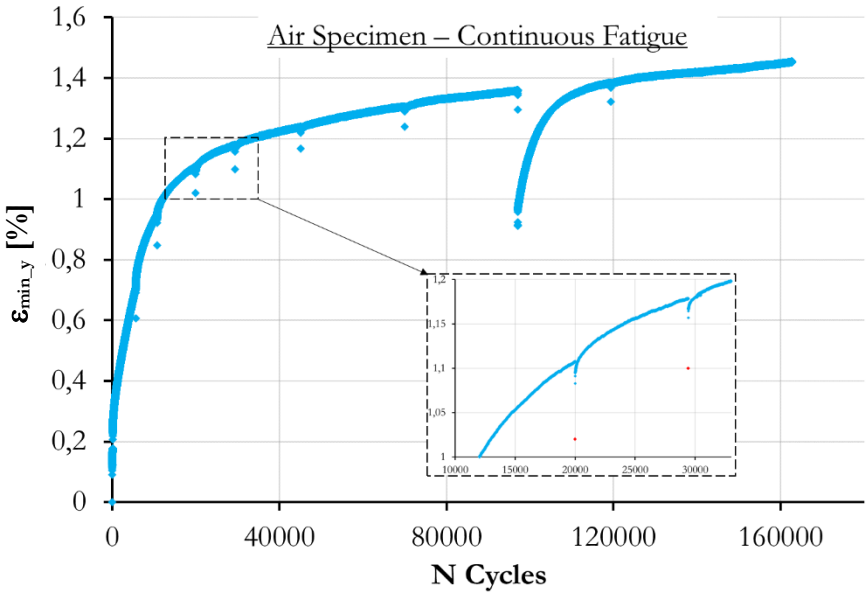

Fig.E 1 : Evolution of the minimum strain (ε_{min_y}) for the air specimen during continuous fatigue. The ε_{min_y} evolution is representative for all the tested specimen in continuous and discontinuous fatigue.

The recovery magnitude is quite visible at this stage, the minimal strain descends of 0.44%. This kind of reduction is also observed in (Tao and Xia, 2007) where the authors tested a pure resin sample in fatigue with multiple resting periods. In the zero-load applied stages, a recovery of the cumulated ratcheting strain was measured, but when the fatigue test restarted, the ratcheting strain grown up until a value that was the same obtained on the specimen tested in fatigue without resting periods. The authors conclude that the ratcheting strain of pure resin is the sum of a viscoelastic and a viscoplastic deformation and only the latter is correlated to a detrimental effect of fatigue life.

In other words, the DIC and the μCT scan stops does not affect the viscous response of the specimens, this means that in terms of ε_{min_y} evolution, continuous and discontinuous specimens have the same behaviour. Nevertheless after each μCT scan stop, the viscoelastic part of ε_{min_y} is recovered and when the test restarts after the μCT scan, the specimen ε_{min_y} value achieved before the stop is reached after 20/30k cycles (*see Fig.E 1*). Concerning the evolution of mechanical specimen properties, the trends seen in *Fig.4. 12-Fig.4. 15* does not show an effect linked to the μCT scan stops: the E_y^{sec} at the restart of fatigue, has the same value it has before the stop and the same goes for E_y^{ch}, G_{12}^{sec} and A.

Appendix F – Virtual ply mechanical properties

The mechanical properties for the virtual unidirectional ply are calculated using the homogenization equations and the fibre volume fraction in the composite reported in the Appendix A. The fibre and the matrix are considered isotropic and the fibre mechanical properties are taken from (Thornel). Fibre thermal properties are issued from (Berthelot, 1999), while for the matrix, the thermal expansion coefficient are taken from (Minervino, 2013). Moreover the Poisson coefficient and the Young *modulus* for the matrix, the values obtained by the FE model presented in Appendix-C are used. The phases properties at the test temperature (T=250°C) are resumed in Table F. *1*.

Phases Properties	**T650-35 Fibre**	**MVK-14 Matrix**
Young Modulus E [MPa]	240000	2500 (by FEM)
Poisson ratio υ	0.2	0.3 (by FEM)
Shear modulus G(*) [MPa]	100000	961 (by FEM)
Thermal expansion coefficient α [K^{-1}]	-10^{7}	$5 \cdot 10^{-5}$

$* \; G = \frac{E}{2(1+\upsilon)}$

Table F. 1 : Mechanical and thermal properties for T650-35 carbon fibre and MVK-14 resin at **250°C**

For the unidirectional ply stiffness matrix, the assumptions reported in (C.T. Herakovich, 1998) are employed: the unidirectional ply is considered as an orthotropic lamina having negligible out-of-plane stress components. Using the plane stress approximation the reduced stiffness matrix for the orthotropic lamina is $\bar{\mathbf{Q}}$ where the index 1 and 2 are referred to the material coordinates illustrated in *Fig.F. 1*.

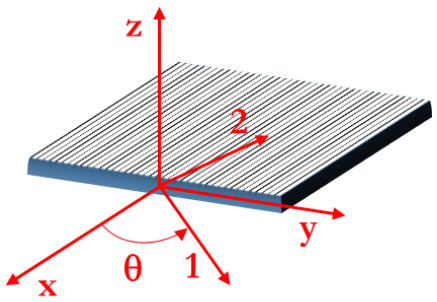

Fig.F. 1 : Global and principal material coordinates.

$$\bar{\mathbf{Q}} = \begin{bmatrix} \bar{Q}_{11} & \bar{Q}_{12} & \bar{Q}_{16} \\ \bar{Q}_{12} & \bar{Q}_{22} & \bar{Q}_{26} \\ \bar{Q}_{16} & \bar{Q}_{26} & \bar{Q}_{66} \end{bmatrix} \qquad \text{Eq.F 1}$$

that in the principal material coordinates is reduced to **Q**:

$$Q = \begin{bmatrix} Q_{11} & Q_{12} & 0 \\ Q_{12} & Q_{22} & 0 \\ 0 & 0 & Q_{66} \end{bmatrix} \quad \text{Eq.F 2}$$

The coefficients Q_{ij} are calculated starting from the engineering constants issued from the homogenization equations using the fibre volume fraction calculated in Chapter 2 for the composite and using the following equations:

$$Q_{11} = \frac{E_1}{1 - v_{12}v_{21}} \quad \text{Eq.F 3}$$

$$Q_{22} = \frac{E_2}{1 - v_{12}v_{21}} \quad \text{Eq.F 4}$$

$$Q_{12} = \frac{v_{21}E_1}{1 - v_{12}v_{21}} = \frac{v_{12}E_2}{1 - v_{12}v_{21}} \quad \text{Eq.F 5}$$

$$Q_{66} = G_{12} \quad \text{Eq.F 6}$$

where:

$$\frac{E_2}{v_{21}} = \frac{E_1}{v_{12}} \quad \text{Eq.F 7}$$

The corresponding stiffness matrix for the virtual unidirectional ply at 250°C oriented along the 0° direction and the 90° direction will be named Q_0 and Q_{90} respectively. The woven ply stiffness is then obtained by virtual superposition of 0° and 90° plies as for an angle-ply, neglecting the weaving region of the real woven ply. Considering the warp and weft tow fraction (n_0 and n_{90} respectively) in the composite obtained by µCT scan segmentation reported in Chapter 2, the ply stiffness matrix Q_{ply} could be calculated as:

$$Q_{ply} = n_0 Q_{UD}^0 + n_{90} Q_{UD}^{90} \quad \text{Eq.F 8}$$

The stiffness matrix for the woven ply having the fibre oriented in the 45° direction, named Q^{45}_{ply}, is calculated using the rotation matrix T_1 and T_2:

$$T_1 = \begin{bmatrix} c^2 & s^2 & 2cs \\ s^2 & c^2 & -2cs \\ -cs & cs & c^2 - s^2 \end{bmatrix} \quad \text{Eq.F 9}$$

$$T_2 = \begin{bmatrix} c^2 & s^2 & -cs \\ s^2 & c^2 & cs \\ 2cs & -2cs & c^2 - s^2 \end{bmatrix} \quad \text{Eq.F 10}$$

$$Q_{ply}^{45} = T_1^{-1} Q_{ply} T_2 \quad \text{Eq.F 11}$$

with c=cosθ and s=sinθ. The specimen stiffness matrix is finally obtained using the following expression:

$$\begin{Bmatrix} N \\ M \end{Bmatrix} = \begin{Bmatrix} A & B \\ B & D \end{Bmatrix} \begin{Bmatrix} \varepsilon \\ k \end{Bmatrix} \quad \text{Eq.F 12}$$

where N and M are matrix representing the in-plane force per unit length and moment per unit length respectively. A is the matrix representing the in-plane stiffness, B defines the bending-stretching coupling and D is the bending stiffness matrix. Finally, ε represents the mid-plane strains and k the laminate curvature. The explicit expression for these terms is reported in (C.T. Herakovich, 1998).

In the following analysis each woven ply is considered as a heterogeneous material along the thickness direction, in other words there is no reasons to suppose that a coupling between the in-plane response and the bending response exists. Consequently the B matrix is null, as for laminate symmetric about their mid-plane. Moreover in the follow, the D matrix will be neglected being null the applied bending moments. *Eq.F 13* is employed for the A matrix calculation.

$$A_{45} = \sum_{i=1}^{l} Q_{ply\_i}^{45} \times t_{ply\_i} \quad \text{Eq.F 13}$$

In *Eq.F 13* t_{ply_i} is the thickness of the ply *i*, l is the number of woven plies in the specimen and A_{45} is the specimen stiffness matrix. The results obtained for E_m=2.5 GPa and υ_m=0.3 are reported in *Table F. 2*.

Experimental		FE model		Analytical model	
E_y^{ch}	G_{12}^{sec}	E_y^{ch}	G_{12}^{sec}	E_y^{ch}	G_{12}^{sec}
13.9	3.8	13.9	4.2	13.7	3.76

Table F. 2 : Experimental, FE model and analytical model founding on longitudinal elastic modulus and secant shear modulus of the woven composite.

In the values in *Table F. 2* the comparison between experimental and analytical founding is made considering the initial elastic longitudinal *modulus* and the stabilized value of the secant shear *modulus*, which is the secant shear *modulus* value after 50k/70k cycles. As could be remarked, the found values for the composite mechanical properties issued from the analytical model, despite the assumptions on the fibre architecture, are quite close to the experimental ones.

Bibliography

Adden, S., & Horst, P. (2010). Stiffness degradation under fatigue in multiaxially loaded non-crimped-fabrics. International Journal of Fatigue, 32(1), 108–122. https://doi.org/10.1016/j.ijfatigue.2009.02.002

Albouy, W., Vieille, B., & Taleb, L. (2014a). Influence of matrix ductility on the high-temperature fatigue behavior of off-axis woven-ply thermoplastic and thermoset laminates. International Journal of Fatigue, 63, 85–96. https://doi.org/10.1016/j.ijfatigue.2014.01.010

Albouy, W., Vieille, B., & Taleb, L. (2014b). Influence of matrix ductility on the high-temperature fatigue behaviour of quasi-isotropic woven-ply thermoplastic and thermoset laminates. Composites Part A: Applied Science and Manufacturing, 67, 22–36. https://doi.org/10.1016/j.compositesa.2014.07.012

Al-Haik, M., Vaghar, M. R., Garmestani, H., & Shahawy, M. (2001). Viscoplastic analysis of structural polymer composites using stress relaxation and creep data. Composites Part B: Engineering, 32(2), 165–170. https://doi.org/10.1016/S1359-8368(00)00042-1

Amiot, F., Bornert, M., Doumalin, P., Dupré, J.-C., Fazzini, M., Orteu, J. J., … Wienin, J. S. (2013). Assessment of digital image correlation measurement accuracy in the ultimate error regime: Main results of a collaborative benchmark. Strain, 49(6), 483–496. https://doi.org/10.1111/str.12054

Asp, L. E., Berglund, L. a., & Talreja, R. (1996a). A criterion for crack initiation in glassy polymers subjected to a composite-like stress state. Composites Science and Technology, 56(11), 1291–1301. https://doi.org/10.1016/S0266-3538(96)00090-5

Asp, L. E., Berglund, L. a., & Talreja, R. (1996b). Prediction of matrix-initiated transverse failure in polymer composites. Composites Science and Technology, 56(9), 1089–1097. https://doi.org/10.1016/0266-3538(96)00074-7

Axelsson, M., Svensson, S., & Borgefors, G. (2006). Reduction of ring artifacts in high resolution X-ray microtomography images. Pattern Recognition, 61–70. Retrieved from http://link.springer.com/chapter/10.1007/11861898_7

Backe, D., Balle, F., & Eifler, D. (2015). Ultrasonic Fatigue of Carbon Fiber Fabric Reinforced Polyphenylene Sulfide in the Very High Cycle Fatigue Regime : Test Procedure and Microstructural Analysis. In 20th International Conferenceon Composite Materials. Copenhagen.

Badel, P., Sallé, E. V., Maire, E., & Boisse, P. (2009). Simulation and tomography analysis of textile composite reinforcement deformation at the mesoscopic scale. International Journal of Material Forming, 2(SUPPL. 1), 189–192. https://doi.org/10.1007/s12289-009-0572-z

Barburski, M., Straumit, I., Zhang, X., Wevers, M., & Lomov, S. V. (2015). Micro-CT analysis of internal structure of sheared textile composite reinforcement. Composites Part A: Applied Science and Manufacturing, 73, 45–54. https://doi.org/10.1016/j.compositesa.2015.03.008

Barranger, Y., Doumalin, P., Dupré, J. C., & Germaneau, A. (2012). Strain measurement by digital image correlation: Influence of two types of speckle patterns made from rigid or deformable marks. Strain, 48(5), 357–365. https://doi.org/10.1111/j.1475-1305.2011.00831.x

Baruchel, J., Buffiere, J. Y., Maire, E., Merle, P., & Peix, G. (2000). X Ray Tomography in Material Science, 204.

Batenburg, K. J., & Sijbers, J. (2011). DART: a practical reconstruction algorithm for discrete tomography. IEEE Transactions on Image Processing : A Publication of the IEEE Signal Processing Society, 20(9), 2542–53. https://doi.org/10.1109/TIP.2011.2131661

Berthelot, J. M., El Mahi, A., & Leblond, P. (1996). Transverse cracking of cross-ply laminates: Part 2. Progressive widthwise cracking. Composites Part A: Applied Science and Manufacturing, 27(10), 1003–1010. https://doi.org/10.1016/1359-835X(96)00064-4

Berthelot, J. M., & Le Corre, J. F. (2000). Statistical analysis of the progression of transverse cracking and delamination in cross-ply laminates. Composites Science and Technology, 60(14), 2659–2669. https://doi.org/10.1016/S0266-3538(00)00140-8

Berthelot, J.-M. (1999). Composite Materials : Mechanical Behavior and Structural Analysis. Springer New York.

Berthelot, J.-M., Leblond, P., El Mahi, A., & Le Corre, J.-F. (1996). Transverse cracking of cross-ply laminates: Part 1. Analysis. Composites Part A: Applied Science and Manufacturing, 27(10), 989–1001. https://doi.org/10.1016/1359-835X(96)80002-A

Blitz, J., & Simpson, G. (1995). Ultrasonic Methods of Non-destructive Testing. Springer Science & Business Media. Retrieved from https://books.google.co.uk/books/about/Ultrasonic_Methods_of_Non_destructive_Te.html?id=d3WWect9zQEC&pgis=1

Böhm, R., Stiller, J., Behnisch, T., Zscheyge, M., Protz, R., Radloff, S., … Hufenbach, W. (2015). A quantitative comparison of the capabilities of in situ computed tomography and conventional computed tomography for damage analysis of composites. Composites Science and Technology, 110, 62–68. https://doi.org/10.1016/j.compscitech.2015.01.020

Book, R., Hoppe, S., Scherl, H., & Hornegger, J. (2007). Beam Hardening Correction with an Iterative Scheme Using an Exact Backward Projector and a Polychromatic Forward Projector, (February 2007). https://doi.org/10.1007/978-3-662-46224-9

Bornert, M., Brémand, F., Doumalin, P., Dupré, J. C., Fazzini, M., Grédiac, M., … Wattrisse, B. (2009a). Assessment of digital image correlation measurement errors: Methodology and results. Experimental Mechanics, 49(3), 353–370. https://doi.org/10.1007/s11340-008-9204-7

Bornert, M., Brémand, F., Doumalin, P., Dupré, J.-C., Fazzini, M., Grédiac, M., … Wattrisse, B. (2009b). Assessment of Digital Image Correlation Measurement Errors: Methodology and Results. Experimental Mechanics, 49(3), 353–370. https://doi.org/10.1007/s11340-008-9204-7

Bouvet, G., Douminge, L., Feaugas, X., Touzain, S., & Mallarino, S. (2013). Fluorescence spectroscopy applied to study cyclic creep behaviour and internal stresses of semi-crystalline high-density polyethylene. Journal of Applied Physics, 113(2). https://doi.org/10.1063/1.4773529

Bowles, K. J. (1998). Thermal and Mechanical Durability of Graphite-Fiber-Reinforced PMR-15 Composites. NASA Tech. Memo., (July). Retrieved from https://ntrs.nasa.gov/archive/nasa/casi.ntrs.nasa.gov/19970035062.pdf

Bowles, K. J., Jayne, D., Leonhardt, T. A., & Park, B. (1993). Thermal Stability Relationships Between PMR-15 Resin and Its Composites. Cleveland, OHIO. Retrieved from https://ntrs.nasa.gov/archive/nasa/casi.ntrs.nasa.gov/19940017015.pdf

Bowles, K. J., McCorkle, L., & Ingrahm, L. (1998). Comparison of graphite fabric reinforced PMR-15 and avimid N composites after long-term isothermal aging at various temperatures. Journal of Advanced Materials. Cleveland, OHIO.

Bowles, K. J., & Meyers, A. (1986). Specimen geometry effects on graphite/ PMR-15 composites during thermo-oxidative ageing. International SAMPE, 3, 1285. Retrieved from https://ntrs.nasa.gov/archive/nasa/casi.ntrs.nasa.gov/19860008007.pdf

Bowles, K. J., Tsuji, L., Kamvouris, J., & Roberts, G. D. (2003). Long-Term Isothermal Aging Effects on Weight Loss, Compression Properties, and Dimensions of T650–35 Fabric-Reinforced PMR–15 Composites—Data. NASA Tech. Memo., 65. Retrieved from https://ntrs.nasa.gov/archive/nasa/casi.ntrs.nasa.gov/20030022738.pdf

Bruyant, P. P. (2002). Analytic and iterative reconstruction algorithms in SPECT. Journal of Nuclear Medicine : Official Publication, Society of Nuclear Medicine, 43(10), 1343–58. Retrieved from http://jnm.snmjournals.org/cgi/content/abstract/43/10/1343\nhttp://jnm.snmjournals.org/cgi/content/full/43/10/1343\nhttp://www.ncbi.nlm.nih.gov/pubmed/12368373

Buch, X., & Shanahan, M. E. R. (2000). Thermal and thermo-oxidative ageing of an epoxy adhesive. Polymer Degradation and Stability, 68(3), 403–411. https://doi.org/10.1016/S0141-3910(00)00028-8

Burgarella, B., Lahellec, N., Charles, M. F., & Lebon, J. (2015). Micromechanical modeling of damaged unidirectional composites with a full eld approach. In Comptes Rendus JNC 19 (pp. 1–9).

C.T. Herakovich. (1998). Mechanics of Fibrous Composites. (I. John Wiley & Sons, Ed.) (First).

Callister, W. D. (2007). Materials Science and Engineering an Introduction. (J. W. and Sons, Ed.) (7th ed.).

Canal, L. P., González, C., Molina-Aldareguía, J. M., Segurado, J., & Llorca, J. (2012). Application of digital image correlation at the microscale in fiber-reinforced composites. Composites Part A: Applied Science and Manufacturing, 43(10), 1630–1638. https://doi.org/10.1016/j.compositesa.2011.07.014

Carvelli, V., D'Ettorre, A., & Lomov, S. V. (2017). Acoustic emission and damage mode correlation in textile reinforced PPS composites. Composite Structures, 163, 399–409. https://doi.org/10.1016/j.compstruct.2016.12.012

Carvelli, V., Gramellini, G., Lomov, S. V., Bogdanovich, A. E., Mungalov, D. D., & Verpoest, I. (2009). Non-crimp 3D weave vs. laminated plane weave composites: tension-tension fatigue behaviour. 17th International Conference on Composite Materials (ICCM-17).

Carvelli, V., Gramellini, G., Lomov, S. V., Bogdanovich, A. E., Mungalov, D. D., & Verpoest, I. (2010). Fatigue behavior of non-crimp 3D orthogonal weave and multi-layer plain weave E-glass reinforced composites. Composites Science and Technology, 70, 2068–2076. https://doi.org/10.1016/j.compscitech.2010.08.002

Carvelli, V., Jain, A., & Lomov, S. V. (2017). Fatigue of Textile and Short Fiber Reinforced Composites (John Wiley).

Carvelli, V., & Lomov, S. V. (2015). Fatigue of Textile Composites. Fatigue of Textile Composites. Elsevier. https://doi.org/10.1016/B978-1-78242-281-5.00018-3

Carvelli, V., Pazmino, J., Lomov, S. V., Bogdanovich, A. E., Mungalov, D. D., & Verpoest, I. (2013). Quasi-static and fatigue tensile behavior of a 3D rotary braided carbon/epoxy composite. Journal of Composite Materials, 47(25), 3195–3209. https://doi.org/10.1177/0021998312463407

Chamis, C. C., & Sendeckyj, G. P. (1968). Critique on Theories Predicting Thermoelastic Properties of Fibrous Composites. Journal of Composite Materials, 2(3), 332–358. https://doi.org/10.1177/002199836800200305

Chateau, C., Gélébart, L., Bornert, M., Crépin, J., Boller, E., Sauder, C., & Ludwig, W. (2011). In situ X-ray microtomography characterization of damage in SiCf/SiC minicomposites. Composites Science and Technology, 71(6), 916–924. https://doi.org/10.1016/j.compscitech.2011.02.008

Chen, Y., Zhang, Y., Zhang, K., Deng, Y., Wang, S., Zhang, F., & Sun, F. (2016). FIRT: Filtered iterative reconstruction technique with information restoration. Journal of Structural Biology, 195(1), 49–61. https://doi.org/10.1016/j.jsb.2016.04.015

Colin, X. (2005). Kinetic modelling of the stabilizing effect of carbon fibres on thermal ageing of thermoset matrix composites. Composites Science and Technology, 65(1), 117–127. https://doi.org/10.1016/j.compscitech.2004.06.009

Colin, X., Audouin, L., & Verdu, J. (2004). Determination of thermal oxidation rate constants by an inverse method. Application to polyethylene. Polymer Degradation and Stability, 86(2), 309–321. https://doi.org/10.1016/j.polymdegradstab.2004.04.022

Colin, X., Marais, C., & Verdu, J. (2001). A new method for predicting the thermal oxidation of thermoset matrices: Application to an amine crosslinked epoxy. Polymer Testing, 20(7), 795–803. https://doi.org/10.1016/S0142-9418(01)00021-6

Colin, X., & Verdu, J. (2005). Strategy for studying thermal oxidation of organic matrix composites. Composites Science and Technology, 65(3-4), 411–419. https://doi.org/10.1016/j.compscitech.2004.09.011

Daggumati, S., Baere, I. De, Paepegem, W. Van, Degrieck, J., Xu, J., & Lomov, S. V. (2011). Local Damage in a 5 – Harness Satin Weave Composite Under Static Tension : Part I - Experimental Analysis. Composites Science and Technology, 71(8), 1–24. https://doi.org/10.1016/j.compscitech.2010.07.002

Daggumati, S., Van Paepegem, W., Degrieck, J., Praet, T., Verhegghe, B., Xu, J., … Verpoest, I. (2011). Local strain in a 5-harness satin weave composite under static tension: Part II - Meso-FE analysis. Composites Science and Technology, 71(9), 1217–1224. https://doi.org/10.1016/j.compscitech.2011.03.020

Daghia, F., Zhang, F., Cluzel, C., & Ladevèze, P. (2015). Thermo-mechano-oxidative behavior at the ply's scale: The effect of oxidation on transverse cracking in carbon-epoxy composites. Composite Structures, 134, 602–612. https://doi.org/10.1016/j.compstruct.2015.08.103

Daniel, I. M., Luo, J. J., & Schubel, P. M. (2008). Three-dimensional characterization of textile composites. Composites Part B: Engineering, 39(1), 13–19. https://doi.org/10.1016/j.compositesb.2007.02.002

De Greef, N., Gorbatikh, L., Lomov, S. V., & Verpoest, I. (2011). Damage development in woven carbon fiber/epoxy composites modified with carbon nanotubes under tension in the bias direction. Composites Part A: Applied Science and Manufacturing, 42(11), 1635–1644. https://doi.org/10.1016/j.compositesa.2011.07.013

De Vasconcellos, D., Touchard, F., & Chocinski-Arnault, L. (2014). Tension-tension fatigue behaviour of woven hemp fibre reinforced epoxy composite: A multi-instrumented damage analysis. International Journal of Fatigue, 59, 159–169. https://doi.org/10.1016/j.ijfatigue.2013.08.029

Decelle, J., Huet, N., & Bellenger, V. (2003). Oxidation induced shrinkage for thermally aged epoxy networks. Polymer Degradation and Stability, 81(2), 239–248. https://doi.org/10.1016/S0141-3910(03)00094-6

Doitrand, a., Fagiano, C., Irisarri, F. X., & Hirsekorn, M. (2015). Comparison between voxel and consistent meso-scale models of woven composites. Composites Part A: Applied Science and Manufacturing, 73, 143–154. https://doi.org/10.1016/j.compositesa.2015.02.022

Doitrand, A., Fagiano, C., Hild, F., Chiaruttini, V., Mavel, A., & Hirsekorn, M. (2017). Mesoscale analysis of damage growth in woven composites. Composites Part A: Applied Science and Manufacturing. https://doi.org/10.1016/j.compositesa.2017.02.018

Doitrand, A., Fagiano, C., Leroy, F. H., Mavel, A., & Hirsekorn, M. (2016). On the influence of fabric layer shifts on the strain distributions in a multi-layer woven composite. Composite Structures, 145(February), 15–25. https://doi.org/10.1016/j.compstruct.2016.02.054

Dong, Y., Kakisawa, H., & Kagawa, Y. (2015). Development of microscale pattern for digital image correlation up to 1400°C. Optics and Lasers in Engineering, 68, 7–15. https://doi.org/10.1016/j.optlaseng.2014.12.003

Drozdov, a. D. (2011). Cyclic viscoelastoplasticity and low-cycle fatigue of polymer composites. International Journal of Solids and Structures, 48(13), 2026–2040. https://doi.org/10.1016/j.ijsolstr.2011.03.009

Duplessis Kergomard, Y., Renard, J., Thionnet, a., & Landry, C. (2010). Intralaminar and interlaminar damage in quasi-unidirectional stratified composite structures: Experimental analysis. Composites Science and Technology, 70(10), 1504–1512. https://doi.org/10.1016/j.compscitech.2010.05.006

Dupré, J. C., Doumalin, P., Husseini, H. A., Germaneau, A., & Brémand, F. (2015). Displacement Discontinuity or Complex Shape of Sample: Assessment of Accuracy and Adaptation of Local DIC Approach. Strain, 51(5), 391–404. https://doi.org/10.1111/str.12150

efunda. (2017). eFunda: Lamina Stress-Strain Relations for Principal Directions. Retrieved July 19, 2017, from http://www.efunda.com/formulae/solid_mechanics/composites/comp_lamina_principal.cfm

ElAgamy, N., Laliberte, J., & Gaidies, F. (2015). Quantitative analysis of fatigue cracks in laminated carbon fibre-reinforced polymer composites using micro-computed tomography. Journal of Composite Materials, (October). https://doi.org/10.1177/0021998315608252

Feissel, P., Schneider, J., Aboura, Z., & Villon, P. (2013). Use of diffuse approximation on DIC for early damage detection in 3D carbon/epoxy composites. Composites Science and Technology, 88, 16–25. https://doi.org/10.1016/j.compscitech.2013.08.027

Feldkamp, L. A., Davis, L. C., & Kress, J. W. (1984). Practical cone-beam algorithm. Journal of the Optical Society of America A, 1(6), 612. https://doi.org/10.1364/JOSAA.1.000612

Fish, J., Markolefas, S., Guttal, R., & Nayak, P. (1994). On adaptive multilevel superposition of finite element meshes for linear elastostatics. Applied Numerical Mathematics, 14(1-3), 135–164. https://doi.org/10.1016/0168-9274(94)90023-X

Gabrion, X., Placet, V., Trivaudey, F., & Boubakar, L. (2016). About the thermomechanical behaviour of a carbon fibre reinforced high-temperature thermoplastic composite. Composites Part B: Engineering, 95, 386–394. https://doi.org/10.1016/j.compositesb.2016.03.068

Gamstedt, E. ., & Sjögren, B. . (1999). Micromechanisms in tension-compression fatigue of composite laminates containing transverse plies. Composites Science and Technology, 59(2), 167–178. https://doi.org/10.1016/S0266-3538(98)00061-X

Gao, F., Boniface, L., Ogin, S. L., Smith, P. a., & Greaves, R. P. (1999). Damage accumulation in woven-fabric CFRP laminates under tensile loading: Part 1. Observations of damage accumulation. Composites Science and Technology, 59(1), 123–136. https://doi.org/10.1016/S0266-3538(97)00231-5

Gao, Y., Wang, Y., Yang, X., Liu, M., Xia, H., Huai, P., & Zhou, X. (2016). Synchrotron X-ray tomographic characterization of CVI engineered 2D-woven and 3D-braided SiCf/SiC composites. Ceramics International, 42(15), 17137–17147. https://doi.org/10.1016/j.ceramint.2016.08.001

Garrett, K. W., & Bailey, J. E. (1977). Multiple transverse fracture in 90° cross-ply laminates of a glass fibre-reinforced polyester. Journal of Materials Science, 12(1), 157–168. https://doi.org/10.1007/BF00738481

Gigliotti, M., Minervino, M., & Lafarie-Frenot, M. C. (2016). Thermo-oxidative induced shrinkage in Organic Matrix Composites for High Temperature Applications: Effect of fibre arrangement and oxygen pressure. Composite Structures, 146, 176–186. https://doi.org/10.1016/j.compstruct.2016.03.007

Gigliotti, M., Minervino, M., Lafarie-Frenot, M. C., & Grandidier, J. C. (2016). Effect of Thermo-oxidation on the local mechanical behaviour of epoxy polymer materials for high temperature applications. Mechanics of Materials, 101, 1339–1351. https://doi.org/10.1016/j.mechmat.2016.07.003

Gilbert, P. (1972). Iterative methods for the three-dimensional reconstruction of an object from projections. Journal of Theoretical Biology, 36(1), 105–117. https://doi.org/10.1016/0022-5193(72)90180-4

González, S., Domínguez, J., & Lasagni, F. (2014). On the Effect of Thermal Ageing in CFRP Mechanical Properties. In ECCM16 - 16th European Conference on Composite Materials. Seville.

Gonzalez, R. C., Woods, R. W. (2007). Digital Image Processing. Education. Prentice Hall. https://doi.org/10.1049/ep.1978.0474

Gordon, R., Bender, R., & Herman, G. T. (1970). Algebraic Reconstruction Techniques (ART) for three-dimensional electron microscopy and X-ray photography. Journal of Theoretical Biology, 29(3), 471–481. https://doi.org/10.1016/0022-5193(70)90109-8

Gornet, L. (2008). Généralités sur les matériaux composites. Retrieved from https://cel.archives-ouvertes.fr/cel-00470296v1

Grail, G., Hirsekorn, M., Wendling, a., Hivet, G., & Hambli, R. (2013). Consistent Finite Element mesh generation for meso-scale modeling of textile composites with preformed and compacted reinforcements. Composites Part A: Applied Science and Manufacturing, 55, 143–151. https://doi.org/10.1016/j.compositesa.2013.09.001

Grass, M., Köhler, T., & Proksa, R. (2000). 3D cone-beam CT reconstruction for circular trajectories. Physics in Medicine and Biology, 45(2), 329–347. https://doi.org/10.1088/0031-9155/45/2/306

Grédiac, M. (2004). The use of full-field measurement methods in composite material characterization: Interest and limitations. In Composites Part A: Applied Science and Manufacturing (Vol. 35, pp. 751–761). https://doi.org/10.1016/j.compositesa.2004.01.019

Green, S. D., Matveev, M. Y., Long, a. C., Ivanov, D., & Hallett, S. R. (2014). Mechanical modelling of 3D woven composites considering realistic unit cell geometry. Composite Structures, 118, 284–293. https://doi.org/10.1016/j.compstruct.2014.07.005

Haddadi, H., & Belhabib, S. (2008). Use of rigid-body motion for the investigation and estimation of the measurement errors related to digital image correlation technique. Optics and Lasers in Engineering, 46, 185–196. https://doi.org/10.1016/j.optlaseng.2007.05.008

Hahn, H. T., & Johannesson, T. (1983). Fracture of unidirectional composites: Theory and applications. In Mechanics of Composite Materials (pp. 135–142). Retrieved from https://scholar.google.fr/scholar?cluster=13308550205500423129&hl=fr&oi=scholarr&sa=X&ved=0ahUKEwimw9qh7cHTAhUGcBoKHRcECq8QgAMIIigAMAA

Han, Y. M. M., Hahn, H. T. T., & Croman, R. B. B. (1988). A simplified analysis of transverse ply cracking in cross-ply laminates. Composites Science and Technology, 31(3), 165–177. https://doi.org/10.1016/0266-3538(88)90008-5

Handel, H. (2007). Analyzing the Influences of Camera Warm-Up Effects on Image Acquisition. Retrieved from http://download.springer.com.gate6.inist.fr/static/pdf/116/chp%253A10.1007%252F978-3-540-76390-1_26.pdf?originUrl=http%3A%2F%2Flink.springer.com%2Fchapter%2F10.1007%2F978-3-540-76390-1_26&token2=exp=1488977835~acl=%2Fstatic%2Fpdf%2F116%2Fchp%25253A10.1007

Haris, K., Efstratiadis, S. N., Maglaveras, N., & Katsaggelos, A. K. (1998). Hybrid image segmentation using watersheds and fast region merging. IEEE Transactions on Image Processing, 7(12), 1684–1699. https://doi.org/10.1109/83.730380

Haschke, M. (2014). Micro-X-Ray Fluorescence Spectroscopy. https://doi.org/10.1007/978-3-319-04864-2

Hashin, Z. (1996). Finite Thermoelastic fracture criterion with application to laminate cracking analysis. J. Mech. Phys. Solids, 44(I), 1129–145. Retrieved from http://ac.els-cdn.com.insis.bib.cnrs.fr/0022509695000801/1-s2.0-0022509695000801-main.pdf?_tid=dd5e5032-2a51-11e7-95d6-00000aacb35f&acdnat=1493191855_dfd8db55bb705a601e4358041e009ca2

Heraldo Costa Da S., M., & Martins, S. D. A. (2013). Plastic behaviour of an epoxy polymer under cyclic tension. Polymer Testing, 32(1), 1–8. https://doi.org/10.1016/j.polymertesting.2012.08.009

Herman, G. T. (1979). Demonstration of Beam Hardening Correction in Computed Tomography of the Head. Journal of Computer Assisted Tomography, 3(3), 373–378. https://doi.org/10.1097/00004728-197906000-00013

Hild, F., Bouterf, A., Roux, S., Hild, F., Bouterf, A., & Roux, S. (2015). Damage measurements via DIC From physical to mechanical damage. Int J Fract, 191, 77–105. https://doi.org/10.1007/s10704-015-0004-7

Hill, R. (1963). Elastic Properties of Reinforced Solids: Some Theoritical Principles. Journal of the Mechanics and Physics of Solids. https://doi.org/10.1016/0022-5096(63)90036-X

Hill, R. (1965). Theory of mechanical properties of fibre-strengthened materials—III. self-consistent model. Journal of the Mechanics and Physics of Solids, 13(4), 189–198. https://doi.org/10.1016/0022-5096(65)90008-6

Hivet, G., & Boisse, P. (2007). Consistent mesoscopic mechanical behaviour model for woven composite reinforcements in biaxial tension. https://doi.org/10.1016/j.compositesb.2007.01.011

Hochard, C., Aubourg, P. a., & Charles, J. P. (2001). Modelling of the mechanical behaviour of woven-fabric CFRP laminates up to failure. Composites Science and Technology, 61(2), 221–230. https://doi.org/10.1016/S0266-3538(00)00199-8

Hochard, C., Miot, S., & Thollon, Y. (2013). Fatigue of laminated composite structures with stress concentrations. Composites Part B: Engineering, 65, 11–16. https://doi.org/10.1016/j.compositesb.2013.10.020

Hochard, C., Payan, J., & Bordreuil, C. (2006). A progressive first ply failure model for woven ply CFRP laminates under static and fatigue loads. International Journal of Fatigue, 28(10 SPEC. ISS.), 1270–1276. https://doi.org/10.1016/j.ijfatigue.2006.02.024

Hochard, C., & Thollon, Y. (2010). A generalized damage model for woven ply laminates under static and fatigue loading conditions. International Journal of Fatigue, 32(1), 158–165. https://doi.org/10.1016/j.ijfatigue.2009.02.016

Hollister, S. J., & Kikuehi, N. (1992). A comparison of homogenization and standard mechanics analyses for periodic porous composites. Computational Mechanics, 10, 73–95. Retrieved from http://home.iitk.ac.in/~mohite/homogenization.pdf

Huchette, C., Lévèque, D., & Carrère, N. (2005). Un modèle multiéchelle séquencé d'endommagement basé sur une approche mixte (contrainte/énergie). 14èmes Journées Nationales Sur Les Composites, Compiègne.

Husseini, H. Al. (2014). Adaptation de la méthode de corrélation d'images numériques pour la gestion des discontinuités du milieu et de la transformation.

Iassonov, P., Gebrenegus, T., & Tuller, M. (2009). Segmentation of X-ray computed tomography images of porous materials: A crucial step for characterization and quantitative analysis of pore structures. Water Resources Research, 45(9). https://doi.org/10.1029/2009WR008087

Ivanov, D., Lomov, S. V., Verpoest, I., Baudry, F., & Xie, H. (2006). Damage Initiation and Development in Triaxial Braid and Fine Structure of Damage. Retrieved from http://www.mtm.kuleuven.ac.be/Research/C2/poly/index.htm

Ivanov, D. S. (2009). Damage analysis of textile composites. Katholieke Universiteit,Leuven.

Ivanov, D. S., Lomov, S. V., Ivanov, S. G., & Verpoest, I. (2010). Stress distribution in outer and inner plies of textile laminates and novel boundary conditions for unit cell analysis. Composites Part A: Applied Science and Manufacturing, 41(4), 571–580. https://doi.org/10.1016/j.compositesa.2010.01.004

Ivens, J., & Verpoest, I. (1996). A Three-Dimensional of Woven-Fabric Micromechanical Analysis Composites: I. Geometric Analysis, 56, 1303–1315.

Jespersen, K. M., Zangenberg, J., Lowe, T., Withers, P. J., & Mikkelsen, L. P. (2016). Fatigue damage assessment of uni-directional non-crimp fabric reinforced polyester composite using X-ray computed tomography. Composites Science and Technology, 136, 94–103. https://doi.org/10.1016/j.compscitech.2016.10.006

Jin, H., Lu, W.-Y., & Korellis, J. (2008). Micro-scale deformation measurement using the digital image correlation technique and scanning electron microscope imaging. The Journal of Strain Analysis for Engineering Design, 43(8), 719–728. https://doi.org/10.1243/03093247JSA412

Johnson, P., & Chang, F.-K. (2001). Characterization of Matrix Crack-Induced Laminate Failure—Part I: Experiments. Journal of Composite Materials, 35(22), 2009–2035. https://doi.org/10.1106/7RN1-PFBN-XQR9-3KDK

Kashtalyan, M., & Soutis, C. (2000). Stiffness degradation in cross-ply laminates damaged by transverse cracking and splitting. Composites Part A: Applied Science and Manufacturing, 31(4), 335–351. https://doi.org/10.1016/S1359-835X(99)00077-9

Khajeh, A., Mustapha, F., Sultan, M. T. H., Bánhegyi, G., Karácsony, Z., & Baranyai, V. (2015). The Effect of Thermooxidative Aging on the Durability of Glass Fiber-Reinforced Epoxy. Advances in Materials Science and Engineering, 2015. https://doi.org/10.1155/2015/372354

Kim, H. J., & Swan, C. C. (2003). Voxel-based meshing and unit-cell analysis of textile composites. International Journal for Numerical Methods in Engineering, 56(7), 977–1006. https://doi.org/10.1002/nme.594

Kristofer Gamstedt, E., Redon, O., & Brøndsted, P. (2002). Fatigue Dissipation and Failure in Unidirectional and Angle-Ply Glass Fibre/Carbon Fibre Hybrid Laminates. Key Engineering Materials, 221-222, 35–48. https://doi.org/10.4028/www.scientific.net/KEM.221-222.35

Ladeveze, P., & Ledantec, E. (1992). Damage modelling of the elementary ply for laminated composites. Composites Science and Technology, 43(3), 257–267. https://doi.org/10.1016/0266-3538(92)90097-M

Lafarie-Frenot, M. C. (2006). Damage mechanisms induced by cyclic ply-stresses in carbon-epoxy laminates: Environmental effects. International Journal of Fatigue, 28(10 SPEC. ISS.), 1202–1216. https://doi.org/10.1016/j.ijfatigue.2006.02.014

Lafarie-Frenot, M. C., & Hénaff-Gardin, C. (1991). Formation and growth of 90° ply fatigue cracks in carbon/epoxy laminates. Composites Science and Technology, 40(3), 307–324. https://doi.org/10.1016/0266-3538(91)90087-6

Lafarie-Frenot, M. C., Hénaff-Gardin, C., & Gamby, D. (2001). Matrix cracking induced by cyclic ply stresses in composite laminates. Composites Science and Technology, 61(15), 2327–2336. https://doi.org/10.1016/S0266-3538(01)00125-7

Lafarie-Frenot, M. C., & Ho, N. Q. (2006). Influence of free edge intralaminar stresses on damage process in CFRP laminates under thermal cycling conditions. Composites Science and Technology, 66(10), 1354–1365. https://doi.org/10.1016/j.compscitech.2005.09.006

Lafarie-Frenot, M. C., & Rouquie, S. (2004). Influence of oxidative environments on damage in c/epoxy laminates subjected to thermal cycling. Composites Science and Technology, 64(10-11), 1725–1735. https://doi.org/10.1016/j.compscitech.2004.01.005

Lafarie-Frenot, M. C., Rouquié, S., Ho, N. Q., & Bellenger, V. (2006). Comparison of damage development in C/epoxy laminates during isothermal ageing or thermal cycling. Composites Part A: Applied Science and Manufacturing, 37(4), 662–671. https://doi.org/10.1016/j.compositesa.2005.05.002

Lam Nguyen, T., Hall, S. A., Vacher, P., & Viggiani, G. (2011). Fracture mechanisms in soft rock: Identification and quantification of evolving displacement discontinuities by extended digital image correlation. Tectonophysics, 503, 117–128. https://doi.org/10.1016/j.tecto.2010.09.024

Lamb, J. T. (2016). Replacement for Toxic Methylenedianiline in PMR-15 : Chemistry and Properties.

Lamouroux, F., Bertrand, S., Pailler, R., Naslain, R., & Cataldi, M. (1999). Oxidation-resistant carbon-fiber-reinforced ceramic-matrix composites. Composites Science and Technology, 59(7), 1073–1085. https://doi.org/10.1016/S0266-3538(98)00146-8

Laurin, F., Charrier, J.-S., Lévêque, D., Maire, J.-F., Mavel, a., & Nuñez, P. (2012). Determination of the Properties of Composite Materials Thanks to Digital Image Correlation Measurements. Procedia IUTAM, 4(0), 106–115. https://doi.org/10.1016/j.piutam.2012.05.012

Laws, N., & Dvorak, G. J. (1988). Progressive Transverse Cracking In Composite Laminates. Composite Materials, 22(October), 900–916. https://doi.org/10.1177/002199838802201001

Lee, J.-W., Allen, D. H., & Harris, C. E. (1989). Internal State Variable Approach for Predicting Stiffness Reductions in Fibrous Laminated Composites with Matrix Cracks. Journal of Composite Materials, 23(12), 1273–1291. https://doi.org/10.1177/002199838902301205

Lee, J.-W., & Daniel, I. M. (1990). Progressive Transverse Cracking of Crossply Composite Laminates. Journal of Composite Materials, 24(11), 1225–1243. https://doi.org/10.1177/002199839002401108

Lemaitre, J., & Desmorat, R. (2005). Engineering Damage Mechanics. Springer Berlin Heidelberg New York Library. Berlin/Heidelberg: Springer-Verlag. https://doi.org/10.1007/b138882

Lévêque, D., Schieffer, A., Mavel, A., & Maire, J. F. (2005). Analysis of how thermal aging affects the long-term mechanical behavior and strength of polymer-matrix composites. Composites Science and Technology, 65(3-4), 395–401. https://doi.org/10.1016/j.compscitech.2004.09.016

Li, S. (2001). General unit cells for micromechanical analyses of unidirectional composites. Composites Part A: Applied Science and Manufacturing, 32(6), 815–826. https://doi.org/10.1016/S1359-835X(00)00182-2

Lin, H., Brown, L. P., & Long, A. C. (2011). Modelling and Simulating Textile Structures Using TexGen. In Advances in Textile Engineering (Vol. 331, pp. 44–47). Trans Tech Publications. https://doi.org/10.4028/www.scientific.net/AMR.331.44

Lin, Y. C., Chen, X. M., & Zhang, J. (2011). Uniaxial ratchetting behavior of anisotropic conductive adhesive film under cyclic tension. Polymer Testing, 30(1), 8–15. https://doi.org/10.1016/j.polymertesting.2010.10.003

Lisle, T., Bouvet, C., Pastor, M.-L., Rouault, T., & Margueres, P. (2015). Damage of woven composite under tensile and shear stress using infrared thermography and micrographic cuts. Journal of Materials Science, 50(18), 6154–6170. https://doi.org/10.1007/s10853-015-9173-z

Lomov, S. V., Boisse, P., Deluycker, E., Morestin, F., Vanclooster, K., Vandepitte, D., … Willems, A. (2008). Full-field strain measurements in textile deformability studies. Composites Part A: Applied Science and Manufacturing, 39(8), 1232–1244. https://doi.org/10.1016/j.compositesa.2007.09.014

Lomov, S. V., Ivanov, D. S., Truong, T. C., Verpoest, I., Baudry, F., Vanden Bosche, K., & Xie, H. (2008). Experimental methodology of study of damage initiation and development in textile composites in uniaxial tensile test. Composites Science and Technology, 68(12), 2340–2349. https://doi.org/10.1016/j.compscitech.2007.07.005

Lomov, S. V., Ivanov, D. S., Verpoest, I., Zako, M., Kurashiki, T., Nakai, H., & Hirosawa, S. (2007). Meso-FE modelling of textile composites: Road map, data flow and algorithms. Composites Science and Technology, 67(9), 1870–1891. https://doi.org/10.1016/j.compscitech.2006.10.017

Lomov, S. V., Ivanov, D. S., Verpoest, I., Zako, M., Kurashiki, T., Nakai, H., … Vautrin, A. (2008). Full-field strain measurements for validation of meso-FE analysis of textile composites. Composites Part A: Applied Science and Manufacturing, 39(8), 1218–1231. https://doi.org/10.1016/j.compositesa.2007.09.011

Long, A. C. A. C. (2007). Composites forming technologies. Woodhead publishing limited (Vol. 53). Woodhead. https://doi.org/10.1201/9781439824344

Lubineau, G., Violeau, D., & Ladevèze, P. (2009). Illustrations of a microdamage model for laminates under oxidizing thermal cycling. Composites Science and Technology, 69(1), 3–9. https://doi.org/10.1016/j.compscitech.2007.10.042

Ma, S., Pang, J., & Ma, Q. (2012). The systematic error in digital image correlation induced by self-heating of a digital camera. Measurement Science and Technology, 23(2), 025403. https://doi.org/10.1088/0957-0233/23/2/025403

Ma, Y., Zhang, Y., Sugahara, T., Jin, S., Yang, Y., & Hamada, H. (2016). Off-axis tensile fatigue assessment based on residual strength for the unidirectional 45° carbon fiber-reinforced composite at room temperature. Composites Part A, 90, 711–723. https://doi.org/10.1016/j.compositesa.2016.09.001

Maillet, E., Godin, N., R 'mili, M., Reynaud, P., Fantozzi, G., & Lamon, J. (2014). Damage monitoring and identification in SiC/SiC minicomposites using combined acousto-ultrasonics and acoustic emission. Composites Part A, 57, 8–15. https://doi.org/10.1016/j.compositesa.2013.10.010

Maillet, E., Godin, N., R'Mili, M., Reynaud, P., Fantozzi, G., Lamon, J., & Fayolle, G. (2012). Analyse de la libération d'énergie des sources d'émission acoustique pour la prévision de la durée de vie de CMC lors d'essais de fatigue statique en température. Matériaux & Techniques, 641, 631–641. https://doi.org/10.1051/mattech/2012025

Malpot, A., Touchard, F., & Bergamo, S. (2015). Effect of relative humidity on mechanical properties of a woven thermoplastic composite for automotive application. Polymer Testing, 48, 160–168. https://doi.org/10.1016/j.polymertesting.2015.10.010

Mangalgiri, P. D. (2005, April 1). Polymer-matrix composites for high-temperature applications. Defence Science Journal. https://doi.org/10.14429/dsj.55.1980

Marais, C., Schieffer, A., & Colin, X. (2003). Multidisciplinary Effects of Aging Factors on Damage in Structural Composites Summary : Time.

Mardiris, V., & Chatzis, V. (2016). A configurable design for morphological erosion and dilation operations in image processing using quantum-dot cellular automata. Journal of Engineering Science and Technology Review, 9(2), 25–30. Retrieved from http://www.jestr.org/downloads/Volume9Issue2/fulltext5922016.pdf

Meador, M. A. B., Lowell, C. E., Cavano, P. J., & Herrera-Fierro, P. (1996). On the Oxidative Degradation of Nadic Endcapped Polyimides: I. Effect of Thermocycling on Weight Loss and Crack Formation. High Performance Polymers, 8(3), 363–379. https://doi.org/10.1088/0954-0083/8/3/003

Megha Goyal. (2011). Morphological Image Processing. Practical Image and Video Processing Using …, 8491(4), 161–165. https://doi.org/10.1117/1.2744044

Mehdikhani, M., Aravand, M., Sabuncuoglu, B., Callens, M. G., Lomov, S. V., & Gorbatikh, L. (2016). Full-field strain measurements at the micro-scale in fiber-reinforced composites using digital image correlation. Composite Structures, 140, 192–201. https://doi.org/10.1016/j.compstruct.2015.12.020

Minervino, M. (2013). Effets de la thermo-oxydation sur le comportement mécanique de matériaux composites pour applications aéronautiques. ENSMA. Retrieved from http://www.theses.fr/2013ESMA0015/document

Moës, N., Dolbow, J., & Belytschko, T. (1999). A finite element method for crack growth without remeshing. International Journal for Numerical Methods in Engineering, 46(1), 131–150. https://doi.org/10.1002/(SICI)1097-0207(19990910)46:1<131::AID-NME726>3.0.CO;2-J

Montagnier, O., Charles, J.-P., Eyer, G., Hochard, C., Lahellec, N., & Mazerolle, F. (2015). Essai et simulation du comportement d ' une structure sandwich entaillée jusqu ' à rupture Test and simulation of behavior of a composite sandwich structure with a notch up to failure. In Comptes Rendus JNC 19.

Montesano, J., Selezneva, M., Fawaz, Z., Poon, C., & Behdinan, K. (2012). Elevated temperature off-axis fatigue behavior of an eight-harness satin woven carbon-fiber/bismaleimide laminate. Composites Part A: Applied Science and Manufacturing, 43(9), 1454–1466. https://doi.org/10.1016/j.compositesa.2012.04.016

Muñoz, R., González, C., & Llorca, J. (2015). Mechanisms of in-plane shear deformation in hybrid three-dimensional woven composites. J. Compos. Mater., 49(30), 1–9. https://doi.org/10.1177/0021998314568333

Naik, R. A. (2001). Tension Fatigue Analysis of Woven Composite Laminates. ICF10, Honolulu, Hawaii - 2001, (i). Retrieved from http://www.icf-wasi.org/documents/proceedings/icf10-honolulu-hawaii-2001/doc_download/5092-tension-fatigue-analysis-for-woven-composite-laminates.html

Nairn, J. a. (1988). Fracture Mechanics of Unidirectional Composites Using the Shear-Lag Model II: Experiment. Journal of Composite Materials, 22(6), 589–600. https://doi.org/10.1177/002199838802200604

Nairn, J. A. (1997). Fracture Mechanics of Composites With Residual Thermal Stresses. Journal of Applied Mechanics, 64(4), 804. https://doi.org/10.1115/1.2788985

Nairn, J. A. (1997). On the Use of Shear-Lag Methods for Analysis of Stress Transfer in Unidirectional Composites. Mechanics of Materials, 26, 63–80. https://doi.org/10.1016/S0167-6636(97)00023-9

Nairn, J. A. (2001). Matrix Microcracking in Composites. Polymer Matrix Composites, 2, 34. https://doi.org/DOI: 10.1016/S0266-3538(01)00110-5

Nairn, J. A., Hu, S., & Bark, J. S. (1993). A critical evaluation of theories for predicting microcracking in composite laminates. Journal of Materials Science, 28(18), 5099–5111. https://doi.org/10.1007/BF00361186

Nairn, J. A., & Mendels, D. A. (2001). On the use of planar shear-lag methods for stress-transfer analysis of multilayered composites. Mechanics of Materials, 33(6), 335–362. https://doi.org/10.1016/S0167-6636(01)00056-4

Nairn, J. A., & Wedgewood, R. (1991). Longitudinal Splitting in Epoxy and K-Polymer Composites : Shear Lag Analysis Including the Effect of Fiber Bridging. https://doi.org/10.1177/002199839102500901

Naouar, N., Vidal-Salle, E., Maire, E., Schneider, J., & Boisse, P. (2016). Simulation E.F a l echelle mésoscopique de la déformation de renforts compositè a partir de microtomographiè a rayon X. Matériaux & Techniques, 104(409). https://doi.org/10.1051/mattech/2016029

Nghiem, H. L., Al-Heib, M., & Emeriault, F. (2015). Method based on digital image correlation for damage assessment in masonry structures. Engineering Structures, 86, 1–15. https://doi.org/10.1016/j.engstruct.2014.12.021

Nicoletto, G., Anzelotti, G., & Riva, E. (2009). Mesoscopic strain fields in woven composites: Experiments vs. finite element modeling. Optics and Lasers in Engineering, 47(3-4), 352–359. https://doi.org/10.1016/j.optlaseng.2008.07.009

Nixon-Pearson, O. J., Hallett, S. R., Harper, P. W., & Kawashita, L. F. (2013). Damage development in open-hole composite specimens in fatigue. Part 2: Numerical modelling. Composite Structures, 106, 890–898. https://doi.org/10.1016/j.compstruct.2013.05.019

Nutting, P. (1921). A study of elastic viscous deformation. Proceedings of the American Society for Testing Materials, XXI, 1162–1171. Retrieved from https://www.astm.org/DIGITAL_LIBRARY/STP/MMR/PAGES/PRO1921-21.htm

Ogi, K., & Takao, Y. (2001). Modeling of time-dependent behavior of deformation and transverse cracking in cross-ply laminates. Advanced Composite Materials, 10(February 2013), 39–62. https://doi.org/10.1163/15685510152546358

Okuta Baba, B. (2006). Behavior of pin-loaded laminated composites. Experimental Mechanics, 46(5), 589–600. https://doi.org/10.1007/s11340-006-8735-z

Oliver, W. C., & Pharr, G. M. (2004). Measurement of hardness and elastic modulus by instrumented indentation: Advances in understanding and refinements to methodology. Journal of Materials Research, 19(01), 3–20. https://doi.org/10.1557/jmr.2004.19.1.3

Olivier, L. (2008). Prévision du vieillissement thermo-oxydant de composites à matrice organique dédiés à l'aéronautique : Prise en compte des couplages multiphysiques. ENSMA.

Olivier, L., Ho, N. Q., Grandidier, J. C., & Lafarie-Frenot, M. C. (2008). Characterization by ultra-micro indentation of an oxidized epoxy polymer: Correlation with the predictions of a kinetic model of oxidation. Polymer Degradation and Stability, 93(2), 489–497. https://doi.org/10.1016/j.polymdegradstab.2007.11.012

Osada, T., Nakai, A., & Hamada, H. (2003). Initial fracture behavior of satin woven fabric composites. Composite Structures, 61(4), 333–339. https://doi.org/10.1016/S0263-8223(03)00058-8

Owens, G. a., & Schofield, S. E. (1988). Thermal cycling and mechanical property assessment of carbon fibre fabric reinforced PMR-15 polyimide laminates. Composites Science and Technology, 33(3), 177–190. https://doi.org/10.1016/0266-3538(88)90059-0

Pan, B., Lu, Z., & Xie, H. Mean intensity gradient: An effective global parameter for quality assessment of the speckle patterns used in digital image correlation. Optics and Lasers in Engineering, 48(4), 469–477. https://doi.org/10.1016/j.optlaseng.2009.08.010

Pan, B., Qian, K., Xie, H., & Asundi, A. (2009). Two-dimensional digital image correlation for in-plane displacement and strain measurement: a review. Meas. Sci. Technol. Meas. Sci. Technol, 20(20), 62001–17. https://doi.org/10.1088/0957-0233/20/6/062001

Pan, B., Wu, D., Wang, Z., & Xia, Y. (2010). High-temperature digital image correlation method for full-field deformation measurement at 1200 °C. Measurement Science and Technology, 22(1), 015701. https://doi.org/10.1088/0957-0233/22/1/015701

Pandita, S. D., Huysmans, G., Wevers, M., & Verpoest, I. (2001). Tensile fatigue behaviour of glass plain-weave fabric composites in on- and off-axis directions. Composites - Part A: Applied Science and Manufacturing, 32(10), 1533–1539. https://doi.org/10.1016/S1359-835X(01)00053-7

Parvizi, A., & Bailey, J. E. (1978a). Constrained cracking in glass fibre-reinforced epoxy cross-ply laminates. Journal of Materials Science, 13(1), 195 – 201. https://doi.org/10.1007/BF00739291

Parvizi, A., & Bailey, J. E. (1978b). On multiple transverse cracking in glass fibre epoxy cross-ply laminates. Journal of Materials Science, 13(10), 2131–2136. https://doi.org/10.1007/BF00541666

Payan, J., & Hochard, C. (2002). Damage modelling of laminated carbon/epoxy composites under static and fatigue loadings. International Journal of Fatigue, 24(2-4), 299–306. https://doi.org/10.1016/S0142-1123(01)00085-8

Pazmino, J., Carvelli, V., & Lomov, S. V. (2014). Micro-CT analysis of the internal deformed geometry of a non-crimp 3D orthogonal weave E-glass composite reinforcemen. Composites Part A: Applied Science and Manufacturing, 61, 76–83. https://doi.org/10.1016/j.compositesa.2014.02.004

Petermann, J. (2004). A contribution to evaluate and predict the strength and life time of angle-ply CFRP laminates under static and cyclic loads. Cuvillier. Retrieved from https://books.google.fr/books?id=4zKwEEd8y5IC&pg=PA45&hl=fr&source=gbs_toc_r&cad=4#v=onepage&q&f=false

Petermann, J., & Schulte, K. (2002). The effects of creep and fatigue stress ratio on the long-term behaviour of angle-ply CFRP. Composite Structures, 57(1-4), 205–210. https://doi.org/10.1016/S0263-8223(02)00084-3

Pochiraju, K. V., Schoeppner, G. A., & Tandon, G. P. (2012). Long-term durability of polymeric matrix composites. Long-Term Durability of Polymeric Matrix Composites (Vol. 9781441993). https://doi.org/10.1007/978-1-4419-9308-3

Pochiraju, K. V., & Tandon, G. P. (2006). Modeling Thermo-Oxidative Layer Growth in High-Temperature Resins. Journal of Engineering Materials and Technology, 128(1), 107. https://doi.org/10.1115/1.2128427

Pochiraju, K. V., & Tandon, G. P. (2009). Interaction of oxidation and damage in high temperature polymeric matrix composites. Composites Part A: Applied Science and Manufacturing, 40(12), 1931–1940. https://doi.org/10.1016/j.compositesa.2009.03.010

Quaresimin, M., Carraro, P. a., & Maragoni, L. (2016). Early stage damage in off-axis plies under fatigue loading. Composites Science and Technology, 128, 147–154. https://doi.org/10.1016/j.compscitech.2016.03.015

Quaresimin, M., Susmel, L., & Talreja, R. (2010). Fatigue behaviour and life assessment of composite laminates under multiaxial loadings. International Journal of Fatigue, 32(1), 2–16. https://doi.org/10.1016/j.ijfatigue.2009.02.012

Quartus. (2017). http://www.quartus.com/resources/white-papers/composites-101/. Retrieved July 19, 2017, from http://www.quartus.com/resources/white-papers/composites-101/

Rakotoarisoa, C. (2013). Prévision de la durée de vie en fatigue des composites à matrice organique tissés interlock. UNIVERSITE DE TECHNOLOGIE DE COMPIEGNE.

Ramakrishna, S. (1997). Characterization and modeling of the tensile properties of plain weft-knit fabric-reinforced composites. Composites Science and Technology, 57(1), 1–22. https://doi.org/10.1016/S0266-3538(96)00098-X

Raz-Ben Aroush, D., Maire, E., Gauthier, C., Youssef, S., Cloetens, P., & Wagner, H. (2005). A study of fracture of unidirectional composites using in situ high-resolution synchrotron X-ray microtomography. https://doi.org/10.1016/j.compscitech.2005.09.010

Réthoré, J., Hild, F., & Roux, S. (2007). Shear-band capturing using a multiscale extended digital image correlation technique. Computer Methods in Applied Mechanics and Engineering, 196. https://doi.org/10.1016/j.cma.2007.06.019>

Réthoré, J., Roux, S., & Hild, F. (2007). From pictures to extended finite elements: extended digital image correlation (X-DIC). Comptes Rendus - Mecanique, 335(3), 131–137. https://doi.org/10.1016/j.crme.2007.02.003

Rotem, A., & Hashin, Z. (1975). Failure Modes of Angle Ply Laminates. Journal of Composite Materials, 9(2), 191–206. https://doi.org/10.1177/002199837500900209

Schapery, R. a. (1968). Thermal Expansion Coefficients of Composite Materials Based on Energy Principles. Journal of Composite Materials, 2(3), 380–404. https://doi.org/10.1177/002199836800200308

Schilling, P. J., Karedla, B. R., Tatiparthi, A. K., Verges, M. a., & Herrington, P. D. (2005). X-ray computed microtomography of internal damage in fiber reinforced polymer matrix composites. Composites Science and Technology, 65(14), 2071–2078. https://doi.org/10.1016/j.compscitech.2005.05.014

Schoeppner, G. a., Tandon, G. P., & Ripberger, E. R. (2007). Anisotropic oxidation and weight loss in PMR-15 composites. Composites Part A: Applied Science and Manufacturing, 38(3), 890–904. https://doi.org/10.1016/j.compositesa.2006.07.006

Schreier, H., & Sutton, M. a. (2002). Systematic Errors in Digital Image Correlation Due to Undermatched Subset Shape Functions. Experimental Mechanics, 42(3), 303–310. https://doi.org/10.1177/001448502321548391

Schreier, H. W., Braasch, J. R., & Sutton, M. A. (2000). Systematic errors in digital image correlation caused by intensity interpolation. Optical Engineering, 39(November), 2915. https://doi.org/10.1117/1.1314593

Scott, a. E., Mavrogordato, M., Wright, P., Sinclair, I., & Spearing, S. M. (2011). In situ fibre fracture measurement in carbon-epoxy laminates using high resolution computed tomography. Composites Science and Technology, 71(12), 1471–1477. https://doi.org/10.1016/j.compscitech.2011.06.004

Scott, a. E., Sinclair, I., Spearing, S. M., Thionnet, a., & Bunsell, a. R. (2012). Damage accumulation in a carbon/epoxy composite: Comparison between a multiscale model and computed tomography experimental results. Composites Part A: Applied Science and Manufacturing, 43(9), 1514–1522. https://doi.org/10.1016/j.compositesa.2012.03.011

Serra, J., & Vincent, L. (1992). An overview of morphological filtering. Circuits Systems and Signal Processing, 11(1), 47–108. https://doi.org/10.1007/BF01189221

Shen, H., Yao, W., Qi, W., & Zong, J. (2017). Experimental investigation on damage evolution in cross-ply laminates subjected to quasi-static and fatigue loading. Composites Part B: Engineering, 120, 10–26. https://doi.org/10.1016/j.compositesb.2017.02.033

Sinchuk, Y., Pannier, Y., Gueguen, M., Tandiang, D., & Gigliotti, M. (2017). Computed-tomography based modeling and simulation of moisture diffusion and induced swelling in textile composite materials. International Journal of Solids and Structures, 1–9. https://doi.org/10.1016/j.ijsolstr.2017.05.045

Singh, C. V., & Talreja, R. (2008). Analysis of multiple off-axis ply cracks in composite laminates. International Journal of Solids and Structures, 45(16), 4574–4589. https://doi.org/10.1016/j.ijsolstr.2008.04.004

Sisodia, S. M., Garcea, S. C., George, a. R., Fullwood, D. T., Spearing, S. M., & Gamstedt, E. K. (2016). High-resolution computed tomography in resin infused woven carbon fibre composites with voids. Composites Science and Technology, 131, 12–21. https://doi.org/10.1016/j.compscitech.2016.05.010

Siulie Liu, & Nairn, J. A. (1992). The Formation and Propagation of Matrix Microcracks in Cross-Ply Laminates during Static Loading. Journal of Reinforced Plastics and Composites, 11(2), 158–178. https://doi.org/10.1177/073168449201100204

Sket, F., Aldareguia, J. M. M., González, C., & Llorca, J. (2014). Damage and defects assessment in composite materials using X-ray Computed Tomography. In 6th International Symposium on NDT in Aerospace. Madrid.

Sket, F., Enfedaque, a., Alton, C., González, C., Molina-Aldareguia, J. M., & Llorca, J. (2014). Automatic quantification of matrix cracking and fiber rotation by X-ray computed tomography in shear-deformed carbon fiber-reinforced laminates. Composites Science and Technology, 90, 129–138. https://doi.org/10.1016/j.compscitech.2013.10.022

Sket, F., Rodriguez-Hortala, M., Molina-Aldareguia, J. M., Llorca, J., Maire, E., & Requena, G. (2015). In situ tomographic investigation of damage development in +/- 45 degrees carbon fibre reinforced laminates. Materials Science and Technology, 31(5), 587–593. https://doi.org/10.1179/1743284714y.0000000561

Song, D.-Y., & Otani, N. (1998). Approximate estimation of fatigue strength of polymer matrix composites by material properties. Materials Science and Engineering, 254, 200–206. Retrieved from http://ac.els-cdn.com.insis.bib.cnrs.fr/S0921509398007035/1-s2.0-S0921509398007035-main.pdf?_tid=5f9d01ac-71ff-11e7-86d6-00000aacb362&acdnat=1501072909_32b0c21c05dc93a206f7645d21e5cdd0

Stock, S. R. (1999). X-ray microtomography of materials. International Materials Reviews, 44(4), 141–164. https://doi.org/10.1179/095066099101528261

Straumit, I., Lomov, S. V., & Wevers, M. (2015). Quantification of the internal structure and automatic generation of voxel models of textile composites from X-ray computed tomography data. Composites Part A: Applied Science and Manufacturing, 69, 150–158. https://doi.org/10.1016/j.compositesa.2014.11.016

Sturgeon, J. B. (1978). Creep. repeated loading, fatigue and crack growth in ~ oriented carbon fibre reinforced plastics. JOURNAL OF MATERIALS SCIENCE, 13, 1490–1498. Retrieved from http://download.springer.com.gate6.inist.fr/static/pdf/59/art%3A10.1007%2FBF00553204.pdf?originUrl=http%3A%2F%2Flink.springer.com%2Farticle%2F10.1007%2FBF00553204&token2=exp=1491900471~acl=%2Fstatic%2Fpdf%2F59%2Fart%25253A10.1007

Sun, C., & Chim, E. (1981). Fatigue Retardation Due to Creep in a Fibrous Composite. In Fatigue of Fibrous Composite Materials (pp. 233–233–10). 100 Barr Harbor Drive, PO Box C700, West Conshohocken, PA 19428-2959: ASTM International. https://doi.org/10.1520/STP27623S

Sun, W., Brown, S. B., & Leach, R. K. (2011). An Overview of Industrial Marketing. Advances in Management, 4(3), 64–65.

Sun, Z., Daniel, I. M., & Luo, J. J. (2003). Statistical damage analysis of transverse cracking in high temperature composite laminates. Materials Science and Engineering A, 341(1-2), 49–56. https://doi.org/10.1016/S0921-5093(02)00241-1

Sutton, M. A., Orteu, J. J., & Schreier, H. (2009). Image correlation for shape, motion and deformation measurements: Basic Concepts, Theory and Applications. Springer.

Sutton, M. A., Yan, J. H., Tiwari, V., Schreier, H. W., & Orteu, J. J. (2008). The effect of out-of-plane motion on 2D and 3D digital image correlation measurements. Optics and Lasers in Engineering, 46(10), 746–757. https://doi.org/10.1016/j.optlaseng.2008.05.005

Tabatabaei, S. a, Bedogni, E., Ivanov, D., Lomov, S. V., & Building, Q. (2014). Meso-Scale Damage Modelling of Textile Composite Using the Embedded Element Technique and Contact, (June), 22–26.

Tabatabaei, S. a., & Lomov, S. V. (2015). Eliminating the volume redundancy of embedded elements and yarn interpenetrations in meso-finite element modelling of textile composites. Computers & Structures, 152, 142–154. https://doi.org/10.1016/j.compstruc.2015.02.014

Tabatabaei, S. a., Lomov, S. V., & Verpoest, I. (2014). Assessment of embedded element technique in meso-FE modelling of fibre reinforced composites. Composite Structures, 107, 436–446. https://doi.org/10.1016/j.compstruct.2013.08.020

Takeda, N., & Ogihara, S. (1994). Initiation and growth of delamination from the tips of transverse cracks in CFRP cross-ply laminates. Composites Science and Technology, 52(3), 309–318. https://doi.org/10.1016/0266-3538(94)90166-X

Talreja, R. (1981). Fatigue of Composite Materials: Damage Mechanisms and Fatigue-Life Diagrams. Proceedings of the Royal Society of London A: Mathematical, Physical and Engineering Sciences, 378(1775), 461–475. https://doi.org/10.1098/rspa.1981.0163

Talreja, R. (1985). Transverse Cracking and Stiffness Reduction in Composite Laminates. Journal of Composite Materials, 19(4), 355–375. https://doi.org/10.1177/002199838501900404

Tandon, G. P., Pochiraju, K. V., & Hall, R. B. (2009). Characterizing Thermo-Oxidative Behaviour of Multi-Directional Laminated Composites. In 17th International Conference on Composite Materials (ICCM-17). Edinburgh.

Tandon, G. P., Pochiraju, K. V., & Schoeppner, G. a. (2008). Thermo-oxidative behavior of high-temperature PMR-15 resin and composites. Materials Science and Engineering A, 498(1-2), 150–161. https://doi.org/10.1016/j.msea.2007.09.103

Tandon, G. P., & Ragland, W. R. (2011). Influence of laminate lay-up on oxidation and damage growth: Isothermal aging. Composites Part A: Applied Science and Manufacturing, 42(9), 1127–1137. https://doi.org/10.1016/j.compositesa.2011.04.018

Tang, C., Hou, C., Hou, Y., Wang, P., & Li, W. (2016). Graphical abstract An effective edge-preserving smoothing method for image. Digital Signal Processing, 63, 10–24. https://doi.org/10.1016/j.dsp.2016.10.009

Tang, X., & Whitcomb, J. D. (2003). General Techniques for Exploiting Periodicity and Symmetries in Micromechanics Analysis of Textile Composites. Journal of Composite Materials, 37(13), 1167–1189. https://doi.org/10.1177/0021998303037013003

Tang, X., Whitcomb, J. D., Li, Y., & Sue, H. J. (2005). Micromechanics modeling of moisture diffusion in woven composites. Composites Science and Technology, 65(6), 817–826. https://doi.org/10.1016/j.compscitech.2004.01.015

Tao, G., & Xia, Z. (2007). Ratcheting behavior of an epoxy polymer and its effect on fatigue life. Polymer Testing, 26(4), 451–460. https://doi.org/10.1016/j.polymertesting.2006.12.010

Thang, V. A. (2009). Endommagement de stratifiés aéronautiques à fibres de carbone et matrice polymère soumis à des chargements monotones ou cycliques à plusieurs températures. Essais et modélisation.

Thollon, Y., & Hochard, C. (2009). A general damage model for woven fabric composite laminates up to first failure. Mechanics of Materials, 41(7), 820–827. https://doi.org/10.1016/j.mechmat.2009.02.009

Thornel. (n.d.). Cytec Thornel. Retrieved June 16, 2017, from http://www.matweb.com/search/datasheet.aspx?matguid=7e9aca60a2e84538a4e8038784f2b629&ckck=1

Topal, S., Baiocchi, L., Crocombe, A. D., Ogin, S. L., Potluri, P., Withers, P. J., … Bogdanovich, A. E. (2015). Late-stage fatigue damage in a 3D orthogonal non-crimp woven composite: An experimental and numerical study. Composites Part A: Applied Science and Manufacturing, 79, 155–163. https://doi.org/10.1016/j.compositesa.2015.08.020

Toubal, L., Karama, M., & Lorrain, B. (2006). Damage evolution and infrared thermography in woven composite laminates under fatigue loading. International Journal of Fatigue, 28(12), 1867–1872. https://doi.org/10.1016/j.ijfatigue.2006.01.013

Truong, T. C., Vettori, M., Lomov, S. V., & Verpoest, I. (2005). Carbon composites based on multi-axial multi-ply stitched preforms. Part 4. Mechanical properties of composites and damage observation. Composites Part A: Applied Science and Manufacturing, 36(9), 1207–1221. https://doi.org/10.1016/j.compositesa.2005.02.004

Tsotsis, T. K., Keller, S., Bardis, J., & Bish, J. (1999). Preliminary evaluation of the use of elevated pressure to accelerate thermo-oxidative aging in composites. Polymer Degradation and Stability, 64(2), 207–212. https://doi.org/10.1016/S0141-3910(98)00190-6

Tsotsis, T. K., Keller, S., Lee, K., Bardis, J., & Bish, J. (1999). 3000 Hours Aging of Polymeric Composite Specimens Under Elevated Pressure and Temperature. 44th International SAMPE Symposium, 61, 75–86.

Valle, V., Hedan, S., Cosenza, P., Fauchille, a. L., & Berdjane, M. (2015). Digital Image Correlation Development for the Study of Materials Including Multiple Crossing Cracks. Experimental Mechanics, 55(2), 379–391. https://doi.org/10.1007/s11340-014-9948-1

Vallons, K., Zong, M., Lomov, S. V., & Verpoest, I. (2007). Carbon composites based on multi-axial multi-ply stitched preforms - Part 6. Fatigue behaviour at low loads: Stiffness degradation and damage development. Composites Part A: Applied Science and Manufacturing, 38(7), 1633–1645. https://doi.org/10.1016/j.compositesa.2007.03.003

Van Gompel, G., Van Slambrouck, K., Defrise, M., Batenburg, K. J., de Mey, J., Sijbers, J., & Nuyts, J. (2011). Iterative correction of beam hardening artifacts in CT. Medical Physics, 38(S1), S36–S49. https://doi.org/10.1118/1.3577758

Verpoest, I., & Lomov, S. V. (2005). Virtual textile composites software WiseTex: Integration with micro-mechanical, permeability and structural analysis. Composites Science and Technology, 65(15-16 SPEC. ISS.), 2563–2574. https://doi.org/10.1016/j.compscitech.2005.05.031

Vieille, B., & Albouy, W. (2015). Fatigue damage accumulation in notched woven-ply thermoplastic and thermoset laminates at high-temperature: Influence of matrix ductility and fatigue life prediction. International Journal of Fatigue, 80, 1–9. https://doi.org/10.1016/j.ijfatigue.2015.04.019

Vieille, B., Albouy, W., & Taleb, L. (2014). About the creep-fatigue interaction on the fatigue behaviour of off-axis woven-ply thermoplastic laminates at temperatures higher than Tg. Composites Part B: Engineering, 58, 478–486. https://doi.org/10.1016/j.compositesb.2013.11.005

Vieille, B., Aucher, J., & Taleb, L. (2013). Overstress accommodation in notched woven-ply thermoplastic laminates at high-temperature: Numerical modeling and validation by Digital Image Correlation. Composites Part B: Engineering, 45(1), 290–302. https://doi.org/10.1016/j.compositesb.2012.06.015

Vignoles, G., & Coindreau, O. (2007). Geometrical and transport properties of a fibrous C/C composite preform as digitized by x-ray computerized microtomography: Part II. Heat and gas transport properties. Journal of Materials …, 22(2007), 16–19. https://doi.org/10.1557/JMR.2005.0311

Vincent, L. (1994). Morphological area openings and closings for grey-scale images. Shape in Picture: Mathematical Description of Shape in Grey-Level Images, 196–208. https://doi.org/10.1007/978-3-662-03039-4_13

Vinogradov, V. (2002). Analysis of transverse cracking in fibre compositelaminates under static and cyclic loadings. Tel-Aviv University.

Vinogradov, V., & Hashin, Z. (2004). Probabilistic energy based model for prediction of transverse cracking in cross - ply laminates. https://doi.org/10.1016/j.ijsolstr.2004.06.043

Vu, A. T. (2010). Endommagement de stratifiés aéronautiques à fibres de carbone et matrice polymère soumis à des chargements monotones ou cycliques à plusieurs températures. Expériences et modélisation. Retrieved from https://tel.archives-ouvertes.fr/tel-00523580/

Vu, D. Q. (2011). Endommagements induits par la thermo oxydation dans les composites Carbone/Epoxy unidirectionnels et stratifiés. ISAE-ENSMA Ecole Nationale Supérieure de Mécanique et d'Aérotechique - Poitiers. Retrieved from https://tel.archives-ouvertes.fr/tel-00653866/

Vu, D. Q., Gigliotti, M., & Lafarie-Frenot, M. C. (2012). Experimental characterization of thermo-oxidation-induced shrinkage and damage in polymer-matrix composites. Composites Part A: Applied Science and Manufacturing, 43(4), 577–586. https://doi.org/10.1016/j.compositesa.2011.12.018

Vu, D. Q., Gigliotti, M., & Lafarie-Frenot, M. C. (2013). The effect of thermo-oxidation on matrix cracking of cross-ply [0/90] S composite laminates. Composites Part A: Applied Science and Manufacturing, 44(1), 114–121. https://doi.org/10.1016/j.compositesa.2012.08.013

Wang, A. S. D., Kishore, N. N., & Li, C. A. (1985). Crack development in graphite—epoxy cross-ply laminates under uniaxial tension. Composites Science and Technology, 24(1), 1–31. https://doi.org/10.1016/0266-3538(85)90058-2

Whitlow, T., Jones, E., & Przybyla, C. (2016). In-situ damage monitoring of a SiC/SiC ceramic matrix composite using acoustic emission and digital image correlation. Composite Structures, 158, 245–251. https://doi.org/10.1016/j.compstruct.2016.09.040

Whitney, J. M. (1967). Elastic Moduli of Unidirectional Composites with Anisotropic Filaments. Journal of Composite Materials, 1(2), 188–193. https://doi.org/10.1177/002199836700100208

Whitney, J. M., & McCullough, R. L. (1990). Micromechanical materials modeling. Technomic. Retrieved from https://www.crcpress.com/Delaware-Composites-Design-Encyc-Micromechanical-Materials-Model-Volume/University-of-Delawa/p/book/9780877626992

Wright, P., Fu, X., Spearing, S. M., & Sinclair, I. (2008). Ultra High Resolution Computed Tomography of Damage in Notched Carbon Fiber Epoxy Composites. Journal of Composite Materials, 42(19), 1993–2002. https://doi.org/10.1177/0021998308092211

Xu, J., Lomov, S. V., Verpoest, I., Daggumati, S., Van Paepegem, W., & Degrieck, J. (2016). A comparative study of twill weave reinforced composites under tension-tension fatigue loading: Experiments and meso-modelling. Composite Structures, 135, 306–315. https://doi.org/10.1016/j.compstruct.2015.09.005

Yu, B., Blanc, R., Soutis, C., & Withers, P. J. (2016). Evolution of damage during the fatigue of 3D woven glass-fibre reinforced composites subjected to tension-tension loading observed by time-lapse X-ray tomography. Composites Part A: Applied Science and Manufacturing, 82, 279–290. https://doi.org/10.1016/j.compositesa.2015.09.001

Zhang, Z., Chen, X., & Wang, Y. (2010). Uniaxial ratcheting behavior of polytetrafluoroethylene at elevated temperature. Polymer Testing, 29(3), 352–357. https://doi.org/10.1016/j.polymertesting.2010.01.001

Zhu, L., Starman, J., & Fahrig, R. (2008). An efficient estimation method for reducing the axial intensity drop in circular cone-beam CT. International Journal of Biomedical Imaging, 2008(1), 1–11. https://doi.org/10.1155/2008/242841

Zrida, H., Fernberg, P., Ayadi, Z., & Varna, J. (2017). Microcracking in thermally cycled and aged Carbon fibre/polyimide laminates. International Journal of Fatigue, 94, 121–130. https://doi.org/10.1016/j.ijfatigue.2016.09.017

List of Tables

List of Figures

Abstract

In the next future, the employment of organic matrix/carbon fibre composites (OMC) is foreseen for the realization of "hot" structures: these parts may be subjected, in service, to mechanical fatigue (e.g. fan blades turbo-engines), thermal cycling and thermo-mechanical fatigue (e.g. aircraft structural parts). Though there is a consistent literature concerning the fatigue behaviour of woven composites, the interaction between fatigue and environmental degradation at high temperature has been poorly explored. Coupling between thermo-oxidation effects, mechanical (viscoelastic, viscoplastic) behaviour of the polymer matrix at high temperatures and degradation due to fatigue may be highly detrimental for the material. This work aims at characterizing and modelling - for carbon fibre/organic matrix (polyimide) textile composites – the thermomechanical behaviour, the onset and the development of damage related to cyclic mechanical mechanisms (fatigue) under controlled (temperature and gas) environment.

A preliminary study on a cross-ply laminate $[0_2/90_2]_s$ has been carried out in order to analyse the environmental effect on a model sample. Digital Image Correlation (DIC) and μ-Computed Tomography (μCT) have been used to monitor and characterize the fatigue damage of 2D woven composites for aeronautical applications. The environmental effect on fatigue degradation have been also explored.

The long-term aim of the study is to provide experimental and numerical tools to strengthen the understanding and the modelling of mechanics/damage/environment coupling for durability prediction.

Keywords: Woven carbon fibre/polyimide matrix composite, high temperature fatigue, Thermo-oxidation effect, Digital Image Correlation, μ-Computed Tomography.

Résumé

Les composites à matrice organiques (CMO) et fibre de carbone sont de plus en plus employés dans la réalisation de structures « tièdes » (aubes de fan, nacelles …) ; ces pièces peuvent être soumises, en service, à la fatigue mécanique, au cyclage thermique et à la fatigue thermo-mécanique. Bien qu'il existe une littérature consistante sur le comportement en fatigue des composites tissés, l'interaction entre fatigue et la dégradation liée à l'environnement à haute température n'a pas été encore bien exploitée. Le couplage entre les effets de la thermo-oxydation, le comportement mécanique (viscoélastique, viscoplastique) de la matrice organique à températures élevées et la dégradation par fatigue peut être néfaste pour le composite.

Le but de ce travail est de caractériser et de modéliser - pour les composites tissés C/matrice organique - le comportement thermomécanique, l'apparition et le développement de l'endommagement liés aux mécanismes mécaniques cycliques (fatigue) sous environnement contrôlé (température et gaz).

Une étude préliminaire sur un composite stratifiée $[0_2/90_2]_s$ a été menée pour pouvoir analyser les effets de l'environnement sur une architecture simple. La corrélation d'image numérique (CIN) et des scans μ-tomographiques (μCT) ont été employés pour le suivi et la caractérisation de l'endommagement de fatigue de composites tissés 2D à architecture complexe pour applications aéronautiques. Les effets de l'environnement sur la dégradation par fatigue ont été également explorés.

L'objectif à long terme de cette étude est de fournir des outils expérimentaux et numériques pour renforcer la compréhension et la modélisation du couplage mécanique/endommagement/environnement pour la prédiction de la durée de vie et pour la proposition de protocoles d'essais accélérés réalistes de pièces « tièdes » en CMO.

Mots-clés: Tissés Carbone/Polyimide, Fatigue haute température, Effet de la Thermo-Oxydation, Corrélation d'Image Numérique, μ-Computed Tomogrphy.